Provenance study on the Karoo sedimentary rocks of the Chicôa-Mecúcoè sub-basin of the Zambezi Basin, Tete Provence, Mozambique: implications for basin development, sedimentary processes and tectonic controls.

MSc

By Llewelyn Whitecross

Student Number: 1395086

Supervisors: Dr. Zubair Jinnah & Dr. John Hancox

School of Geosciences, East Campus, University of the Witwatersrand, 1 Jan Smuts Avenue, Johannesburg, South Africa.

I declare that this dissertation is my own, unaided work. It is being submitted for the Degree of Master of Science at the University of Witwatersrand, Johannesburg. It has not been submitted before for any degree or examination at any other University.

(Signature of Candidate)

04th Day of June 2020

I am indebted to my supervisors Dr. John Hancox and Dr. Zubair Jinnah for their invaluable guidance, insight and expert knowledge on the Karoo Supergroup of southern Africa. Completing this research topic while working in remote areas of Africa has been extremely challenging. Their individual contributions and support were pivotal in keeping me focussed and motivated. I'm also grateful to the University of Johannesburg and in particularly Dr. Clarisa Vorster and Laura Bowden for hosting and giving permission to utilize their facilities for detrital zircon analysis and Laser Ablation Inductively Coupled Plasma Mass Spectrometry.

To Joseph Hwata from Anglo American for supporting me in the final stages of this research and allowing me time off to visit my supervisors.

Lastly to my former employer Eurasian Natural Resources Corporation Mozambique Limitada (ENRC) for giving me permission to retrieve and transport samples from Mozambique to South Africa for analysis.

The Chicôa-Mecúcoè sub-basin of the Zambezi Basin in northern Mozambique hosts Karoo Supergroup rocks of the Vúzi, "Transitional," Moatize and Matinde formations, deposited from the Late Carboniferous to the Early Jurassic. The strata record periods of changing depositional environments resulting in cyclic sedimentary sequences and coal measures. This project focuses on the Vúzi Formation, a conglomeratic unit of glacial outwash gravel, the "Transitional" formation, a deltaic coarsening upward clastic sequence, and the Matinde formation, a sequence of fluviatile/lacustrine clastic sediments and coal measures. A single borehole intersection drilled from surface into basement rock provided a continuous intersection of Karoo Supergroup rocks for analysis and interpretation. The borehole was drilled in 2011 by Eurasian Natural Resources Corporation ("ENRC") and made available for research in 2015 and forms the basis for the deglaciation and provenance study.

Detrital zircon age population data obtained from Laser Ablation Inductively Coupled Plasma Mass Spectrometry ("LA-ICP-MS") analysis was compared to published aged data for the surrounding area. The age data in northern Mozambique is not well documented and often based on a limited number of analysis. Predominant Mesoproterozoic age data from 1000 - 1100 Ma suggest Kibaran and Irumide Orogen Monte Capirimpica granitoids and the Cassacatiza suite as primary source areas, confirming a westward and south westward directed paleoflow during Karoo sedimentation with zircon morphology suggesting a relatively short transport history. The Cambrian to Neoproteroic aged data from 500 - 999 Ma suggests a secondary south easterly directed palaeoflow from localised elevated areas associated with late Pan African Matunda, Monte Inchinga and Atchiza suites. Zircon data from samples taken from the Vúzi Formation show a relatively stable supply, indicating that the glaciers were possibly fault bounded, while deepening existing valleys.

A detailed lithological log of 11MTD001 identified a ~120 m thick intersection of Vúzi Formation stratigraphy which assisted in the identification of cycles associated with advancing and retreating glaciers and confirm a glacial origin for the Vúzi Formation in the Chicôa-Mecúcoè sub-basin. The four cycles identified were compared to similar deglaciation cycles in South Africa, Botswana, Zimbabwe and Tanzania. Clast composition and percentages indicates that maximum glacial advance was achieved in the first cycle and progressively becoming less prominent with each successive cycle, with the period between glacial advance and retreat increasing.

Table of Contents

CHAPTER 1: INTRODUCTION

Despite having large coal deposits, the geology of the Tete Province in Mozambique is poorly researched and understood. Although some studies have recently been published (Hatton *et al.*, 2012; Bicca *et al.*, 2017, 2018; Key *et al.*, 2015; Lakshminarayana, 2015; Pereira *et al.*, 2016; Phiri *et al.*, 2016; Galasso *et al*., 2019), poor infrastructure has hampered efforts.

The Karoo deposits in the Zambezi Basin of northern Mozambique occur in three main groupings of sub-basins; the Chicôa-Mecúcoè, Sanângoà-Mefidézi and Moatize Minjova sub-basins with the stratigraphy divided into a lower and upper group. The lower group is divided into the Vúzi, Moatize and Matinde formations, while the upper group is sub-divided into the Cádzi, Zumbo and Lualadzi formations. (Catuneanu *et al*., 2005; GTK Consortium, 2006; Lächelt, 2014). Correlations between the sub-basins are complicated by varying tectonism and basement controls (Orpen *et al*., 1989; Cairncross, 2001; GTK Consortium, 2006). The study area of this project falls within the Chicôa-Mecúcoè sub-basin on the northern shore of Cahora Bassa.

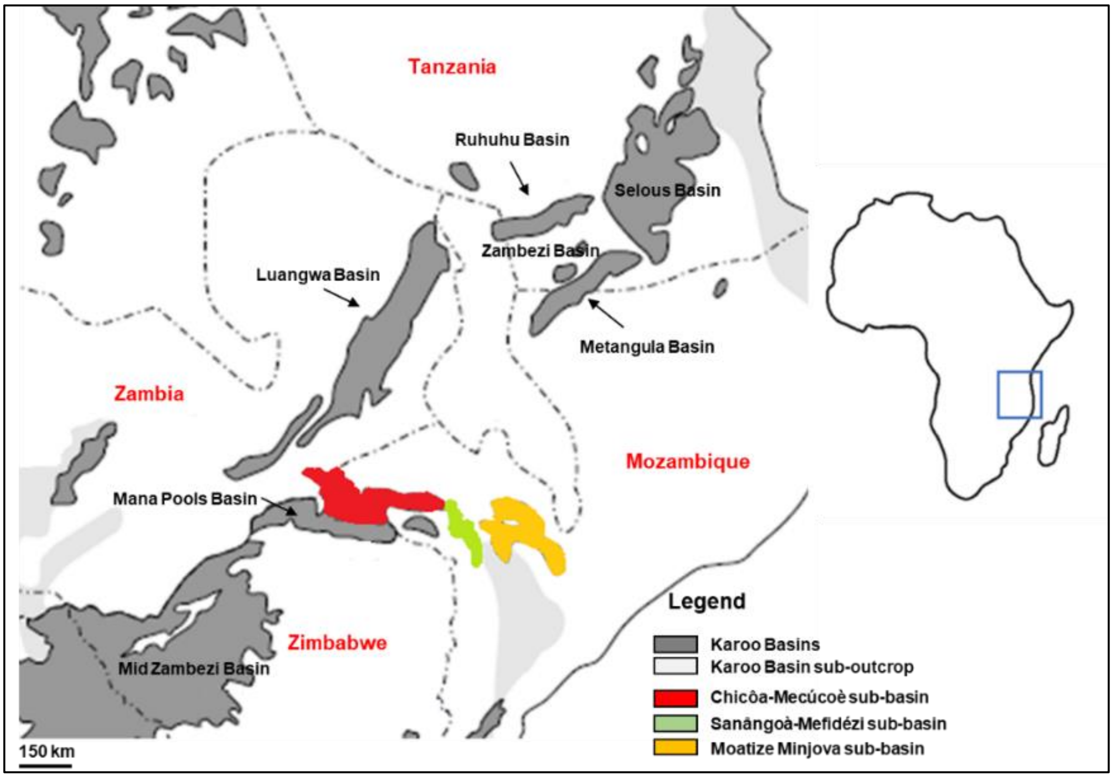

Figure 1: Karoo basins of southern Africa and sub-basins of the Tete Province, Mozambique. Adapted from Lächelt, (2004); Catuneanu *et al*. (2005); Pereira *et al*. (2016). Zambezi sub-basins shown in red, green and gold.

1.1 Objectives and outcomes

Much of the research conducted on the Karoo aged rocks of Mozambique has focussed on the Moatize-Minjova sub-basin in Tete. It is hoped that this dissertation will provide valuable geological information in an area that has previously been poorly researched. The research will focus on identifying deglaciation sequences and determining the provenance of Karoo sediments by detrital zircon analysis.

A single borehole, 11MTD001, drilled in 2011 contains a continuous intersection of lower Karoo rocks. Typically, exploration boreholes would have ended just below the coal seams in the Vúzi Formation. A decision was made to end borehole 11MTD001 in the basement, which presents an excellent research opportunity on the Karoo rocks of the Chicôa-Mecúcoè sub-basin.

Several deglaciation sequences have been identified in Karoo deposits across southern Africa, with four noted in the main Karoo Basin of South Africa, three to four noted in the Kalahari Basin of Botswana, three noted in the Mid-Zambezi Basin of Zimbabwe and one noted in the Ruhuhu Basin of Tanzania (Bond and Stocklmayer, 1967; Visser, 1997; Wopfner, 2002). The lithological log of 11MTD001 was compared with deglaciation sequences described for southern Africa to determine the number of deglaciation sequences present in the study area.

Recent research by Dietrich *et al*. (2019) indicates that glacial environments were localised north of the main Karoo basin with the view that glacial deposits identified in the past may not be glacial, while diamictites in Brazil similarly indicate a non-glacial origin (Vesely *et al*., 2018). Evidence of glacial deposits north of Cahora Bassa are rare, and it was hoped that this research would assist in determining the glacial or non-glacial history for the Vúzi Formation of the Chicôa-Mecúcoè sub-basin.

Palaeoflow data for the Karoo sediments in the Chicôa-Mecúcoè sub-basin are limited to field observations by Key *et al*. (2015). While palaeoflow directions have been determined through detrital zircon analysis by Bicca *et al.* (2018) on a single lower Karoo rock of the Moatize-Minjova sub-basin, no known detrital zircon provenance studies have been conducted for the study area. This study will provide data to support or dispute observations by Key *et al*. (2015). Six samples (B1764, B1766, B1775, B1778, Tete 1 and Tete 3) were taken from borehole 11MTD001 from different stratigraphic units for detrital zircon analysis.

The Karoo rocks were deposited in a rift basin during a period of active tectonism and changing climate (Cairncross *et al*., 2001; Wopfner, 2002; Catuneanu *et al*., 2005; GTK, 2006). The effects of climate and tectonism on the sedimentary processes and source regions were investigated by comparing samples from the Vúzi, “Transitional” and Matinde Formations which associated with changing climatic conditions. U-Pb age data were compared with published ages of igneous and metamorphic rocks, published paleo-current and paleo-ice directions to determine possible changes in source areas related to changes in climate.

The thesis will therefore seek to answer the following questions:

- Do the conglomeritic sequences intersected represent glacial deposits?
- Are deglaciation cycles present and how do they compare to cycles observed in adjacent Karoo basins?
- How does the intersected Vúzi Formation compare with published research for Chicôa-Mecúcoè sub-basin?
- Do detrital zircon analysis confirm a paleoflow direction from the north east and west as reported by Key *et al* (2015)?
- Does the paleoflow direction change with warming conditions?

CHAPTER 2: LITERATURE REVIEW

2.1: Previous Work

The first reported geological investigation of Karoo rocks in Tete Province of northern Mozambique occurred in the 1880s in the Moatize area, where the lithostratigraphy was broadly described. Investigations in the Chicôa-Mecúcoè sub-basin began in the 1930s where Karoo rocks were identified for the first time north of the Cahora Bassa dam. From the 1950s to 1980s work focussed on the economic potential of the coal deposits in Mozambique. The Tete Province was geologically mapped from 1980 to 1984 by the French Bureau de Recherches Géologiques et Minières ("BRGM"), which published a 1:1 000 000 map. Falcon *et al*. (1984) investigated the palynostratigraphy of the Chicôa-Mecúcoè sub-basin Permian coal to assist in coal correlations. In the 2000s an extensive mapping exercise was initiated by the Mozambique government resulting in the Geological Survey of Finland publishing 1:250 000 maps in 2005 (Mäkitie *et al*., 2005). Most recently, Hatton and Fardell (2011) summarised the discoveries of coal in Mozambique, while Key *et al*. (2015) investigated the Zambezi River and source areas for the Chicôa-Mecúcoè sub-basin. Recent research is focussed on the Moatize-Minjova sub-basin. Deglaciation sequences have not previously been investigated in the Chicôa-Mecúcoè sub-basin, with the nearest investigated sequences described in the Zimbabwean and Tanzanian basins (Bond and Stocklmeyer, 1967; Wopfner, 2002).

2.2: Study Area

The samples were taken from a single borehole drilled by Eurasian Natural Resources Corporation Mozambique Limitada ("ENRC") during their 2011 exploration campaign. The borehole has an end of hole depth of 319 m intersecting Karoo rocks and ending in granite gneiss basement. The 1:250 000 scale map published by the GTK Consortium indicates that the borehole falls within the sub-outcrop area of the Matinde Formation (Mäkitie *et al*., 2005). Access to the area is limited to the dry season. There are no formal roads and the informal roads are in a poor condition, which are often inaccessible unless repaired. The area is best accessed by a helicopter.

The Karoo rocks form a relatively flat terrain with a gradual downwards slope towards the Cahora Bassa dam, while metamorphic and igneous rocks of the Fíngoè Supergroup form mountainous terrains approximately 3 km towards the north and 10 km towards the southwest. A Cretaceous carbonatite intrusion located approximately 12 km to the west forms a prominent mountainous feature with an elevation of ~1050 m above sea level (Mäkitie *et al*., 2005; GTK Consortium, 2006).

According to the 1:250 000 map mafic pyroclastic rock and mica schist of the Monte Rupanjaze Formation (~1200 - 1300 Ma) of the Monte Messuco Group outcrop towards the north of the borehole (Mäkitie *et al*., 2005). Pyroclastic material mixed with epiclastic deposits in the area indicates volcanism and sedimentation occurred simultaneously. (GTK Consortium, 2006).

The Fíngoè Supergroup is intruded by Ualádze Suite (age unknown) gabbro bodies and layered igneous rocks of the Atchiza Suite (~864 Ma). Three gabbro bodies have been mapped in the Monte Rupanjaze Formation towards the north of 11MTD001, while the Atchiza Suite occurs predominantly to the west. (GTK Consortium, 2006). The suites are related to a magmatic period following the break-up of Rodina (~750 Ma) to the Pan African orogeny (~600 Ma). (Hanson, 2003; GTK Consortium, 2006).

The Monte Inchinga Granites (age unknown) occur as intrusions throughout the Fíngoè Supergroup in the area, with the largest intrusion towards the South West of 11MTD001. The contacts of the intrusion are often deformed suggesting a tectonic setting during emplacement. The east-west trend suggests that the intrusions are related to the Sanangoè Shear Zone during the late Pan African Orogeny. (Mäkitie *et al*., 2005; GTK Consortium, 2006).

2.3: Geodynamics

The Zambezi Belt (Figure 2) consists of a variety of metamorphic, igneous and sedimentary rocks of varying ages (Goscombe *et al*., 2000; Hanson, 2003; Westerhof *et al*., 2008). A complex geology exists from several geodynamic events. Archaean, Kaapvaal, Zimbabwean and Tanzanian cratons were subjected to compressive and extensional forces related to the formation and break-up of the supercontinents Rodinia and Gondwana, forming a varied tectonic framework across southern Africa (Munyanyiwa *et al*., 1997; Hanson, 2003). Four main events have been identified; Ubendian - Usagaran Orogen (2 - 1.9 Ga), Kibaran and Irumide Orogen (1.4 - 1 Ga), Pan-African Orogenic System (950 - 470 Ma) and Karoo Rift Phase (~500 Ma) (Hanson, 2003). The formation and break-up of Rodinia and Gondwana respectively resulted in the formation of several tectonic belts between the Tanzania and Zimbabwe cratons (Figure 2). (Hanson, 2003).

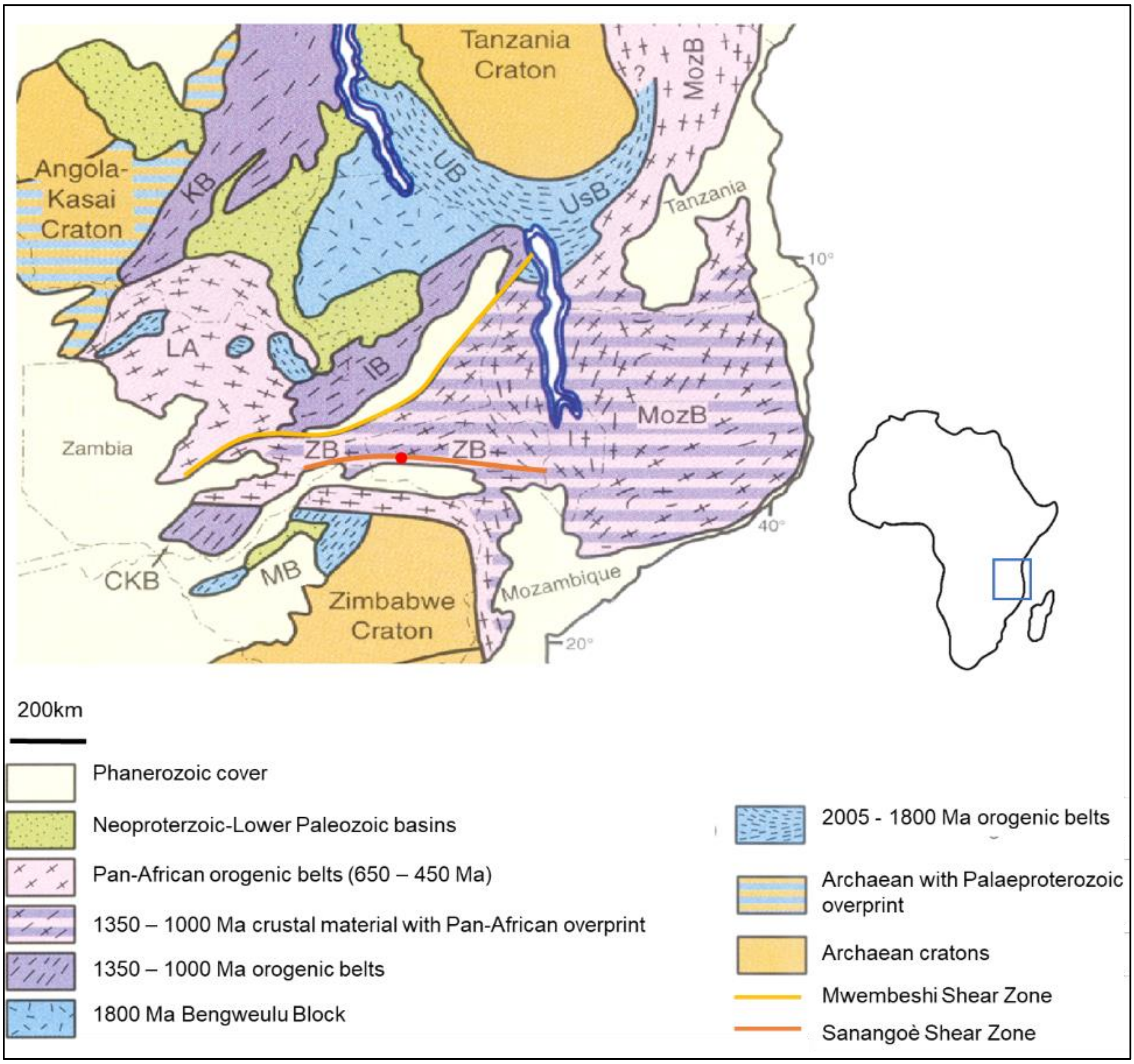

Figure 2: Tectonic framework of southern Africa, Adapted from Hanson, 2003 and references therein CKB - Choma-Kalomo Block; KB – Kibaran Belt; IB - Irumide Belt; LA - Lufilian Belt; MB - Magondi Belt; MozB - Mozambique Belt; UB - Ubendian Belt; UsB - Usagaran Belt; ZB – Zambezi Belt. Red dot indicates approximate 11MTD001 borehole position.

2.3.1: Ubendian and Usagaran orogen (2 - 1.9 Ga)

The Ubendian and Usagaran orogens formed during a period of compressional tectonics during the Paleoproterozoic. Orogenic belts formed near the southern and eastern margins of the Tanzanian Craton. A series of tectonic and volcanic episodes resulted in folding and varies degrees of metamorphism resulting in an overprinting of zircon ages (Goscombe *et al*., 2000; Porada *et al*., 2000; Hansen, 2013). U-Pb ages of ~2 Ga schists are associated with high pressure metamorphism while ~1.9 Ga eclogites are associated with cooling during decompression. The Pan-African orogenesis resulted in further overprinting of the ages. Ages of 2002 - 2022 Ma identified in the basement rocks of the Zambezi Belt may be related to the Ubendian and Usagaran orogenesis (Hansen, 2013).

2.3.2: Kibaran and Irumide orogen (1.4 - 1 Ga)

The Kibaran and Irumide orogens formed during compressional tectonics related to the formation of Rodinia approximately 1.4 Ga to 1.0 Ga. The Irumide orogen occurred south of the Tanzanian Craton margins and extended southwards towards the Zimbabwean Craton (Porada *et al*., 2000; Hanson, 2003). Multiple folding and faulting events resulted in the reworking of the Proterozoic basement with structural and metamorphic grade increasing away from the margins of the cratons. Granitoid plutons intruding in areas of higher tectonic activity. U-Pb dating has identified ages of ~ 1386 Ma to 1289 Ma with granitic intrusions dated ~1006 to 966 Ma. U-Pb ages recorded between 1.4 – 1.0 Ga in the Zambezi Belt may be related to the Irumide Orogen (Hansen, 2013).

2.3.3: Pan-African orogenic system (950 - 470 Ma)

The Pan African Orogenic system is a period related to extensional and compressional tectonics associated with the break-up of Rodinia (~750 Ma) and the reassembly of the continental fragments into Gondwana (~600 Ma) (Hanson, 2003). The initiation of the break-up of Rodinia is associated with a period of magmatism and rifting with igneous rocks recording ages of ~881 - 795 Ma in the Zambezi Belt and which are believed to have intruded prior to or contemporaneously with rifting (Hanson, 2003; Meert and Torsvik., 2003). In Mozambique the Pan African event is represented by granitic, monzanitic and syenite intrusives, metamorphism, formation of nappes and klippens which are separated by mylonite zones (Lächelt, 2004). The presence of ophiolites in the Mozambique Belt suggests that rifting, subduction and continental collision occurred from Mozambique to the Red Sea (Porada, 1989).

Three major orogenic systems (Lufilian Arc, Zambezi and Damara Belt) have been identified along the margins of the Kalahari and Congo Cratons (Hanson, 2003). The orogenic systems extend from present day northern Namibia, through Zambia and into northern Mozambique. (Porada *et al*., 2000; Hanson, 2003). The main orogenic event recorded in the Zambezi Belt occurred from ~ 900 - 750 Ma during the Katangan episode, during which time deformation resulted from spreading along the South Atlantic Ocean and continental collision along the Mozambique Belt (Porada, 1989; Porada *et al*., 2000; Hanson, 2003). A sustained period of compressional tectonics occurred between 650 - 420 Ma throughout southern Africa during the Damara episode, with possible uplift and cooling towards the end of the episode. The Damara event resulted in the closing of the South Atlantic Ocean with a second phase of deformation in the Zambezi Belt where deformation is associated with southerly directed thrusting and shearing along the southern margin. Shearing occurred as a result of differing plate velocities between the Kalahari and Angolan plates. Metamorphic overprinting of igneous rocks, with overgrowths recording ages of ~525 Ma in the Zambezi Belt, may indicate the final stage of deformation (Porada, 1989; Hanson, 2003).

2.3.4: Karoo Rift Phase

Rifting occurred approximately 500 Ma ago forming grabens and half grabens in northern Mozambique where sediments were deposited to form the Karoo Supergroup. Orpen *et al.*, (1989) identified two major fault lines influencing Karoo basin development in the mid and lower Zambezi basins, a north east – south west trending normal fault system and an east - west trending dextral wrench fault system, describing the lower Zambezi Basin as a simple pull apart basin. Oesterlen and Blenkinsop (1994) describes four fault sets in the Zambezi Belt that formed during the Lower Triassic to Upper Cretaceous during a single tectonic event which may represent a failed triple junction between the mid-Zambezi, lower Zambezi and

Luangwa Rift zones and dispels the possibility of a simple pull apart basin. Oesterlen and Blenkinsop (1996) further argue against a simple pull apart basin and favours a dextral strike-slip component in the formation of the lower Zambezi Basin. Extensional tectonics eventually resulted in the break-up of Gondwana from the Jurassic to Palaeogene and coincided with flood basalts marking the end of Karoo sedimentation. (Smith, 1999; Catuneanu *et al*., 2005).

2.4: REGIONAL GEOLOGY - PRE KAROO

The Neoproterozoic to early Palaeozoic Pan African orogenic Zambezi Belt, which formed during the collision of the Congo and Kalahari Cratons, provided the source material during Karoo sedimentation (Hargrove *et al*., 2003).

The Pre-Karoo basement is complex and is dominated by a series of terranes (west, south and east Gondwana) with linear orogens that often intersected during the Mesoproterozoic and Neoproterozoic era. The Mozambique and Zambezi Belts formed during the Pan African Orogeny between ~750 - 470 Ma (Goscombe *et al*., 2000; GTK Consortium, 2006; Westerhof *et al*., 2008). The Zambezi Belt falls largely within the west Gondwana terrane with the late Pan African strike-slip Sanangoè Shear Zone in the south and Mwembeshi Dislocation in the northwest (Figure 2) (Westerhof *et al*., 2008). Towards the east the belt is bounded by a major thrust fault that separates east and west Gondwana terranes. Four metamorphic terranes are identified; Granulite/Charnockite domain (granulite facies), Fíngoè domain (lower amphibolite facies), Zâmbuè domain (upper amphibolite facies) and the Matunda domain (amphibolite facies). (GTK Consortium, 2006). The Zambezi Belt consists of a variety of supracrustal material that underwent varying degrees of metamorphism and emplacement of granitoids and igneous rocks associated with the Grenville orogenic cycle (GTK Consortium, 2006., Westerhoff *et al*., 2008). A stacked microterrane model is proposed by the GTK Consortium (2006) for the Zambezi Belt in the West Gondwana terrane. The boundaries are complex with limited data, preventing the accurate delineation between the terranes and are not currently included in the 1:250 000 maps composed by the GTK Consortium (2006).

2.4.1: Mozambique Belt

The current limit of the east coast of Africa is believed to be the margin of the Mozambique Belt ("MozB") (GTK Consortium, 2006). The MozB developed over pre-existing crust with tectonic zones of weaknesses (Lächelt, 2004). The pressure-temperature signatures recorded in the MozB indicate a large mountain range, approximately 8000 km long, like the present-day Himalayans. (Engvik et al., 2007). Nyambe and Utting (1997) note a lack of preserved evidence of weathering and sedimentation of the MozB, except for the Sinakumbe Group in Zambia which indicates that glaciation during the Carboniferous eroded the landscape, exposing the Precambrian basement.

2.4.2: Zambezi Belt

The Zambezi Belt formed between the Congo and Kalahari cratons and consists of a complex arrangement of reworked Archaean , Palaeoproterozoic, , Mesoproterozoic and Neoproterozoic rocks, which exhibit varying degrees of deformation and metamorphism (Munyanyiwa *et al.,* 1997; Hargrove *et al.,* 2003). Lächelt (2004) notes that Archaean rocks may occur along the margin of the Zimbabwean Craton in the Tete Province. Several fault-bounded inliers occur throughout the Zambezi Belt (Goscombe *et al.,* 2000). Johnson *et al.* (2004) sub-divided the Zambezi Belt into a quartzo-feldspathic augen gneiss and aluminous schist South Zambezi terrane and a layered calc-silicate and quartzofeldspathic orthogneiss north Zambezi terrane, which are often grouped together as the Tete-Chipota Belt ("TCB"). The lack of age data and variations throughout the Zambezi Belt are poorly understood which complicates the understanding and development of the various terranes (Westerhof *et al.,* 2008).

Hunting (1984) defined litho-stratigraphic units and igneous suites in northern Mozambique which was redefined during the work carried out by the GTK Consortium (2006). Several units defined by Hunting (1984) were removed, while others were reinterpreted. The Karoo Supergroup sediments were deposited in basins and sub-basins formed in the Zambezi Belt basement, the basement predominantly consists of the Físngoè and Zâmbuè Supergroups. A new stratigraphy for Tete Province was published by the GTK Consortium (2006) and is summarized in Tables 1 and 2.

Table 1: Summary of the Pre-Karoo geological deposits of the Tete Province, Mozambique. Summarised from Hunting (1984); Barr and Brown (1987) and GTK Consortium (2006).

Supergroup	Group	Formation	Description
Fíngoè	Monte Tchicombe	Monte Puéque	Banded and foliated calc-silicate gneiss and schist
		Rio Mucanba	Polymictic conglomerate; weakly banded metasandstone and quartzites; quartz-feldspar schists and interlayers of metavolcanics
		Not assigned	Marble; metavolcanics, meta-tuff and agglomerates
	Monte Messuco	Monte Muinga	Volcanic breccia and agglomerate; mafic amygdaloidal to felsic metavolcanics; amygdaloidal mafic metavolcanics; mica schist and gneiss; marbles
		Monte Rupanjaze	Matachert; banded ironstone; mica schist; mafic to ultramafic metavolcanics.
Zâmbuè	Muze	Musamba	Marble with calc-silicate interbeds
		Caduco	Calc-silicate gneiss, metachert and skarn
	Not assigned		Arkosic quartzites
	Malowera	Sale-Sale	Orthoquartzite and biotite-garnet gneiss
		Metamboa	Meta-arkose, quartz feldspar gneiss and interbeds of metavolcanics
		Rio Mese	Garnet rich ortho-paragneiss; amphibolites; gneiss and tonalites

The ages of the various stratigraphic units in western Gondwana is not well documented with available data based on a limited number of samples, summarized by the GTK Consortium (2006). Geochemical results and lithologies resemble ocean floor and island arc rocks. A meta-arkose sample from the Zâmbuè Supergroup recorded a range of ages from Archaean (~ 2.7 - 2.5 Ga) - Paleoproterozoic (~ 2.1 - 1.9 Ga) - Mesoproterozoic (~ 1.3 - 1.2 Ga) forming in a passive margin of the Central African Craton. (GTK Consortium, 2006).

2.4.3: Intrusive Rocks

The Fíngoè and Zâmbuè Supergroups were intruded by several mafic to felsic suites during the Pan-African period which are summarized below.

Table 2: Summary of the igneous intrusions of the Tete Province, Mozambique. Summarised from GTK Consortium, (2006).

Suites	Lithology	Age
Cassacatiza Suite	Predominantly granite and granodiorite with minor monzonite and seyenite	~1077 Ma
Monte Sanja	Felsic granites, granodiorites and monzonites intruding into the Fingoè Supergroup	~1050 Ma related to possible volcanic-arc style granite intrusions.
Matunda Suite	Mafic to Felsic gneisses and granite gneisses which are intruded by pegmatites.	~528 Ma related to metamorphism during the Pan-African orogeny.
		~700 - 830 Ma related to post-Grenville rifting
Atchiza Suite	Igneous complex intruded with dolerite dykes and granite veins. The complex has an upper zone comprising gabbro-norite and diorite with lower zone of ultramafic sequence.	~864 Ma related to extension and igneous activity in the period of Rodinia - Pan-African Orogeny.
Ualádze Suite	Mafic dykes and gabbro bodies	~864 Ma, intruded contemporaneously with the Atchiza Suite sharing a common magma source.
Monte Inchinga Granite	Large plutons intruded into the Fingoè Supergroup along the Sanangoè Shear Zone.	No age available, proposed Neoproterozoic to Palaeozoic age.
Sinda Suite	Coarse grained porphyritic microcline granites intruding into the Zâmbuè Supergroup	~502 Ma

2.5: REGIONAL GEOLOGY – KAROO SUPERGROUP

The sedimentary rocks of the Karoo Supergroup were deposited in basins and sub-basins throughout southern Africa from the Late Carboniferous to the Early Jurassic. The main Karoo Basin of South Africa formed in a retro-arc foreland tectonic setting while the rest of the basins formed in extensional rift systems and intracratonic sag basins with sedimentation often occurring contemporaneously with tectonism (Orpen *et al*., 1989; Nyambe, 1999; Turner, 1999; Cairncross, 2001; Delvaux, 2001; Catuneanu *et al*., 2005; GTK Consortium, 2006). The Karoo sedimentary sequence was strongly influenced by tectonics related to the break-up of Gondwana and climate shifting from cold dry conditions in the Carboniferous to hot and humid in the Permian and Triassic, while becoming increasingly arid towards the Jurassic. (Visser, 1995; Wopfner, 2002; Catuneanu *et al*., 2005; GTK Consortium, 2006).

Table 3: Karoo Supergroup stratigraphy summary for the main Karoo basin of South Africa and the Zambezi Basin of Mozambique. Summarised from Johnson *et al*. (1996); Catuneanu *et al*. (2005); GTK Consortium (2006).

	South Africa			Mozambique		
	Main Karoo Basin			Zambezi Basin		
	Group	**Formation**	**General Lithology**	**Group**	**Formation**	**General Lithology**
Jurassic	Stormberg	Clarens	Sandstones	Upper Karoo	Lualadzi	Red sandstones
		Elliot	Thinly laminated mudstones and siltstones. Red sandstones			
Triassic		Molteno	Sandstones, mudstones and siltstones		Zumbo	Sandstones, often silicified
	Beaufort	Burgersdorp	Mudstones with minor sandstones		Cádzi	Arkosic sandstones, limestones and conglomerates
		Katberg	Sandstones with minor mudstones			
		Balfour	Mudstones with minor feldspathic sandstones			
Permian		Koonap & Middleton	Sandstones and siltstones	Lower Karoo	Matinde	Sandstones, marl, minor coal seams and argillite
	Ecca	Waterford & Fort Brown	Sandstones and Rhythmites			
		Ripon	Poorly sorted sandstones and minor rhythmites		Moatize	Siltstones, sandstones, coal seams and argillite
		Collingham & Whitehill	Fine grained sandstones with carbonate concretions and chert			
Carboniferous		Prince Albert Formation	Dark coloured chert			
	Dwyka	Tshidzi/ Mbizane/ Elandsvlei Formation	Diamictites, tillites and mudstones		Vúzi	Gritty sandstones, basal conglomerates and tillites

2.6: Lower Karoo

The lower Karoo sedimentary strata were deposited from the Late Carboniferous to Early Permian, with sedimentation taking place in cold arid conditions to form the Dwyka equivalent Vúzi Formation and warm to hot and humid conditions in the Ecca equivalent Moatize and Matinde formations (Visser, 1995; Wopfner, 2002; Catuneanu *et al*., 2005; GTK Consortium, 2006). Changes in palynomorph assemblages recorded in the Moatize sub-basin indicate a climatic shift from cool to warm conditions during the Lopingian times (Götz, *et al*., 2017). Assemblages in the Sanângoà-Mefidézi sub-basin indicate an Artinskian - Capitanian age for the Vúzi, Moatize and Matinde formations. (Mahabeer, 2017).

2.6.1: Vúzi Formation

Visser (1987) described the paleogeography of southern Africa prior to glaciation as an area dominated with highlands and rivers feeding into a flat-lying platform with shallow oceans, which may have been bounded by island arcs. The rivers incised deep valleys into the highlands, which were further eroded by glaciers. Glacial deposits of the Vúzi Formation are sparsely distributed and may have been restricted to pre-existing depressions associated with the Sanangoè Shear Zone. (GTK Consortium, 2006; Key *et al*., 2015). Thicknesses vary in the Chicôa-Mecúcoè sub-basin, with sequences noted by the GTK Consortium (2006) as ~100 m at the Vúzi River in the east to a few metres noted in the Rio Mucangádzi area to the west. Conglomerates, siltstones, sandstones, mudstones and occasional coal-bearing seams were deposited in fluvio-glacial and fluvial depositional environments. (GTK Consortium, 2006; Key *et al*., 2015). A “Transitional” formation or “platform” facies occurs between the Vúzi and Moatize formations, consisting of an upward-coarsening sequence deposited in a deltaic setting (Hancox, 2014, Lakshminarayana, 2015).

2.6.2: Moatize Formation

The Moatize Formation is regarded as the main coal bearing unit of the Karoo sequence in Mozambique, deposited unconformably over pre-existing crystalline basement or conformably over Vúzi Formation rocks. The Moatize Formation is dominated by arkosic sandstones, which may be pebbly in places, fine grained sandstones, argillite's and coal seams deposited in a low energy, fluviatile and lacustrine environment. (GTK Consortium, 2006; Key *et al*., 2015). Ripple laminations and lenticular bedding observed in the argillites at the Rio Mucangádzi area suggest localised tidal influences in the Chicôa-Mecúcoè sub-basin (GTK Consortium, 2006).

2.6.3: Matinde Formation

The Matinde Formation is a succession of alternating fine to coarse grained sandstones, which are often pebbly or gritty and may contain siltstones, mudstones, coal measures and conglomerate horizons in the Chicôa-Mecúcoè sub-basin. Bedding is predominantly massive towards the south, while in the north sandstones are often cross-stratified. Petrified logs are often observed in the north-western area of the Cahora Bassa dam (GTK Consortium, 2006). The presence of siltstone and mudstone units interbedded with sandstones in the Chicôa-Mecúcoè sub-basin suggest a low energy lacustrine/fluvial environment (Key *et al*., 2015).

2.7: Deglaciation Sequences

Three glacial episodes have been noted for Gondwana during the late Palaeozoic with the relative position of the South Pole shifting positions from 360 Ma to 250 Ma, (Cradock *et al*., 2019). Geochemical proxies indicate three shifts in climatic conditions in southern Africa during the Carboniferous to Permian, suggesting three major deglaciation events (Scheffler *et al*., 2003).

In the main Karoo and Kalahari basins of southern Africa four deglaciation cycles were described, each cycle beginning with a basal massive diamictite, overlain by stratified diamictites, sandstones and mudrocks (Visser, 1997; Isbell *et al*., 2008). Each deglaciation cycle lasted approximately 3.6 - 8.2 Ma with the onset of the next cycle influenced by a changing climate and tectonic setting, resulting in a modified depositional environment (Isbell *et al*., 2008; Wopfner *et al*., 2009). The glaciomarine, lacustrine and tillite deposits have a maximum thickness of 800 m and 500 m in the main Karoo and Kalahari basins respectively (Visser, 1997).

Lower Karoo rocks in northern Zimbabwe contain three glacial cycles related to deglaciation events, with each cycle consisting of a series of lower tillites, outwash gravels, diamictites and ending with an upper fine-grained shale unit (Bond and Stocklmayer., 1967; Bond, 1970; Visser, 1996; Opdyke *et al*., 2001). In Tanzania the Idusi Formation is divided into the Lilangu and Lisimba members, which Wopfner (2002) describes as being consistent throughout central Africa.

The Lisimba Member consists of a basal unit with matrix-supported cobble to boulder-sized conglomerate with pentagonal to sub-rounded clasts, which may have striations and pressure flaking associated with glaciation (Wopfner and Kreuser, 1986). This is overlain by flow banded tillites, washout conglomerates and sandstones. Scheffler *et al*. (2003) notes that the chemical alteration indicates rapid changes between glaciation cycles. The Lilangu Member represents the cap of deglaciation and is dominated by laminites and shales (Catuneanu *et al*., 2005). The glacial deposits of Tanzania can be correlated with Karoo basins in eastern Africa into Oman, India, China and Australia suggesting a single glacial event (Catuneanu *et al*., 2005). To the east, glacial deposits in the Congo are however poorly represented. The Kiralo ya Mungu Beds consist predominantly of matrix supported diamictites and conglomerates associated with washout deposits in a lacustrine environment (Catuneanu *et al*., 2005).

Craddock *et al*. (2019) suggests five main ice caps for southern Gondwana with a general ice flow away from central Gondwana over large distances, >1000 km and sometimes up to >2000 km. The limited extent of glacial deposits in the Mid-Zambezi basin suggests that the ice cap was static and only occurred on higher grounds (Bond, 1970). Evidence of glaciation sequences in Zimbabwe and Mozambique are poorly studied with research limited to describing and mapping glacial rocks, most recently by the GTK Consortium (2006). Glacial deposits outcrop over large areas in the main Karoo and Kalahari basins, making the identification of broadscale deglaciation sequences possible. In contrast, the identification of deglaciation sequences in Mozambique are restricted by the limited and intermittent outcrop of glacial deposits. The GTK Consortium (2006) noted a limited glacial occurrence in the Chicôa-Mecúcoè sub-basin, supporting the work done by Dietrich, *et al*. (2019), which indicates glacial deposits were localised north of the main Karoo basin. Exploration activities in the

Tete sub-basin, however, indicate thick conglomeratic units (pers. comm. Hancox, 2019). It is unclear if identified deglaciation cycles are localized or extensive.

2.7.1: Glacial Cycles - Southern Africa (main Karoo and Kalahari basins)

Basal massive sequence

The sequence typically consists of massive to poorly sorted diamictites up to 250m in thickness in the main Karoo and Kalahari basins, clasts are 1 - 5 mm in diameter, typically angular to sub-rounded and supported in a sandy to muddy matrix (Visser, 1997). Sandstone lenses may occur and are often pebbly. Minor mudstone layers have been identified, but are typically less than 50 cm in thickness (Visser, 1997).

Upper stratified sequence

The sequence typically consists of stratified diamictites, sandstones, conglomerates, rhythmites and mudstone (Visser, 1997). Stratified layers consist of beds of diamictite (0.5 to 5 m thick) and lenses of mudstone (0.01 to 1.0 m thick) and sandstone, which may be pebbly in places. Poorly-sorted sandstones may be 8 to 100 m thick and are either massive or cross-stratified. Mudstone forms the top of the sequence and is dark grey to black and graded forming thick sequences (Visser, 1997).

2.7.2: Glacial Cycles – Mid Zambezi Basin

Glacial Series Cycle 1

Reddish-grey conglomerate made up of clasts from the underlying basement rocks, suggesting a local source area (Bond and Stocklmayer., 1967). Conglomerates are clast-poor with poorly sorted, sub-angular to sub-rounded pebbles in a poorly sorted fine-grained sandy matrix. This is overlain by a grey-coloured conglomerate exhibiting some uniformity and minor stratification, pebbles are more abundant and rounded. Pebbles of the basement rock still dominate the conglomerate while additional pebble types indicate a widening source. The cycle is capped off by grey-varved shales, with a total thickness of roughly 40 m (Bond and Stocklmayer, 1967).

Glacial Series Cycle 2

The second cycle commences with a coarse sandstone and conglomerate sequence, the sandstone fines upwards, while the overlying conglomerates mirror the sequence described in Cycle 1, suggesting that the source areas remained local becoming broader as the cycle developed (Bond and Stocklmayer, 1967). This sequence is overlain by a grey mudstone with minor sandy layers and is approximately 29 m thick. It is suggested that the sandy material was sourced from ice-rafts dropping material onto the mud (Bond and Stocklmayer, 1967).

Glacial Series Cycle 3

It commences with a poorly-sorted, dark pebbly sandstone that grades into a fine-grained grey sandstone. The conglomerate unit is poorly sorted and clast-poor resembling the first unit conglomerate in Cycles 1 and 2. This is overlain by shales that are sandy in sections and lack the varving identified in Cycle 1. The last cycle is thinner and is approximately 19 m thick (Bond and Stocklmayer, 1967).

2.7.3: Glacial Cycle – Tanzania

The glacial cycle consists of a basal unit of matrix-supported cobble to boulder sized conglomerate overlain by flow banded tillites and washout conglomerates. The cycle is capped off by a sandstone rich diamictite layer (Wopfner, 2002).

2.7.4: Non-glacial late Palaeozoic Ice Age Cycles

Investigations on deglaciation cycles by Visser (1997) focussed on the main Karoo basin of South Africa and the western portion of the Kalahari basin of Botswana, where a basal massive sequence and upper stratified sequence was identified to represent deglaciation cycles. Dietrich *et al*. (2019) investigated Dwyka equivalent Karoo rocks in the eastern portion of the Kalahari Basin and identified six lithological facies interpreted to represent scree and mass-flow deposits of non-glaciogenic origin. Whereas diamictites investigated in Brazil indicates a non-glacial origin where material was sourced during delta collapse at maximal glacial retreat rather than a glacial origin (Vesely, *et al*., 2018)

Scree and mass-flow sequence

- The lowermost first facies unit unconformably overlies the basement rocks and predominantly consists of a clast supported massive breccia with a maximum thickness of 10 m. The clasts are sourced from the underlying basement as colluvial or scree slope deposits and may be interbedded with thin siltstone units (Dietrich *et al*., 2019).
- The second facies consist of interbedded thin sandstones and siltstones reaching a maximum thickness of 3 m and is interpreted to represent a lacustrine deposit. (Dietrich *et al*., 2019).
- The third facies consist predominantly of matrix-supported diamictites with a maximum thickness of 15 m. Clasts are angular to sub-angular deposited as mass-flow deposits. (Dietrich *et al*., 2019).
- The fourth facies consist predominantly of clast to matrix-supported conglomerates between 3 - 10 m in thickness and are cross-bedded in places interpreted to represent alluvial fan or braided fluvial deposits (Dietrich *et al*., 2019).
- The fifth facies consist predominantly of muddy sandstones between 2 - 3 m in thickness with poorly developed planar to ripple cross-laminations interpreted to represent a crevase-splay deposit (Dietrich *et al*., 2019).
- The sixth facies consist predominantly of a cross-bedded, coarse-grained sandstone between 5 - 10 m in thickness interpreted to represent a braided or proximal crevasse splay deposit (Dietrich *et al*., 2019).

Delta collapse sequence

- The first facies are dominated by a ~8 m thick matrix-supported, clast poor diamictite interpreted to represent mass flow deposits. The clasts are poorly faceted and lack striations associated with glaciers. Although the unit is deformed, sedimentary structures are generally preserved (Vesely, *et al*., 2018).
- The second facies are dominated by cycles of rhythmites, shale and diamictites. Rhythmites have a general upward-fining sequence and are disrupted by poorly stratified, clast poor diamictites with occasional rip-up mudstone clasts. This

cycle is interpreted to represent deceleration flow deposits (Vesely, *et al*., 2018).

2.8: Upper Karoo

The upper Karoo Supergroup rocks of Mozambique were deposited from the Late Permian to Jurassic, with sedimentation taking place in hot arid conditions in a terrestrial setting. Volcanic rocks form interstratified horizons from the Early Triassic to Jurassic. (GTK Consortium, 2006).

The Cádzi Formation is predominantly coarse-grained cross-stratified sandstones with minor pebble conglomerate and carbonate horizons. Sediments were deposited as aeolian sands or in fluviatile systems with perennial rivers (GTK Consortium, 2006; Key *et al*., 2015).

The Zumbo Formation consists of a lower fine-grained silicified sandstone unit deposited in a high energy environment and an upper feldspathic sandstone unit, which is believed to have formed in a low energy arid environment (GTK Consortium, 2006; Key *et al*., 2015). An unconformity exists between the Cádzi and Zumbo formations (GTK Consortium, 2006).

The overlying Lualádzi Formation consists of well-sorted fine to medium-grained goethite-rich sandstone, giving it a characteristic red colour (GTK Consortium, 2006).

2.9: River flow direction

The modern Zambezi River archives the events that resulted in the assembly and break-up of Gondwana over a period of approximately 280 million years (Key *et al*., 2015). During the Gondwana time the paleo-Zambezi River flowed westwards from the East Africa-Antarctica-Orogenic Belt, eroding the mountain range and providing the source material for the glacial deposits of the Vúzi Formation and sediments of the overlying marine and non-marine deposits of the Karoo. With the break-up of Gondwana and the resulting rifting the river changed drainage and began to flow westwards around 165 Ma ago towards the present-day Indian Ocean (Key *et al*., 2015).

Table 4: Events affecting the development of the proto-Zambezi and Zambezi, a major river affecting the Karoo Supergroup Zambezi Basin. Summarised from GTK Consortium (2006) and Key *et al*. (2015).

Event	Age (Ma)	Zambezi River events
East African Rift System	93	The establishment of the present day East African shoreline.
	130 - 90	Isostatic uplift of central and eastern Africa and subsequent erosion.
	135	Madagascar separates from Africa
	145 - 100	Development of East African coastline with high energy sedimentation.
	165	Start of Gondwana break-up, associated extensional tectonics and rift basins results in the **Zambezi River flowing eastwards**.
	201 - 165	Formation of half grabens along the line of separation between Africa and Madagascar.
Karoo Volcanism	184 - 173	Period of magmatism associated with extensional tectonics, formation of flood basalts and regional dyke swarms.
Karoo Sedimentation	258 - 210	Period of erosion and sedimentation during hot dry conditions, Upper Karoo.
	280 - 237	Fluvio-lacustrine depositional system associated with a **westward flowing Zambezi River**, Lower Karoo.
	~302 - 280	Glaciation with westwards flowing glaciers, Lower Karoo.
Hiatus	420 - 302	Period of hiatus with geological record mostly scoured by glaciers.
Pan African Orogeny	480 - 420	End of the Pan African orogenic system magmatism.
	750 - 470	Formation of East Africa-Antarctica-Orogenic Belt.

2.10: ZIRCON GEOCHRONOLOGY

Zircons ($ZrSiO_4$) are found in a wide range of sedimentary, metamorphic and igneous rocks and are valuable minerals in assisting our understanding of the Earth's history (Cocherie and Robert, 2008). With the advent of Laser Ablation Inductively Coupled Plasma Mass Spectrometry ("LA-ICP-MS") in isotope analysis, statistically significant numbers of zircons can be analysed at a low cost in a short space of time. They are particularly useful in determining the source areas of sediments, providing a window to determine the timing of tectonic events, basin development, sedimentary processes and metamorphic events (Fedo *et al*., 2003; Andersen *et al*., 2015).

Zircons have several characteristics that make them useful for geochronological studies, most importantly they are resistant to sedimentary processes, magmatically stable and contain high concentrations of uranium (“U”) and thorium (“Th”) isotopes. The stability of zircons in differing hydrothermal and supergene conditions is poorly understood. Stability plays a key role in mobility of trace elements and therefore can play an important role in determining the conditions and timing of rock transformations (Poitrasson *et al*., 2002). These isotopes are incorporated into the crystal lattice at concentrations of 10 - 1000 ppm and 1 - 100 ppm, respectively, during formation, while lead is predominantly excluded. This results in a high uranium to lead isotope ratio which is favourable for accurate age determinations. (Parrish and Noble, 2003). A very high U content, however, results in increased lead (“Pb”) loss through leaching with age. This occurs when U decays and causes damage to the lattices in the zircon grains, which results in a volume change of the zircon grain. Excessive changes in the zircon lattices and volume increases results in Pb leaching out (Parish and Noble, 2003; Nasdala *et al*., 2005; Kramers *et al*., 2009). Pb concentrations in zircons are affected by Pb loss during metamorphism, diagenesis and weathering and uptake of common Pb (Andersen *et al*., 2019).

Zircon grains can survive several sedimentary cycles and metamorphic events, making them ideal for provenance studies (Fedo *et al*., 2003; Flowerdew *et al*., 2006). The internal zoning of zircons is a function of zircon/melt interface, cation substitution, diffusion, structure and polymerisation (Poitrasson *et al*., 2002). This is a representation of the geological history as events change the zircons, elemental and isotopic compositions (Nemchin *et al*., 2013).

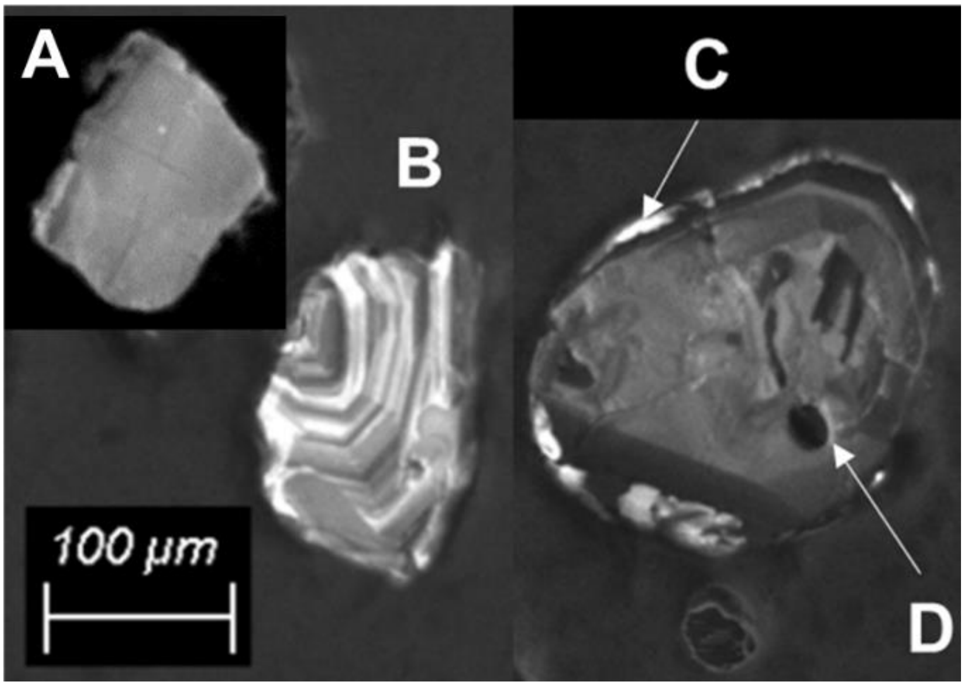

Figure 3: Cathode-luminescence image of three zircons from sample Tete 3 to illustrate varying internal zonation and structures; A – No zonation, B – oscillatory zonation C – growth rim, D – inclusion.

2.10.1: Age Determination

The determination of the age of a zircon crystal is dependent on radioactive decay of a parent nuclide to a daughter nuclide where the decay constant is known (Schoene *et al*., 2013). The two U isotopes used in age determinations are ^{238}U and ^{235}U, which decay to ^{206}Pb and ^{207}Pb, respectively with the age of the zircon calculated using the following equations (Jaffey *et al*., 1971):

$$t_{206} = \frac{1}{\lambda_{238}} \text{In} \left(\frac{206_{Pb_r}}{238_U} + 1 \right)$$

$$t_{207} = \frac{1}{\lambda_{235}} \text{In} \left(\frac{207_{Pb_r}}{235_U} + 1 \right)$$

λ_{238} = 1.55125 e^{-10} (Decay constant for ^{238}U) and λ_{235} = 9.8485 e^{-10} (decay constant for ^{235}U) (Jaffey *et al*., 1971; Steiger & Jäger, 1977).

Focused energy on a zircon grain results in ablation and the release of an aerosol over a specified time. The aerosol is transported to an inductively coupled plasma source, where the individual isotopes are measured. (Pickhardt *et al*., 2005; Košler, 2012). LA-ICP-MS differentially fractionates Pb in relation to U as a result of differing volatilities (Jackson *et al*., 2004; Košler, 2012).

The depositional age of a sedimentary rock occurs before the age of the youngest zircon found in the rock (Fedo *et al*., 2003). Zircons are refractory and the formation of zones in zircon crystals assists in determining the rocks geological history (Poitrasson *et al*., 2002; Nemchin *et al*., 2013). LA-ICP-MS dominates the method of age determination of detrital zircons used in geochronology studies (Jackson *et al*., 2004).

2.10.2: Wetherill Concordia Diagram

A concordia diagram represents a curve where $^{206}Pb/^{238}U$ and $^{207}Pb/^{235}U$ or $^{206}Pb/^{238}U$ and $^{207}Pb/^{206}Pb$ ratios for all ages are plotted. Should the two age calculations give similar ages, which plots and intersects the concordia curve, then the age is referred to as ‘concordant,’ while the opposite yields a ‘discordant’ age (Parrish and Noble, 2003). Factors that influence the ratio between Pb and U therefore determine a discordant or concordant age.

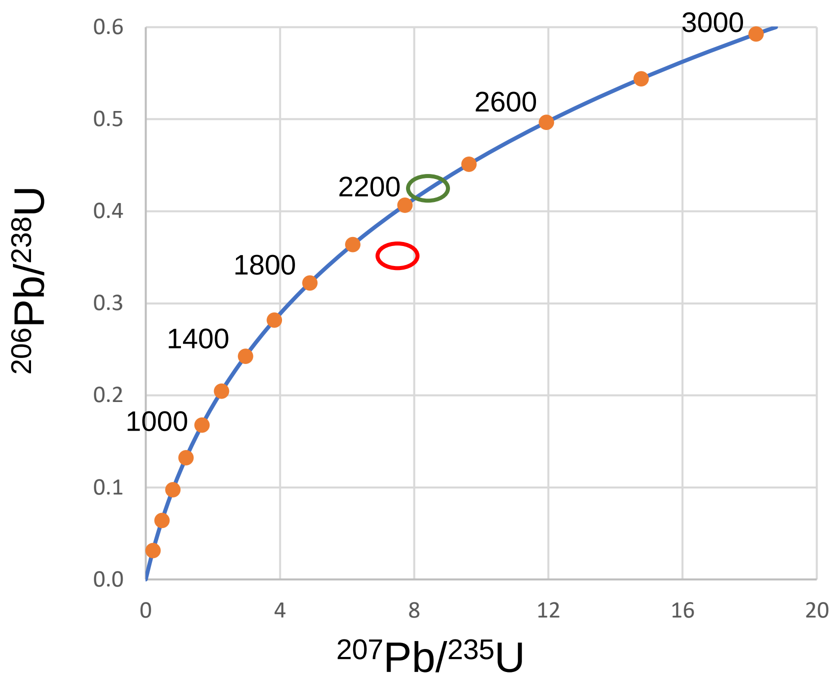

Figure 4: Wetherill Concordia diagram generated from the Excel integrated Isoplot software to indicate a concordant age (green circle) and a discordant age (red circle). (Ludwig, 2003).

The Concordia age is measurement where the data point intersects the Concordia curve, this is considered the most precise age (Ludwig, 2003; Košler, 2012). The percentage discordance can be calculated as follows:

Discordance = 100 - 100 * ($^{206}Pb/^{238}U$ age / $^{207}Pb/^{206}Pb$ age), or
Discordance = 100 - 100 * ($^{206}Pb/^{238}U$ age / $^{207}Pb/^{235}U$ age)

Zircons that record a higher percentage of discordance, typically greater than 10%, are generally filtered out. Discordance filters may exclude older grains where current Pb corrections are affected by concealed Pb loss resulting in a incorrect correction and discordance calculation (Andersen *et al*., 2019). Older grains may therefore be underrepresented in the distribution curves where Pb loss is more prevalent (Košler, 2012).

2.10.3: Reliability and complexity of zircon analysis

The refractory nature of zircons, although beneficial for the purpose of provenance studies, poses questions on the reliability and accuracy of results. Andersen *et al*. (2015) notes that zircons present in sedimentary units may be subjected to several sedimentary recycling events which poses a problem in determining the transport route of sediments. Zircons present may have been sourced from the recycling of older units. The size and shape of zircon grains affects their hydraulic equivalence. If assessed in addition to age determinations, may reduce the risk of incorrectly assessing the geological history of the sedimentary rock (Augustsson *et al*., 2018).

Sample contamination poses a major risk, with risks high during sample preparation and zircon extraction. If the laboratory and equipment is not cleaned sufficiently after each step, zircons from previous samples may contaminate later samples. The process of sieving to a certain size fraction may exclude larger or smaller zircons and introduce a bias. (Fedo *et al*., 2003).

Not all rocks are equal in their zircon content, this introduces an immediate bias where a low-zircon bearing source rock will supply fewer zircons than a source rock high in zircon concentration. The final zircons picked for analysis will therefore be weighted towards source rocks with high abundances of zircons and misrepresent the geological history of the sedimentary rock being analysed. Further bias may be introduced in the manual picking stage where the smaller zircon fraction may be excluded in favour for larger easier to pick zircons. (Fedo *et al*., 2003).

Elemental fractionation during laser ablation remains a problem with LA-ICP-MS method as the parameters are dependent on each other. Differential fractionation may therefore affect the accuracy and precision of the age calculations which can be corrected with the use of matrix-matched calibration standards (Jeffries *et al*., 1996; Koch *et al*., 2002).

2.10.4: Statistical requirements

There is still a fair amount of debate on the minimum number of zircon grains required to accurately determine the provenance area for a sedimentary unit. Dodson *et al*. (1988) proposed 60 grains as a minimum representing at least 5% of the total population of grains which will result in a 95% confidence level. A minimum number of 50 zircon grains were suggested by Morton *et al*. (1996). More recently, 80 grains have been suggested as a minimum for accurate results, with a best practice of randomly selecting 35 to 70 zircon grains and then deliberately selecting zircons based on colour, size and shape to ensure that the minor component is represented without introducing a bias (Anderson, 2005; Košler, 2012).

CHAPTER 3: METHODS

3.1: Lithological logging (11MTD001)

Borehole 11MTD001 (Coordinates; X: 303000, Y: 8282060; WGS 84, UTM 36L) was drilled in 2011 as part of coal exploration activities in the area by ENRC. The borehole would normally have ended above the conglomerate sequence, but in this instance the decision was made to drill into basement rocks. The PQ sized core, with a diameter of 83 mm, was handled and packed into metal core boxes at the drilling site by geological technicians before being transported to the core yard. Downhole geophysics was done by a contracting company to determine the density of the rocks. Geologists at the core yard used the downhole geophysics to accurately measure and mark the metre depth intervals using the coal horizons as reference points. Geophysical depths were compared to the drillers depth to ensure correct depth measurements of the borehole. Once the borehole was logged and sampled the core was stored in core racks under cover from the weather.

In 2015 the borehole was retrieved and lithologically logged in detail by the author for the purpose of this dissertation. The 2015 log was compared to the original log in 2011, logged by an exploration geologist at ENRC, to ensure accuracy as handling and sampling may have disturbed the core after the original log was completed. The Vúzi Formation intersection was identified and transported to the University of Witwatersrand in South Africa. Medium grained sandstones from the lower Karoo were selected for LA-ICP-MS analysis. Samples that recorded less than 70 zircons were discarded for data reduction. The Vúzi Formation intersection was logged in detail in order to correlate the intersection with sequences described by Bond and Stocklmayer (1967) and Visser (1997).

3.2: Zircon Analysis

In 2015 four sandstone samples (B1764, B1766, B1775 and B1778) from the Vúzi, "Transitional," and Matinde formations (Table 7) were taken in Mozambique and transported to South Africa. Three additional sandstone samples (Tete 1, Tete 2 and Tete 3) were taken from the Vúzi Formation in 2016. The 2015 and 2016 batches of samples were then prepared and analysed at the University of Johannesburg, with each sample undergoing the following steps as described by Vorster (2013): milling, sieving, density separation, zircon picking, mounting, SEM imaging, LA-ICP-MS analysis and data procession. The author conducted the sample preparation and mineral separation at the University of Johannesburg. The samples were picked and mounted by Laura Bowden a PhD student at the University of Johannesburg. The author conducted LA-ICP-MS analysis on two of the six samples used in this thesis, the rest was conducted by Dr. Clarisa Vorster from the University of Johannesburg. All data reduction and interpretation for this thesis was done by the author.

3.2.1: Milling and Sieving

Samples were placed into a plastic sample bag and gently crushed to pebble sized proportions using a hammer. Caution was taken to prevent contamination and surfaces were cleaned with ethanol at each step with new sample bags used for each sample. The pebble sized fractions were washed and dried before being milled using a Siebtechnik disk swing with metal rings. Each sample was milled for five seconds and sieved to obtain a <250 μm fraction, >250 μm material was then crushed again and sieved with the process repeated until all the material passed through the 250 μm sieve. Care was taken to prevent over milling and the equipment was cleaned with water and ethanol. The plastic sieves were discarded and replaced with a clean sieve for each sample.

3.2.2: Density Separation

Each sample was washed in the lab to remove fine material before being suspended in Lithium Sodium Polytungstate with a density of ~2.95 g/ml. Heavy minerals, including zircons, were separated from the minerals with a specific gravity ("SG") of less than 2.95. The lighter material was discarded. The material was washed with sterile water and dried in a drying oven.

3.2.3: Zircon picking and mounting

The material was then placed under a microscope where zircons could be hand-picked with a target of >100 zircons per sample. Due to the limited number of zircons present the method of picking randomly and non-randomly to prevent a bias was not possible. The picked zircons were then mounted in an epoxy disk, which was then polished to prepare the zircons for analysis by exposing the grains core and creating a flat surface.

3.2.4: SEM imaging

The epoxy disks were coated with carbon and placed under a Tescan Vega 3 Scanning Electron Microscope ("SEM") for cathode luminescence imaging ("CL"). These images are important to determine the point of ablation for analysis in order to prevent analysing metamorphic overprint rims or mixed zircon domains. SEM imaging was done by personnel at the University of Johannesburg.

3.2.5: LA-ICPMS analysis

Once the points of ablation were determined the epoxy disc was placed in the LA-ICP-MS for age determination with the operating conditions indicated in Table 5. GJ1 with an age of 608.5 +- 0.4 Ma (Jackson *et al*., 2004) and 91500 with an age of 1065 +- 0.4 Ma (Wiedenbeck *et al*., 1995) reference material was analysed on a regular basis between zircons to assist with the data correction. Each sample (B1764, B1766, B1775, B1778, Tete 1, Tete 3) started and ended off with a duplicate analysis of GJ1 and a single 91500 analysis to enable correction for elemental fractionation and mass discrimination. The regular analysis of reference materials is an indication on the precision and accuracy of the analysis. NIST 612 was used to tune the machine.

Table 5: LA-ICP-MS operating conditions (Vorster, 2013; pers. comm. Vorster, 2020).

ICP-MS	Type	Quadropole
	Model	Thermo Electron X Series (X237)
Gas Flow Rates	Plasma (Ar)	13.0 l/min
	Auxiliary (Ar)	0.8 l/min
	Carrier (He)	0.53 to 0.55 l/min
	Nebulizer (Ar)	0.74 l/min
	Chamber pressure	22 mbar
Laser	Type	Excimer laser
	Model	ASI RESOlution SE 193 nm
	Repetition rate	2 Hz
	Spot size	30 µm

	Fluency	1.3 J/cm2
	Nominal energy output	3mJ
	Antenuator setting	12.50%
Data aqcuisition	Protocol	Time - resolved analysis
	Quadrupole settling time	1500 to 15000 µSec
	Detector mode	Pulse counting
	Detector dead time	55 ns
	Isotopes measured	^{202}Hg, ^{204}Hg, ^{204}Pb, ^{206}Pb, ^{207}Pb, ^{208}Pb, ^{232}Th, ^{235}U, ^{238}U.
	Dwell time	10 ms
	Sample data acquisition	40 sec
	Background collection	20 sec

3.2.6: Data Reduction

Software provided by the University of Johannesburg and developed by Professor Jan Kramers was used in the data reduction process (Kramers, 2017). Calculated ages were displayed in concordia and probability density diagrams using Excel integrated Isoplot software (Ludwig, 2003). Results with <90% concordance were discarded.

3.3: Glacial cycle analysis

The portion of the borehole transported to the University of Johannesburg in 2015 was photographed in a wet state to assist in the logging of the conglomerates in detail, with focus on the clasts and matrix of each conglomeratic unit. Fining upward sequences were identified and compared to work done by Bond and Stocklmayer (1967) and Visser (1997).

3.4: Point Counting

Core photographs were loaded into JMicroVision version 1.2.7 for point counting. One-metre lengths of each conglomeratic unit identified were selected for clast composition analysis. The point counting area domain was selected over the core with a random grid type selected. Clasts and matrix were identified at the position of the pointer during the random grid selection. At least 100 points were counted per one-metre length of core.

CHAPTER 4: RESULTS

The results gathered during the zircon and deglaciation sequence analysis for borehole 11MTD001 drilled in 2011 during the exploration activities by ENRC are reported below.

4.1: Lithofacies

Detailed logging of 11MTD001 identified various lithofacies which have been summarized in Table 6 and illustrated in Figure 5.

Table 6: Lithofacies and general interpretation,

Lithofacies	Description	Thickness	Depositional Interpretation
Matrix supported diamictite (Gm)	Consists of angular with occasional sub-rounded to rounded clasts in a fine to medium grained matrix. The diamictites are structureless with very weak stratification in places where clasts are crudely aligned.	< 1m and > 0.2m	Subaqueous debris flows in a glaciolacustrine environment with current reworking. (Miall, 1996; Keys, 2012)
Matrix supported conglomerate (Gmm)	Consists of angular to sub-rounded granule to boulder sized clasts in a poorly sorted coarse to very course grained matrix. Clasts are dominated by granite/gneiss from the underlying basement. The conglomerate is massive and structureless.	~1m to ~8m	Material dropped by ice rafts in a glaciolacustrine environment or mass flow deposits during delta collapse (Bond and Stocklmayer, 1967; Vesely *et al*., 2018).
Clast supported conglomerate (Gcm)	Consists of sub-rounded pebble to boulder sized clasts in a poorly to moderately well sorted coarse to very course grained matrix. Angular granule sized clasts are visible in places. Clasts are dominated by granite/gneiss and mafic material. The conglomerate is massive and structureless, crude alignment of clasts are visible in places	~1.5 to ~9m	Outwash gravels in a high energy fluvio-glacial environment
Gritstone (Gm1)	Very coarse to granule gritstone. Poorly sorted and structureless.	~1.5m	Debris flows in a high energy regime.

Lithofacies	Description	Thickness	Depositional Interpretation
Massive sandstone (Sm)	Medium to coarse grained. Moderately well to poorly sorted. Structureless and massive.	Few cms to ~1m	Bed flow in a low flow regime (Miall, 1996).
Ripple cross-laminated sandstone (Sr)	Fine to coarse grained. Poorly sorted. Ripples are occasionally disturbed by bioturbation in finer grained portions.	<1m to ~6m	Migration of current ripples in low flow regime (Miall, 1996).
Convoluted sandstone (Scon)	Medium to coarse grained. Poorly sorted. bedding has been disturbed. Occurs near a diamictite.	~3.4m	Reworked sand during high energy debris flows.
Cross-bedded sandstone (Sc)	Moderately well sorted coarse grained sandstone. Occasional coarsening upwards.	~3m	Migration of dune forms in a low flow regime (Miall, 1996).
Horizontally stratified sandstone (Sh)	Fine to coarse grained. Poorly sorted. Minor birturbation in finer grained portions.	~1m	Planar bed flow in a low flow regime (Miall, 1996).
Laminated Siltstone (Fsc)	Silt to very fine grained. Poorly sorted and bioturbated.	~45m	Lacustrine with a quiescent environment (Key, 2015; Cairncross and Winter, 1984).
Laminated Siltstone/ Sandstone (Fl)	Interbedded siltstone and fine to medium grained sandstone. Poorly sorted and bioturbated. Occasional fining-up sequences. Minor cross-bedding in places.	~1m to ~4m	Alternating flow conditions with low energy currents forming alternating sand and silt layers. Occasional sheet flows from floods form thicker sand layers (Allen and Fielding, 2007).
Carbonaceous mudstone with coal (Co)	Interbedded coal and carbonaceous mudstone.	Few centermeters to ~9m	Vegetated mires in a quiescent environment (Miall, 1996).

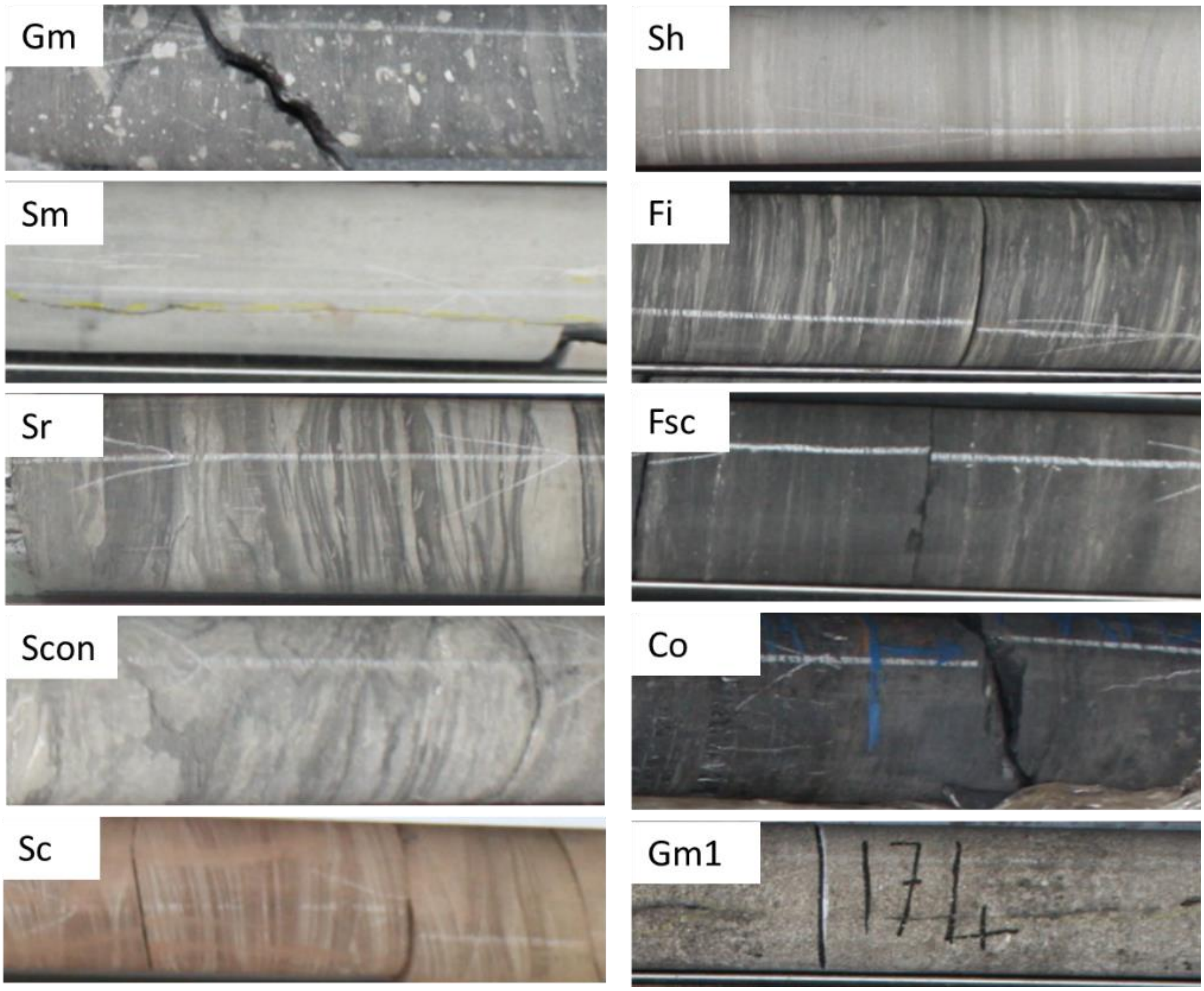

Figure 5: Core photography of lithofacies identified in 11MTD001. Gm – Massive diamictite; Sm – Massive sandstone; Sr – Ripple cross-laminated sandstone; Scon – Convoluted sandstone; Sc – Cross-bedded sandstone; Sh – Horizontally stratified sandstone; Fi – Laminated siltstone/sandstone; Fsc – Laminated siltstone; Co – Carbonaceous mudstone with coal measures; Gm1 – Gritstone.

4.2: Zircon Analysis

Five samples were prepared and analysed from the lower Karoo stratigraphy from borehole 11MTD001 (Table 7 and Figure 6). The results of these samples are presented below.

Table 7: Summary of zircons analysed and accepted for samples B1766, B1775, B1778, Tete 1 and Tete 3. Zircons with discordance better than 10% were accepted.

Sample ID	Lithology	Stratigraphy	From (m)	To (m)	Zircons Analysed	Zircons Accepted
B1764	Sandstone	Matinde Formation	14.23	14.30	0	0
B1766	Sandstone	Matinde Formation	112.62	112.83	90	36
B1775	Sandstone	"Transitional" Formation	179.24	179.46	126	63
B1778	Sandstone	Vúzi Formation	191.2	191.4	86	58
Tete 1	Sandstone	Vúzi Formation	269.42	269.72	132	99
Tete 3	Sandstone	Vúzi Formation	277.77	278	71	54

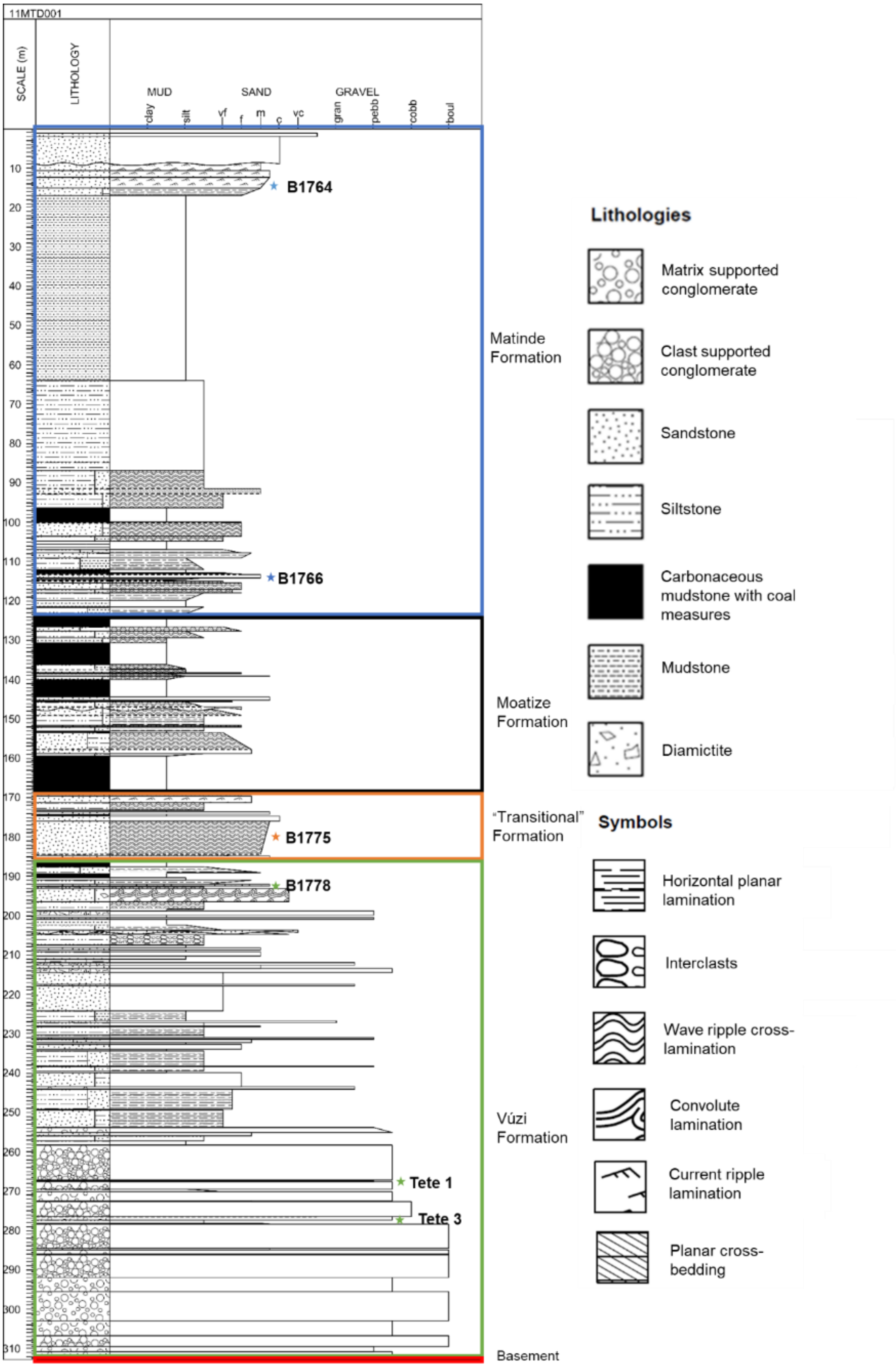

Figure 6: Lithological log for 11MTD001 indicating the positions of samples Tete 3, Tete 1, B1778, B1775 and B1766 in relation to the Vúzi, Moatize, Matinde and Cádzi Formations. Scale bar represents intervals in metres. Sample positions are represented by coloured stars.

A total of 310 zircons had a discordance of less than 10% and were accepted for interpretation. All Th/U ratios (Figure 6) of the analysed zircons exceeded 0.07, indicating the calculated ages are of a magmatic origin.

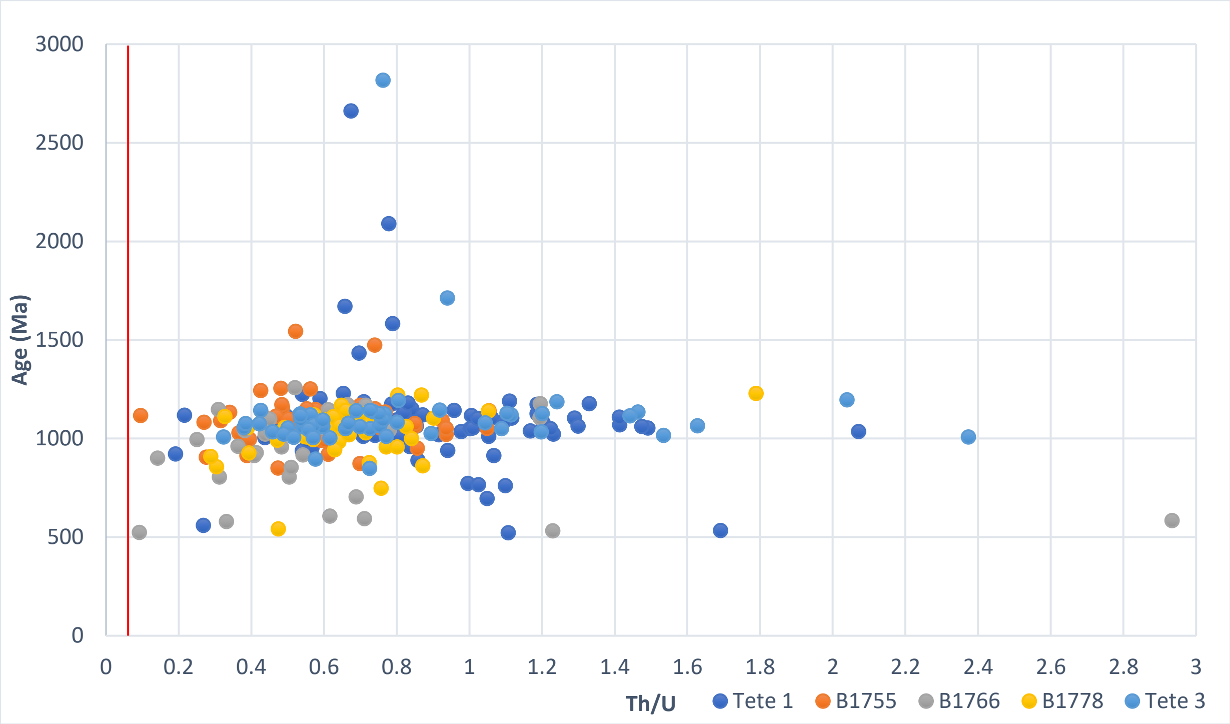

Figure 7: Th/U ratios for all zircons accepted for samples Tete 1, Tete 3, B1755, B1766 and B1778. The cut-off 0.07 Th/U ratio (Rubatto, 2002.) for the determination of igneous versus metamorphic origin is indicated by the red line.

4.1.1: Density Probability Plots

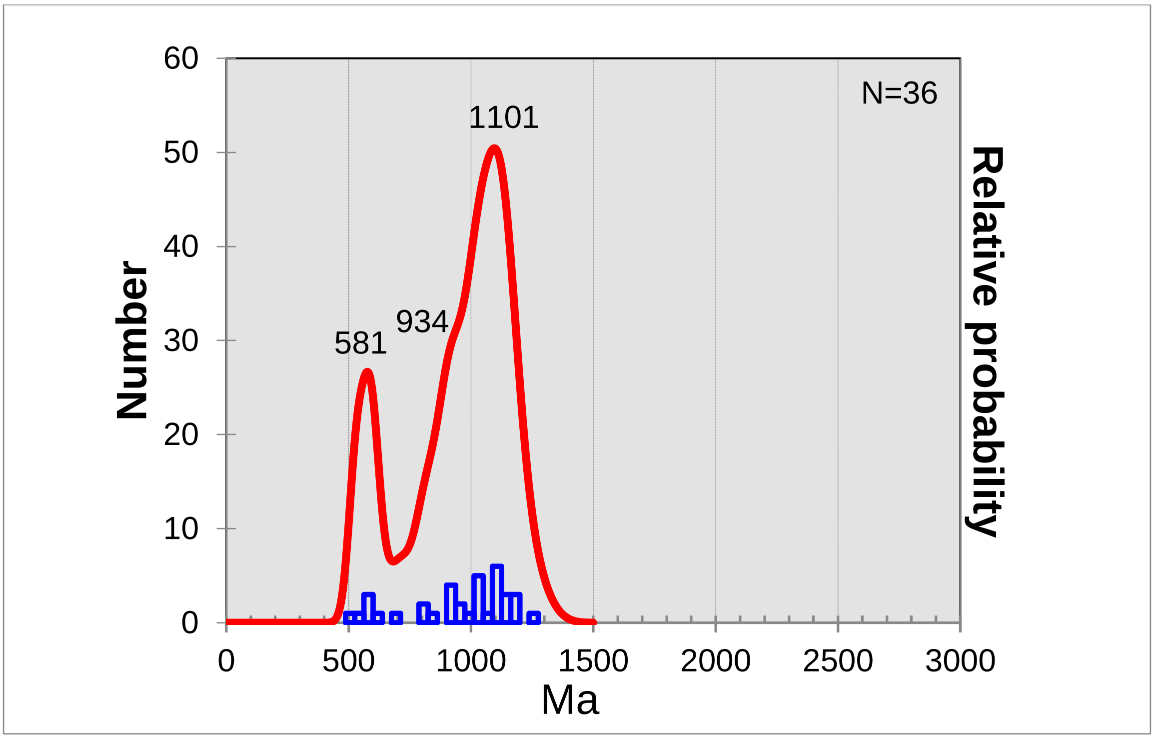

Figure 8: Probability density plot for sample B1766 (Matinde Formation). Three prominent age populations are indicated with peaks at 581 Ma, 934 Ma and 1100 Ma.

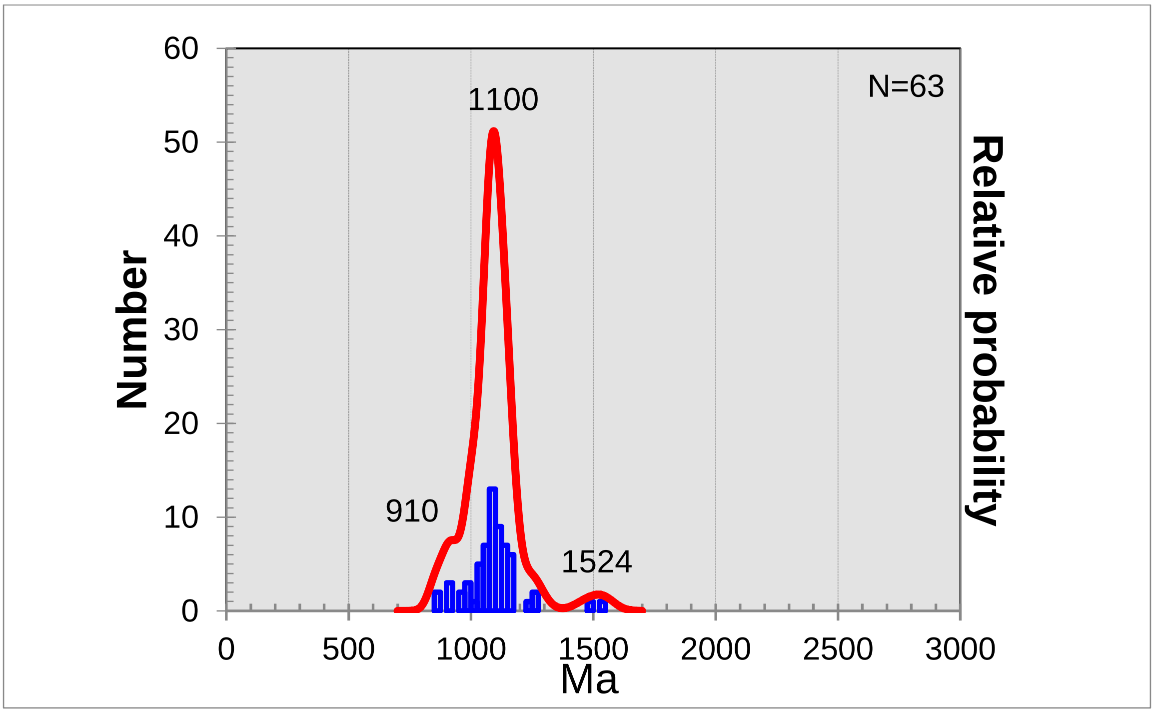

Figure 9: Probability density plot for sample B1775 ("Transitional" Formation). One prominent age population is indicated with a significant peak at 1100 Ma, minor peaks are recorded at 910 Ma, 1252 Ma and 1524 Ma.

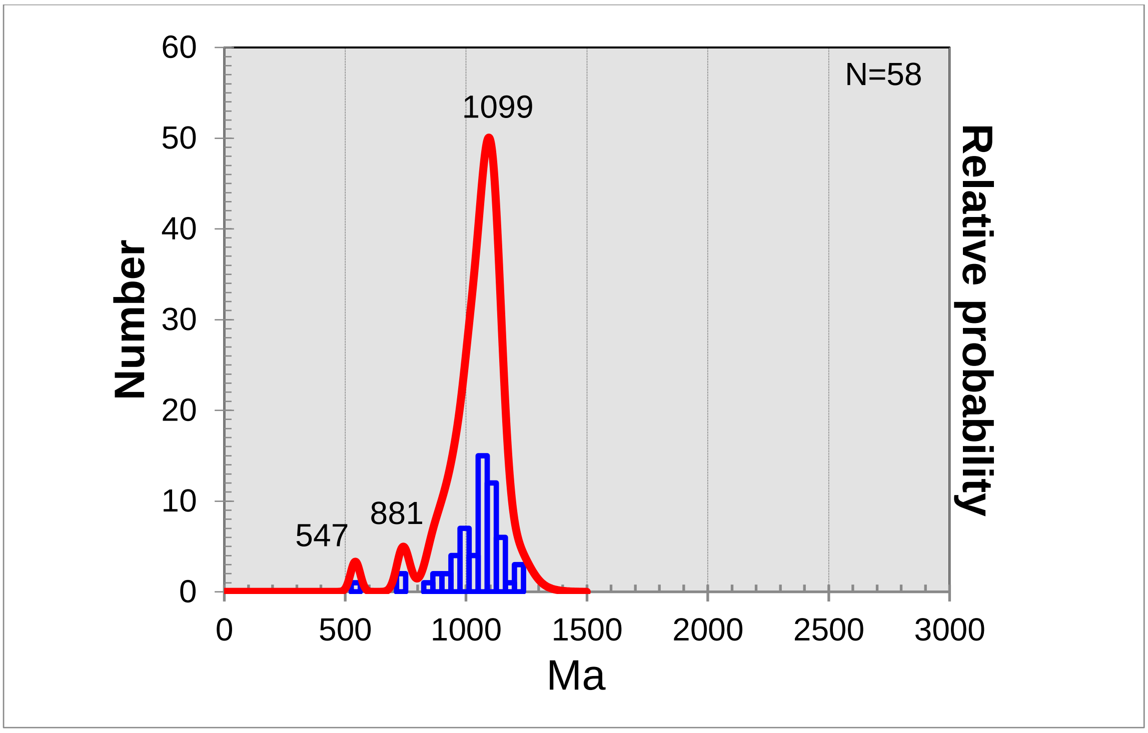

Figure 10: Probability density plot for sample B1778 (Vúzi Formation). One prominent age population is indicated with a significant peak at 1099 Ma. Minor peaks are recorded at 547 Ma, 750 Ma and 881 Ma.

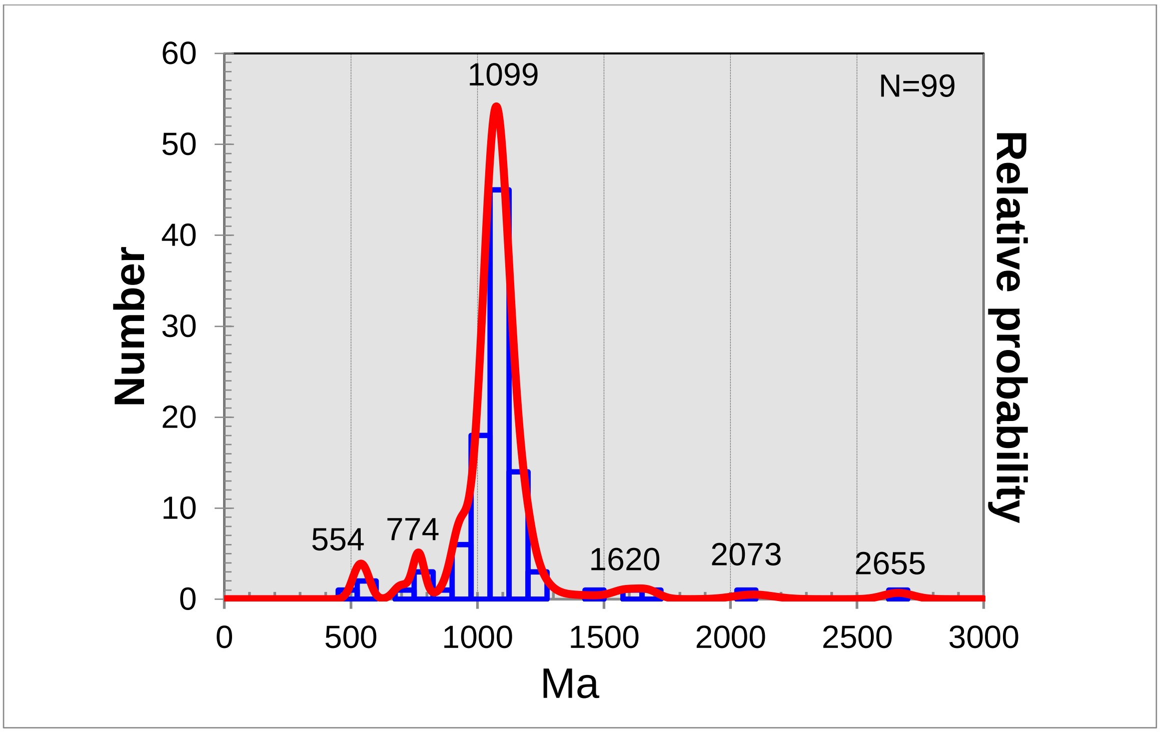

Figure 11: Probability density plot for sample Tete 1 (Vúzi Formation). One prominent age population is indicated with a significant peak at 1099 Ma. Minor peaks are recorded at 554 Ma and 774 Ma. Single crystal ages were recorded at 1620 Ma, 2073 Ma and 2655 Ma.

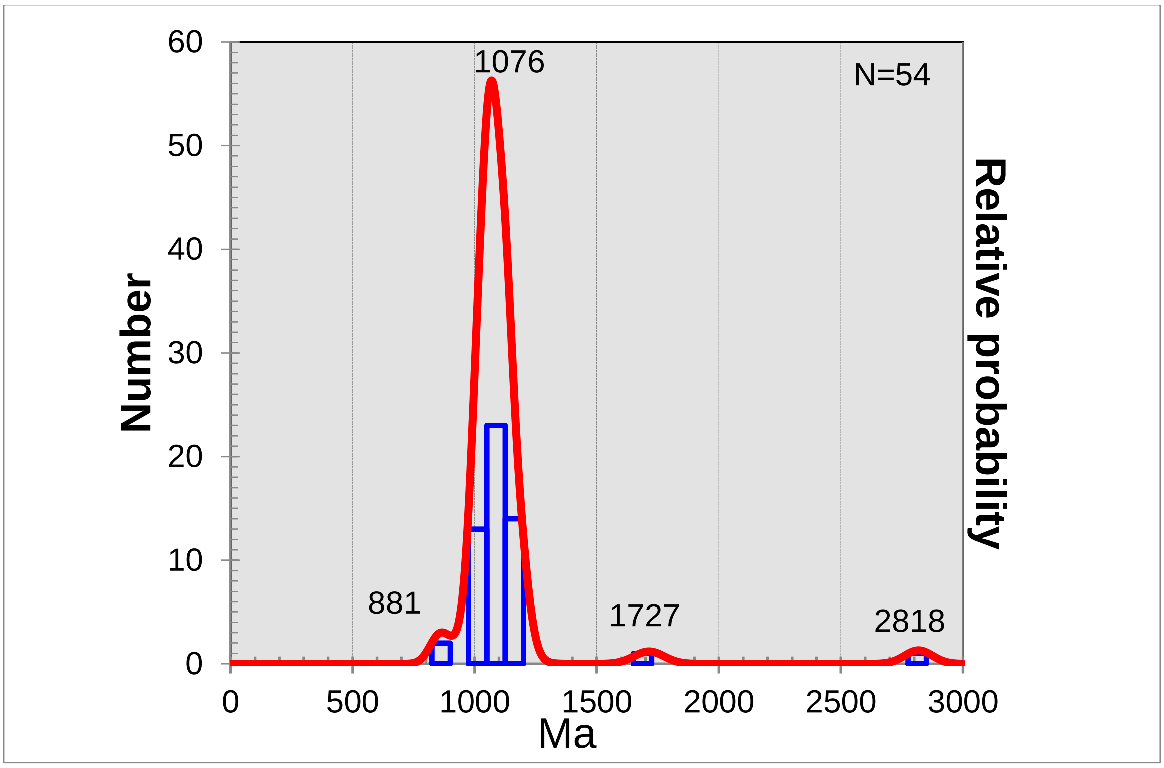

Figure 12: Probability density plot for sample Tete 3 (Vúzi Formation). One prominent age population is indicated with a significant peak at 1076 Ma with a minor peak at 881 Ma. Single crystal ages were recorded at 1727 Ma and 2818 Ma.

4.1.2: B1764

A well-sorted reddish-brown cross-bedded moderately weathered medium grained sandstone. The sample occurs in sandstone sequence overlying a thick mudstone unit. This sample was zircon poor and was not analysed.

4.1.3: B1766

A moderately well-sorted light off white grey massive medium to coarse grained sandstone with irregular carbonaceous flecks. The sample occurs in a fining upwards sequence which ends with the formation of carbonaceous mudstone with coal measures. Of the 90 zircons picked for analysis only 33 were concordant, the ages of these zircons are displayed in the probability density plot in Figure 8.

Most of the zircons fall within the Mesoproterozoic age with a strong peak at ~1104 Ma, with the youngest aged zircon 1022 ± 51 Ma representing the lower limit and 1259 ± 68 Ma representing the upper limit as the oldest aged zircon. Two peaks occur in the Neoproterozoic age with peaks at ~581 Ma (525 ± 30 Ma and 607 ± 42 Ma representing the lower and upper limits respectively) and ~934 Ma (705 ± 41 Ma and 996 ± 48 Ma representing the lower and upper limits respectively).

Table 8: Summary of zircons with discordance <10 % from sample B1766, with general descriptions on the zircon textures, U content and Th/U ratios for each age population.

	Population	Number of zircons (Concordant)	Predominant grain textures (internal and external)	U content and Th/U ratio range
Cambrian	524 - 533 Ma	2 representing 5% of concordant zircons accepted	Subhedral, 80 µm long and 40 µm wide with an aspect ratio of 2.0.	Average U ppm: 238; Th/U: 0.09 - 1.22
Neoproterozoic	579 - 607 Ma	4 representing 11% of concordant zircons accepted	Subhedral to euhedral varying in size from 60 µm to 200 µm long and 40 µm to 140 µm wide with an aspect ratio of 1.0 - 2.0 with elongated grains up to a ratio of 5. Grains predominantly have oscillatory zonation with no to minor bright overgrowths.	Average U ppm: 135; Th/U: 0.33 - 2.93
	705 - 996 Ma	11 representing 30% of concordant zircons analysed	Subhedral to euhedral varying in size from 70 µm to 250 µm long and 40 µm to 200 µm wide with an aspect ratio of 1.1 – 4.5. Most grains have oscillatory zonation with minor cracking, inclusions and bright overgrowths.	Average U ppm: 129; Th/U: 0.14 - 0.54
Mesoproterozoic	1022 - 1259 Ma	19 representing 53% of concordant zircons analysed	Subhedral to anhedral with a minor population of euhedral grains varying in size from 60 µm to 320 µm long and 40 µm to 140 µm wide with an aspect ratio of 1.0 - 3.5. Internal zonation is predominantly oscillatory with minor cracking, inclusions and bright overgrowths. Minor population of grain's have sector zonation.	Average U ppm: 124; Th/U: 0.31 - 1.95

Three age populations were identified with approximately 53% of zircons accepted falling in the Mesoproterozoic (1022 - 1259 Ma) age. Selected cathode luminescence SEM images of the zircons described in Table 8 are displayed in Figure 13.

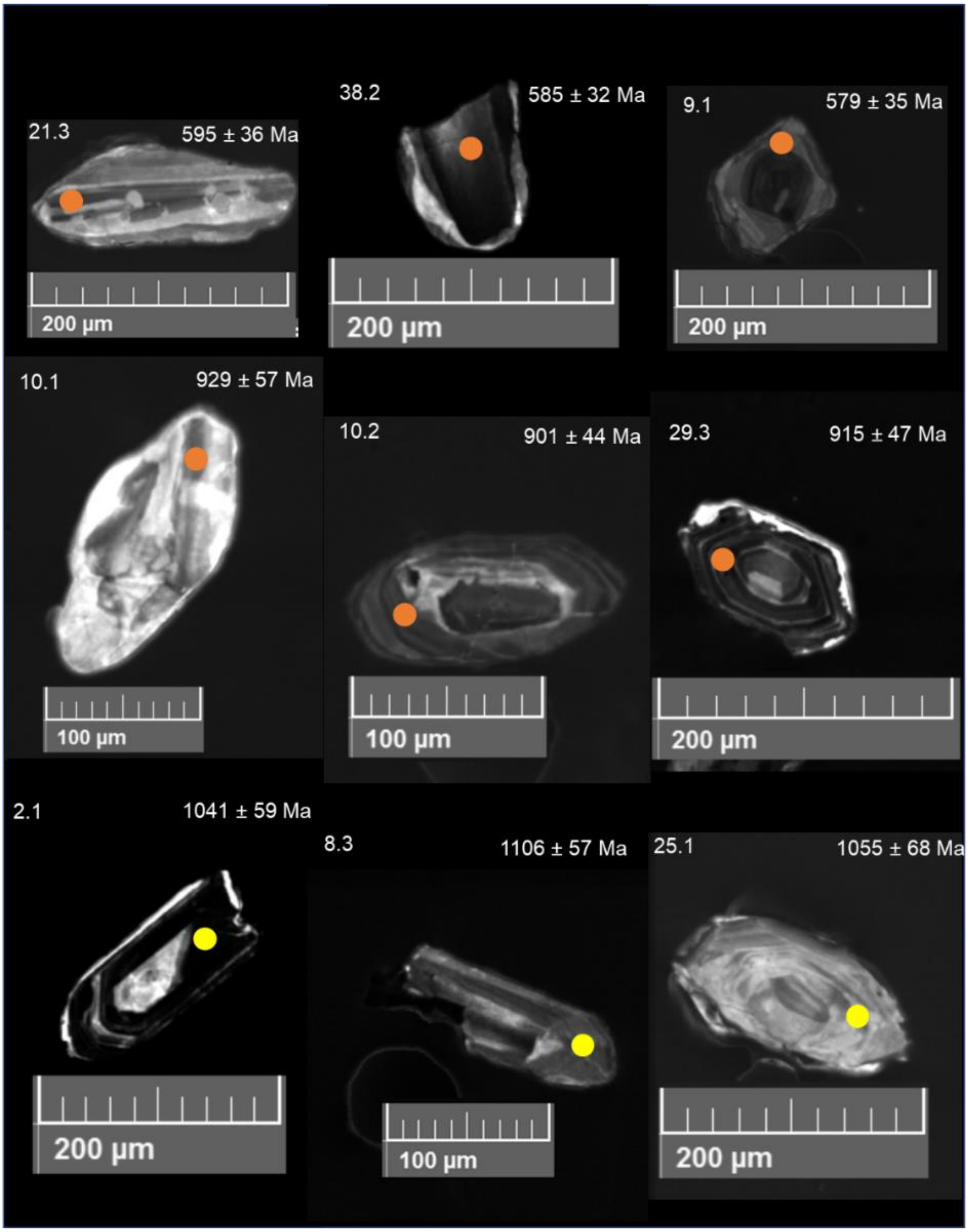

Figure 13: Cathode luminescence SEM images of selected zircons from sample B1766 indicating the laser ablation points, the internal structures and zonation. The sample number and age calculation

for each zircon is indicated, laser ablation point indicated by coloured dots. Yellow dots indicate Mesoproterozoic ages (dominant age population) while orange indicates Neoproterozoic.

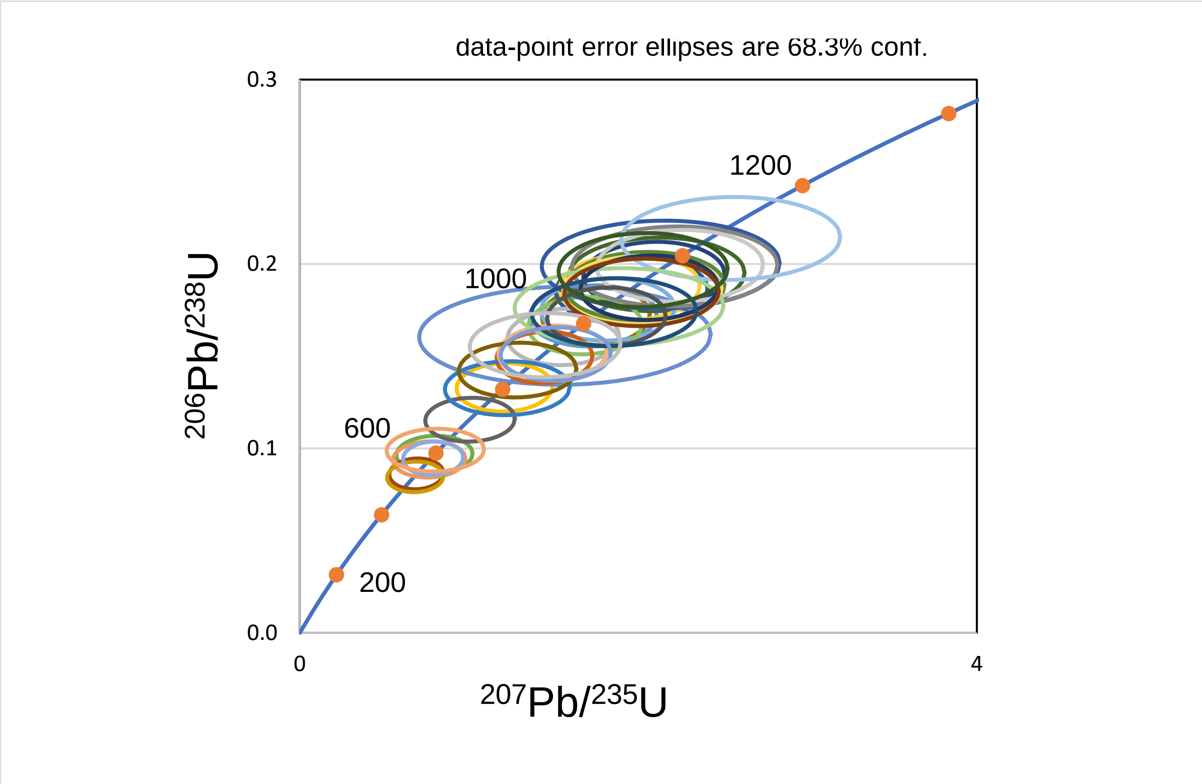

Figure 14: Concordia diagram for zircons analysed and accepted, all results plot on the concordia line.

The samples plot well on the Concordia curve indicating a high level of concordance for the samples accepted

4.1.4: B1775

A moderately well-sorted, irregular bedded, light off white grey, medium to coarse grained sandstone. The sample occurs in the middle of a coarsening upwards sequence and is overlain by a coarse grained 'sugary' sandstone which is the base of a unit of carbonaceous mudstone with coal measures. Of the 126 zircons picked for analysis only 63 were concordant, the ages of these zircons are displayed in the probability density plot in Figure 9.

Most of the zircons fall within the Mesoproterozoic age with a strong peak at ~1100 Ma (1021 ± 31 Ma and 1172 ± 36 Ma representing the lower and upper limits respectively) and minor peaks at ~1252 Ma (1244 ± 38 Ma and 1256 ± 50 Ma representing the lower and upper limits respectively) and ~1524 Ma (1475 ± 53 Ma and 1544 ± 46 Ma representing the lower and upper limits respectively). A Neoproterozoic peak occurs at ~910 Ma (851 ± 30 Ma and 997 ± 25 Ma representing the lower and upper limits respectively).

Table 9: Summary of zircons with discordance <10 % from sample B1775, with general descriptions on the zircon textures, U content and Th/U ratios for each age population.

	Population	**Number of zircons (Concordant)**	**Predominant grain textures (internal and external)**	**U content and Th/U ratio range**
Neoproterozoic	851 - 997 Ma	10 representing 16% of concordant zircons accepted	Subhedral to euhedral with a minor population of anhedral grains varying in size from 80 µm to 180 µm long and 40 µm to 70 µm wide an aspect ratio of 1.25 - 3.6. Most grains have oscillatory zonation with bright overgrowths.	Average U ppm: 168.2; Th/U: 0.27 - 0.69
Mesoproterozoic	1021 - 1172 Ma	48 representing 76% of concordant zircons analysed	Subhedral to euhedral grains varying in size from 70 µm to 200 µm long and 40 µm to 140 µm wide with an aspect ratio of 1.0 - 2.7. Most grains have oscillatory zonation with minor cracking, inclusions and bright overgrowths.	Average U ppm: 226.6; Th/U: 0.14 - 0.54
	1244 - 1256 Ma	3 representing 5% of concordant zircons analysed	Subhedral to euhedral varying in size from 70 µm to 140 µm long and 60 µm wide with an aspect ratio of 1.2 - 2.3. Grains have oscillatory zonation, with one exhibiting inclusions and bright overgrowths.	Average U ppm: 67.5; Th/U: 0.42 - 0.56
	1475 - 1544 Ma	2 representing 3% of concordant zircons analysed	Subhedral to euhedral with varying in size from 100 µm to 120 µm long and 50 µm to 60 µm wide with an aspect ratio of 1.7 - 2.4. Both grains have oscillatory zonation while one exhibits minor cracking, inclusions and bright overgrowths.	Average U ppm: 68; Th/U: 0.52 - 0.74

Four age populations were identified with approximately 76% of zircons accepted falling in the Mesoproterozoic (1021 - 1172 Ma) age. Selected cathode luminescence SEM images of the zircons described in Table 9 are displayed in Figure 15.

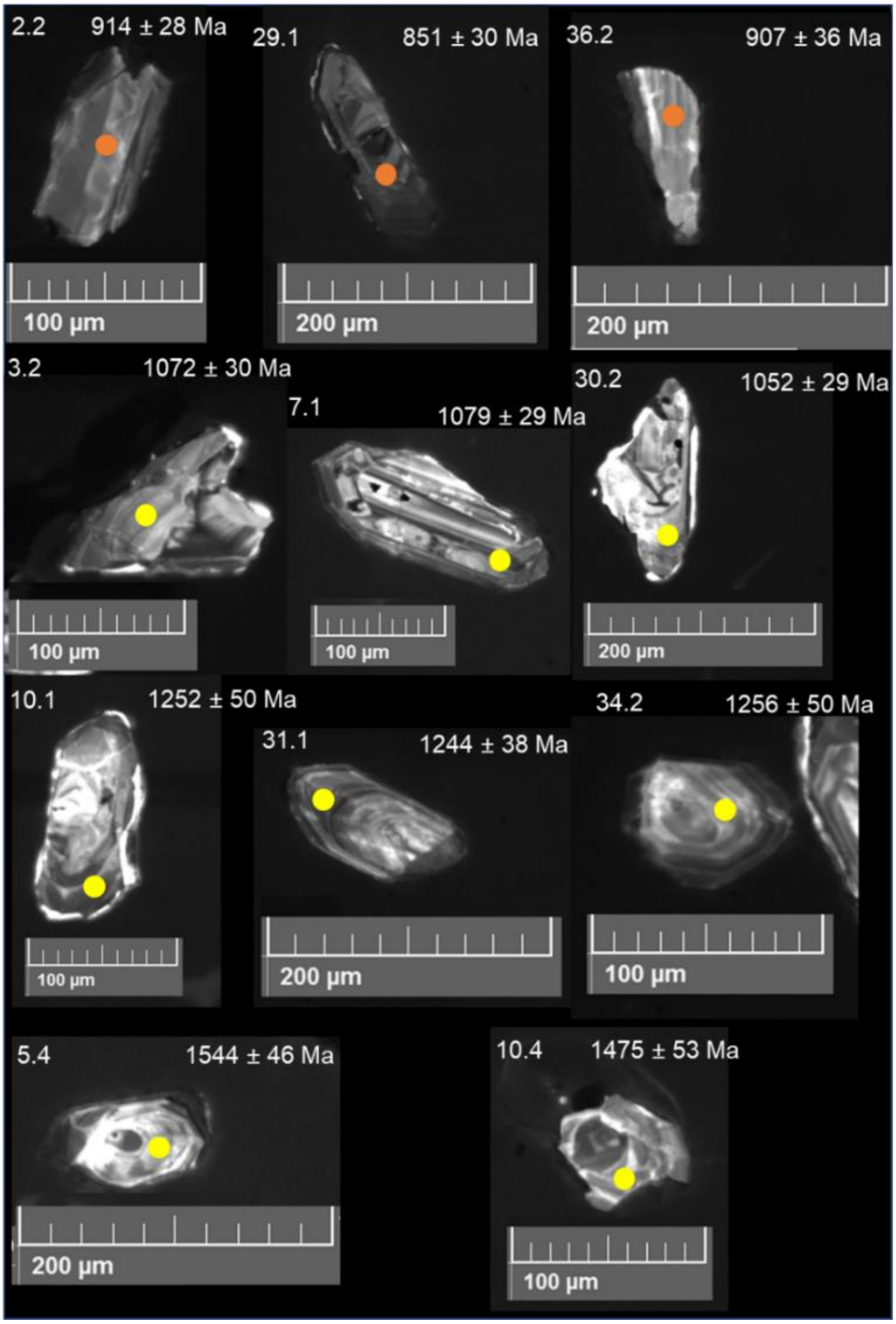

Figure 15: Cathode luminescence SEM images of selected zircons from sample B1755 indicating the laser ablation points, the internal structures and zonation. The sample number and age calculation

for each zircon is indicated, laser ablation point indicated by coloured dots. Yellow dots indicate Mesoproterozoic ages (dominant age population), while orange indicates Neoproterozoic.

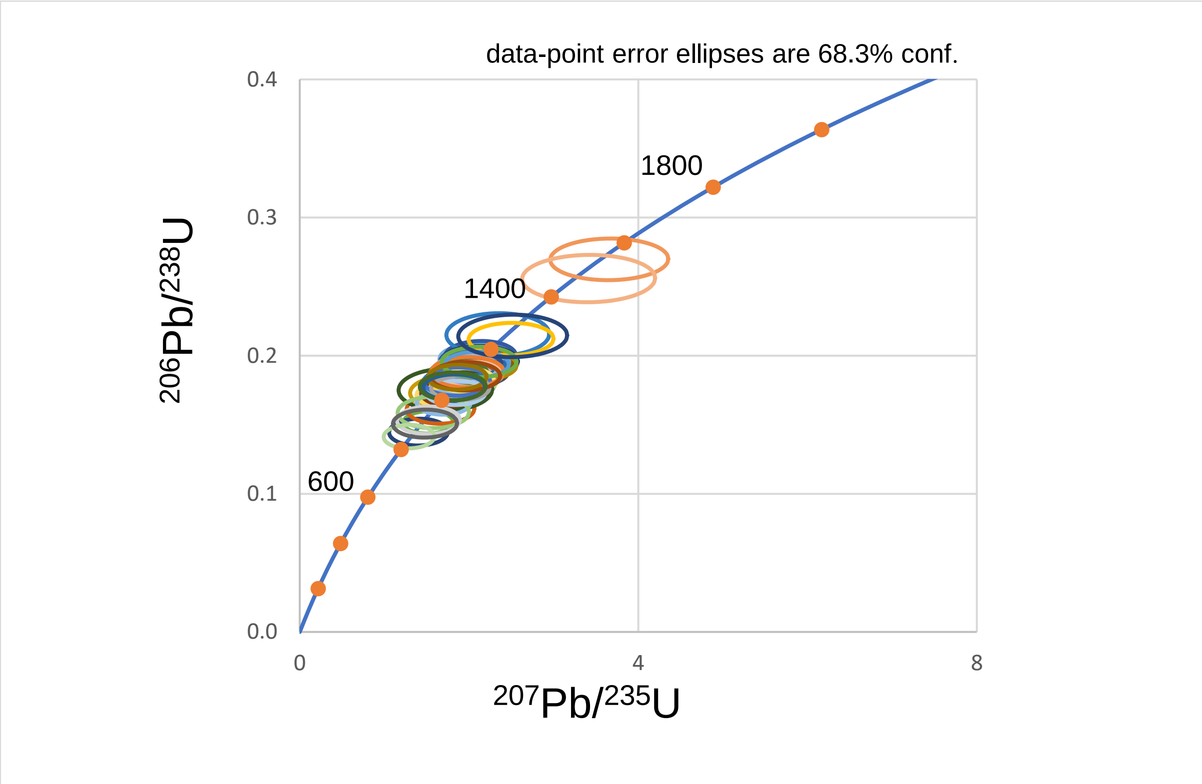

Figure 16: Concordia diagram for zircons analysed and accepted, all results plot on the concordia line.

The samples plot well on the Concordia curve indicating a high level of concordance for the samples accepted.

4.1.5: B1778

A poorly sorted, massive, light off white grey, medium to coarse-grained sandstone. The sample overlies a diamictite unit and forms the base of a fining upward sequence ending with a unit of carbonaceous mudstone with coal measures. Of the 86 zircons picked for analysis only 58 were concordant, the ages of these zircons are displayed in the probability density plot in Figure 10.

Most of the zircons fall within the Mesoproterozoic age with a strong peak at ~1099 Ma (1000 ± 30 Ma and 1169 ± 46 Ma, representing the lower and upper limits respectively), minor peaks occur in the Mesoproterozoic (1222 ± 44 Ma and 1229 ± 84 Ma representing the lower and upper limits respectively) Neoproterozoic with peaks at ~881 Ma (857 ± 32 Ma and 995 ± 29

Ma representing the lower and upper limits respectively) and ~749 Ma (749 ± 28 Ma) with one population in the Cambrian with a peak at ~547 Ma (542 ± 20 Ma).

Table 10: Summary of zircons with <10 % discordance from sample B1778, with general descriptions on the zircon textures, U content and Th/U ratios for each age population.

	Population	Number of zircons (Concordant)	Predominant grain textures (internal and external)	U content and Th/U ratio range
Cambrian	542 Ma	1 representing 2% of concordant zircons accepted	Subhedral and is 200 µm long and 80 µm wide with an aspect ratio of 2.5. Grain has weak oscillatory zonation.	U ppm: 353.2; Th/U: 0.47
Neoproterozoic	749 Ma	1 representing 2% of concordant zircons accepted	Anhedrea and is 110 µm long and 90 µm an aspect ratio of 1.20. Grains exhibit oscillatory zonation and bright overgrowths.	U ppm: 206.48; Th/U: 0.76
	910 - 995 Ma	11 representing 19% of concordant zircons accepted	Subhedral to anhedral varying in size from 90 µm to 220 µm long and 60 µm to 130 µm wide an aspect ratio of 1.40 - 1.7. Grains have oscillatory zonation to no zonation with minor cracking, inclusions and bright overgrowths.	Average U ppm: 331.75; Th/U: 0.28 - 0.87
Mesoproterozoic	1000 - 1169 Ma	42 representing 72% of concordant zircons analysed	Subhedral to euhedral varying in size from 80 µm to 180 µm long and 50 µm to 120 µm wide with an aspect ratio of 1.25 - 2.0. Grains have oscillatory zonation to no zonation with minor cracking, inclusions and bright overgrowths.	Average U ppm: 303.46; Th/U: 0.32 - 1.05

	Population	Number of zircons (Concordant)	Predominant grain textures (internal and external)	U content and Th/U ratio range
	1222 - 1229 Ma	3 representing 5% of concordant zircons analysed	Subhedral varying in size from 110 µm to 150 µm long and are 80 µm wide with an aspect ratio of 1.35 - 1.9. Grains have oscillatory zonation.	Average U ppm: 58.52; Th/U: 0.80 - 1.79

Four age populations were identified with approximately 72% of zircons accepted falling in the Neoproterozoic (1000 - 1169 Ma) age. Selected cathode luminescence SEM images of the zircons described in Table 10 are displayed in Figure 17.

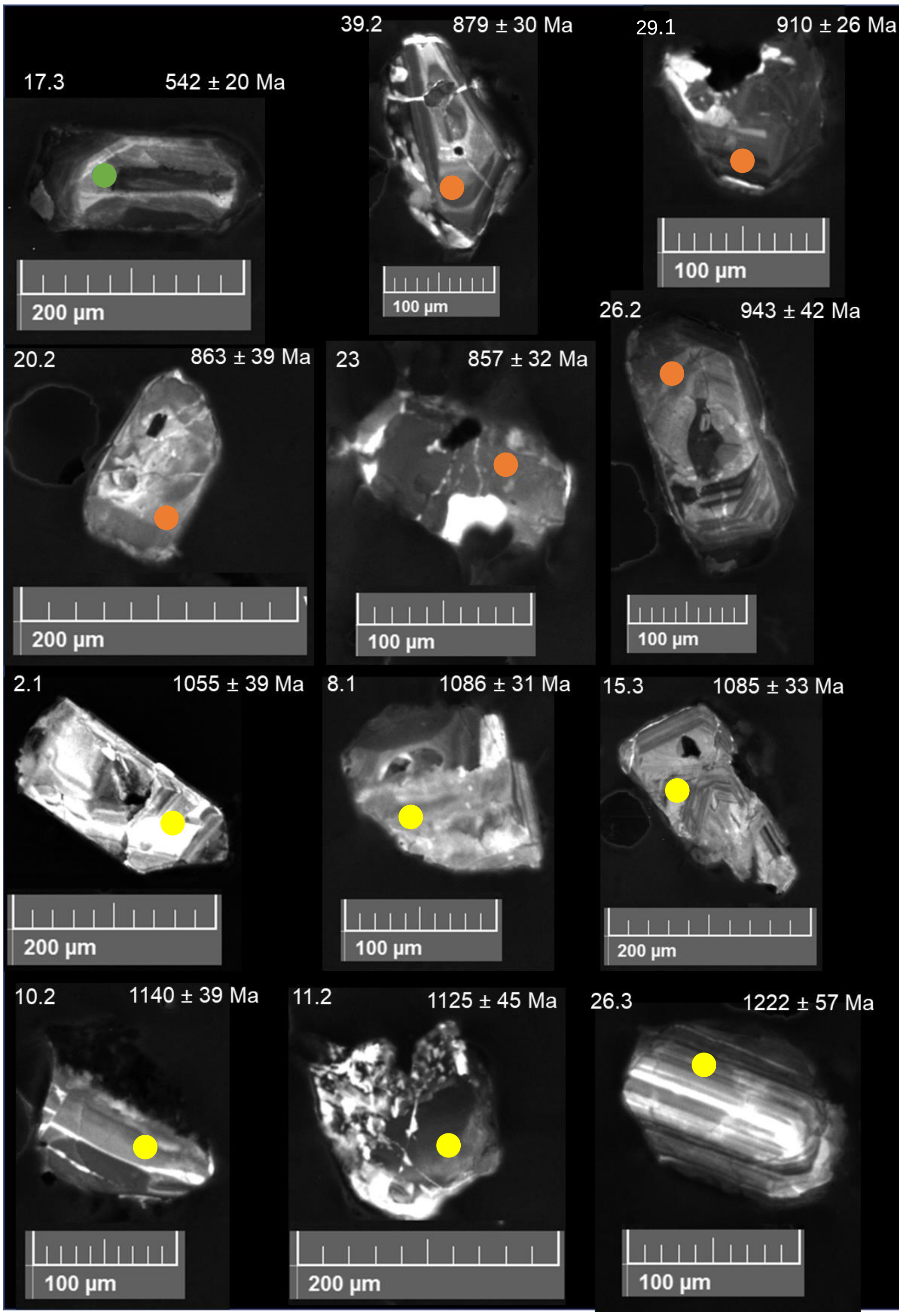

Figure 17: Cathode luminescence SEM images of selected zircons from sample B1788 indicating the laser ablation points, the internal structures and zonation. The sample number and age calculation for each zircon is indicated, laser ablation point indicated by coloured dots. Green dots indicate Cambrian age, Yellow dots indicate Mesoproterozoic ages while orange indicates Neoproterozoic (dominant age population).

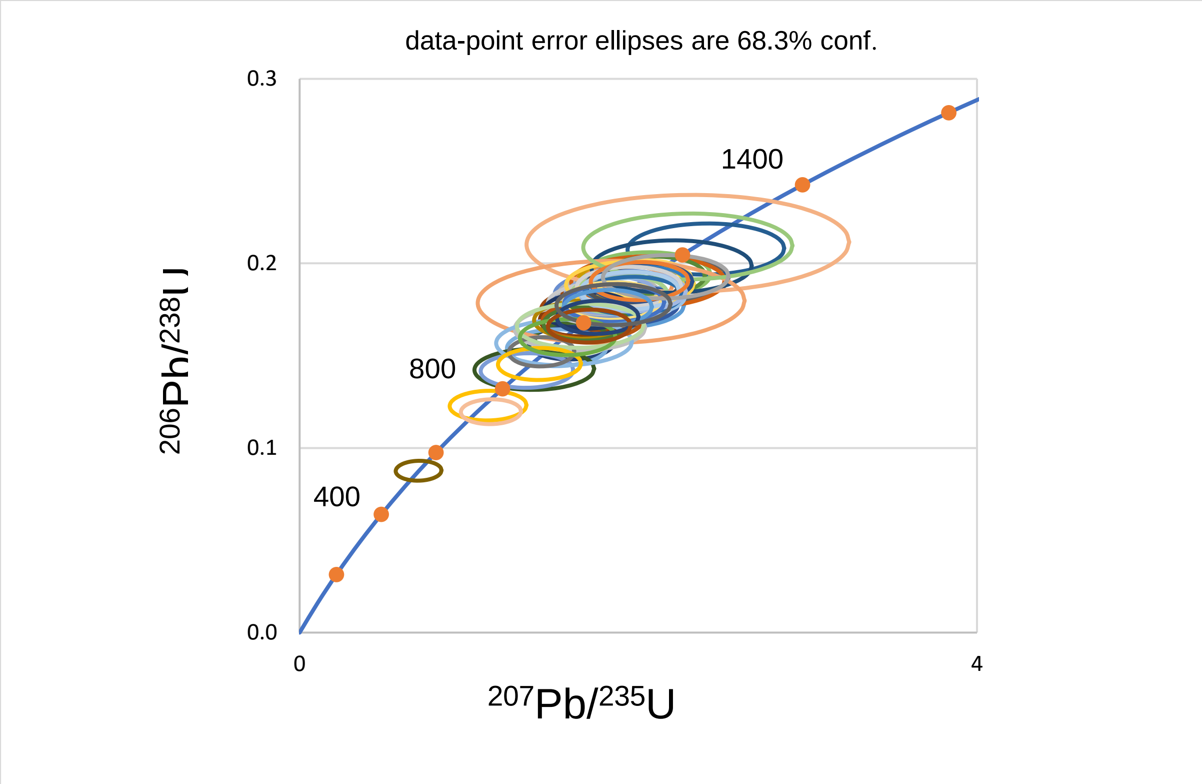

Figure 18: Concordia diagram for zircons analysed and accepted, all results plot on the Concordia line.

The samples plot well on the Concordia curve indicating a high level of concordance for the samples accepted.

4.1.6: Tete 1

A well-sorted, massive, light off white grey, fine to medium-grained sandstone. The sample forms the base of a fining upward sequence deposited between two conglomeratic units. Of the 132 zircons picked for analysis only 99 were concordant, the ages of these zircons are displayed in the probability density plot in Figure 11.

Most of the zircons fall within the Mesoproterozoic age with a strong peak at ~1073 Ma (1006 ± 37 Ma and 1229 ± 50 Ma representing the lower and upper limits, respectively). Minor peaks occur in the Cambrian ~554 Ma (523 ± 26 Ma and 560 ± 24 Ma representing the lower and upper limits, respectively), Neoproterozoic ~760 Ma (697 ± 28 Ma and 773 ± 25 Ma representing the lower and upper limits respectively), ~940 (890 ± 47 Ma and 999 ± 43 Ma representing the lower and upper limits respectively), Mesoproterozoic ~1620 Ma (1434 ±

110 Ma and 1672 ± 44 Ma representing the lower and upper limits, respectively), Paleoproterozoic ~2073 Ma (2091 ± 79 Ma) and Neoarchaean ~2662 (2662 ± 79 Ma).

Table 11: Summary of zircons with <10 % discordance from sample Tete 1, with general descriptions on the zircon textures, U content and Th/U ratios for each age population.

	Population	**Number of zircons (Concordant)**	**Predominant grain textures (internal and external)**	**U content and Th/U ratio range**
Cambrian	523 - 560 Ma	3 representing 3% of concordant zircons accepted	Anhedral to subhedral varying in size from 100 µm to 180 µm long and 80 µm to 100 µm wide with an aspect ratio of 1.0 - 3.0. Subhedral grains have weak oscillatory zonation.	Average U ppm: 125.35; Th/U: 0.27 - 1.69
Neoproterozoic	697 - 773 Ma	4 representing 4% of concordant zircons analysed	Subhedral to euhedral varying in size from 50 µm to 150 µm long and 30 µm to 100 µm wide with an aspect ratio of 1.5 - 2.4. Grains have oscillatory zonation to no zonation with minor cracking, inclusions and bright overgrowths.	Average U ppm: 376.76; Th/U: 1.00 - 1.09
	890 - 999 Ma	9 representing 9% of concordant zircons analysed	Anhedral with a minor population of subhedral to euhedral. Grains vary in size from 80 µm to 200 µm long and 80 µm to 120 µm wide with an aspect ratio of 1.00 - 1.8. Most grains have oscillatory zonation with minor cracking, inclusions and bright overgrowths.	Average U ppm: 174.04; Th/U: 0.19 - 1.07
	1006 - 1229 Ma	78 representing 79% of concordant zircons analysed	Subhedral to euhedral with a minor population of anhedral grains. Grains vary in size from 90 µm to 200 µm long and 80 µm to 100 µm wide an aspect ratio of 1.0 - 4.0. Most grains have oscillatory zonation with minor cracking, inclusions and bright overgrowths.	Average U ppm: 209.5 Th/U: 0.22 - 2.07

	Population	Number of zircons (Concordant)	Predominant grain textures (internal and external)	U content and Th/U ratio range
Mesoproterozoic	1434 - 1583 Ma	2 representing 2% of concordant zircons analysed	Anhedral with a size of 100 µm to 120 µm long and 30 µm to 90 µm wide with an aspect ratio of 1.0 - 3.3. One grain has oscillatory zonation.	Average U ppm: 67.77; Th/U: 0.70 - 0.79
Paleoproterozoic	1672 Ma	1 representing 1% of concordant zircons analysed	Euhedral, 80 µm long and 80 µm wide with an aspect ratio of 1.0. Grain has weak oscillatory zonation.	U ppm: 188.72; Th/U: 0.65
	2091 Ma	1 representing 1% of concordant zircons analysed	Anhedral, 60 µm long and 50 µm wide with an aspect ratio of 1.2. Grain has weak oscillatory zonation.	U ppm: 35.09; Th/U: 0.78
Neoarchaean	2662 Ma	1 representing 1% of concordant zircons analysed	Subhedral, 120 µm long and 40 µm wide with an aspect ratio of 3. Grain has weak sector zonation.	U ppm: 217.80; Th/U: 0.67

Seven age populations were identified with approximately 79% of zircons accepted falling in the Mesoproterozoic (1006 - 1229 Ma) age. Selected cathode luminescence SEM images of the zircons described in Table 11 are displayed in Figure 19.

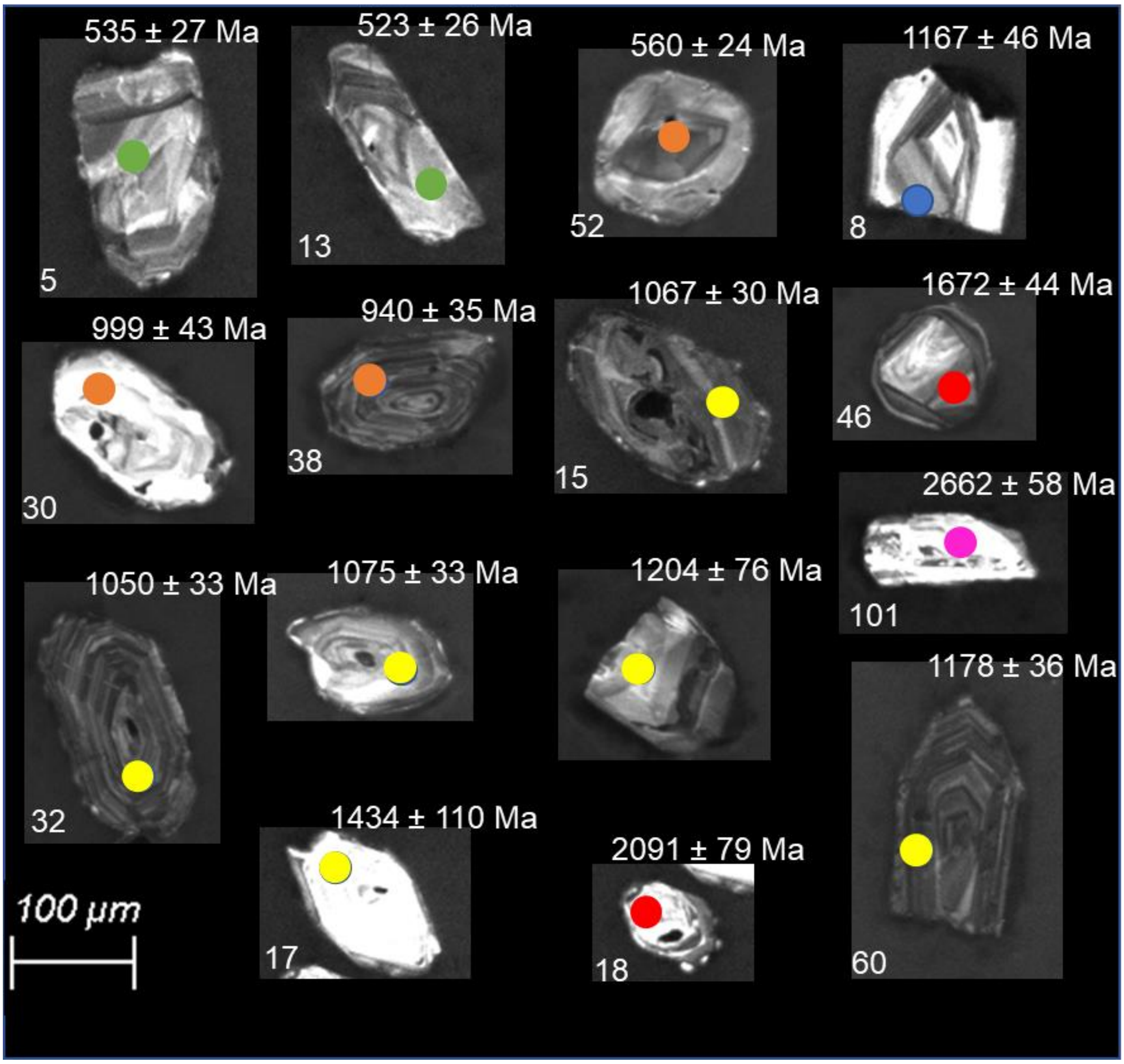

Figure 19: Cathode luminescence SEM images of selected zircons from sample Tete 1 indicating the laser ablation points, the internal structures and zonation. The sample number and age calculation for each zircon is indicated, laser ablation point indicated by coloured dots. Green dots indicate Cambrian age, yellow dots indicate Mesoproterozoic ages (Dominant age population), orange indicates Neoproterozoic, red indicates Paleoproterozoic age, while pink indicates Neoarchaean age.

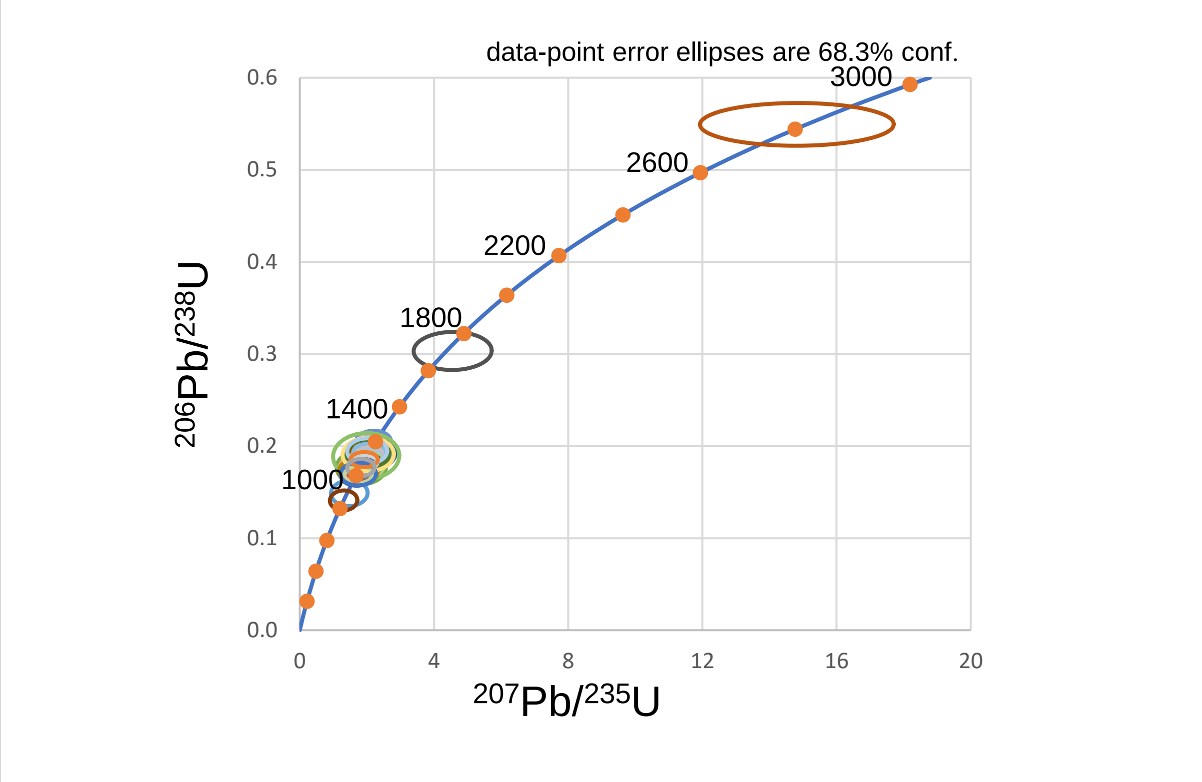

Figure 20: Concordia diagram for zircons analysed and accepted, all results plot on the Concordia line.

The samples plot well on the concordia curve indicating a high level of concordance for the samples accepted.

4.1.7: Tete 3

A moderately well-sorted, massive, light off white grey, fine to medium-grained sandstone. The sample forms the base of a fining upward sequence deposited between two conglomeratic units. Of the 71 zircons picked for analysis only 54 were concordant, the ages of these zircons are displayed in the probability density plot in Figure 12.

Most of the zircons fall within the Mesoproterozoic age with a strong peak at ~1076 Ma (1004 ± 40 Ma and 1197 ± 40 Ma, representing the lower and upper limits, respectively). Minor peaks occur in the Neoproterozoic ~881 Ma (850 ± 39 Ma and 897 ± 49 Ma, representing the lower and upper limits respectively), Paleoproterozoic ~1714 Ma (1714 ± 62 Ma) and Mesoarchaean ~2818 Ma (2818 ± 57 Ma).

Table 12: Summary of zircons with <10 % discordance from sample Tete 3, with general descriptions on the zircon textures, U content and Th/U ratios for each age population.

	Population	Number of zircons (Concordant)	Predominant grain textures (internal and external)	U content and Th/U ratio range
Neoproterozoic	850 - 897 Ma	2 representing 3% of concordant zircons accepted	Subhedral varying in size from 120 µm to 200 µm long and 80 µm to 200 µm wide with an aspect ratio of 1. 0 - 1.5. Grains have weak oscillatory zonation with minor inclusions.	Average U ppm: 59.5; Th/U: 0.58 - 0.73
Mesoproterozoic	1004 - 1197 Ma	50 representing 93% of concordant zircons accepted	Subhedral to euhedral varying in size from 80 µm to 220 µm long and 70 µm to 150 µm wide with an aspect ratio of 1.0 - 2.75. Most grains have oscillatory zonation with minor cracking, inclusions and bright overgrowths.	U ppm: 218.7; Th/U: 0.32 - 2.37
Paleoproterozoic	1714 Ma	1 representing 2% of concordant zircons analysed	Subhedral, 140 µm long and 80 µm wide with an aspect ratio of 1.75. Grain has oscillatory zonation.	U ppm: 50.3; Th/U: 0.94
Mesoarchaean	2818 Ma	1 representing 2% of concordant zircons analysed	Anhedral, 100 µm long and 60 µm wide with an aspect ratio of 1.7. Grain has weak oscillatory zonation and bright overgrowths.	U ppm: 288.1; Th/U: 0.76

Four age populations were identified with approximately 93% of zircons accepted falling in the Mesoproterozoic (1004 - 1197 Ma) age. Selected cathode luminescence SEM images of the zircons described in Table 12 are displayed in Figure 21.

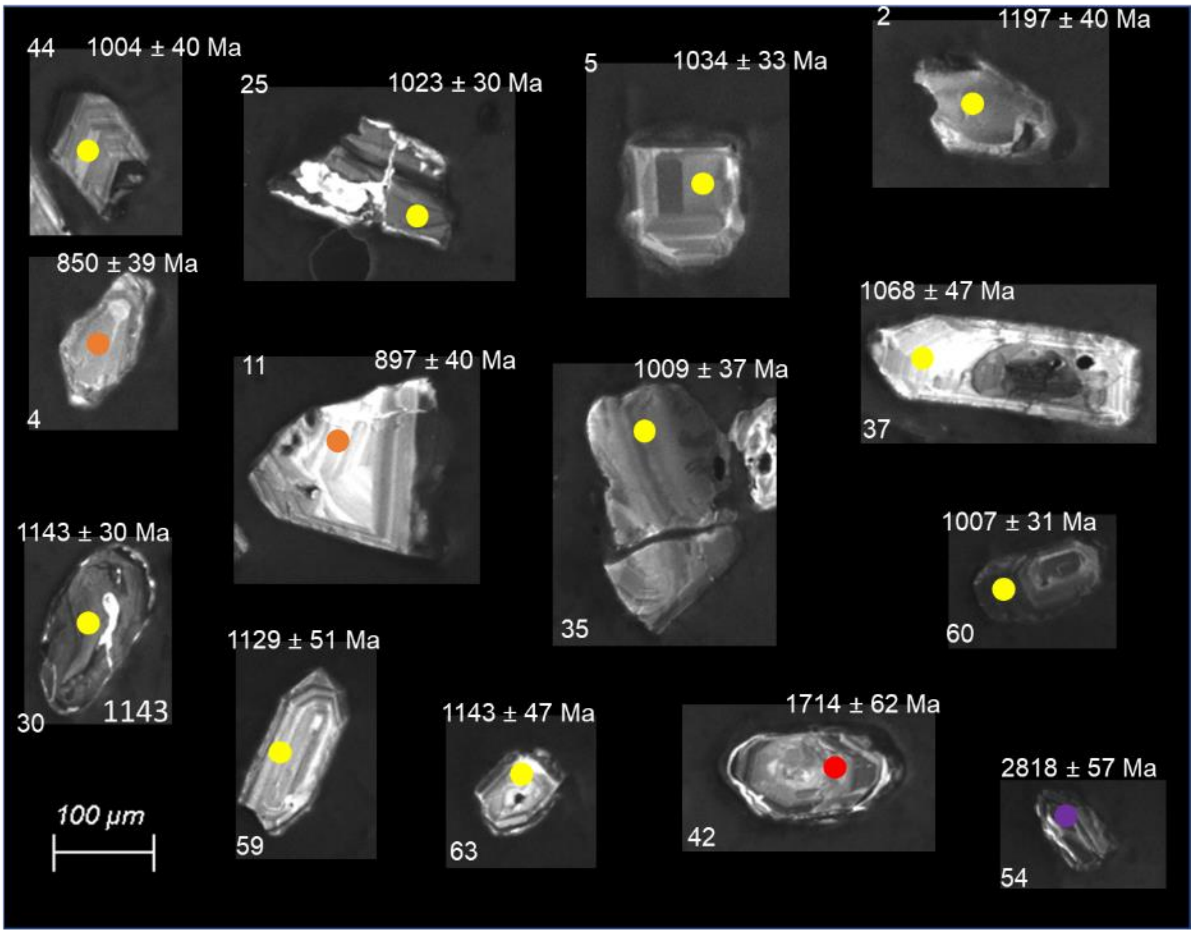

Figure 21: Cathode luminescence SEM images of selected zircons from sample Tete 3 indicating the laser ablation points, the internal structures and zonation. The sample number and age calculation for each zircon is indicated, laser ablation point indicated by coloured dots, Yellow dots indicate Mesoproterozoic ages (Dominant age population), orange indicates Neoproterozoic, red indicates Paleoproterozoic age, while purple indicates Mesoarchaean age.

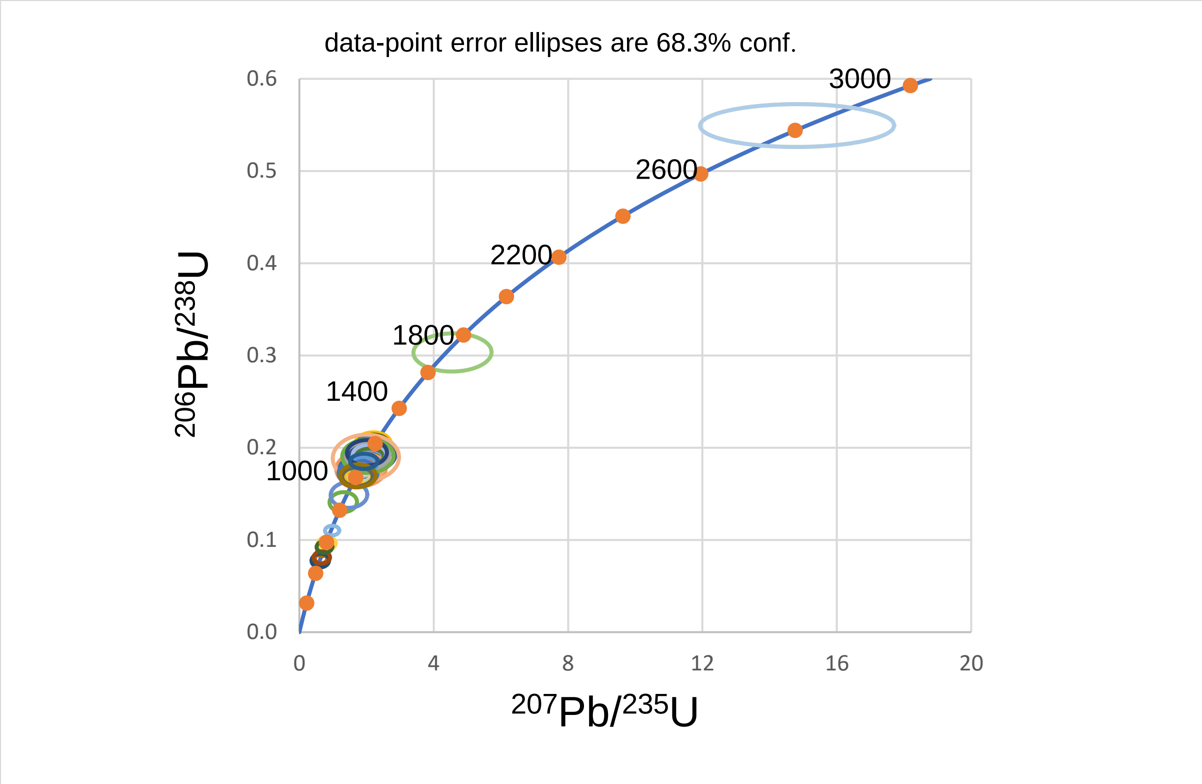

Figure 22: Concordia diagram for zircons analysed and accepted, all results plot on the Concordia line.

The samples plot well on the concordia curve indicating a high level of concordance for the samples accepted.

4.2: Deglaciation Analysis

The interpretation of the Vúzi Formation intersection, with emphasis on identifying deglaciation cycles, is presented below (Figure 23).

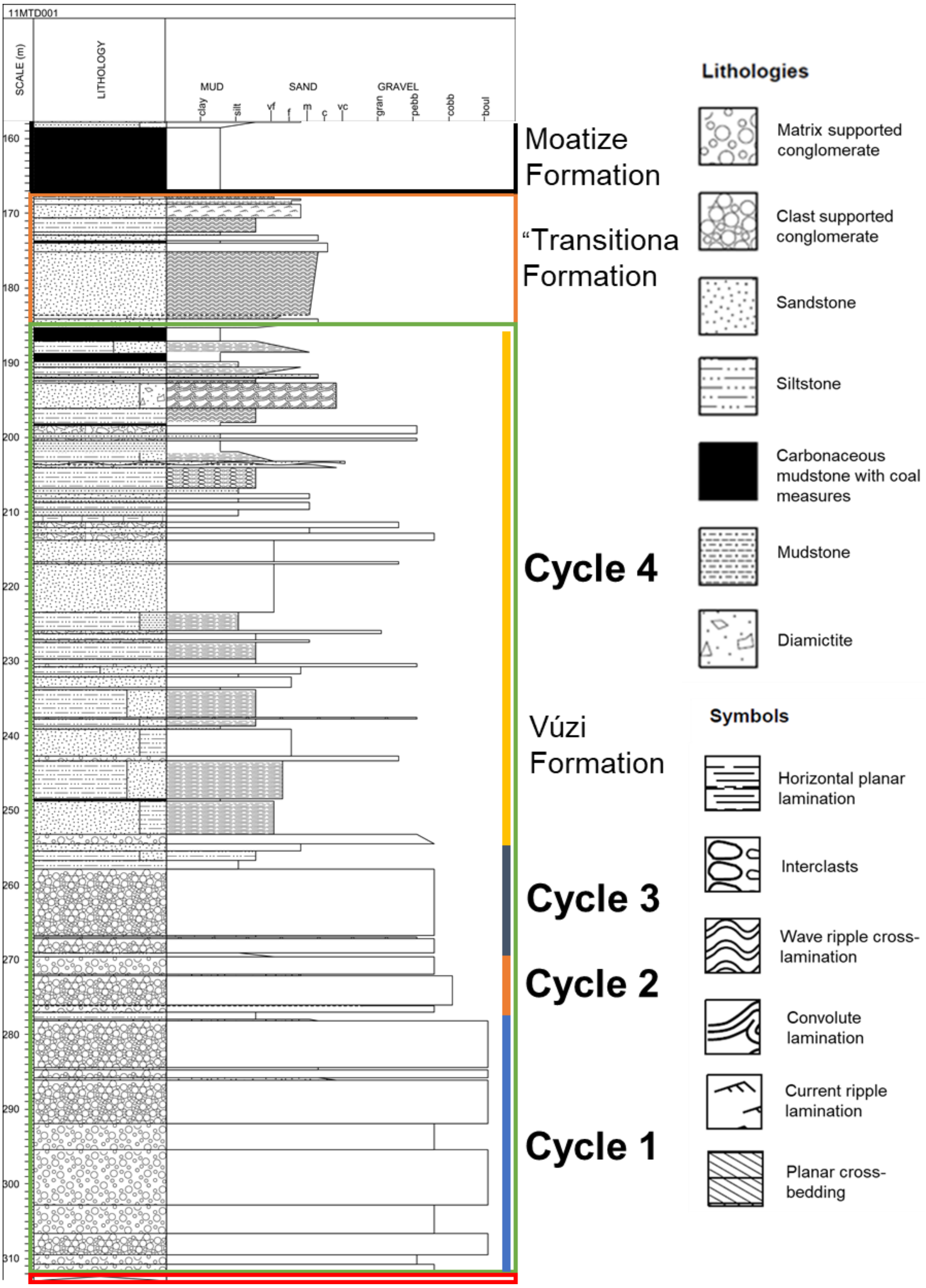

Figure 23: Lithological log of the Vúzi Formation, indicated by green box, intersected in 11MTD001. Scale bar represents intervals in metres. Deglaciation cycles are represented by coloured bars.

4.2.1 : Glacial Series Cycle 1

The basal unit is irregular and poorly-sorted, matrix-supported yellow brown polymictic conglomerate (Figure 24) with angular to rounded granule to boulder-sized clasts. Cycle has a thickness of 5.2 m. The matrix is poorly sorted with coarse to very coarse material, while clast sizes are irregular with no apparent dominant size fraction. The unit is predominantly composed of matrix material with the clast components dominated by granite/gneiss from the underlying basement.

Figure 24: Poorly-sorted, matrix-supported polymictic conglomerate in deglaciation cycle 1 from the Vúzi Formation.

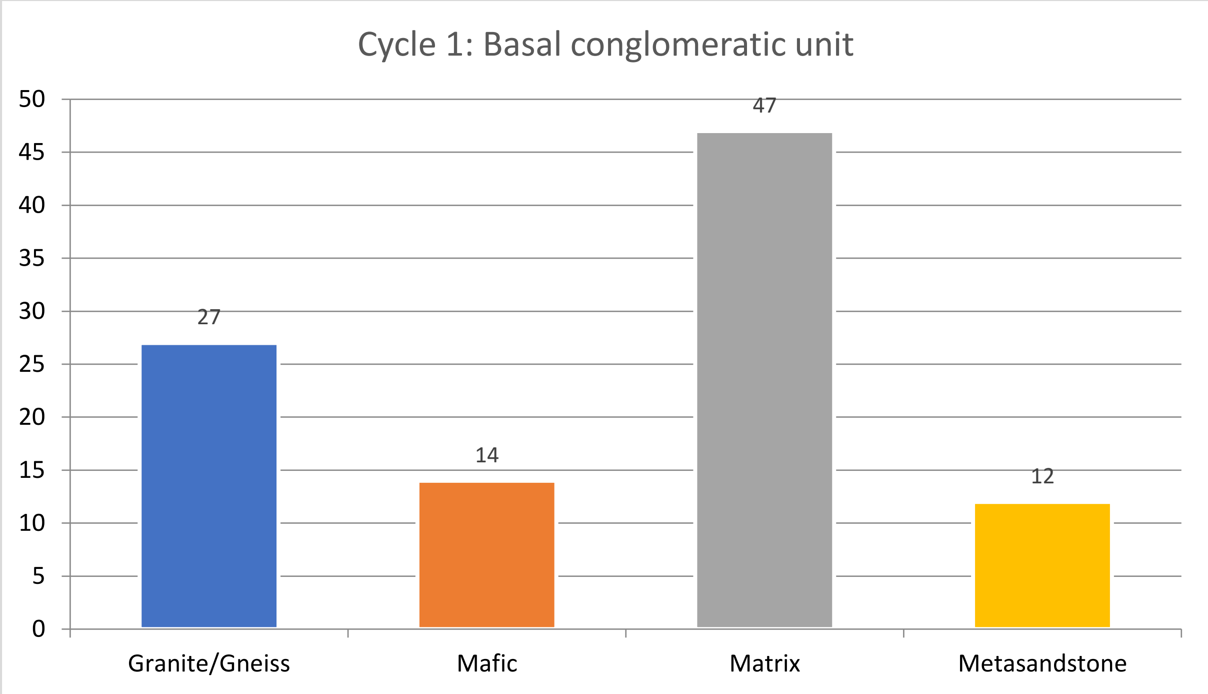

Figure 25: Major clast percentages relative to the matrix determined by point counting on one-metre lengths of core intersections for the basal conglomeratic unit in deglaciation cycle 1 (Vúzi Formation) in 11MTD001.

The basal unit grades into the second unit, which consists or a higher number of clasts. The matrix percentage drops from 47% in the basal conglomeratic unit to 23% in the middle conglomeratic unit. This unit is a poorly-sorted, clast-supported red brown polymictic conglomerate (Figure 26 and 27) with rounded to angular granule to cobble-sized clasts, with a thickness of 34.96 m. The unit is dominated by cobble sized granite/gneiss and mafic rich clasts which are more consistent in size and roundness than the underlying unit.

Figure 26: Poorly-sorted, clast-supported polymictic conglomerate in deglaciation cycle 1 from the Vúzi Formation.

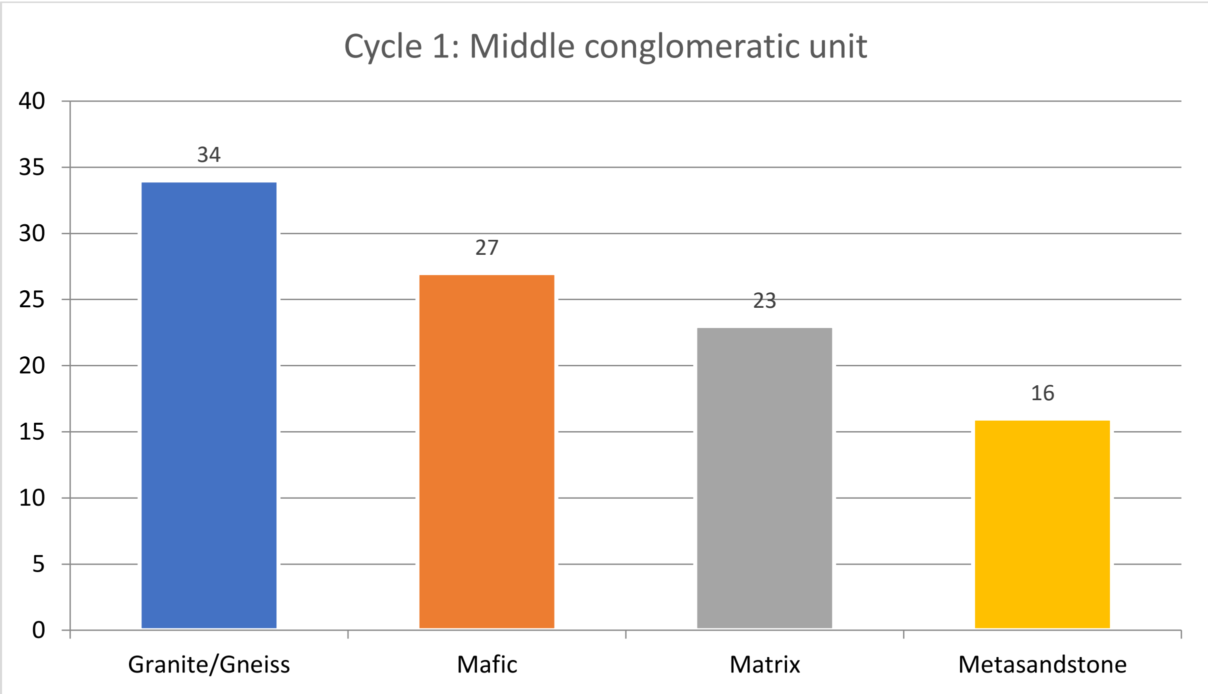

Figure 27: Major clast percentages relative to the matrix determined by point counting on one-meter lengths of core intersections for the middle conglomeratic unit in deglaciation cycle 1 (Vúzi Formation) in 11MTD001.

The middle conglomeratic unit grades into a clast-supported, brownish green upper polymictic conglomeratic unit (Figure 28 and 29). Two poorly sorted, medium to very coarse-sandstones with minor granule clasts occur as possible sandstone lenses. The cycle is capped off with fine-grained brown siltstone with a thickness of 0.9 m.

Figure 28: Brownish green polymictic conglomerate overlain by a brown siltstone, representing the end of deglaciation cycle 1 from the Vúzi Formation.

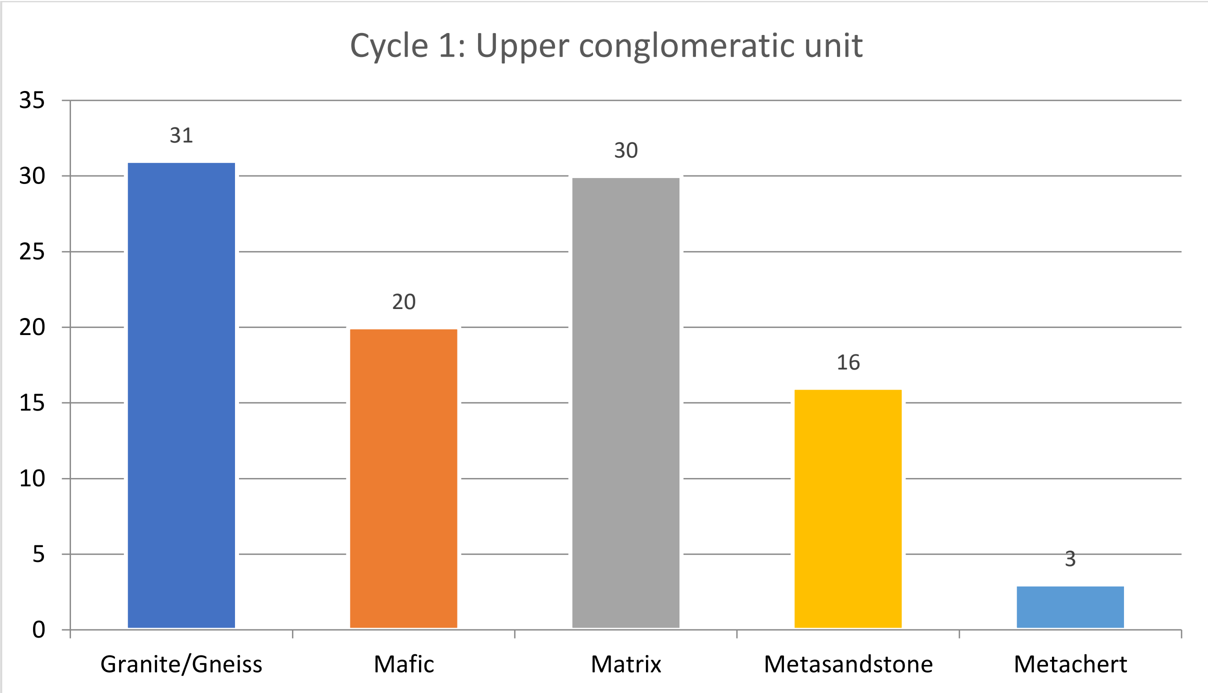

Figure 29: Major clast percentages relative to the matrix determined by point counting on one-metre lengths of core intersections for the upper conglomeratic unit in deglaciation cycle 1 (Vúzi Formation) in 11MTD001.

Cycle 1 has a total thickness of roughly 41.1 m.

4.2.2: Glacial Series Cycle 2

The contact between the first and second glacial cycles is unclear, with the contact appearing to either be erosional or sharp. The second unit begins with a poor to moderately well sorted predominantly clast supported greenish brown basal polymictic conglomerate with sub-rounded pebble to cobble sized clasts dominated by mafic rich and granitic material (Figure 30), with a thickness of 4.77 m. The bottom contact is characterized by matrix supported polymictic conglomerate which becomes clast supported after approximately 0.8 m.

Figure 30: Poor to moderately well sorted, clast supported polymictic conglomerate in deglaciation cycle 2 from the Vúzi Formation.

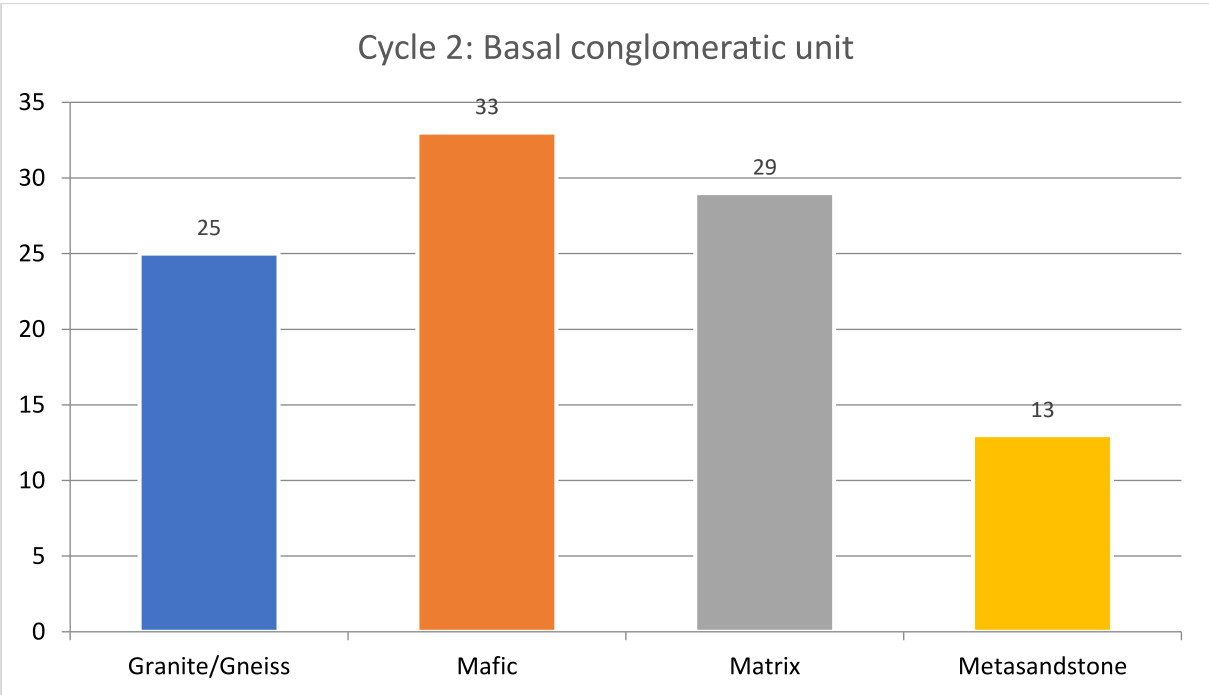

Figure 31: Major clast percentages relative to the matrix determined by point counting on one-metre lengths of core intersections for the basal conglomeratic unit in deglaciation cycle 2 (Vúzi Formation) in 11MTD001.

A thick sandstone unit separates the clast-rich conglomerate from a matrix supported conglomerate above. This unit is a moderately well-sorted, matrix to clast-supported light yellow polymictic conglomerate with sub-rounded to rounded pebble to cobble sized clasts, with a thickness of 2.29 m. The upper conglomeratic unit represents an increased metasedimentary clast component (Figure 33). The bottom contact with the sandstone is erosional. The unit is capped off with a brown to dark brown siltstone becoming slightly carbonaceous towards the top with a thickness of 0.5 m (Figure 32).

Figure 32: Well-sorted, clast-supported conglomerate overlain by a siltstone, which represents the end of deglaciation cycle 2 from the Vúzi Formation.

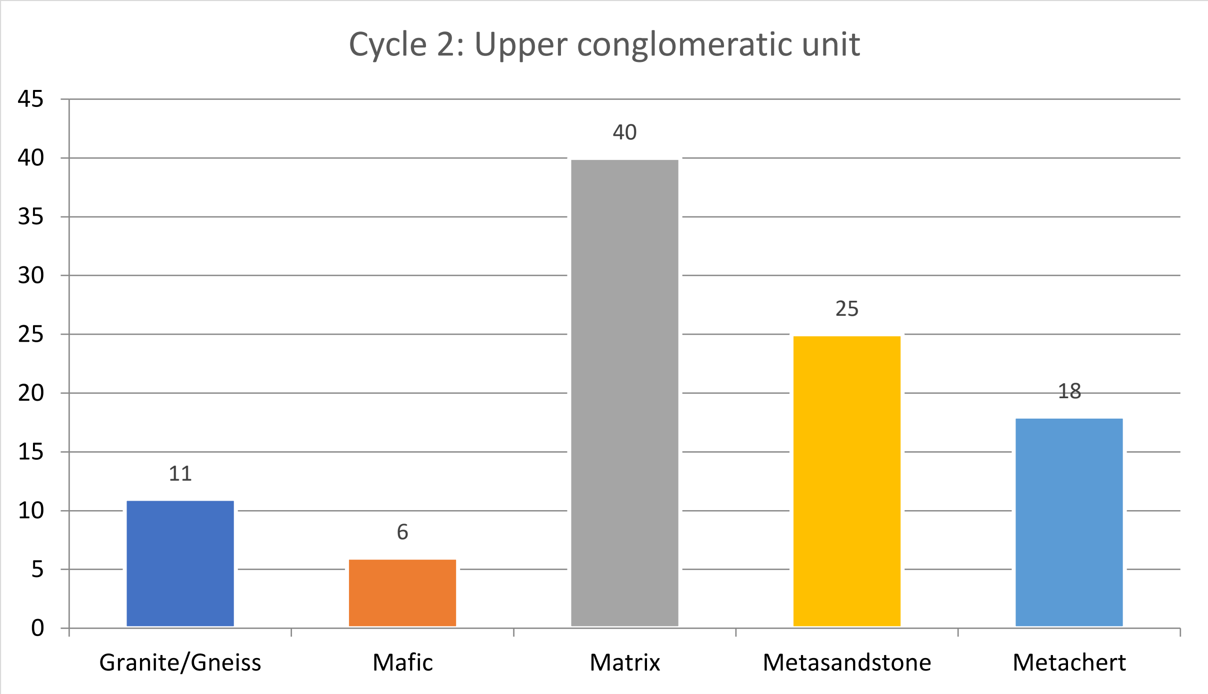

Figure 33: Major clast percentages relative to the matrix determined by point counting on one-meter lengths of core intersections for the upper conglomeratic unit in deglaciation cycle 2 (Vúzi Formation) in 11MTD001.

The total cycle 2 thickness is roughly 7.64 m.

4.2.3: Glacial Series Cycle 3

The third glacial cycle consists of two sub-cycles, with the first cycle commencing with an erosional contact. The unit is relatively thin (1.93 m thick) and is a moderately well sorted, clast supported light yellow brown basal polymictic conglomerate with sub-rounded to rounded pebble to cobble-sized clasts dominated by granitic material (Figure 34 and 35). The unit is capped by a 0.2 m thick dark brown siltstone.

Figure 34: Moderately well-sorted, clast-supported conglomerate overlain by a thin siltstone in deglaciation cycle 3 from the Vúzi Formation.

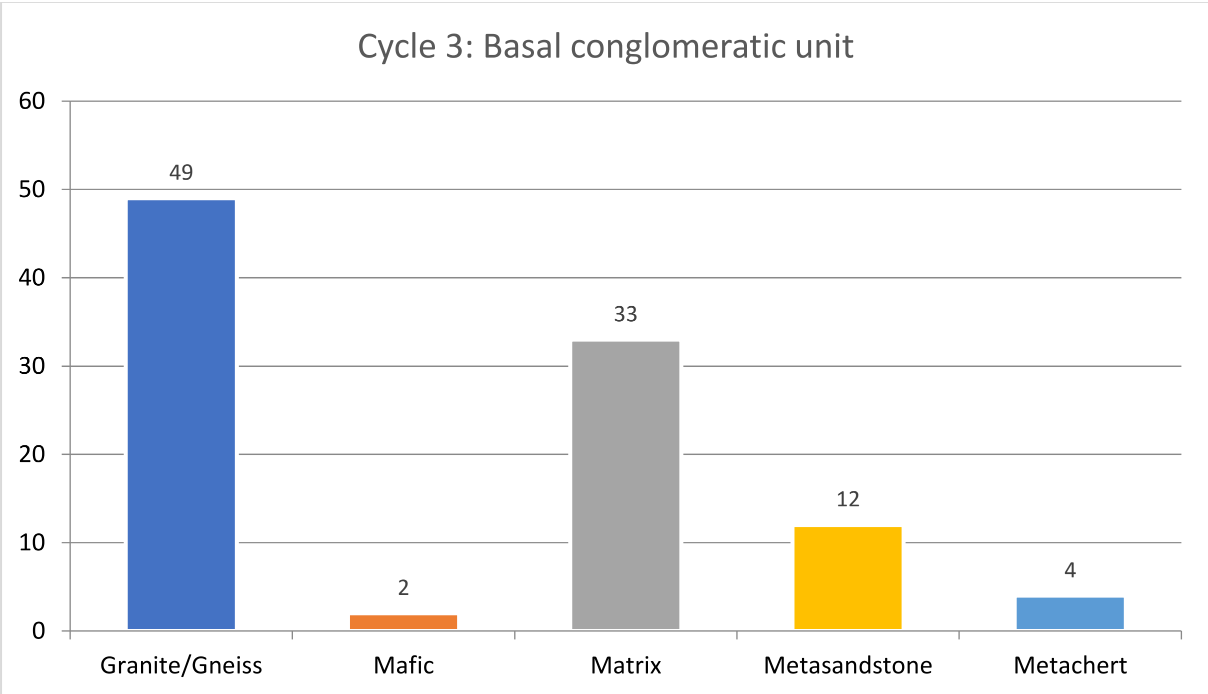

Figure 35: Major clast percentages relative to the matrix determined by point counting on one-meter lengths of core intersections for the basal conglomeratic unit in deglaciation cycle 3 (Vúzi Formation) in 11MTD001.

An erosional contact separates the two cycles, with the second cycle dominated by a light brown upper conglomerate with the same characteristics as the conglomerate described in the first sub-cycle. Thin brown medium to course grained sandstones occur as lenses towards the top of the unit. The unit is 8.91 m thick and is overlain with a fine-grained grey to brown siltstone (1.12 m), which grades into a dark grey mudstone (1.28 m), which is carbonaceous in places (Figure 36 and 37).

Figure 36: Moderately well-sorted, clast-supported conglomerate with thin sandstone lenses (B). Thick siltstone grading into a mudstone, which is carbonaceous in places (A), representing the end of deglaciation in cycle 3 from the Vúzi Formation.

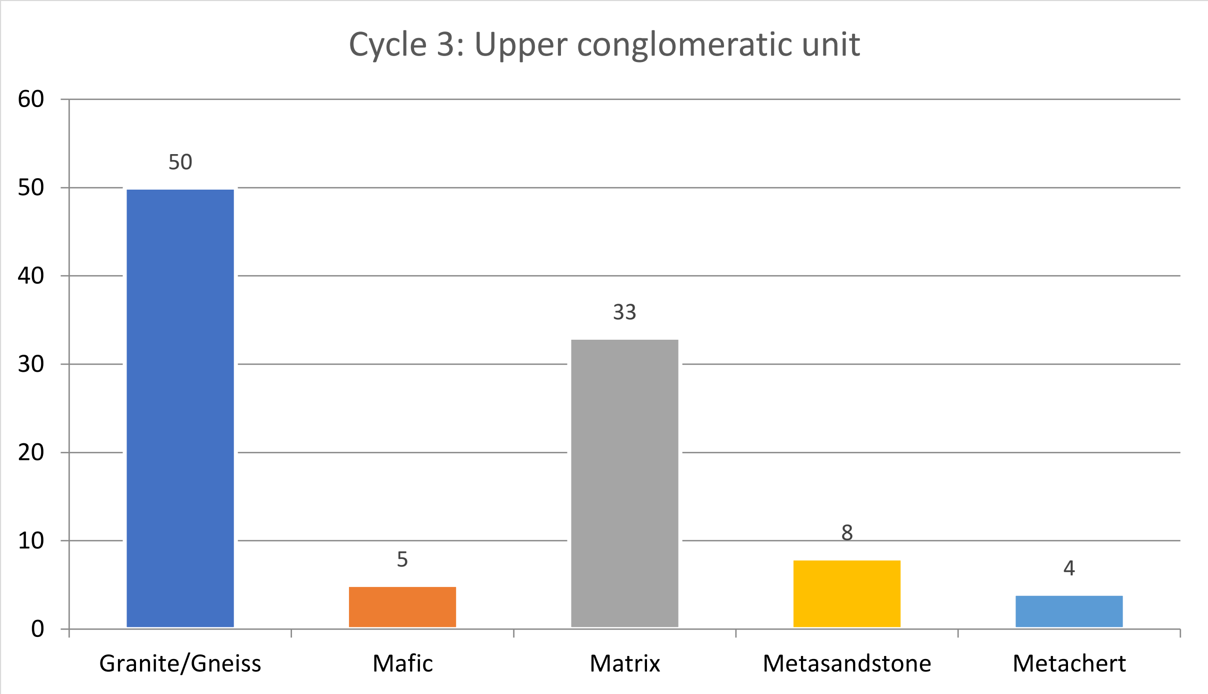

Figure 37: Major clast percentages relative to the matrix determined by point counting on one-meter lengths of core intersections for the upper conglomeratic unit in deglaciation cycle 3 (Vúzi Formation) in 11MTD001.

The total thickness of cycle 3 is 13.44 m.

4.2.4: Glacial Series Cycle 4

The fourth glacial cycle consists of two sub-cycles with the first cycle representing a shift from the conglomerate dominated cycles 1 - 3. The bottom contact of cycle 4 is sharp with a basal unit of brownish grey fine to medium-grained sandstone (Figure 38 - F), which contains angular granule to pebble-sized clasts towards the top contact (0.95 m). This is overlain by a matrix supported polymictic conglomerate with sub-rounded to rounded pebble to cobble sized clasts (Figure 38 - E). An interbedded grey brown very fine to fine-grained sandstone/siltstone (Figure 38 - D) unit with poorly developed horizontal lamination and thin diamictite bands (Figure 38 - C) grading into a thin (0.29 m) carbonaceous mudstone with coal measures (Figure 38 - B). The first sub-cycle ends with a thick brown grey to grey interbedded very fine to fine siltstone/sandstone (Figure 38 - A) unit with poorly developed horizontal lamination and minor bioturbation (5.04 m).

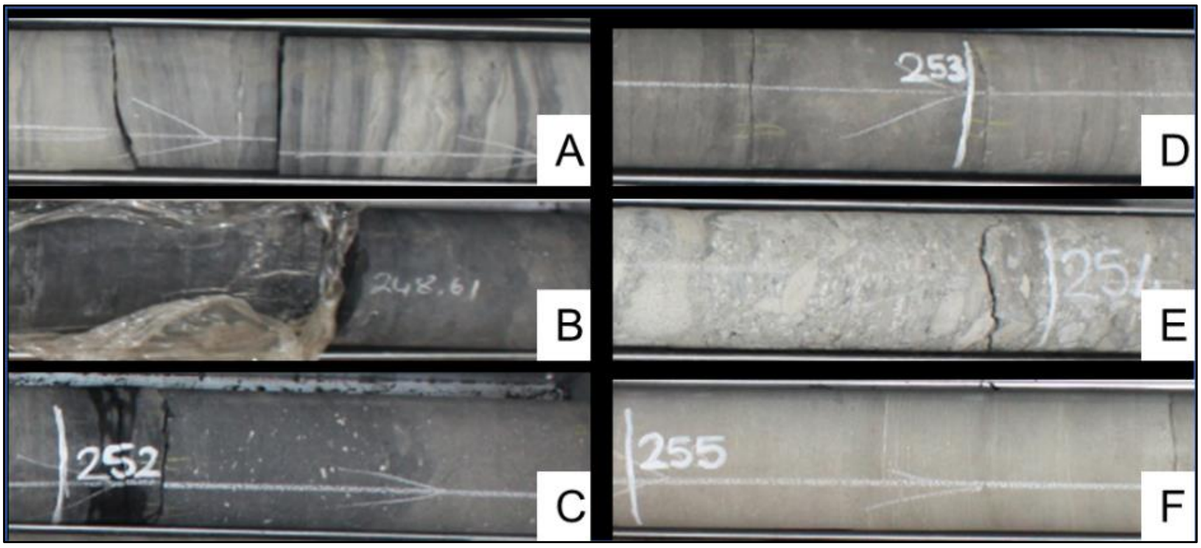

Figure 38: Series of core photos representing the units described for the first sub-cycle of deglaciation cycle 4 from the Vúzi Formation. A - Interbedded siltstone/sandstone; B – Carbonaceous mudstone with coal measures; C - Diamictite; D - Siltstone; E – Matrix-supported conglomerate; F - Fine to medium-grained sandstone. Each core piece is 30 cm long.

The second sub-cycle represents a stratified sequence with a mixture of sandstone (Figure 39 - D), siltstones (Figure 39 - B), siltstones (Figure 39 - C), diamictites (Figure 39 - E) and polymictic conglomerates (Figure 39- A). The interbedded siltstones and sandstones are like the first sub-cycle. The siltstone units are grey to dark grey very fine to silt grained with poorly defined horizontal lamination with bioturbation. The sandstones are massive, fine to medium grained and are grey to off white in colour. Grey to dark grey diamictites occur occasionally and are characterised by angular granule to pebble sized clasts. Fining upward sequences generally end in dark grey mudstones which are bioturbated in places. The unit is capped off with a carbonaceous mudstone unit (0.47 m) which is overlain by a fine to medium grained sandstone, with wave rippled cross-lamination (1.95 m). The total thickness of cycle 4 is 57.67 m.

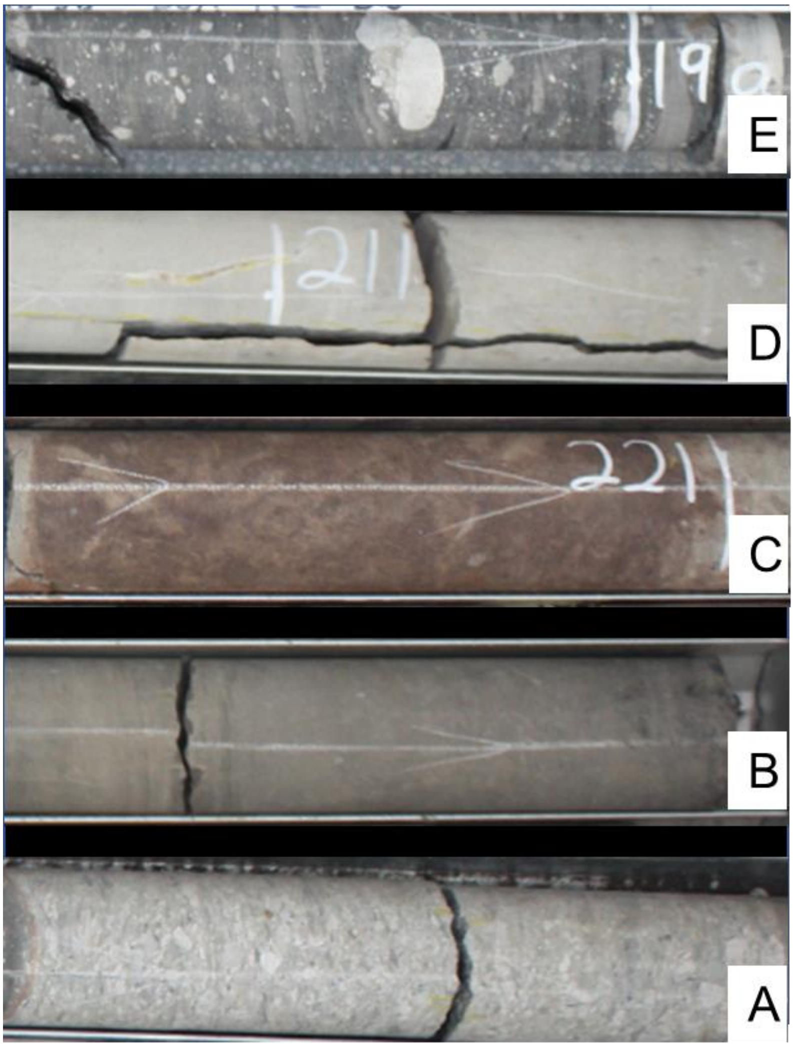

Figure 39: Series of core photos representing the units described for the second sub-cycle of deglaciation cycle 4 from the Vúzi Formation. A - Conglomerate; B - Siltstone; C - Siltstone; D - Fine to medium grained sandstone; E - Diamictite. Each core piece is 35 cm long.

CHAPTER 5: Provenance of the lower Karoo rocks of the Chicôa-Mecúcoè sub-basin

5.1: Introduction

The detrital zircon results of the six samples (B1764, B1766, B1775, B1778, Tete 1 and Tete 3) presented in Chapter 4 will be discussed and interpreted to determine possible source areas of the lower Karoo rocks of the Chicôa-Mecúcoè sub-basin of Mozambique. The zircon age populations will be compared to known ages of possible source areas with reference to published paleo-ice flow and paleocurrent directions from the Carboniferous to the Triassic. Several physical characteristics of zircons are important to assist in the interpretation and may influence the abundance and composition of zircon groupings. The size and shape of zircon grains affect its hydraulic potential while the internal structures and degree of abrading may assist in determining possible source areas.

Twelve age groups were identified for the lower Karoo rocks, summarized below in Table 11.

Table 13: Relative ages for all lower Karoo samples from borehole 11MTD001 drilled into the Chicôa-Mecúcoè sub-basin of Mozambique.

Population Group	Age	Number of results	Percentage %	
1	523 - 560	6	1.9	Cambrian
2	579 - 607	4	1.3	Neoproterozoic
3	697 - 773	6	1.9	
4	805 - 897	11	3.5	
5	901 - 999	31	10.0	
6	1000 - 1178	236	76.1	Mesoproterozoic
7	1222 - 1259	7	2.3	
8	1434 - 1583	4	1.3	
9	1672 - 1714	2	0.6	Paleoproterozoic
10	2091	1	0.3	
11	2662	1	0.3	Neoarchaean
12	2818	1	0.3	Mesoarchaean

The Tete Chipata Belt is an amalgamation of a series of terranes, with varying ages and formational histories, bounded by the Angónia thrust, Mwembeshi Dislocation and the Sanangoè Shear Zone in the east, north and south respectively (Westerhof *et al*., 2008). Age determinations of rock outcrops in the Zambezi Belt are limited with some outcrops having no age data.

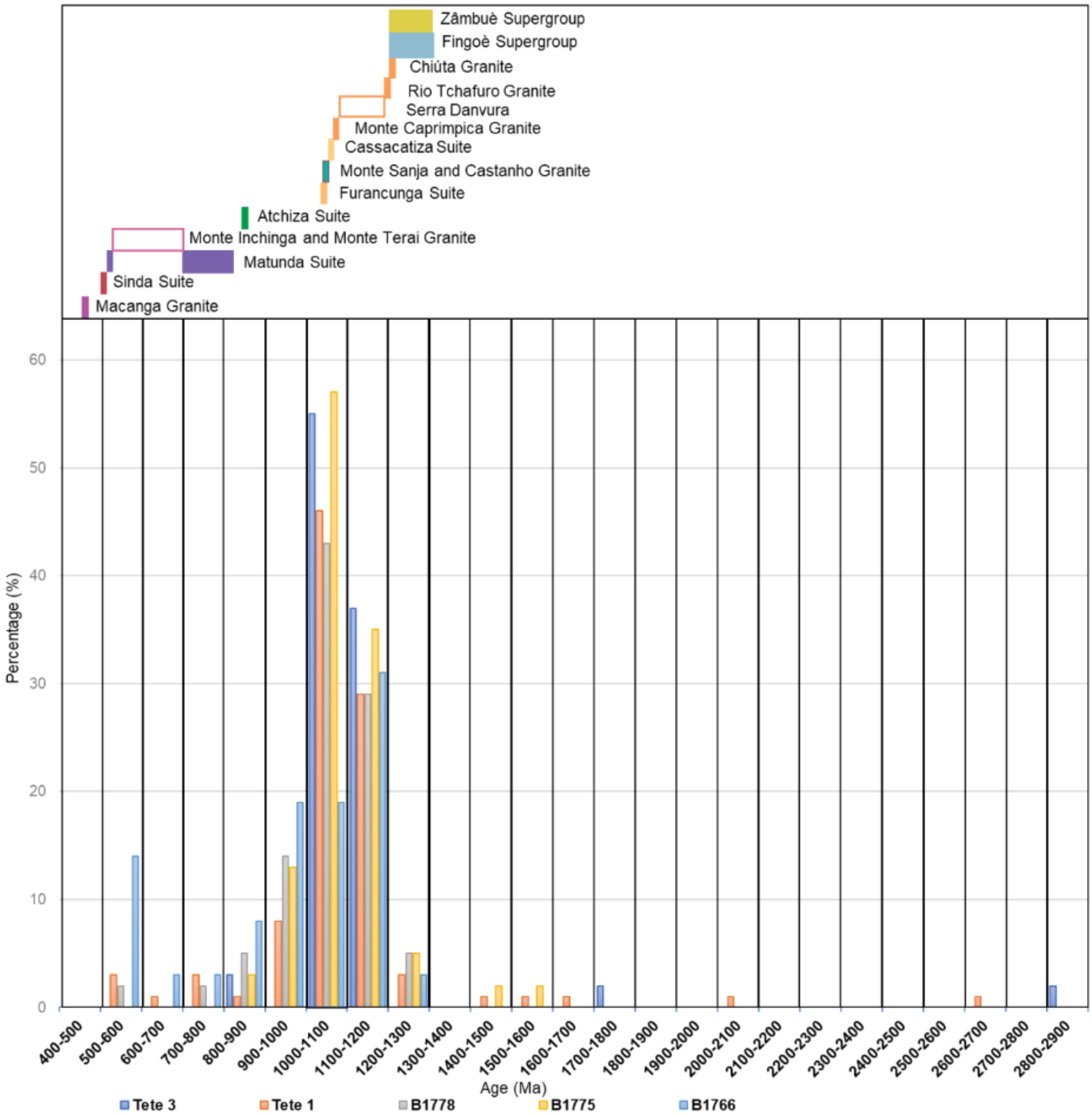

Figure 40: Possible source areas for zircon ages encountered in the lower Karoo rocks. Colours represent the unit colours in Figure 40. Blocks not filled in indicate approximate ages. (GTK Consortium, 2006; Mänttäri, 2006).

Age calculations on the various source areas indicated in figure 40 were conducted by Mänttäri (2006) using Sensitive high-resolution ion microprobe (“SHRIMP”) U-Pb dating and Sm-Nd dating indicated in Tables 14 and 15. The number of zircons used for SHRIMP U-Pb dating were below twenty zircons for each sample. Age calculations plotted poorly on the Concordia curve with discordant ages discarded. Mafic rich rocks were dated by Mänttäri, (2006) using Sm-Nd ratios. (GTK Consortium, 2006; Mänttäri, 2006).

The absence of Karoo aged Carboniferous to Triassic zircon populations indicates that igneous activity was not prevalent in the source areas during the deposition of the lower Karoo rocks. Sediments of the lower Karoo strata were sourced from older basement material giving rise to the Vúzi, “Transitional” and Matinde formations.

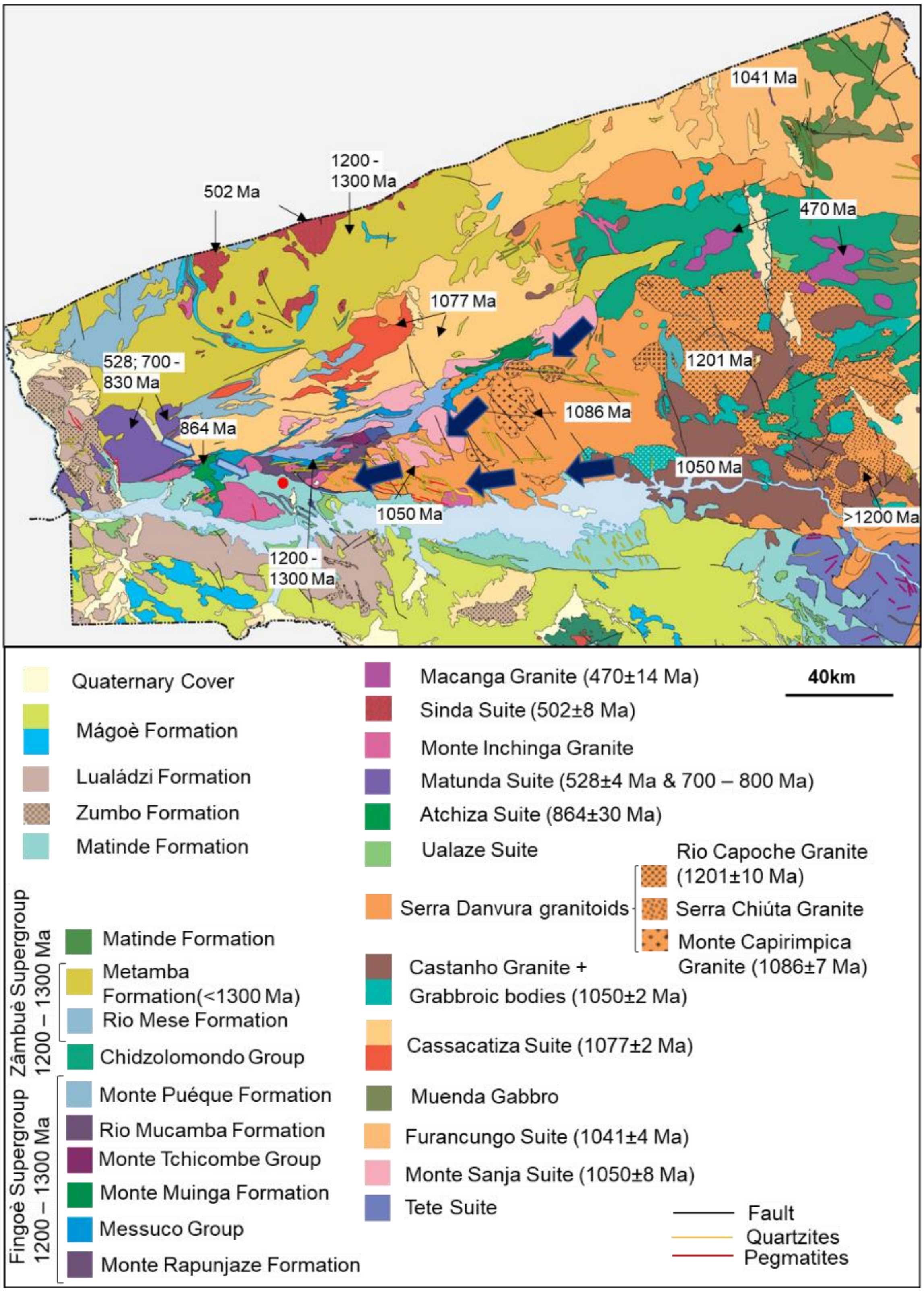

Figure 41: Published paleoflow directions for the Zambezi river system during Karoo sedimentation. Dark blue arrows indicate dominant flow directions while light blue arrows indicate minor flow directions identified from borehole 11MTD001 indicated with a red dot. Adapted from Hanson (2003), Mäkitie *et al*. (2005), GTK Consortium (2006), Mänttäri (2006), Key *et al.* (2015).

5.1.1: Cambrian and Neoproterozoic

Cambrian aged rocks are relatively rare in the Tete Province and are associated with the Pan African Orogeny during the formation of the Mozambique and Zambezi belts (Goscombe *et al*., 2000; GTK Consortium, 2006; Westerhof *et al*., 2008). Magmatism during the final stages of the Pan African event formed several granite suites (Macanga, Sinda and Matunda intrusions) with magmatic age ranges from 470 - 528 Ma (GTK Consortium, 2006; Westerhof *et al*., 2008). The Matunda Suite is fault-bounded and intruded by pegmatitic bodies, age determination on the Matunda gneisses indicates a younger population at ~528 Ma and an older population with an age range from ~700 - 830 Ma representing early stage magmatism during the Pan African Orogeny. The Monte Inchinga and Monte Terai Granite have not been dated but are believed to be part of the late stage Pan African magmatism. (GTK Consortium, 2006; Mänttäri, 2006)

Table 14: Late Pan African granite suites near borehole 11MTD001 with approximate magmatic ages. (GTK Consortium, 2006; Mänttäri., 2006)

	Late Pan African intrusions	**Age (Ma)**	**Dating method**	**Mineral and zircon interpretation**	**Approximate distance and direction from 11MTD001**
Cambrian	Macanga Granite	470 ± 14	SHRIMP U-Pb dating	Zircons have a high level of metamictization and are U rich. No metamorphic rims are visible. Age is based on a weighted average of $^{207}Pb/^{206}Pb$ on undisturbed magmatic zoning of zircons.	~150 km to the NW
	Sinda Suite	502 ± 8	SHRIMP U-Pb dating	Zircons have magmatic zoning with some rim growths. U and Th concentrations from the different zircon domains indicate phases during the magmatic event.	~80 km to the N
	Matunda Suite (Younger Population)	528 ± 4	SHRIMP U-Pb dating		~40 km to the W

	Late Pan African intrusions	Age (Ma)	Dating method	Mineral and zircon interpretation	Approximate distance and direction from 11MTD001
Unknown	Monte Inchinga Granite	Unknown			~10km to the SW, N and NE and ~80km to the W
	Monte Terai Granite	Unknown			~120 km to the NW
Neoproterozoic	Matunda Suite (Older Population)	700 - 830	SHRIMP U-Pb dating	The zircons are zoned with growth rims and metamictization in places. A weighted average of $^{207}Pb/^{206}Pb$ indicates an age of 784 ± 36 Ma. The ages plot poorly on the concordia curve indicating a range in age. Ages are metamorphic.	~40 km to the W
	Atchiza Suite	864 ± 30	Sm-Nd dating	Sample yielded fresh plagioclase and pyroxene minerals. REE levels are low indicating sample is chondritic. Age is magmatic.	~20 km to the W

The predominantly subhedral shape of the Cambrian aged zircons suggests that the grains were transported a relatively short distance, Cambrian – Neoproterozoic aged granite intrusions are summarized in Table 14.

5.1.2: Mesoproterozoic

The Tete Chipata Belt is dominated by the Mesoproterozoic aged Zâmbuè and Fingoè supergroups. The ~1300 Ma Fingoè Supergroup represents a volcano-sedimentary sequence with compositions suggestive of an Oceanic Island Arc or Ophiolite origin (GTK Consortium, 2006; Westerhof *et al*., 2008). The 1200 - 1300 Ma Zâmbuè Supergroup represents a series of metamorphosed rocks that formed in a passive margin setting (GTK Consortium, 2006; Mänttäri, 2006).

Table 15: Mesoproterozoic aged units located near borehole 11MTD001 with approximate ages. (GTK Consortium, 2006; Mänttäri, 2006).

	Mesoproterozoic intrusions	Age (Ma)	Dating method	Mineral and zircon interpretation	Approximate distance and direction from 11MTD001
Mesoproterozoic	Furancungo Suite	1041 ± 4 Ma	SHRIMP U-Pb dating	Zircons are translucent to turbid and contain inclusions. U concentrations and $^{208}Pb/^{206}Pb$ ratios are low. Age is magmatic.	~40 km to the NE
	Monte Sanja	1050 ± 8 Ma	Not specified	Zircons are short prismatic, transparent to translucent with inclusions in places. Zircons have low U concentrations, extremely low $^{206}Pb/^{204}Pb$ ratios and uniform $^{208}Pb/^{206}Pb$ ratios. Age is magmatic.	~30 km to the WNW and 15 km to the NE
	Castanho Granite	1050 ± 2 Ma	SHRIMP U-Pb dating	High concentration of two zircon fractions. Coarser fraction is prismatic with inclusions in places. Finer fraction is subhedral and oval. Zircons are low in U and have high $^{206}Pb/^{204}Pb$ ratios and uniform $^{208}Pb/^{206}Pb$ ratios. Age is magmatic.	~115 km to the E
	Cassacatiza Suite	1077 ± 2 Ma	SHRIMP U-Pb dating	High concentration of zircons which are generally prismatic and translucent. Zircons have moderate U concentrations,	~20 km to the NW

	Mesoproterozoic intrusions	**Age (Ma)**	**Dating method**	**Mineral and zircon interpretation**	**Approximate distance and direction from 11MTD001**
				varying $^{206}Pb/^{204}Pb$ ratios and uniform $^{208}Pb/^{206}Pb$ ratios. Age is magmatic.	
Mesoproterozoic	Monte Capirimpica Granite	1086 ± 7 Ma	SHRIMP U-Pb dating	Zircons are prismatic and transparent to translucent. Zircons have moderate U concentration, varying $^{206}Pb/^{204}Pb$ ratios and uniform $^{208}Pb/^{206}Pb$ ratios. Age is magmatic.	~65 km to the E and ~80 km to the NE.
	Rio Capoche Granite	1201 ± 10 Ma	SHRIMP U-Pb dating	Zircons vary from prismatic to tabular and are transparent to translucent. Age is magmatic.	~125 km to the NE
	Chiúta Serra	> 1200 Ma	Inferred		~35 km to the E, ~45 km to the NE and ~20 km to the N.
	Zâmbuè Supergroup	1200 - 1300 Ma	Inferred		~40 km to the NW
	Fingoè Supergroup	~1300 Ma	Inferred		~36 km to the WNW, ~10 km to the N and ~20km to the NE

Several granitoids with Mesoproterozoic ages from 1041 - 1200 Ma (Table 15 and Figure 41) occur throughout the Tete Chipata Belt and are associated with magmatism during the Grenvillian orogenic cycle (GTK Consortium, 2006; Westerhof *et al*., 2008). The Cazula and Chidzolomondo groups are undated. The Castanho Granites are however restricted as intrusions in the Chidzolomondo Group indicating a maximum age of 1050 Ma (Westerhof *et al*., 2008).

5.1.3: Paleoproterozoic – Mesoarchaean

Paleoproterozoic, Neoarchaean and Mesoarchaean igneous rocks have not been dated in the Tete Chipata Belt in Mozambique. A single meta-arkose sedimentary rock in the Zâmbuè Supergroup gave Proterozoic and Archaean age populations of ~2.7 - 2.5 Ga and ~2.1 - 1.9 Ga respectively (GTK Consortium, 2006; Mänttäri., 2006; Westerhof *et al*., 2008). In Zambia the Muva Supergroup metasediments are dated ~1880 Ma and are intruded by granitoids with ages ~1660 - 1550 Ma (Westerhof *et al*., 2008). The Zambian Chewore-Rufunsa Gneiss and Chipata quartzite on the western and northern limits of the Tete Chipata Belt recorded ages between ~2670 - 2030 Ma and ~2992 - 1434 Ma respectively, with the younger populations interpreted to represent Paleoproterozoic basement rocks while the older population represents ages related to reworking of Archaean aged craton material (Johnson *et al*., 2006; Alessio *et al*., 2019;).

5.2: Vúzi Formation

Vúzi Formation sediments were deposited in glacio-lacustrine or fluvial glacial settings (Key *et al*., 2015 and references within). The detrital zircon age data gathered from the three samples (Tete 1, Tete 3 and B1788) indicate that material was sourced predominantly from the same area with a Mesoproterozoic peak age population of 1080 – 1100 Ma. This correlates to magmatism related to the Kibaran and Irumide orogeny between 1.4 Ga to 1.0 Ga corresponding with the formation of Rodinia (Porada *et al*., 2000; Hanson, 2003). The Serra Danvura granitoids (Monte Capirimpica), and Cassacatiza Suite are probable sources. The north east/south west trending Monte Capirimpica occurs 60 - 80 km towards the east and north east from borehole 11MTD001. The ~1200 - 1300 Ma Fingoè Supergroup outcrops between the Monte Capirimpica and borehole 11MTD001.

Secondary Cambrian to Neoproterozoic age peaks with ranges from 523 - 560 Ma, 697 - 773 Ma and 850 - 897 Ma for the three samples. These ages correspond to the Pan African Orogeny between 950 Ma and 470 Ma which resulted in the formation of Gondwana (Hanson, 2003). Magmatism resulted in the formation of the ~864 Ma

Achiza and ~528 Ma Matunda Suites which outcrops 20 - 40 km to the west and northwest of borehole 11MTD001.

Single Paleoproterozoic and Archaean zircons with ages of ~1714 Ma, ~2662 Ma and ~2818 Ma, respectively, were encountered in samples Tete 1 and Tete 3 may have been sourced from the metasedimentary Chipata quartzite in the north east, which recorded a range of ages from ~2992 - 1434 Ma (Johnson *et al*., 2006; Alessio *et al*., 2019). It is also possible that the Archaean and Proterozoic ages are reworked zircons from the metasedimentary arkoses dated in the Zâmbuè Supergroup. Currently no known bodies in the Mozambique portion of Tete Chipata Belt support an age population of 910 - 995 Ma. Granite and syenite bodies with ages ~940 Ma in the Chipata Terrane, located in Zambia, support this region as a source area (Johnson *et al.*, 2006).

Published palaeoflow directions indicate a predominant south-westerly and westerly directed ice flow across southern Africa with glaciers confined to structurally controlled valleys (Key *et al*., 2015; Craddock *et al*., 2019). The probability density diagrams age peak correlates closely with ages of the Monte Capirimpica granitoids, which conforms with the published palaeoflow directions for southern Africa. Zircons with Cambrian to Neoproterozoic ages however suggest a paleoflow from the northwest with subhedral to euhedral zircons and the preservation of rims suggesting a relatively short transport distance. A north west source region is further supported by the presence of single aged zircons of Archaean ages. These zircons may represent reworked quartzites from the Zâmbuè Supergroup, where sediments were sourced from Archaean aged cratons along a passive margin. (GTK Consortium, 2006). The relatively rounded, high width-to-length ratio of the two Archaean aged zircons suggest that these zircons may have gone through several transport cycles.

Sample B1778 is located towards the top of deglaciation cycle 4 and the end of glaciation in the Vúzi Formation. The varying characteristics of the zircons in the prominent age group of 1000 - 1169 Ma with a peak of 1099 Ma is reflective of several Mesoproterozoic aged bodies. The subhedral to euhedral zircons with oscillatory zonation correspond to zircons of similar ages in samples Tete 1 and Tete 3, sourced from the Monte Capirimpica and Cassacatiza Suite while zircons with no zonation may indicate the Monte Sanje Suite as a new source area. The presence of zircon data pointing to a new source area and shift in drainage may be reflective of the gradual change in climate towards the end of glaciation in the Vúzi Formation.

The Vúzi Formation zircon data suggests a predominant south westerly and westerly directed palaeoflow, with a minor component being sourced from the northwest and west. The samples were taken towards the top of identified deglaciation cycles (Figures 6 and 23). The Cambrian to Neoproterozoic zircons sourced from Pan African igneous intrusions located to the west and north west of 11MTD001 and may represent melt waters eroding local elevated regions during periods of deglaciation.

5.3: Transitional Formation

The detrital zircon data from sample B1775 indicates a dominant Mesoproterozoic age population with a peak of 1100 Ma, correlating with the north east and south west trending Serra Danvura granitoids (Monte Capirimpica) approximately 30 km to the east associated with the Kibaran and Irumide orogeny. (Porada *et al*., 2000; Hanson, 2003). The subhedral to euhedral zircon grains and the preservation of rims suggest a short transport history. Minor age population peaks at 910 Ma and 1524 Ma suggest a source component from the north west and north east, correlating with the Pan African Orogeny Atchiza Suite and Kibaran and Irumide orogeny. No known ages of ~1500 Ma have been noted in the Zambezi Belt. The Chipata Terrane has gneisses with age ranges of 2000 - 1020 Ma recorded (Johnson *et al*., 2006). With the absence of similarly aged bodies in Mozambique and information of published palaeoflow data, the Chipata Terrane is a possible source region for material dated ~1524 Ma. The subhedral to euhedral shape of the zircons, preservation of rims and presence of elongated grains, however, indicates a relatively short travel distance. The Chipata Terrane is therefore not a likely source area with zircon grains aged ~1524 Ma possibly representing recycled material.

The presence of age populations correlating with the Atchiza Suite in the north west and Monte Capirimpica in the north east suggests material was sourced from the north west and north east respectively, with a dominant south westerly directed palaeoflow.

Zircons with a minor age peak at 1252 Ma could have been sourced from the Zâmbuè Supergroup or Fingoè Supergroup in either direction.

5.4: Matinde Formation

Matinde Formation sediments were deposited in a low energy fluvial lacustrine setting with palaeoflow measurements unable to indicate a primary flow direction (Key *et al*., 2015). The detrital zircon data from samples B1766 and B1764 generated little to no zircons. Sample B1766 recorded a primary age of 1104 Ma related to the Kibaran and Irumide orogeny and minor ages of 530 Ma and 581 Ma related to the Pan African Orogeny. A minor age peak on the density probability curve at 934 Ma represents an age that is not identified in the Tete Chipata Belt in Mozambique. Subhedral to euhedral zircons and the preservation of bright overgrowths suggest a short transport history. The 530 Ma age population suggests Matunda Suite as a possible source area while no known igneous rocks have been dated at ~581 Ma and ~934 Ma. The zircon grains aged 900 - 996 Ma may represent magmatism associated with extensional tectonics prior to the break-up of Rodinia at approximately 750 Ma (Hanson, 2003). Zircons with ages of 579 - 607 Ma may represent Pan African igneous bodies that have not been dated, the elongated and euhedral grains suggest a short transport distance with the Monte Inchinga Granite located within 20km a possible source area.

The low number of zircons in sample B1766 and B1764 may reflect depositional environments not conducive to the concentration of zircons.

5.5: Palaeoflow Reconstruction

Strata in the main Karoo basin in southern Africa represents a period of climatic shift from dry arctic conditions in the Carboniferous Period to warm conditions in the Mesozoic Period with depositional environments shifting from glacial to shallow marine and finally non-marine fluvial to aeolian. (Visser, 1995; Catuneanu *et al.,* 2005; Hatton *et al.,* 2011; Hancox and Götz., 2014). Climatic shifts across Gondwana were relatively consistent across all Karoo basins experiencing similar shifts associated with a change in palaeolatitude from approximately 70°S to 50°S (Visser, 1995; Wopfner, 2013; Craddock *et al*., 2019). Detrital provenance studies on lower Karoo rocks in Southern

Africa and Australia indicate that material was sourced from a central Antarctic mountainous area (Veevers et al., 2007).

Rift tectonics was at its early stage prior to and at the start of glacial sedimentation in the Vúzi Formation with glaciers forming deep valleys (Catuneanu *et al*., 2005; Isbell *et al*., 2008). Glacial deposits of the main Karoo basin were deposited in a cyclical manner with four main sequences identified (Visser *et al*., 1997). The depositional environment changed from an ice sheet flowing along the ground, to a floating ice sheet and finally a period of rapid disintegration and melting as conditions warmed (Visser *et al*., 1997). Samples Tete 1, Tete 3 and B1778 were taken at the end of proposed deglaciation cycles, which may represent a disintegrating ice sheet with sandstones deposited in a fluvial-lacustrine or fluvial setting (Catuneanu *et al*., 2005).

A highland region in the Mozambique Belt existed between Malawi and Mozambique with a roughly north-south trend separating the Karoo basins of Mozambique from the Tanzania and Madagascar basins. Palaeoflow directions were directed away in an easterly and westerly-direction respectively. (Stratten., 1968; Bond., 1970; Catuneanu *et al*., 2005; Key *et al*., 2015;). An easterly-directed palaeoflow into the Tanzania and Madagascar basins are supported by sandstones of the Umbuvura Formation, where grain size decreases from the west to east and coal seams in the Mhukuru Formation increases in thickness from the west to east. (Semkiwa, 1992; Catuneanu *et al*., 2005). A westerly and south-westerly directed palaeoflow direction has been identified in the Vúzi Formation by Key *et al*. (2015).

Mesoproterozoic aged detrital zircon data from the Vúzi Formation samples indicates sediments were predominantly sourced from the northeast and east. The low representation of Pan African Cambrian to Neoproterozoic aged detrital zircons are interpreted to represent a natural trend associated with a secondary eastward directed palaeoflow direction resulting from periods of ice cap melting. It is proposed that glaciers followed and deepened structurally controlled paleo valleys with palaeoflow directions remaining stable throughout deglaciation sequences. The source feeds from the northeast and east suggest two major palaeoflow systems, while the source feed from the west may have been active during periods of warming, resulting in a periodic supply of sediments during periods of ice cap melting.

Several granitic and mafic bodies occur in the region of 11MTD001. Clasts identified in the conglomeratic units provide little evidence on the provenance of the material. Conglomerates from deglaciation cycles one and two have high granitic and mafic clasts components with the upper conglomerate from cycle two containing increasing percentages of metasedimentary clasts. The upper conglomeratic unit may represent a shift in the glacial source area from an area eroding predominantly granitic and mafic bodies to sourcing an increasing amount of material from the Zâmbuè Supergroup or Fingoè Supergroup. The conglomerates from the identified deglaciation cycle 3 indicates a shift from the Zâmbuè Supergroup or Fingoè Supergroup with an increased supply of material from granitic bodies. It is unclear which source areas provided the clasts during the formation of the conglomerates.

The predominantly subhedral to euhedral detrital grain shapes and the preservation of metamorphic rims indicate a short transport history. Lithofacies analysis on Karoo rocks in the Sanângoà-Mefidézi sub-basin indicates a stratigraphy dominated by immature sediments sourced nearby, which is supported by detrital zircon data (Smith, 2018).

The "Transitional Formation" represents a period of warming conditions where melting glaciers resulted in bed load glacial outwashes and braided fan deltas resulting in a succession of poorly sorted diamictites, sandstones, conglomerates and thin coal seams (Hancox, 2014, 2015). The detrital zircon information from sample B1775 indicates a south-westerly palaeoflow direction with the Monte Capirimpica granitoid in the north east providing the dominant source material. Due to the closeness in ages and emplacement setting for the Monte Capirimpica granitoid and Castanho granites the zircon age population may represent a combination of the two. This would suggest that the westerly and south westerly directed palaeoflow systems remained in place at the onset of the Moatize Formation. The absence of Pan African Cambrian and Neoproterozoic aged zircons indicates a possible end of the easterly-directed palaeoflow systems. This may be indicative of the end of melting ice caps in localized high areas to the east.

The Moatize and Matinde formations formed in low energy lacustrine and fluvial environments (Key *et al*., 2015). Although detrital zircon data is not available for the

Moatize Formation, the palaeoflow directions probably remained stable from the "Transitional" through to the Matinde formation. This is supported by palaeoflow measurements taken by Ait-Kaci Ahmed (2003) from Moatize sandstones in the Mid-Zambezi Basin and a general shift from proximal to distal sediments towards the west in the Kalahari and Mid-Zambezi basins indicating a westerly directed flow (Key *et al*., 2015).

The Matinde Formation represents the end of the lower Karoo strata in the project area. Large lakes formed in the Cahora Bassa area during deposition of the Matinde Formation during a period of low-energy fluviatile and lacustrine depositional environments influenced by isostatic uplift resulting from melting ice sheets. (Key *et al*., 2015). This low energy environment may have resulted in virtually no zircons present in sample B1764. It is also possible that the zircons were destroyed or selectively removed during the sieving and grinding stage. Available zircon data from B1766 indicate a probability density peak at approximately 1100 Ma which correlates with the Monte Capirimpica, however the larger range of ages of 1022 Ma - 1259 Ma, around the Mesoproterozoic indicates several source areas. This is further supported by the differing zircon characteristics. This may be indicative of increased precipitation during the formation of lakes resulting in increased drainage features from local elevated areas (Wopfner, 2002). The presence of thick siltstone/mudstone units of ~80m logged in 11MTD001 indicates that a large lake formed in the Chicôa-Mecúcoè sub-basin. The presence of Cambrian aged zircons suggests a secondary eastward directed palaeoflow.

The number of zircons accepted for samples B1766, B1778 and Tete 3 fell below the statistical minimum of 60 proposed by Dodson *et al*. (1988). Sample B1775 exceeded 60 zircons accepted while Tete 1 exceeded 80 zircons. Sample size and sample preparation may therefore have introduced a bias resulting in a skewed representation in the palaeoflow reconstruction. Sample Tete 1 however does not contradict palaeoflow reconstructions indicated by samples B1766, B1775, B1778 and Tete 3 and confirm palaeoflow measurements and interpretations by Key *et al*. (2015) and Ait-Kaci Ahmed (2003). Age data from all the lower Karoo samples plotted well on the concordia curve with ages representing concordant ages. Published age data are however based on a statistically low number of zircon grains with some ages plotting poorly on Concordia curves. The lack of published age data for the Zambezi Belt limits the confidence on palaeoflow reconstructions using detrital zircon data.

Palaeoflow directions interpreted from the zircon age data from the Vúzi Formation to Matinde Formation are proposed in Figure 40, which illustrates a primary westward and south-westward-directed palaeoflow, and an additional secondary eastward-directed palaeoflow is proposed during periods of ice sheet melt and increased precipitation.

CHAPTER 6: Deglaciation Sequences

The Vúzi Formation in Mozambique is the equivalent of the Dwyka Group in southern Africa and the Idusi Formation in Tanzania. Glacial sedimentary strata are best preserved and described in South Africa, Botswana, Tanzania and more recently Ethiopia (Visser, 1997; Wopfner, 2002; Bussert, 2010). Although climatic conditions remained relatively consistent across southern Africa during glacial sedimentation, tectonic and depositional environments across the Karoo basins resulted in varying glacial deposits across the Karoo basins (Visser, 1997; Catuneanu *et al*., 2005; Cradock *et al*., 2018).

Dwyka Group strata in South Africa are highly influenced by the topography of the basement with marine facies in the south and non-marine depozones in the north. The marine facies consisting predominantly of diamictites deposited from floating ice sheets as a suspended load and reaches approximately 800 m in the deepest reaches of the basin. (Visser, 1987; Visser *et al*., 1997; Catuneanu *et al*., 2005; Isbell *et al*., 2008). Glacial deposits to the north are difficult to correlate, with irregular thicknesses attributed to upliftment along the forebulge related to the foreland setting (Catuneanu *et al*., 2005). Palaeoflow directions indicate glacier movement north and south from the forebulge into South Africa and the Kalahari-Karoo Basin respectively scouring deep glacial valleys (Isbell *et al.*, 2008). Glacial deposits originating from the forebulge include debris flow and outwash fan deposits, consisting of conglomerates, sandstones and mudrocks (Visser, 1983; Catuneanu *et al*., 2005).

Table 16: Summary of published number of deglaciation sequences in southern Africa.

Country	Number of Deglaciation cycles	Reference
South Africa	4	Visser (1997)
Botswana	3 to 4	Visser (1997)
Zimbabwe	3	Bond and Stocklmeyer (1967)
Tanzania	1	Wopfner (2002)
Congo	Unknown	
Zambia	Unknown	
Mozambique	4	This paper

Sedimentation during glaciation is largely dependent on the relief of the source area and transport dynamics into the basin. A high mountainous relief with an exposed bedrock setting would result in a poorly sorted deposit with a range of grain size and clast shapes. In contrast, a relatively flat relief will result in better sorted finer-grained deposit. Although climate change may be similar across an area the contrasting relief and rock types plays a significant role in determining the glacial deposits of a basin. (Eyles *et al*., 1983). One needs to be cognisant of this when comparing glacial deposits across southern Africa. Varying tectonic activity across the Karoo basins of southern Africa would influence the relief of the margins of the basins, where sedimentation occurred contemporaneously with faulting (Eyles *et al*., 1983; Catuneanu *et al*., 2005). In the foreland setting of South Africa for example, contrasting glacial deposits are observed in the foredeep and forebulge portions of the basin (Catuneanu *et al*., 2005). Detrital work on glacial deposits indicates five main ice caps across Gondwana with smaller ice caps across the continent (Isbell *et al*., 2008; Cradock *et al*., 2019). It is possible that differential melting rates related to varying reliefs and a changing South Pole position from 338-265 Ma resulted in differential melting rates for the ice caps, with increased variability on minor thinner ice caps (Eyles *et al*., 1983; Key *et al*., 2015; Craddock *et al*., 2019;). The thermal regime at the base of an ice sheet has a large influence on the amount of outwash generated which influences the type and amount of sedimentation (Eyles *et al*., 1983). The varying conditions across southern Africa influencing the glacial sequences are illustrated in Figure 42.

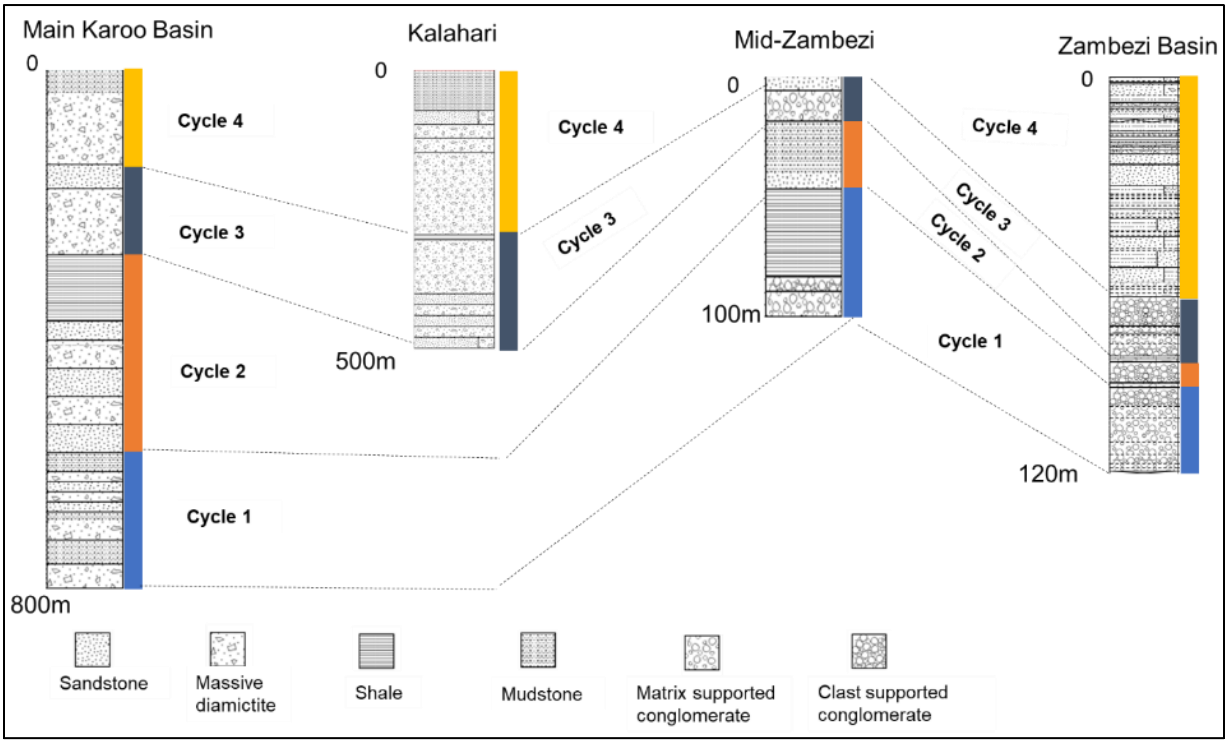

Figure 42: Simplified stratigraphic columns of deglaciation cycles identified in this project by Bond and Stocklmayer (1967) and Visser (1997). Coloured blocks match sequence colours indicated in Figure 23. Columns are not to scale.

Detailed lithological logging of borehole 11MTD001 indicates thick conglomeratic units ranging in clast size from cobble to occasional boulder sized units which may be clast- or matrix-supported. These conglomerates are often overlain by siltstones, which are interpreted to represent deglaciation cycles.

The conglomeratic units identified in 11MTD001 are predominantly clast supported with sub-rounded to rounded clasts. Point counting indicates a matrix percentage range of 23 - 47 %. Dietrich *et al*. (2019) described cycles containing diamictites, breccias and conglomerates to represent scree and mass-flow deposits. In 11MTD001, the lower cycles are dominated by conglomerates with thin layers of sandstones and siltstones with sedimentary structures identified. Although there were no glacial striations or other glacial features identified in 11MTD001, the lack of glacial evidence does not dispel a glacial origin. Glacial deposits described by Bond and Stocklmayer (1967) in Zimbabwe similarly lacked glacial evidence. It is interpreted that the conglomerates in 11MTD001 are of glacial origin and represent glacial outwash gravels during glacial retreat. Diamictites identified in 11MTD001 from deglaciation cycle 4 are associated with wave ripple cross-lamination and convoluted bedding and may represent a non-glacial origin as described by Vesely *et al*. (2018). However, the absence of rythmites in 11MTD001 described by Vesely *et al*. (2018) suggests a glacial origin for deglaciation cycle 4. The diamictites occur at the top of the sequence and are interpreted to represent the maximum retreat of glacier and end of glaciation.

6.1: Deglaciation cycle 1

The first three conglomeratic units are predominantly matrix supported with a high matrix to clast proportion suggesting these conglomerates are tillites. The matrix of the first tillite units consist of fragments of the underlying basement suggesting that initially the material was sourced from a short distance during the initial stages of the basin development. The gradual change in the colour and composition of the matrix, together with a gradual increase in the roundness of the clasts, indicates that material was sourced from a larger area as the Karoo basin developed or alternatively represents periods of fluvial reworking fuelled by glacial retreat. The upper clast supported conglomerate with a decrease in the percentage of matrix material represents a glacial outwash conglomerate representing the onset of glacial retreat. This unit is capped off with a siltstone deposited in calmer sedimentary conditions, with a further glacial retreat into the mountainous highlands. Palaeoflow conditions were not established from the core in this study, zircon information higher up in the sequence indicates a south westerly and westerly directed palaeoflow direction, while Key *et al*. (2015) proposes that the glaciers followed deep glacial valleys. The glaciers probably retreated up to these valleys towards the north west and west.

The cycle intersected conforms with the first glacial sequence described by Bond and Stocklmayer (1967), with tillites, outwash conglomerates and siltstones representing a retreating ice front.

6.2: Deglaciation cycle 2

The second cycle represents a second period of glaciation where the maximum extent of the glacier advance was less than the first cycle. The conglomerates consist of a bottom outwash conglomerate overlain by a conglomerate that is clast to matrix supported in places. The cobbles and pebbles of the upper conglomerate were supplied by rafts from a retreating glacier, which became less prevalent in the upper sequence of the unit. This cycle is capped by a siltstone like the unit intersected in the first cycle.

6.3: Deglaciation cycle 3

The third glacial cycle commences with a clast supported outwash conglomerate supplied by a retreating glacier. Bond and Stocklmeyer (1967) reported tillites in the third cycle in the Mid-Zambezi basin in Zimbabwe. The glacial advance identified in the Chicôa-Mecúcoè sub-basin was not as prominent, this may reflect different tectonic controls for the two basins or closer proximity to the relative position of the poles (Craddock *et al*., 2019). The cycle is capped off with a comparatively thicker siltstone unit, suggesting an overall warming climate with longer periods between glacial advances.

6.4: Deglaciation cycle 4

The fourth and final deglaciation cycle identified in 11MTD001 represents the stratified unit described by Visser (1997). The unit commences with an outwash conglomerate and is overlain by a series of sandstones, mudstones and diamictites. The end of glaciation was associated gradual warming characterised by periods of small glacial advances followed by longer periods of glacial retreat. Diamictites were formed from glacial rafts of the position of the borehole, dropping pebble to gravel sized clasts into silty material. The cycle is capped off by a carbonaceous mudstone and coal measures and an end in glacial advance and the final stages of the Vúzi Formation.

6.5: Implications

Three deglaciation cycles have been identified in northern Zimbabwe in the Mid-Zambezi Basin by Bond and Stocklmeyer (1967), with each cycle influenced by climatic shifts, with or without tectonic controls. With the rarity of Vúzi Formation sub-outcrop in the rift basins of central Africa, 11MTD001 confirms that deglaciation cycles identified in South Africa, Botswana and Zimbabwe occur further north in the Chicôa-Mecúcoè sub-basin. Deglaciation cycles described by Bond and Stocklmayer (1967) and Visser (1997) are absent in Tanzania, although glacial deposits are well represented in Tanzania only one deglaciation sequence is identified in available literature. (Stratten., 1968; Bond., 1970; Catuneanu *et al*., 2005; Key *et al*., 2015). This suggests that the tectonism and the relief of the basin margins of Tanzania may have been different to the Zimbabwe and Mozambique basins and supports the model of several ice sheets across central Africa with glaciation localised (Dietrich *et al*., 2019). 11MTD001 contains thick glacial deposits indicating that glacial activity was extensive for the Chicôa-Mecúcoè sub-basin.

CHAPTER 7: Conclusion

- The vertical extent of the Vúzi Formation observed in 11MTD001 correlates with field observations in adjacent areas of the Chicôa-Mecúcoè sub-basin and indicates a thicker glacial stratigraphy for the area than is published.
- Cambrian to Neoproteroic aged detrital zircons are associated with igneous bodies formed during the Pan African Orogeny suggesting a paleoflow from the north west and west of 11MTD001. The low proportion of these grains indicate that sediment supply may have been restricted to periods of glacial melting resulting in meltwaters eroding localised elevated areas or most likely igneous bodies to the east and north east that have not been dated and may be of Pan African Origin.
- Mesoproterozoic aged detrital zircons are associated with igneous bodies formed during the Grenvillian orogen. Density probability plots indicate age peaks at 1100 Ma and 1076 Ma suggesting the Monte Capirimpica granatoids and the Cassacatiza suite as the most likely source with a south eastward and eastward directed palaeoflow.
- No known rocks have been dated to have formed between 1300 – 2900 Ma in the region. Paleoproterozoic, Neoarchaean and Mesoarchaean aged zircons probably represent reworked material in the Zambezi Belt, sourced from the cratons surrounding the Zambezi Belt prior to the Pan African Orogeny.
- Samples taken from the Vúzi, “Transitional” and Matinde formations indicate a dominant palaeoflow from the north east and east with a secondary, possibly periodic, source from north west and west. The subhedral to euhedral shape and preservation of rims indicate a relatively short transport history, possibly less than 100km.
- Rocks in the Zambezi Belt are poorly researched with limited published age data which are based on low number of zircon grains and falling short of statistical requirements. More work is required to accurately date the rocks in northern Mozambique to facilitate improved sedimentary and tectonic reconstructions.
- Conglomerates identified in 11MTD001 are interpreted as glacial outwash gravels indicating a glacial origin for the Vúzi Formation in the Chicôa-Mecúcoè sub-basin.

- Four deglaciation cycles have been identified in the Vúzi Formation in the Chicôa-Mecúcoè sub-basin, with each cycle beginning with a series of matrix to clast supported conglomerates, which are capped off with siltstones. The cycles represent advancing and retreating glaciers with glaciers achieving a maximum advance in the first cycle while a relatively thicker siltstone unit in cycle 3 suggests longer periods between glacial retreat and advance.
- Glacial cycle 4 represents the stratified glacial sequence for southern Africa where glaciers advanced and then retreated for long periods to form a sequence of diamictites, sandstones and siltstones culminating in carbonaceous mudstones and coal measures which represent the end of glaciation and the commencement of the Moatize Formation.

References

Ait-Kaci Ahmed, A., 2003: The geology of the area north of Gokwe, Gokwe and Kadoma Districts, Middle Zambezi Valley. Bulletin, Geological Survey of Zimbabwe, 105, 85.

Allen, J.P., Fielding, C.R., 2007: Sedimentology and stratigraphic architecture of the Late Permian Betts Creek Beds, Queensland, Australia. Sedimentary Geology, 202, 5-34.

Anderson, T., 2005: Detrital zircons as tracers of sedimentary provenance: limiting conditions from statistical and numerical simulations. Chemical Geology, 216, 249-270.

Andersen, T., Kristoffersen, M., Elburg, M. 2015: How far can we trust provenance and crustal evolution information from detrital zircons? A south African case study. Gondwana Research, 34, 129-148.

Andersen, T., Elburg, M.A., Magwaza, B., 2019: Sources of bias in detrital zircon geochronology: Discordance, concealed lead loss and common lead correction. Elsevier, Earth Science Reviews, 197, 102899.

Augustsson, C., Voigt, T., Bernhart, K., Kreibler, M., Gaupp, R., Gartner, A., Hofmann, M., Linnermann, U., 2018: Zircon size-age sorting and source-area effect: The German Triassic Buntsandstein Group, Sedimentary Geology. 375, 218-231.

Barr, M. W. C., Brown, M. A., 1987: Precambrian gabbro-anorthosite complexes, Tete province, Mozambique. Geology Journal, 22, 139-159.

Bicca, M.M., Philipp, R.P., Jelinek, A.R., Ketzer, J.M.M., dos Sandtos Scherer, C.M., Jamal, D.L., dos Reis, A.D., 2017: Permian-Early Triassic tectonics and stratigraphy of the Karoo Supergroup in northwestern Mozambique. Elsevier, Journal of African Earth Sciences, 130, 8-27.

Bicca, M.M., Jelinek, A.R., Philipp, R.P., Lana, C.C., and A.R. Alkmim. 2018: Precambrian-Cambrian provenance of Matinde Formation, Karoo Supergroup, northwestern Mozambique, constrained from detrital zircon U-Pb age and Lu-Hf isotope data. Journal of African Earth Sciences, 138, 42-57.

Blenkinsop, T.G., Oesterlen., P.M., 1994: Extension directions and strain near the failed triple junction of the Zambezi and Luangwa Rift zones, southern Africa. Journal of African Earth Sciences, 18, 2, 175-180.

Blenkinsop, T.G., Oesterlen., P.M., 1996: Extension directions and strain near the failed triple junction of the Zambezi and Luangwa Rift zones, southern Africa – Reply. Journal of African Earth Sciences, 22, 4, 621-622.

Bond, G., Stocklmayer, V.R.C., 1967: Possible Ice-Margin Fluctuations in the Dwyka series in Rhodesia. Palaeogeography, Palaeoclimatology, Palaeoecology, 3, 433-446.

Bond, G. 1970: The Dwyka Series in Rhodesia. Proceedings of the Geologists Association, 81, 3, 463-472.

Bussert, R., 2010: Exhumed erosional landforms of the Late Palaeozoic glaciation in northern Ethiopia: Indicators of ice-flow direction, palaeolandscape and regional ice dynamics. Gondwana Research, 18, 356–369.

Cairncross, B., Winter, M.F., 1984: High-constructive lobate deltas in the lower Permian Vryheid Formation, Rietspruit, South Africa. Transactions of the Geological Society of South Africa, 87, 101-109.

Cairncross, B. 2001: An overview of the Permian (Karoo) coal deposits of southern Africa. Journal of African Earth Sciences, 33, 529–562.

Catuneanu, O., Wopfner, H., Eriksson, P.G., Cairncross, B., Rubidge, B.S., Smith, R.M.H., Hancox, P.J. 2005: The Karoo basins of south-central Africa. Journal of African Earth Sciences, 43, 211-253.

Cradock, J.P., Ojakangas, R.W., Malone, D.H., Konstantinou, A., Mory, A., Bauer, W., Thomas, R.J., Affinati, S.C., Pauls, K., Zimmerman, U., Botha, G., Rochas-Campos., A., dos Santos, P.R., Tohver., E., Riccomini., C., Martin., J., Redfern., J., Horstwood., M., Gehrels., G., 2019: Derital zircon provenance of Permo-Carbineferous glacial diamictites across Gondwana. Elsevier, 192, 285-316.

Cocherie, A., Robert, M., 2008: Laser ablation coupled with ICP-MS applied to U-Pb zircon geochronology: A review of recent advances. Gondwana Research, 14, 597-608.

Delvaux, D., 2001: Karoo Rifting in western Tanzania: precursor of Gondwana break-up? Contributions to Geology and Palaeontology of Gondwana in Honour of Helmut Wopfner, 111-125.

Dietrich, P., Franchi, F., Setlhabi, L., Prevec, R., Bamford, M., 2019: The nonglacial diamictite of Toutswemogala Hill (Lower Karoo Supergroup, central Botswana): Implications on the extent of the late Paleozoic Ice Age in the Kalahari–Karoo basin. Journal of Sedimentary Research, 89, 875-889.

Dodson, M.H., Compston, W., Ireland, I.S., Wilson, J.F., 1988: A search for ancient detrital zircons in Zimbabwean sediments. Journal of the Geological Society, London, 145, 977–983.

Engvik, A.K., Tveten, E. Bingen, B. Viola, G. Erambert, M. Feito, P. and Azavedo de S., 2007: P-T-t evolution and decompression textures of Pan-African high-pressure granulites, Lurio Belt, northeastern Mozambique. Journal of Metamorphic Geology, 25, 935-952.

Eyles, N., Eyles, C.H., Miall, D., 1983: Lithofacies types and vertical profile models; an alternative approach to the description and environmental interpretation of glacial diamict and diamictite sequences. Sedimentology, 30, 393-410.

Falcon R.M.S., Lemos de Sousa M.J., Pinheiro H.J., Marques M.M, 1984: Petrology and Palynology of Mozambique coals – Mucanha- Vúzi Region. Comuni- cações, Serviços Geológicos Portugal, 70, 321–338.

Fedo, C.M., Sircombe, K.N., Rainbird, R.H., 2003: Detrital zircon analysis of the sedimentary record. Reviews in Mineralogy and Geochemistry 53(1), 277-303.

Flowerdew, M.J., Millar, I.L., Vaughan, A.P.M., Horstwood, M.S.A., Fanning, C.M., 2006: The source of granitic gneisses and migmatites in the Antarctic Peninsula: a combined U-Pb SHRIMP and laser ablation Hf study of complex zircons. Contributions to Mineralogy and Petrology, 151, 751-768.

Hirata, T., Nesbitt, R.W., 1995: U-Pb isotope geochronology of zircon: Evaluation of the laser probe-inductively coupled plasma mass spectrometry technique. Geochimica et Cosmochimica Acta, 59, 12, 2491-2500.

Galasso, F., Fernandes, P., Montesi, G., Marques, J., Spina, A., Pereira, Z., 2019: Thermal history and basin evolution of the Moatize – Minjova Coal Basin (N' Condédzi sub-basin, Mozambique) constrained by organic maturation levels. Elsevier, Journal of African Earth Sciences, 153, 219-238.

Götz, A.E., Honcox, P.J., Lloyd, A., 2017: Permian climate change recorded in the palynomorph assemblages of Mozambique (Moatize Basin, eastern Tete Province). Acta Palaeobotanica, 57(1).

Goscombe, B., Armstrong, R., Barton, J.M., 2000: Geology of the Chewore Inliers, Zimbabwe: constraining the Mesoproterozoic to Palaeozoic evolution of the Zambezi Belt. Journal of African Earth Sciences, 30, 589-627.

GTK Consortium, 2006: Map Explaination., 4, Sheets 1430 - 1432 and 1530 - 1534. Geology of Degree Sheets Inhamambo, Maluwera, Chifunde, Zumbo, Fíngoè-Mágoè, Songo, Cazula and Zóbuè. Maputo, Mozambique.

Hanson, R.E., 2003: Proterozoic geochronology and tectonic evolution of southern Africa., Proterozoic East Gondwana: Supercontinent Assembly and Breakup. Geological Society of London, Special Publications, 206, 427-463.

Hatton, W., Fardell, A., 2011: New discoveries of coal in Mozambique - Development of the coal resource estimation methodology for International Resource Reporting Standards. International Journal of Coal Geology, 89, 2-12.

Hancox, P. J., 2014: Competent persons report on the Estima Project (Mining Right 6127C), Mozambique. Unpublished report for ENRC.

Hancox P.J., 2015: Competent persons report on the Mucangadzi north project of concession 6195C (formally prospecting licence 869L), Tete Province, Mozambique. Unpublished report for ENRC.

Hancox, P.J., Götz, A.E., 2014: South Africa's coalfields - A 2014 perspective. International Journal of Coal Geology, 132, 170-254.

Hancox, P.J., 2019: Personal communication. CCIC, Johannesburg, South Africa.

Hargrove, U.S., Hanson, R.E., Martin, M.W., Blenkinsop, T.G., Bowring, S.A., Walker, N., Munyanyiwa, H., 2003: Tectonic evolution of the Zambezi orogenic belt: geochronological, structural, and petrological constraints from northern Zimbabwe. Precambrian Research, 123, 159-186

Hunting Geology and Geophysics Limited, 1984: Mineral Inventory Project. Unpubl. Rept., 329 pp., DNG, Maputo. Referenced from: GTK Consortium, 2006: Map Explanation., 4, Sheets 1430 - 1432 and 1530 - 1534. Geology of Degree Sheets Inhamambo, Maluwera, Chifunde, Zumbo, Fíngoè- Mágoè, Songo, Cazula and Zóbuè. Maputo, Mozambique.

Isbell, J.L., Cole, D.I., Catuneanu, O., 2008: Carboniferous-Permian glaciation in the main Karoo Basin, South Africa: Stratigraphy, depositional controls, and glacial dynamics. The Geological Society of America, Special Paper 441.

Jackson, S.E., Pearson, N.J., Griffin, W.L., Belousova, E.A., 2004: The application of laser ablation-inductively coupled plasma-mass spectrometry to in situ U-Pb zircon geochronology. Chemical Geology, 211, 47-69.

Jaffey, A.H., Flynn, K.F., Glendenin, L.E., Bentley, W.C., Essling, A.M., 1971: Precision measurement of half-lives and specific activities of ^{235}U and ^{238}U. Physical Review, 104, 1629.

Jeffries, T.E., Pearce, N.J.G., Perkins, W.T., Raith, A., 1996: Chemical fractionation during Infrared and Ultraviolet Laser Ablation Inductively Coupled Plasma Mass Spectrometry-Implications for mineral microanalysis. Analytical Communication, 33, 35-39.

Johnson, M.R., Van Vuuren, C.J., Hegenberger, W.F., Key, R., Shoko, U., 1996: Stratigraphy of the Karoo Supergroup. Journal of African Earth Sciences, 23, 3 - 15.

Johnson, M.R., Van Vuuren, C.J., Visser, J.N.J., Cole, D.I., Wichens, H. de V., Christie, A.D.M., Roberts, D.L., Brandl, G., 2006: Sedimentary rocks of the Karoo Supergroup. Referenced from: Johnson, M.R., Anhaeusser, C.R. and Thomas, R.J. (Eds.), 2006: The Geology of South Africa, Geological Society of South Africa, Johannesburg/Council for Geoscience, Pretoria, 461–499.

Johnson, S.P., Oliver, G.J.H., 2004: Tectonothermal history of the Kaourera Arc, northern Zimbabwe: implications for the tectonic evolution of the Irumide and Zambezi Belts of south-central Africa. Precambrian Research, 130, 71-97

Key, R.M., Cotterill, F.P.D., Moore A.E., 2015: The Zambezi River: An archive of tectonic events linked to the amalgamation and disruption of Gondwana and subsequent evolution of the African plate. South African Journal of Geology, 118, 425-438.

Koch, J., Feldmann, I., Jakubowski, N., Niemax, K., 2002: Elemental composition of laser ablation aerosol particles deposited in the transport tube to an ICP. Spectrochimica Acta Part B, 57, 975–985.

Košler, J., 2012: U-Pb Geochronology and Hf isotope geochemistry of detrital zircon in sedimentary systems. In: Sylvester, P., Quantitative Mineralogy and Microanalysis of Sediments and Sedimentary Rocks. Short Course Series 42, Mineralogical Association of Canada, 185–202.

Kramers, J., Frei, R., Newville, M., Kober, B., Villa, I., 2009: On the valency state of radiogenic lead in zircon and its consequences. Chemical Geology, 261, 3-10.

Kramers, J., 2017: Data reduction program version U-Pb_UJ_July_2017_W10. University of Johannesburg.

Lächelt, S., 2004: Geology and Mineral Resources of Mozambique. Pretoria: Council for Geoscience South Africa.

Lakshminarayana, G., 2015: Geology of Barcode type coking coal seams, Mecondezi sub-basin, Moatize Coalfield, Mozambique. International Journal of Coal Geology, 146, 1–13.

Ludwig, K.R., 2003: Isoplot/Ex 3.00. A Geochronological Toolkit for Microsoft Excel. Special Publications, 4, Berkeley Geochronological Centre. Berkeley, CA.

Mahabeer, K.C., 2017: Palynology of the Permian Sanangoe- Mefidezi Coal Basin, Tete Province, Mozambique And Correlations With Gondwanan Microfloral Assemblages, Mozambique. MSc thesis, University of Witwatersrand, South Africa.

Mäkitie, H., Manninen, T., Lehtonen, M.I., 2005: GTK Consortium, Zumbo/Fíngoè-Mágoè 1:250 000 map, 1530_1531. Component 2, Geological Infrastructure Development Project, Geological mapping (LOT 2). Ministério Dos Recursos Minerais, República De Moçambique.

Mänttäri, I., 2006: Zircon U-Pb ages of three Mozambican rock samples. Intern. Rept., Geological Survey of Finland (GTK), Espoo, Finland, CK21.42/2006/1, 15. Referenced from: GTK Consortium, 2006: Map Explanation, 4, Sheets 1430-1432 and 1530-1534. Geology of Degree Sheets Inhamambo, Maluwera, Chifunde, Zumbo, Fíngoè - Mágoè, Songo, Cazula and Zóbuè. Maputo, Mozambique.

Miall, A.D., 1996: The Geology of Fluvial Deposits: sedimentary facies, basin analysis and petroleum geology. Springer-Verlag, 582.

Meert, J.G., Torsvik, T.H., 2003: The making and unmaking of a supercontinent: Rodinia revisited. Tectnophysics, 375, 261-288.

Morton, A.C., Claoué-Long, J.C., Berge, C., 1996: SHRIMP constraints on sediment provenance and transport history in the Mesozoic Statfjord Formation, North Sea. Journal of the Geological Society, 153, 915-929.

Munyanyiwa, H., Hanson, R.E., Blenkinsop, T.G., Treloar, P.J., 1997: Geochemistry of amphibolites and quartzofeldspathic gneisses in the Pan-African Zambezi belt, northwest Zimbabwe: evidence for bimodal magmatism in continental rift setting. Precambrian Research, 81, 179-196

Nasdala, L., Hanchar, J.M., Kronz, A., Whitehouse, M.J., 2005: Long-term stability of alpha particle damage in natural zircon. Chemical Geology, 220, 83-103.

Nemchin, A.A., Hostwood, M.S.A., Whitehouse, M.J., 2013: High-Spatial-Resolution Geochronology. Elements, 9, 31-37.

Nyambe, I. A., Utting, J., 1997: Stratigraphy and palynostratigraphy, Karoo Supergroup (Permian and Triassic), mid-Zambezi Valley, southern Zambia. Journal of African Earth Sciences, 24(4), 563–583.

Nyambe, I. A.,1999: Tectonic and climatic controls on sedimentation during deposition of the Sinakumbe Group and Karoo Supergroup, in the mid-Zambezi Valley Basin, southern Zambia. Journal of African Earth Sciences, 28(2), 443-463.

Opdyke, N.D., Mushayandebvu, M., De Wit, M.J., 2001: A new palaeomagnetic pole for the Dwyka System and correlative sediments in sub-Saharan Africa. Journal of Earth Sciences, 33, 1, 143-153.

Orpen, J.L., Swain, C.J., Nugent, C., 1989: Wrench-fault and half-graben tectonics the development of the Palaeozoic Zambezi Karoo Basins in Zimbabwe – the "Lower Zambezi" and "Mid-Zambezi" basins respectively - and regional implications. Journal of African Earth Sciences, 8, 2/3/4, 215-229.

Parrish, R.R., Noble, S.R., 2003: Zircon U-Th-Pb Geochronology by Isotope Dilution-Thermal Ionization Mass Spectrometry (ID-TIMS) Referenced from: Hanchar, J.M., Hoskin, P.W.O. (Eds). Reviews in Mineralogy and Geochemistry, 53, 1, 183-213.

Pereira, Z., Fernandes, P., Lopes, G., Marques, J., Vasconcelos, L., 2015: The Permian–Triassic transition in the Moatize–Minjova Basin, Karoo Supergroup, Mozambique: A palynological perspective. Review of Palaeobotany and Palynology, 226, 1-19.

Pereira, Z., Fernandes, P., Lopes, G., Marques, J., Vasconcelos, L., 2016: The Permian-Triassic transition in the Moatize-Minjova Basin, Karoo Supergroup, Mozambique: A palynological perspective. Review of Palaeobotany and Palynology, 226, 1–19.

Pickhardt, C., Dietze, H-J., Becker, J.S., 2005: Laser ablation inductively coupled plasma mass spectrometry for direct isotope ratio measurements on solid samples. International Journal of Mass Spectrometry, 242, 273-280.

Poitrasson, F., Hanchar, J.M., Shaltegger, U., 2002: The current state and future of sccessory mineral research. Elsevier, Chemical Geology, 191, 3-24.

Porada, H., 1989: Pan-African Rifting and Orogenesis in Southern to Equatorial Africa and Eastern Brazil. Precambrian Research, 44, 103-136.

Porada, H., Berhorst, V., 2000: Towards a new understanding of the Neoproterozoic-Early Palaeozoic Lufilian and northern Zambezi Belts in Zambia and the Democratic Republic of Congo. Journal of African Earth Sciences, 30, 3, 727-771.

Phiri, C., Wang., P., Nyambe., I.A., 2016: Geology and potential hydrocarbon play system of Lower Karoo Group in the Maamba Coalfield Basin, southern Zambia. Journal of African Earth Sciences, 118, 245-262.

Rubatto, D., 2002: Zircon trace element geochemistry: partitioning with garnet and the link between U-Pb ages and metamorphism. Chemical Geology, 184, 123-138.

Scheffler, K., Hoemes, S., Schwark, L., 2003: Global changes during Carboniferous–Permian glaciation of Gondwana: Linking polar and equatorial climate evolution by geochemical proxies. Geological Society of America, 31, 7, 605–608.

Schoene, B., Condon, D.J., Morgan, L., Mclean., N., 2013: Precision and Accuracy in Geochronology. Elements, 9, 19-24.

Semkiwa, P.Z., 1992: Depositional environment and coal petrography of Permian coal deposits in Karoo basins of SW Tanzania. Geologisches Institut, Universitat Koln Sonderveroffentlichungen, vol. 84, 184. Referenced from: Catuneanu, O., Wopfner, H., Eriksson, P.G., Cairncross, B., Rubidge, B.S., Smith, R.M.H., Hancox, P.J. 2005: The Karoo basins of south-central Africa. Journal of African Earth Sciences, 43, 211-253.

Smith, A.G., 1999: Gondwana: its shape, size and position from Cambrian to Triassic times. Journal of African Earth Sciences, 28, 1, 71-97.

Smith, C.B., 2018: Stratigraphy of the Lower Carboniferous to Middle Permian Vúzi, Moatize and Matinde formations of the Sanângoà-Mefidézi sub-basin, Tete Province Mozambique. Unpublished MSc Thesis, University of Witwatersrand University, South Africa, 247.

Stratten, T., 1968: The Dwyka Glaciation and its relationship to the pre-Karoo surface. Unpublished PhD thesis, University of Witwatersrand, South Africa, 196.

Steiger, R,H. & Jäger, E., 1977: Subcommission on geochronology: Convention on the use of decay constants in geo- and cosmochronology. Elsevier, Earth and Planetary Science Letters, 36, 359-362.

Turner, B.R., 1999: Tectonostratigraphy development of the Upper Karoo foreland basin: orogenic unloading versus thermally - Induced Gondwana rifting. Journal of African Earth Resources, 28, 1, 215-238.

Veevers, J.J., Saeed, A., 2007: Central Antartic provenance of Permian sandstones in Dronning Maud Land and the Karoo Basin: Integration of U-Pb and T_{DM} ages and host-rock affinity from detrital zircons. Elsevier, Sedimentary Geology, 202, 653-676.

Vesely, F.F., Rodrigues, M.C.N.L., da Rosa, E.L.M., Amato, J.A., Trzaskos, B., Isbell, J.L., Fedorchuk, N.D., 2018: Recurrent emplacement of non-glacial diamictite during the late Paleozoic ice age. Geology, The geological society of America.

Visser, J.N.J., 1983: Submarine debris flow deposits from the Upper Carboniferous Dwyka Tillite Formation in the Kalahari Basin, South Africa. Sedimentology, 30, 511–523.

Visser, J.N.J., 1987: The Palaeogeography of the part of southwestern Gondwana during the Permo-Carboniferous glaciation. Palaeogeography, Palaeoclimatology, Palaeoecology, 61, 205-219

Visser, J. N. J. ,1995: Post-glacial Permian stratigraphy and geography of southern and central Africa: boundary conditions for climatic modelling. Palaeogeography, Palaeoclimatology, Palaeoecology, 118(3-4), 213–243.

Visser, J.N.J., 1996: Controls on Early Permian shelf deglaciation in the Karoo Basin of South Africa. Palaeogeography, Palaeoclimatology, Palaeoecology, 125, 129-139.

Visser, J.N.J. 1997: Deglaciation sequences in the Permo–Carboniferous Karoo and Kalahari basins of southern Africa: A tool in the analysis of cyclic glaciomarine basin fills. Sedimentology, 44, 507-521.

Vorster, C., 2013: Laser ablation ICP-MS age determination of detrital zircon populations in the Phanerozoic Cape and lower Karoo Supergroups (South Africa) and correlatives in Argentina, Unpublished PhD thesis. Geology Thesis, University of Johannesburg, South Africa, 648.

Vorster, C., 2020: Personal communication. University of Johannesburg, Department of Geology, Johannesburg, South Africa.

Westerhof, A.B., Lehtonen, M.I., Makitie, H., Manninen, T., Pekkala, Y., Gustafsson, B., Tahon, A., 2008: The Tete-Chipata Belt: A new multiple terrane element from Western Mozambique and Southern Zambia. Geological Survey of Finland, 48, 145-166

Wopfner, H. 2002: Tectonic and climatic events controlling deposition in Tanzanian Karoo basins. Journal of African Earth Sciences, 34, 167–177.

Wopfner, H., Kreuser, T., 1986: Evidence for Late Palaeozoic glaciation in southern Tanzania. Palaeogeography, Palaeoclimatology, Palaeoecology, 56, 275-295. Referenced from Wopfner, H. 2002: Tectonic and climatic events controlling deposition in Tanzanian Karoo basins. Journal of African Earth Sciences, 34, 167–177.

Wopfner, H., Jin, X.C., 2009: Pangea Megasequences of Tethyan Gondwana-margin reflect global changes of climate and tectonism in Late Palaeozoic and Early Triassic times - A review. Palaeoworld, Nanjing Institute of Geology and Palaeontology, Elsevier, 169-192.

Wopfner, H., 2013: Late Palaeozoic – Early Triassic deposition and climates between Samfrau and Tethys : A review. Geological Society, London, Special Publications, 376, 5-32.

APPENDIX A: DETRITAL ZIRCON CATHODE LUMINESCENCE SEM IMAGES

B1766: Cathode luminescence SEM images, red dot indicates ablation position.

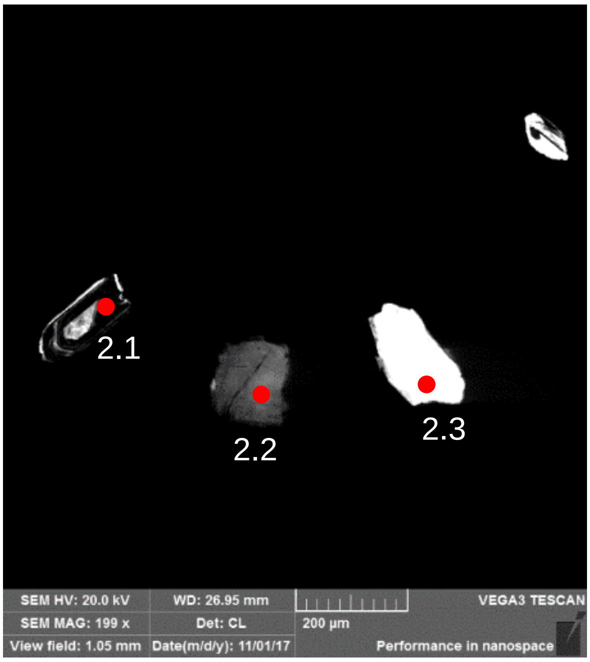

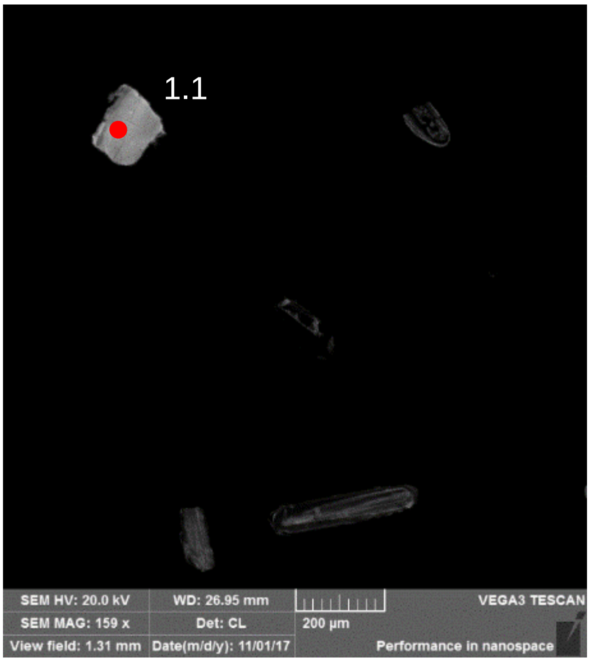

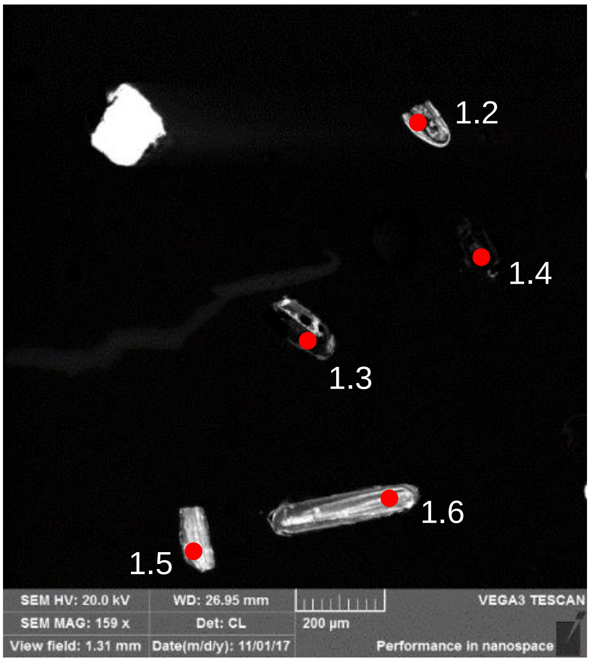

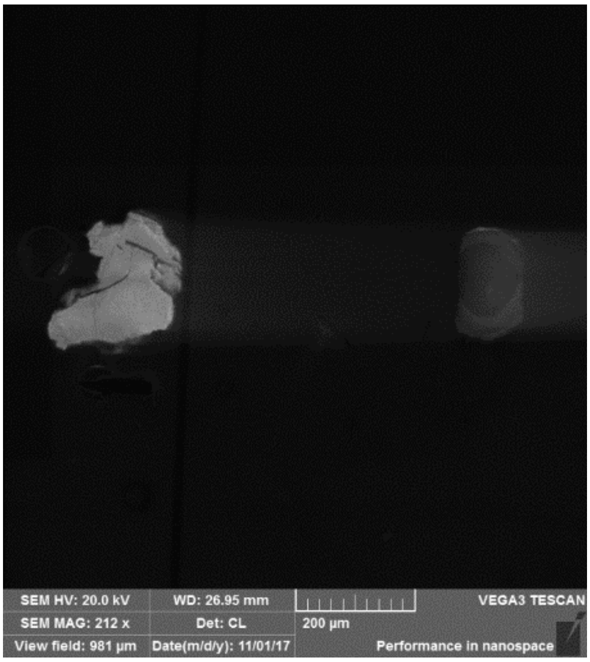

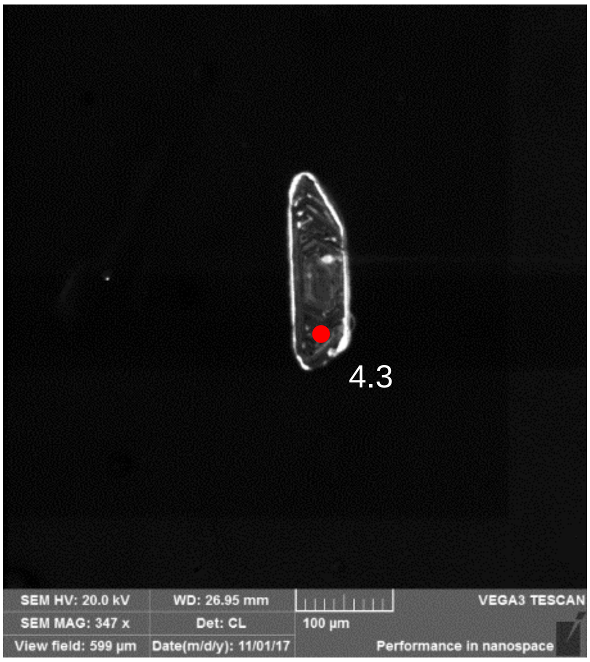
4.3
SEM HV: 20.0 kV
WD: 26.95 mm
VEGA3 TESCAN
SEM MAG: 347 x
Det: CL
100 µm
View field: 599 µm
Date(m/d/y): 11/01/17
Performance in nanospace

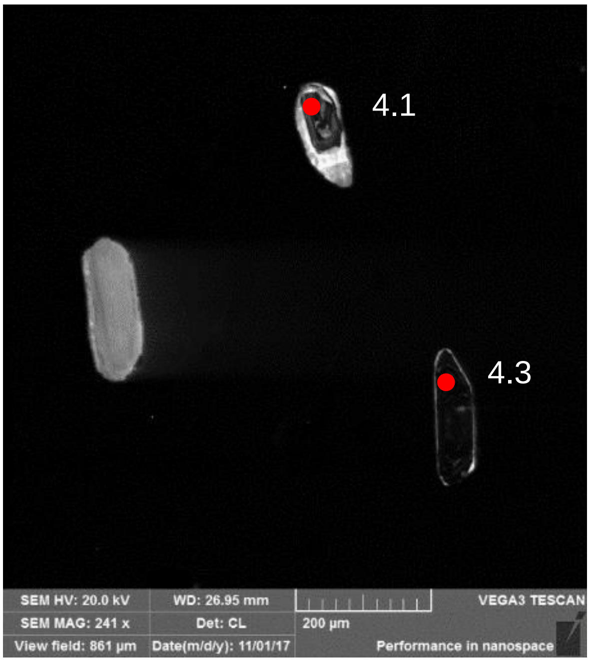
4.1
4.3
SEM HV: 20.0 kV
WD: 26.95 mm
VEGA3 TESCAN
SEM MAG: 241 x
Det: CL
200 µm
View field: 861 µm
Date(m/d/y): 11/01/17
Performance in nanospace

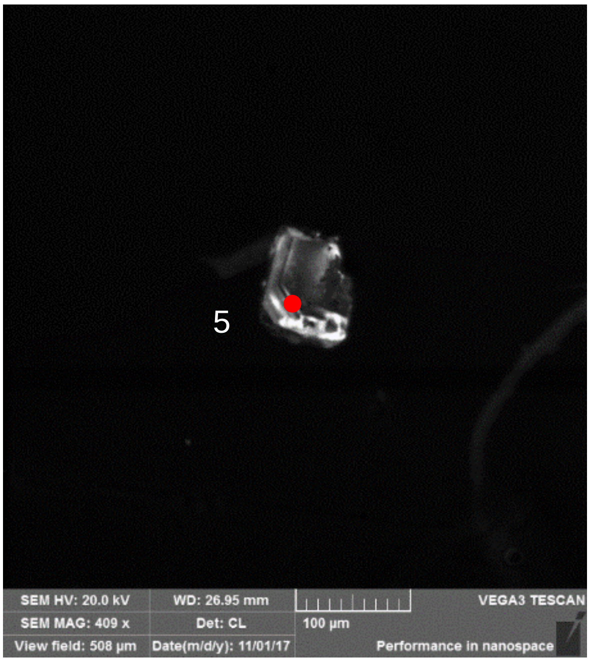
5
SEM HV: 20.0 kV
WD: 26.95 mm
VEGA3 TESCAN
SEM MAG: 409 x
Det: CL
100 µm
View field: 508 µm
Date(m/d/y): 11/01/17
Performance in nanospace

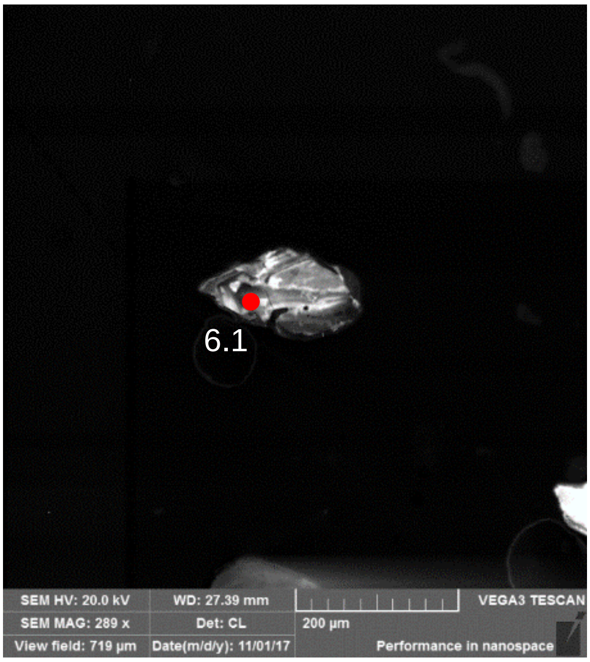
6.1
SEM HV: 20.0 kV
WD: 27.39 mm
VEGA3 TESCAN
SEM MAG: 289 x
Det: CL
200 µm
View field: 719 µm
Date(m/d/y): 11/01/17
Performance in nanospace

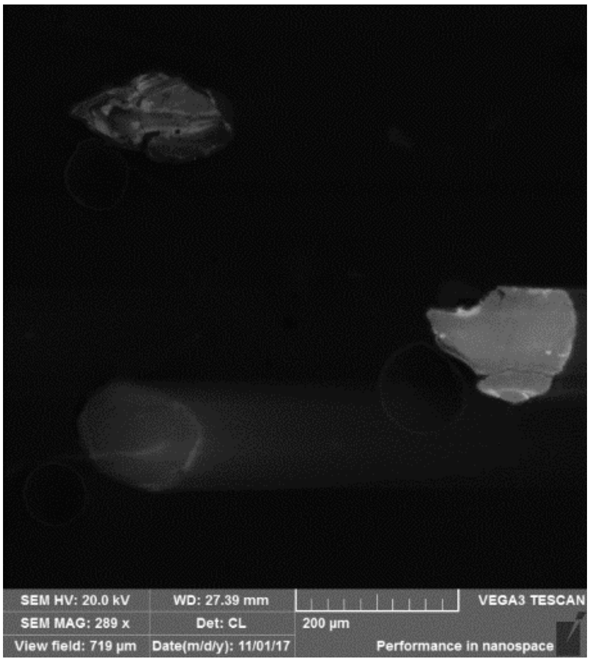
SEM HV: 20.0 kV
WD: 27.39 mm
VEGA3 TESCAN
SEM MAG: 289 x
Det: CL
200 μm
View field: 719 μm
Date(m/d/y): 11/01/17
Performance in nanospace

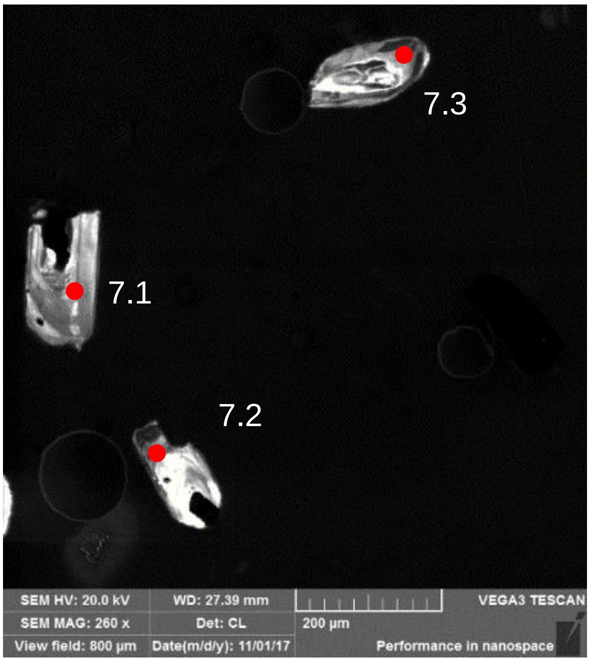
7.3
7.1
7.2
SEM HV: 20.0 kV
WD: 27.39 mm
VEGA3 TESCAN
SEM MAG: 260 x
Det: CL
200 μm
View field: 800 μm
Date(m/d/y): 11/01/17
Performance in nanospace

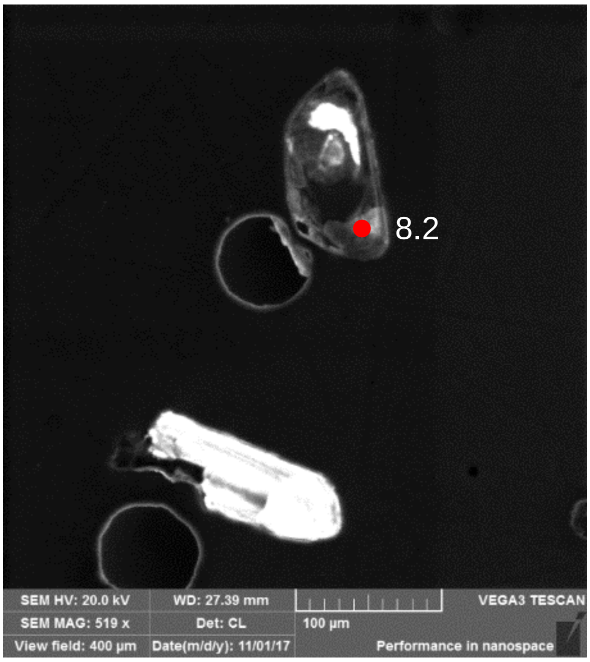
8.2
SEM HV: 20.0 kV
WD: 27.39 mm
VEGA3 TESCAN
SEM MAG: 519 x
Det: CL
100 μm
View field: 400 μm
Date(m/d/y): 11/01/17
Performance in nanospace

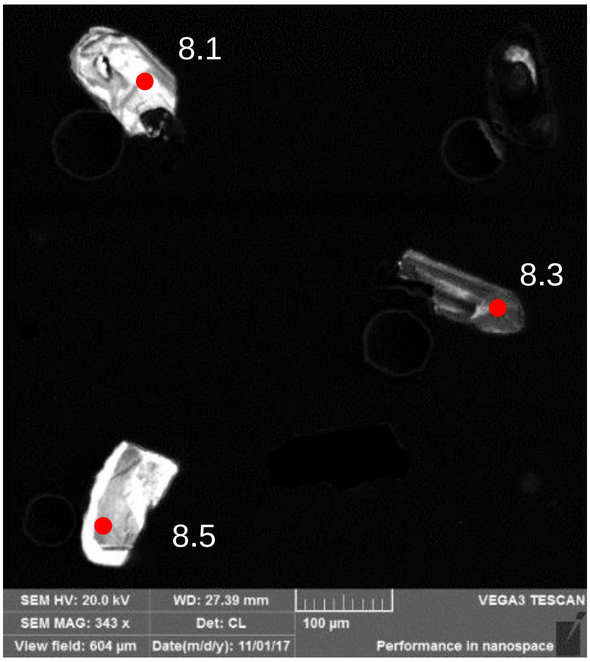
8.1
8.3
8.5
SEM HV: 20.0 kV
WD: 27.39 mm
VEGA3 TESCAN
SEM MAG: 343 x
Det: CL
100 μm
View field: 604 μm
Date(m/d/y): 11/01/17
Performance in nanospace

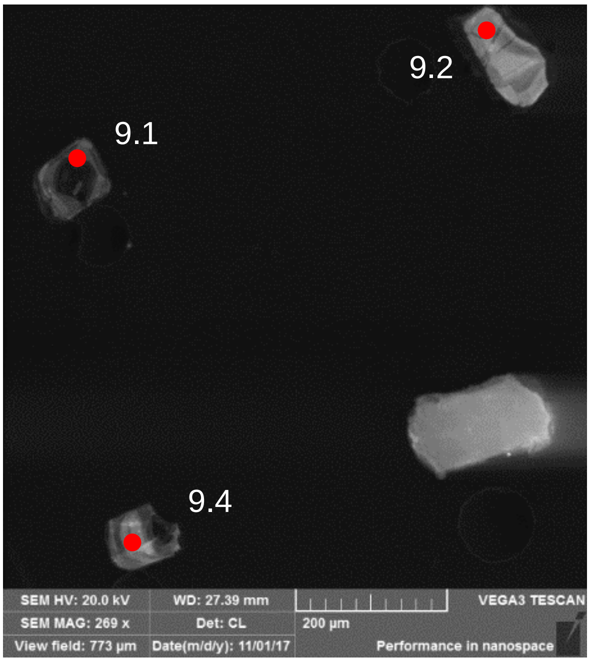
9.2
9.1
9.4
SEM HV: 20.0 kV
WD: 27.39 mm
VEGA3 TESCAN
SEM MAG: 269 x
Det: CL
200 µm
View field: 773 µm
Date(m/d/y): 11/01/17
Performance in nanospace

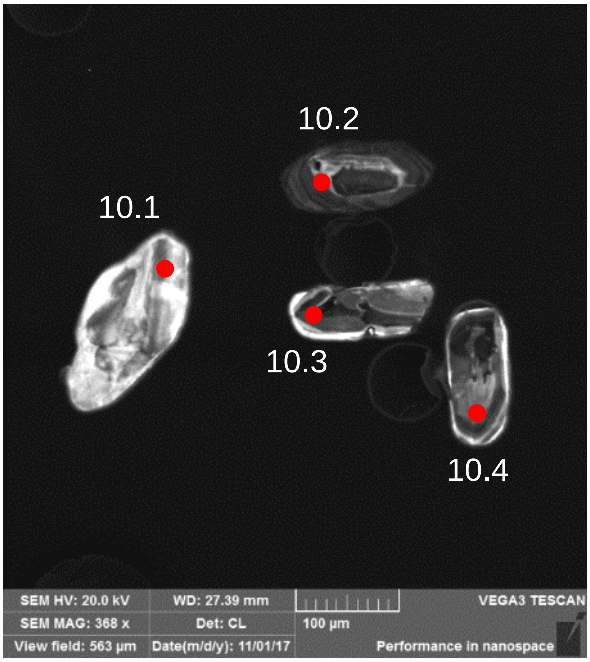
10.2
10.1
10.3
10.4
SEM HV: 20.0 kV
WD: 27.39 mm
VEGA3 TESCAN
SEM MAG: 368 x
Det: CL
100 µm
View field: 563 µm
Date(m/d/y): 11/01/17
Performance in nanospace

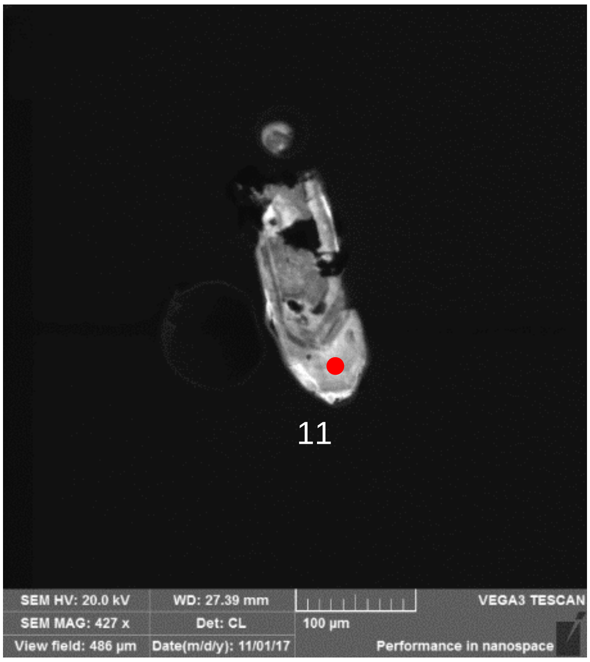
11
SEM HV: 20.0 kV
WD: 27.39 mm
VEGA3 TESCAN
SEM MAG: 427 x
Det: CL
100 µm
View field: 486 µm
Date(m/d/y): 11/01/17
Performance in nanospace

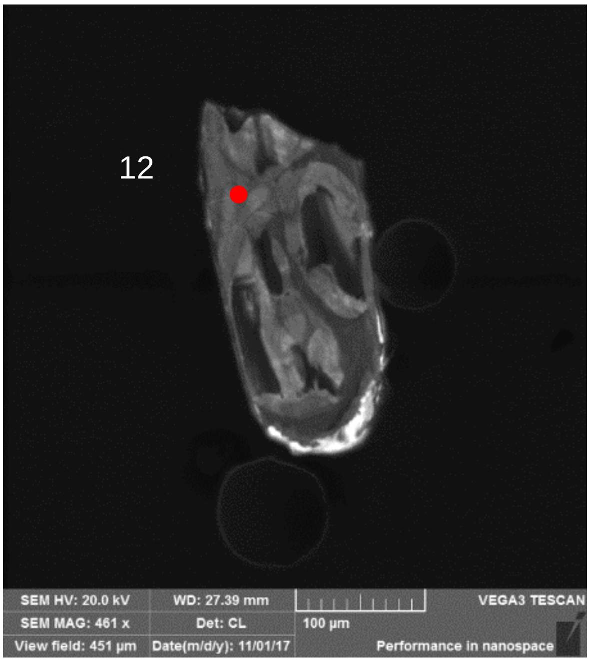
12
SEM HV: 20.0 kV
WD: 27.39 mm
VEGA3 TESCAN
SEM MAG: 461 x
Det: CL
100 µm
View field: 451 µm
Date(m/d/y): 11/01/17
Performance in nanospace

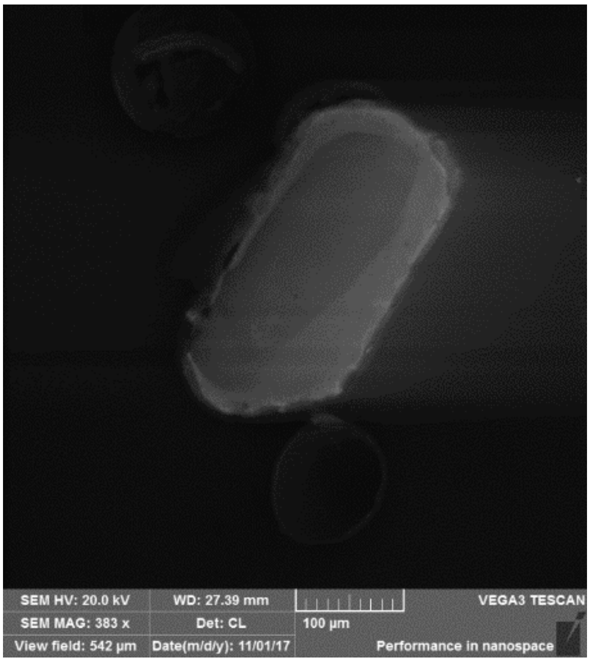
SEM HV: 20.0 kV
WD: 27.39 mm
VEGA3 TESCAN
SEM MAG: 383 x
Det: CL
100 µm
View field: 542 µm
Date(m/d/y): 11/01/17
Performance in nanospace

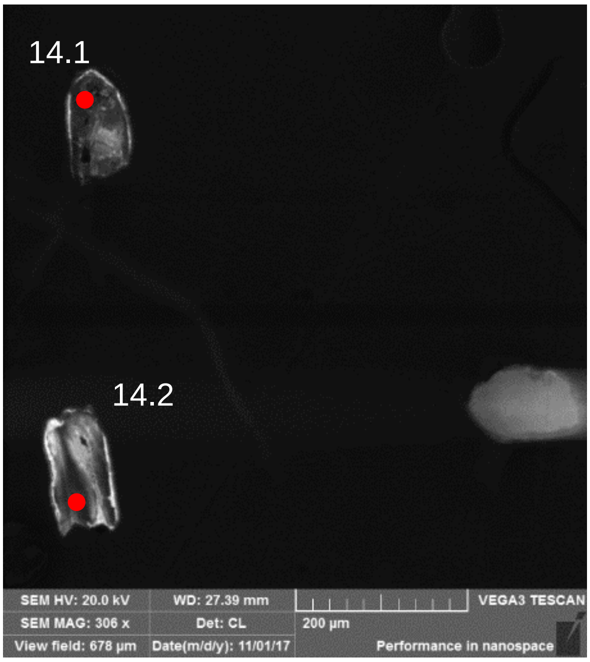
14.1
14.2
SEM HV: 20.0 kV
WD: 27.39 mm
VEGA3 TESCAN
SEM MAG: 306 x
Det: CL
200 µm
View field: 678 µm
Date(m/d/y): 11/01/17
Performance in nanospace

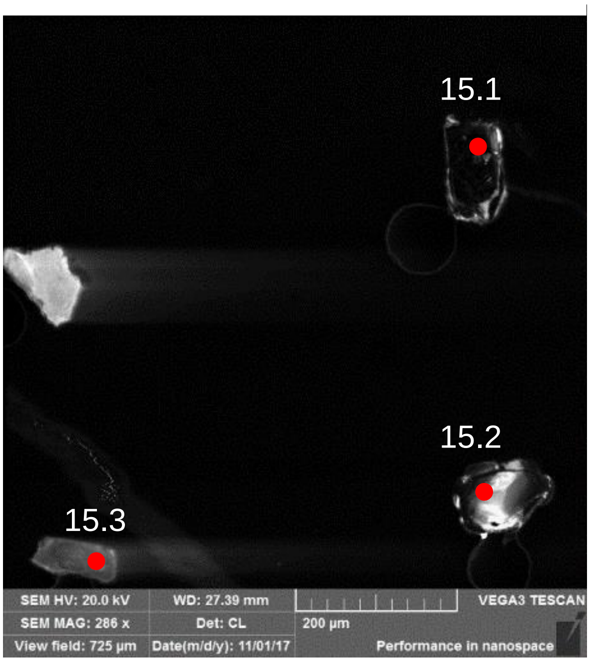
15.1
15.2
15.3
SEM HV: 20.0 kV
WD: 27.39 mm
VEGA3 TESCAN
SEM MAG: 286 x
Det: CL
200 µm
View field: 725 µm
Date(m/d/y): 11/01/17
Performance in nanospace

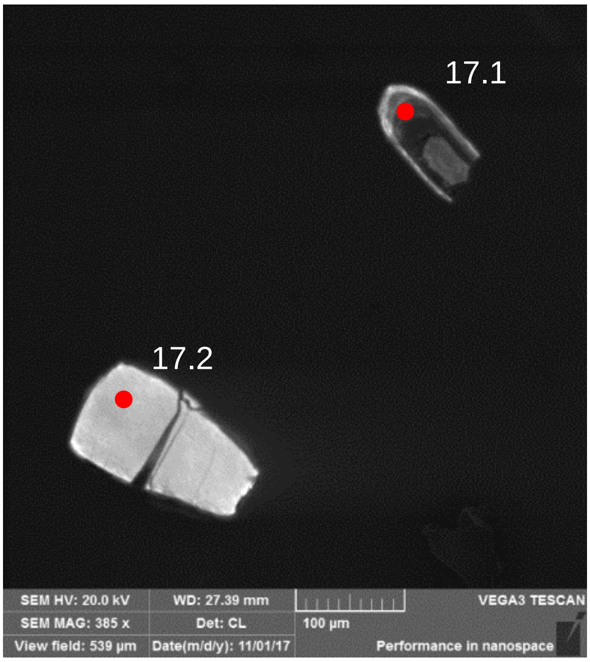
17.1
17.2
SEM HV: 20.0 kV
WD: 27.39 mm
VEGA3 TESCAN
SEM MAG: 385 x
Det: CL
100 µm
View field: 539 µm
Date(m/d/y): 11/01/17
Performance in nanospace

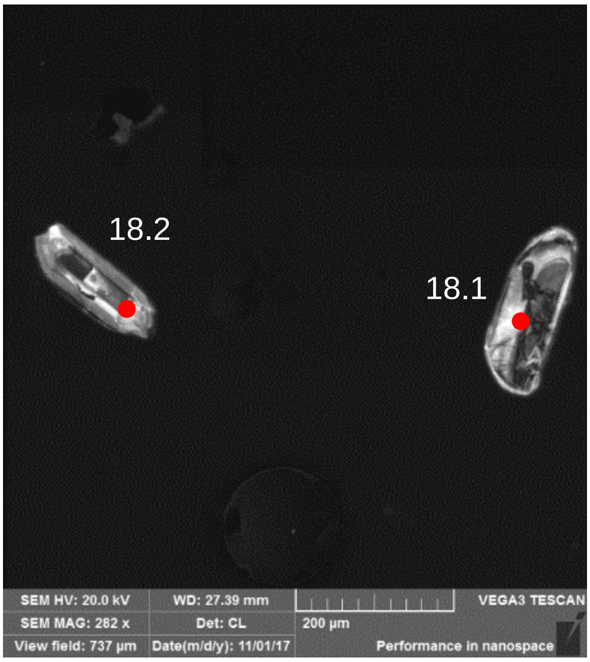
18.2
18.1
SEM HV: 20.0 kV
WD: 27.39 mm
VEGA3 TESCAN
SEM MAG: 282 x
Det: CL
200 µm
View field: 737 µm
Date(m/d/y): 11/01/17
Performance in nanospace

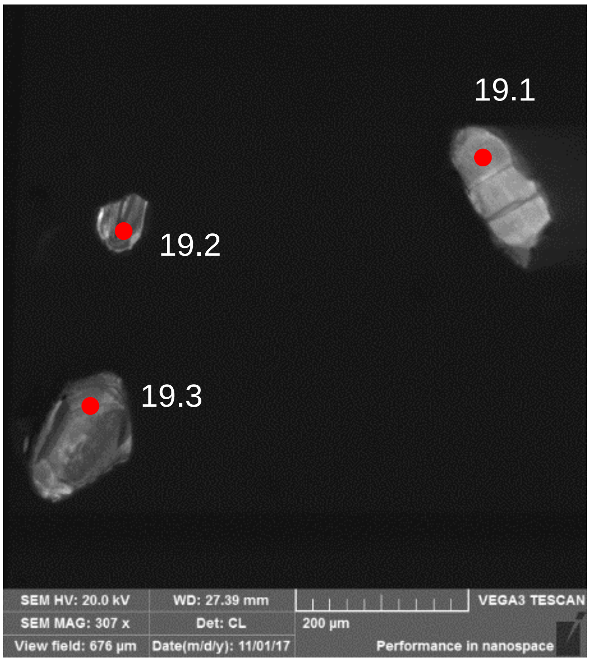
19.1
19.2
19.3
SEM HV: 20.0 kV
WD: 27.39 mm
VEGA3 TESCAN
SEM MAG: 307 x
Det: CL
200 µm
View field: 676 µm
Date(m/d/y): 11/01/17
Performance in nanospace


20.1
20.2
SEM HV: 20.0 kV
WD: 27.39 mm
VEGA3 TESCAN
SEM MAG: 321 x
Det: CL
100 µm
View field: 647 µm
Date(m/d/y): 11/01/17
Performance in nanospace

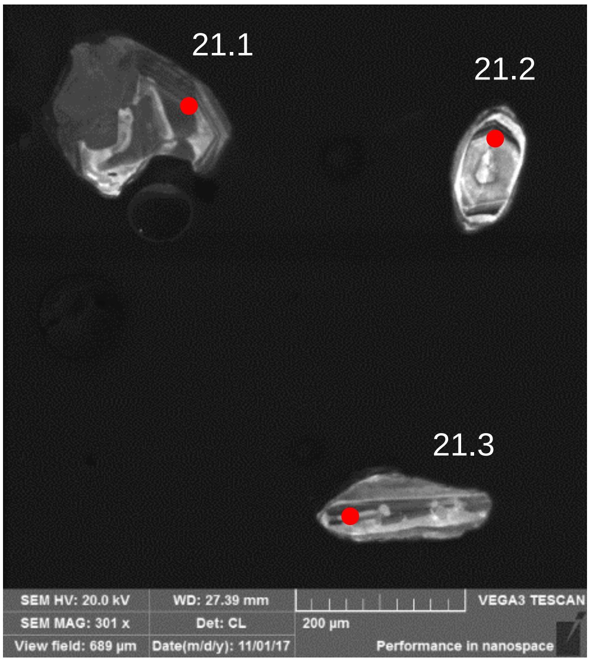
21.1
21.2
21.3
SEM HV: 20.0 kV
WD: 27.39 mm
VEGA3 TESCAN
SEM MAG: 301 x
Det: CL
200 µm
View field: 689 µm
Date(m/d/y): 11/01/17
Performance in nanospace

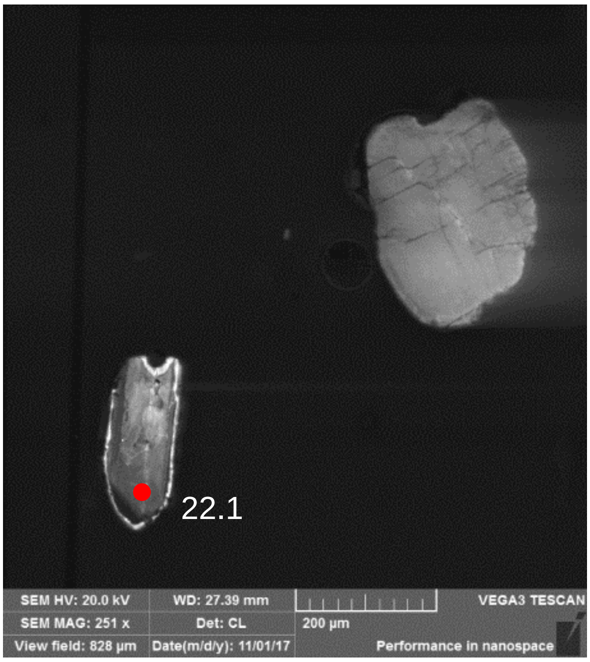
22.1
SEM HV: 20.0 kV
WD: 27.39 mm
VEGA3 TESCAN
SEM MAG: 251 x
Det: CL
200 µm
View field: 828 µm
Date(m/d/y): 11/01/17
Performance in nanospace

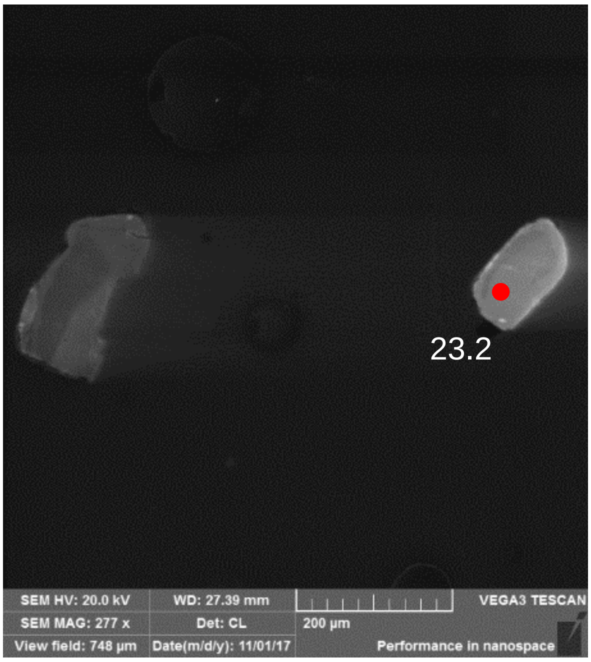
23.2
SEM HV: 20.0 kV
WD: 27.39 mm
VEGA3 TESCAN
SEM MAG: 277 x
Det: CL
200 µm
View field: 748 µm
Date(m/d/y): 11/01/17
Performance in nanospace

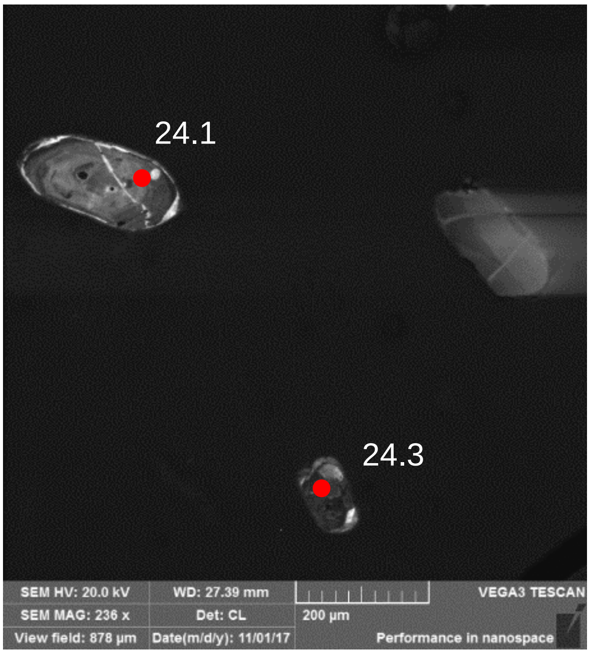
24.1
24.3
SEM HV: 20.0 kV
WD: 27.39 mm
VEGA3 TESCAN
SEM MAG: 236 x
Det: CL
200 µm
View field: 878 µm
Date(m/d/y): 11/01/17
Performance in nanospace

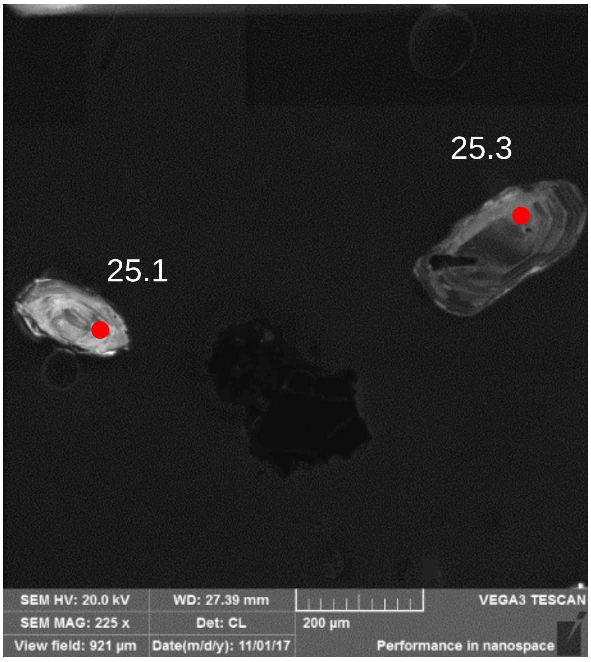
25.3
25.1
SEM HV: 20.0 kV
WD: 27.39 mm
VEGA3 TESCAN
SEM MAG: 225 x
Det: CL
200 µm
View field: 921 µm
Date(m/d/y): 11/01/17
Performance in nanospace

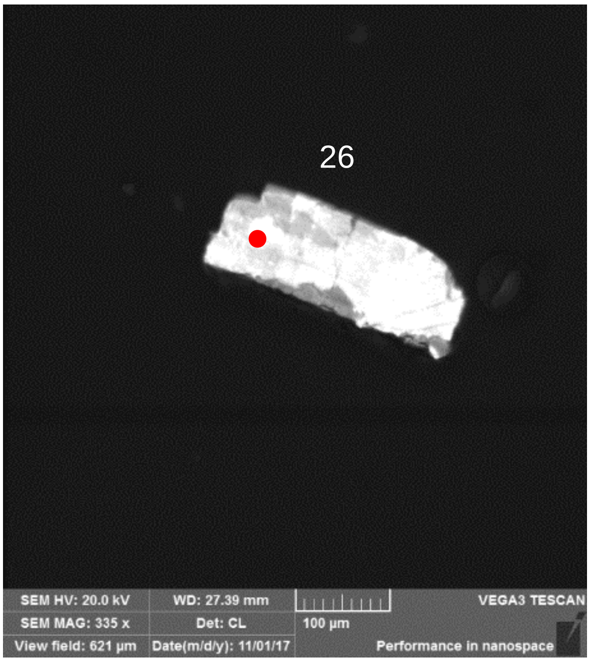
26
SEM HV: 20.0 kV
WD: 27.39 mm
VEGA3 TESCAN
SEM MAG: 335 x
Det: CL
100 µm
View field: 621 µm
Date(m/d/y): 11/01/17
Performance in nanospace

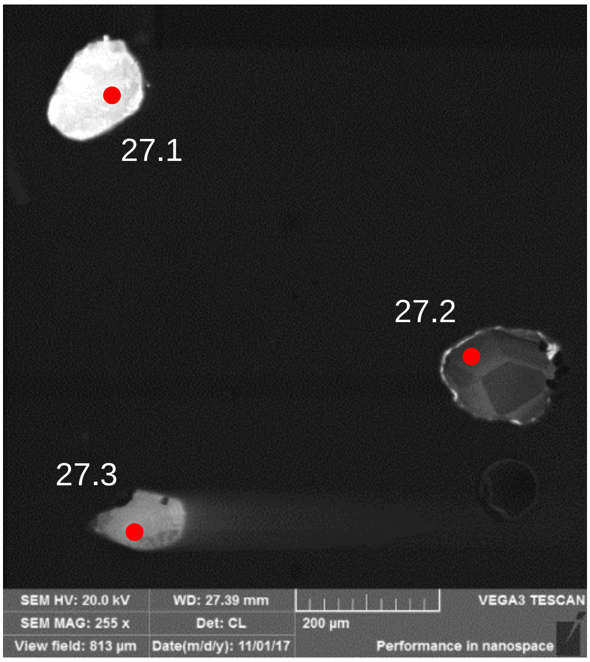
27.1
27.2
27.3
SEM HV: 20.0 kV
WD: 27.39 mm
VEGA3 TESCAN
SEM MAG: 255 x
Det: CL
200 µm
View field: 813 µm
Date(m/d/y): 11/01/17
Performance in nanospace

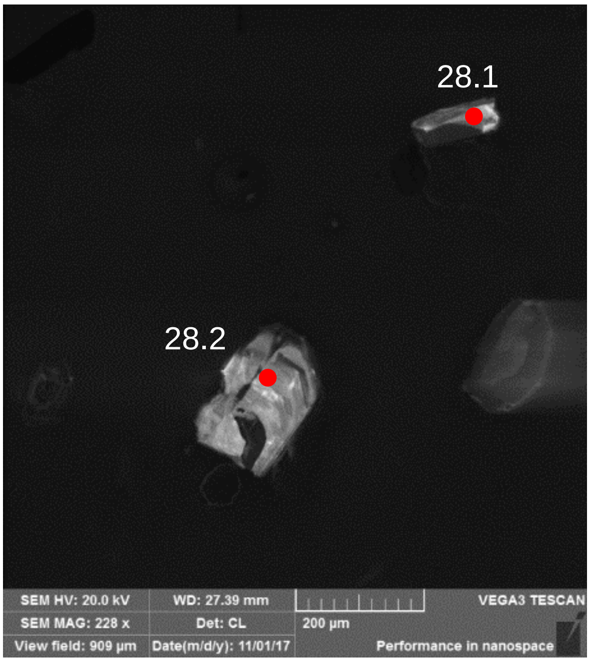
28.1
28.2
SEM HV: 20.0 kV
WD: 27.39 mm
VEGA3 TESCAN
SEM MAG: 228 x
Det: CL
200 µm
View field: 909 µm
Date(m/d/y): 11/01/17
Performance in nanospace

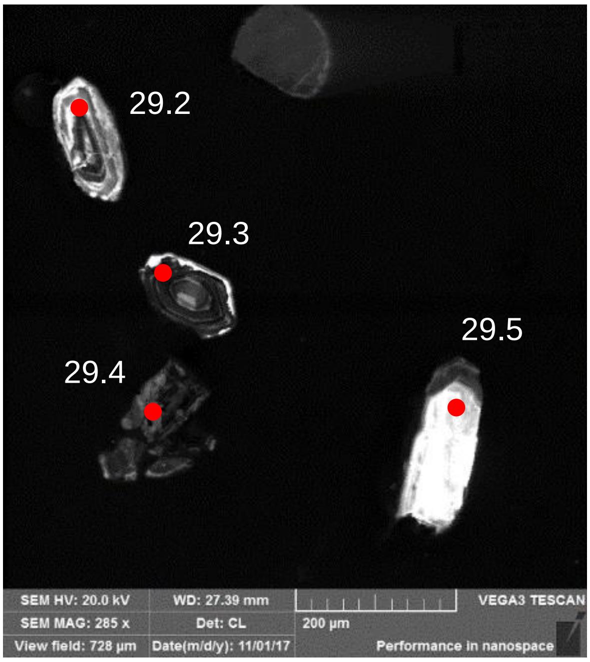
29.2
29.3
29.4
29.5
SEM HV: 20.0 kV
WD: 27.39 mm
VEGA3 TESCAN
SEM MAG: 285 x
Det: CL
200 µm
View field: 728 µm
Date(m/d/y): 11/01/17
Performance in nanospace

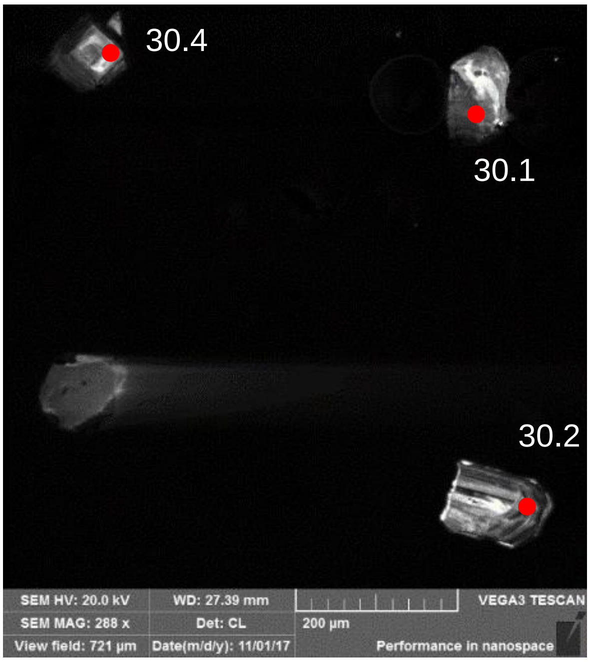
30.4
30.1
30.2
SEM HV: 20.0 kV
WD: 27.39 mm
VEGA3 TESCAN
SEM MAG: 288 x
Det: CL
200 μm
View field: 721 μm
Date(m/d/y): 11/01/17
Performance in nanospace

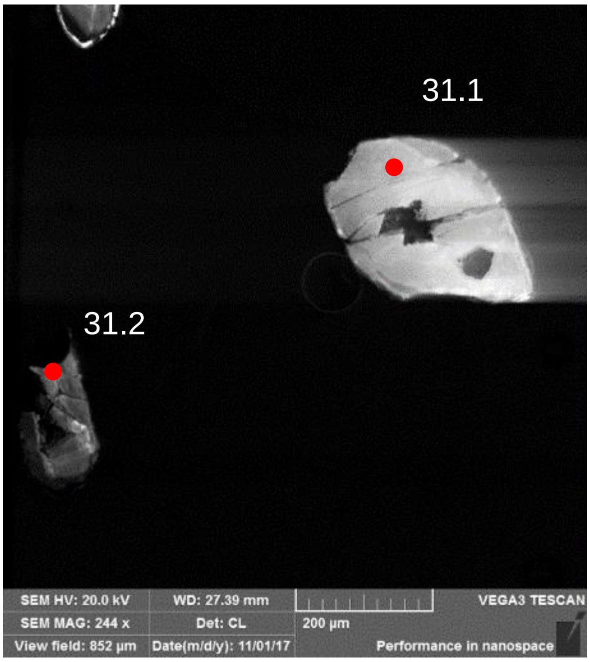
31.1
31.2
SEM HV: 20.0 kV
WD: 27.39 mm
VEGA3 TESCAN
SEM MAG: 244 x
Det: CL
200 μm
View field: 852 μm
Date(m/d/y): 11/01/17
Performance in nanospace

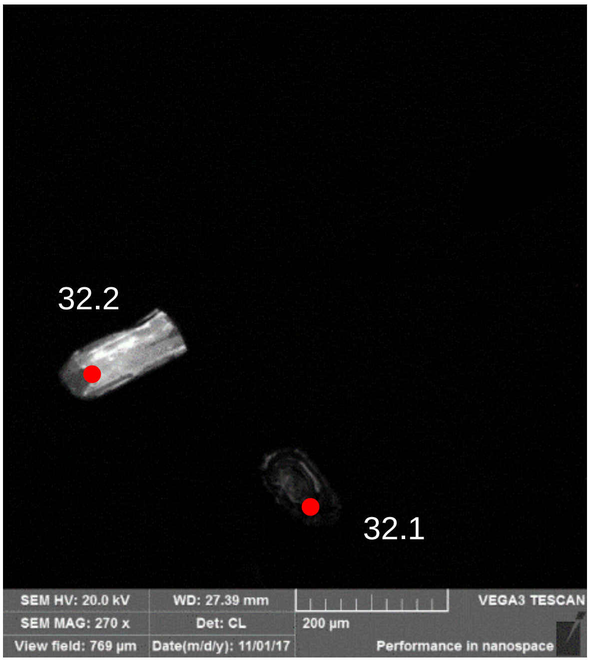
32.2
32.1
SEM HV: 20.0 kV
WD: 27.39 mm
VEGA3 TESCAN
SEM MAG: 270 x
Det: CL
200 μm
View field: 769 μm
Date(m/d/y): 11/01/17
Performance in nanospace

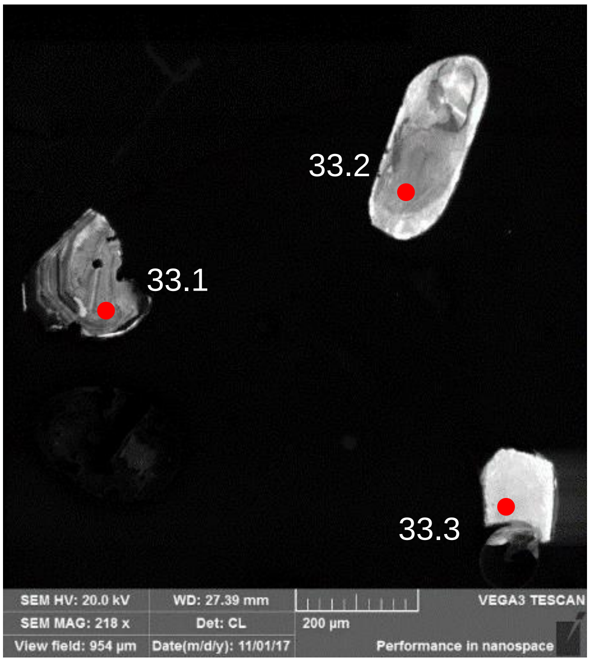
33.2
33.1
33.3
SEM HV: 20.0 kV
WD: 27.39 mm
VEGA3 TESCAN
SEM MAG: 218 x
Det: CL
200 μm
View field: 954 μm
Date(m/d/y): 11/01/17
Performance in nanospace

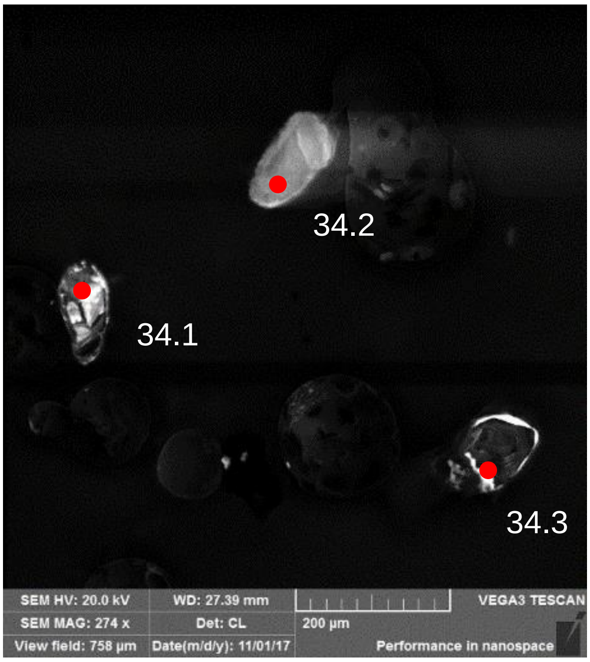
34.2
34.1
34.3
SEM HV: 20.0 kV
WD: 27.39 mm
VEGA3 TESCAN
SEM MAG: 274 x
Det: CL
200 µm
View field: 758 µm
Date(m/d/y): 11/01/17
Performance in nanospace

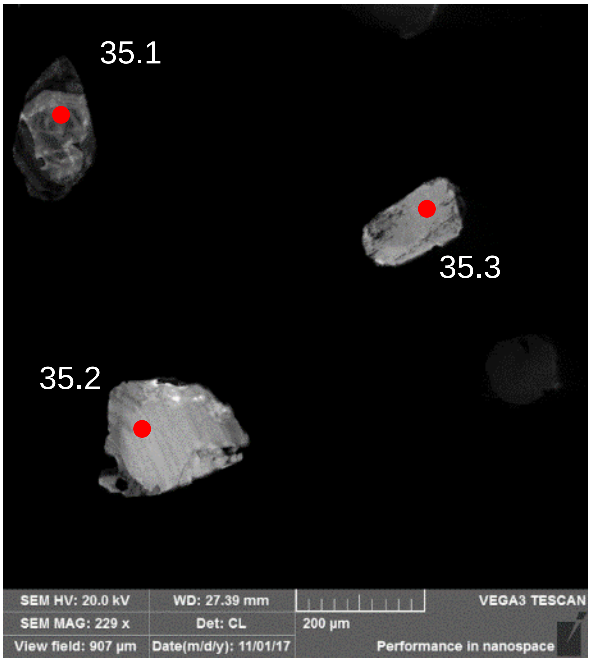
35.1
35.3
35.2
SEM HV: 20.0 kV
WD: 27.39 mm
VEGA3 TESCAN
SEM MAG: 229 x
Det: CL
200 µm
View field: 907 µm
Date(m/d/y): 11/01/17
Performance in nanospace

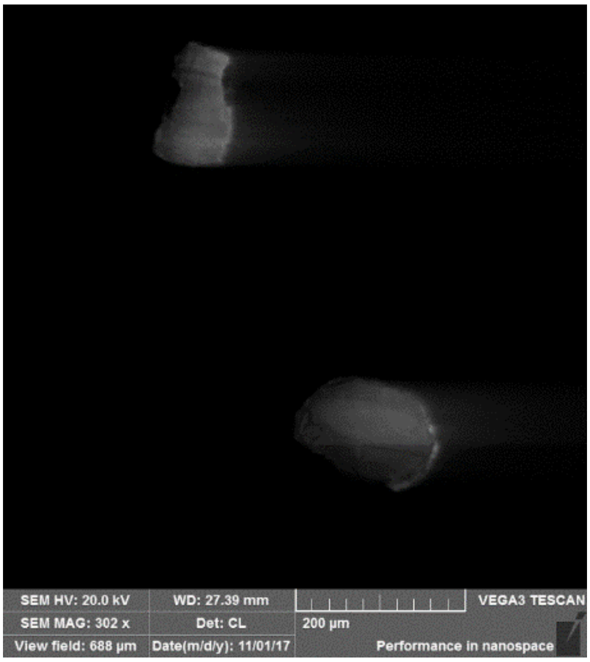
SEM HV: 20.0 kV
WD: 27.39 mm
VEGA3 TESCAN
SEM MAG: 302 x
Det: CL
200 µm
View field: 688 µm
Date(m/d/y): 11/01/17
Performance in nanospace

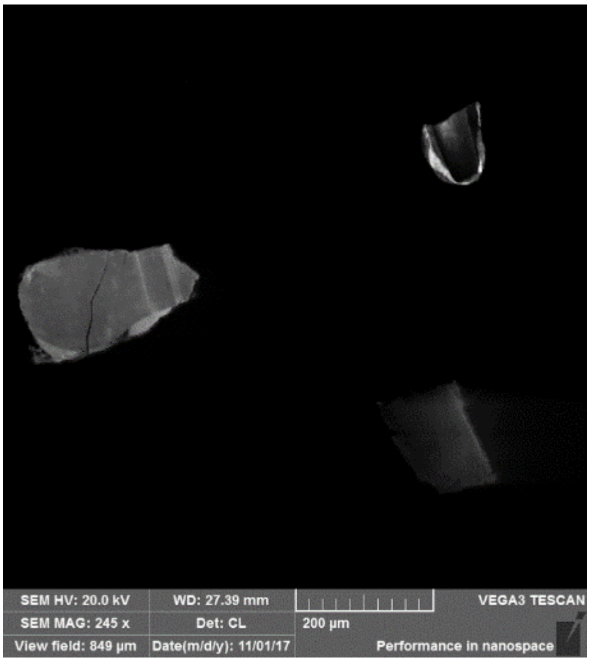
SEM HV: 20.0 kV
WD: 27.39 mm
VEGA3 TESCAN
SEM MAG: 245 x
Det: CL
200 µm
View field: 849 µm
Date(m/d/y): 11/01/17
Performance in nanospace

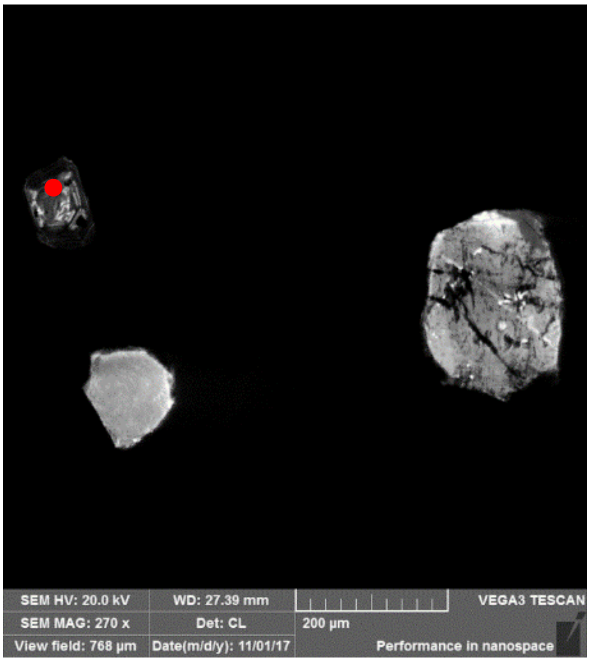
SEM HV: 20.0 kV
WD: 27.39 mm
VEGA3 TESCAN
SEM MAG: 270 x
Det: CL
200 µm
View field: 768 µm
Date(m/d/y): 11/01/17
Performance in nanospace

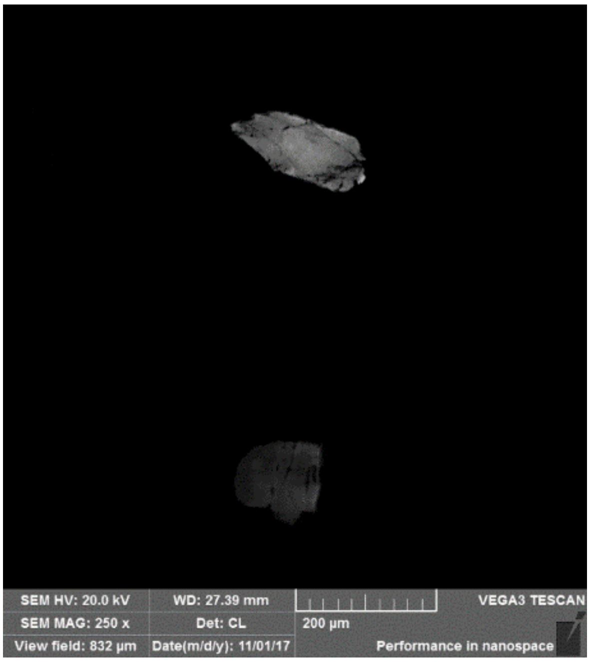
SEM HV: 20.0 kV
WD: 27.39 mm
VEGA3 TESCAN
SEM MAG: 250 x
Det: CL
200 µm
View field: 832 µm
Date(m/d/y): 11/01/17
Performance in nanospace


SEM HV: 20.0 kV
WD: 27.39 mm
VEGA3 TESCAN
SEM MAG: 210 x
Det: CL
200 µm
View field: 988 µm
Date(m/d/y): 11/01/17
Performance in nanospace

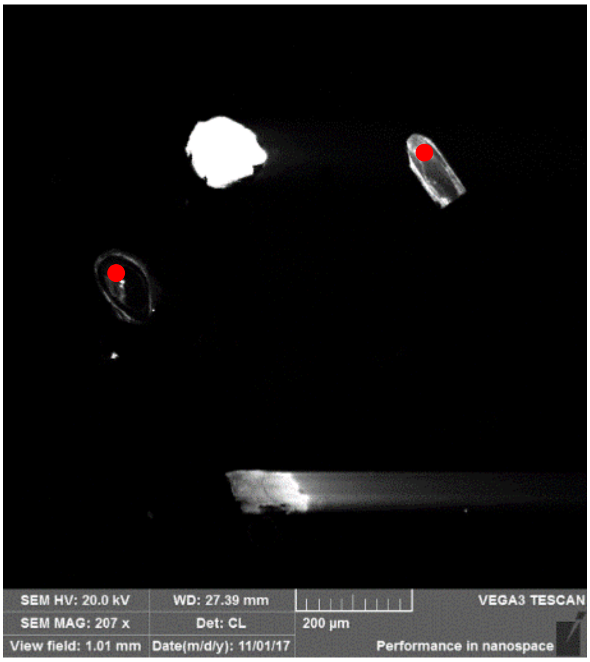
SEM HV: 20.0 kV
WD: 27.39 mm
VEGA3 TESCAN
SEM MAG: 207 x
Det: CL
200 µm
View field: 1.01 mm
Date(m/d/y): 11/01/17
Performance in nanospace

B1775: Cathode luminescence SEM images, red dot indicates ablation position.

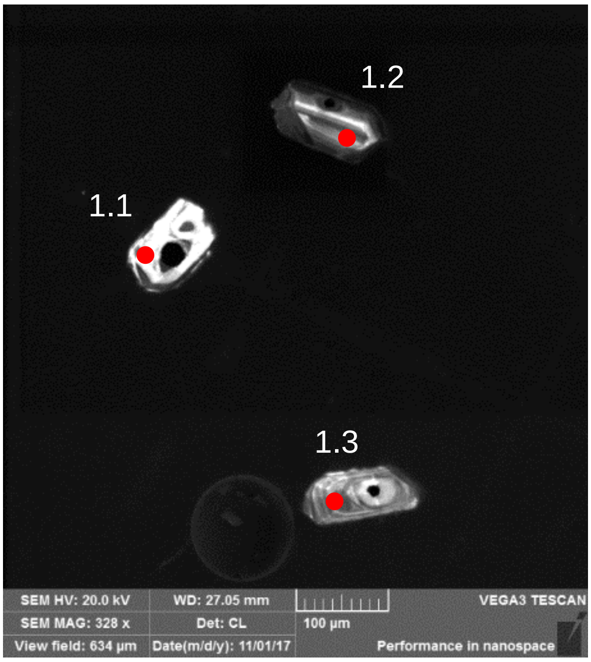

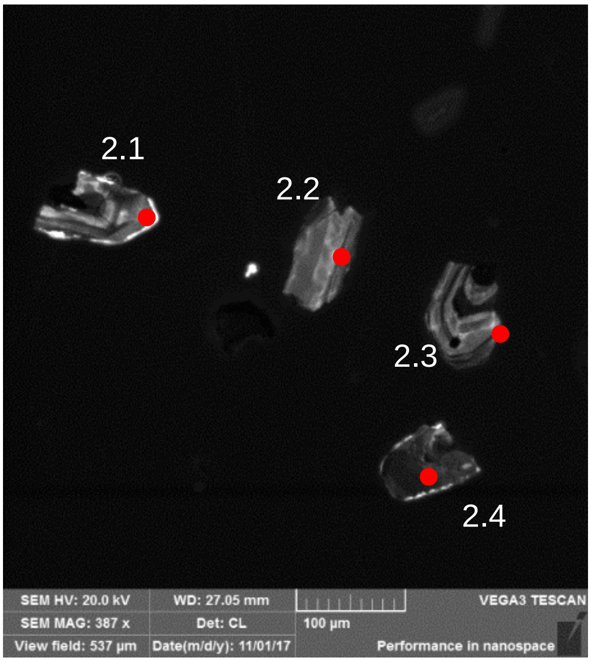

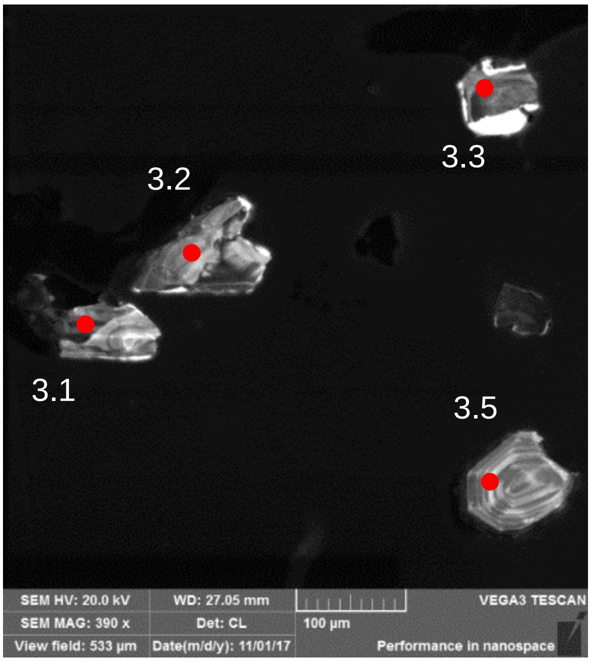

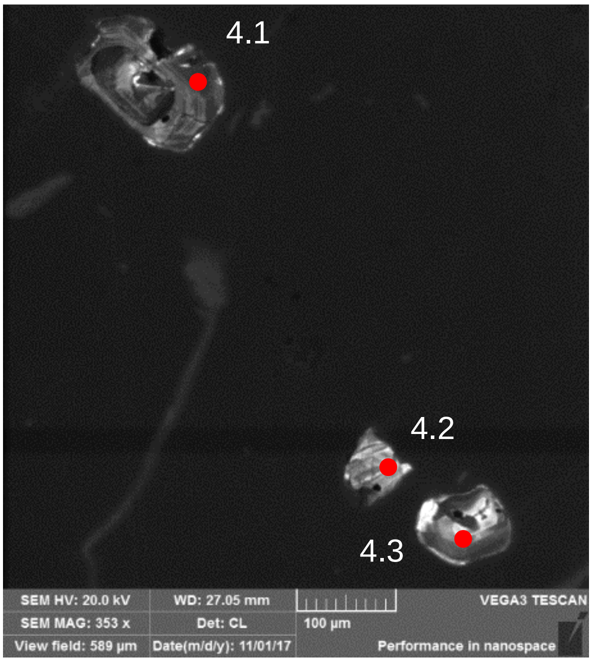

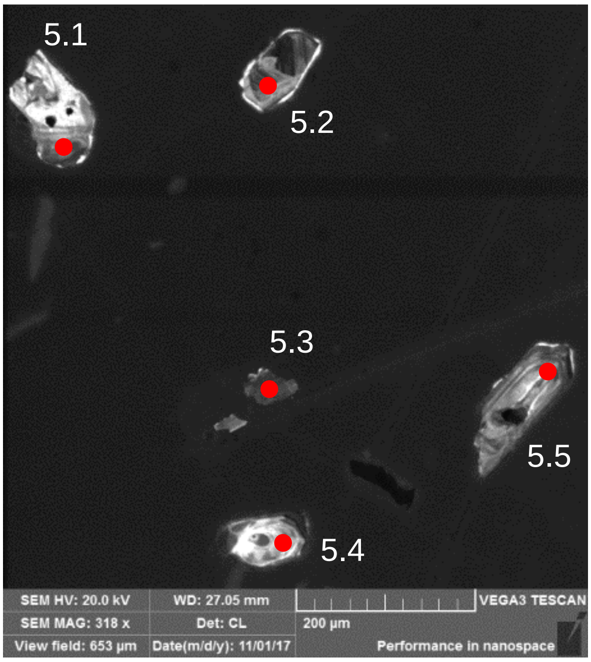
5.1
5.2
5.3
5.5
5.4
SEM HV: 20.0 kV
WD: 27.05 mm
VEGA3 TESCAN
SEM MAG: 318 x
Det: CL
200 µm
View field: 653 µm
Date(m/d/y): 11/01/17
Performance in nanospace

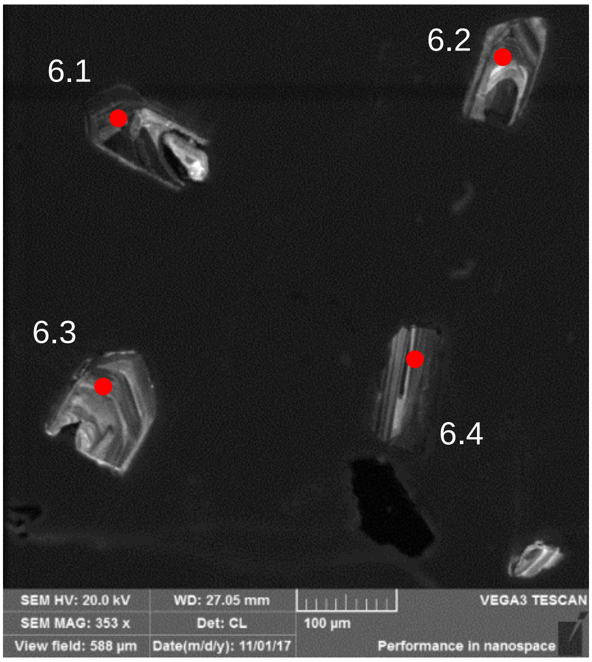
6.2
6.1
6.3
6.4
SEM HV: 20.0 kV
WD: 27.05 mm
VEGA3 TESCAN
SEM MAG: 353 x
Det: CL
100 µm
View field: 588 µm
Date(m/d/y): 11/01/17
Performance in nanospace

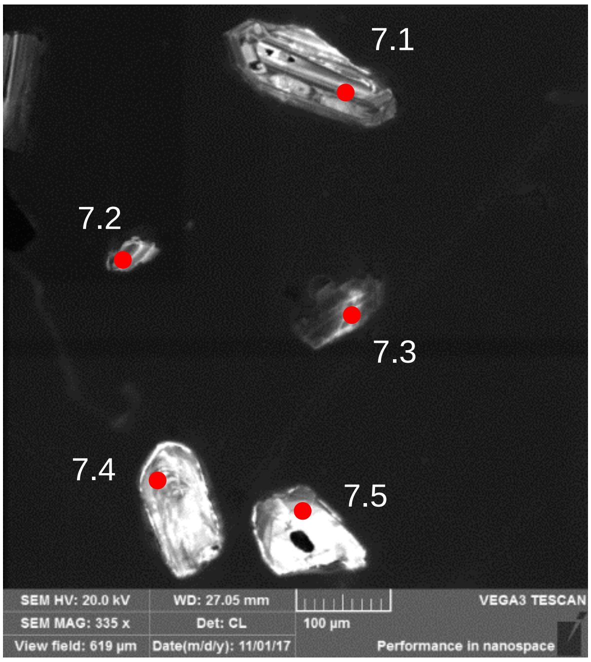
7.1
7.2
7.3
7.4
7.5
SEM HV: 20.0 kV
WD: 27.05 mm
VEGA3 TESCAN
SEM MAG: 335 x
Det: CL
100 µm
View field: 619 µm
Date(m/d/y): 11/01/17
Performance in nanospace

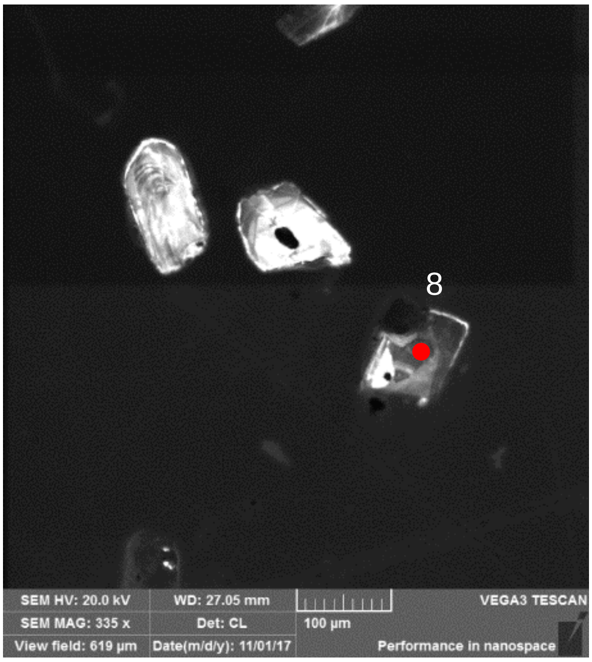
8
SEM HV: 20.0 kV
WD: 27.05 mm
VEGA3 TESCAN
SEM MAG: 335 x
Det: CL
100 µm
View field: 619 µm
Date(m/d/y): 11/01/17
Performance in nanospace

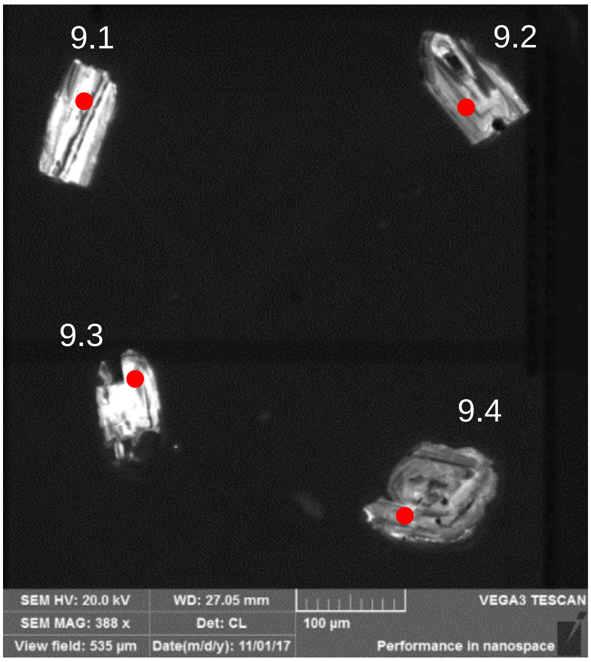
9.1
9.2
9.3
9.4
SEM HV: 20.0 kV
WD: 27.05 mm
VEGA3 TESCAN
SEM MAG: 388 x
Det: CL
100 µm
View field: 535 µm
Date(m/d/y): 11/01/17
Performance in nanospace

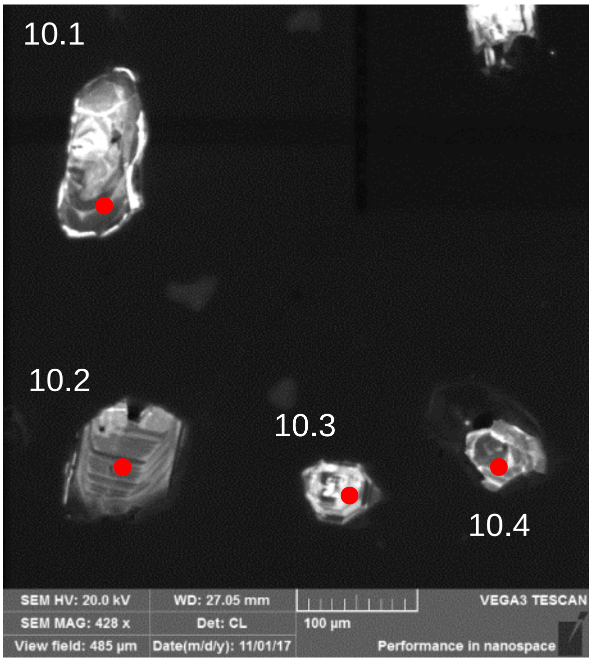
10.1
10.2
10.3
10.4
SEM HV: 20.0 kV
WD: 27.05 mm
VEGA3 TESCAN
SEM MAG: 428 x
Det: CL
100 µm
View field: 485 µm
Date(m/d/y): 11/01/17
Performance in nanospace

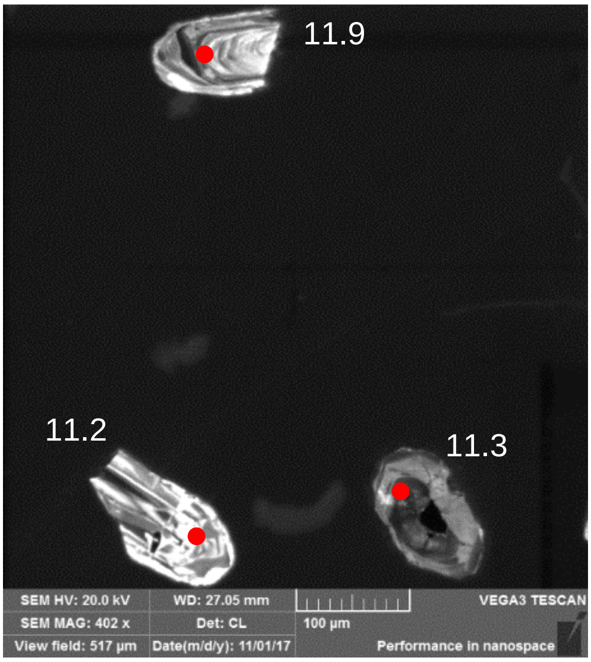
11.9
11.2
11.3
SEM HV: 20.0 kV
WD: 27.05 mm
VEGA3 TESCAN
SEM MAG: 402 x
Det: CL
100 µm
View field: 517 µm
Date(m/d/y): 11/01/17
Performance in nanospace

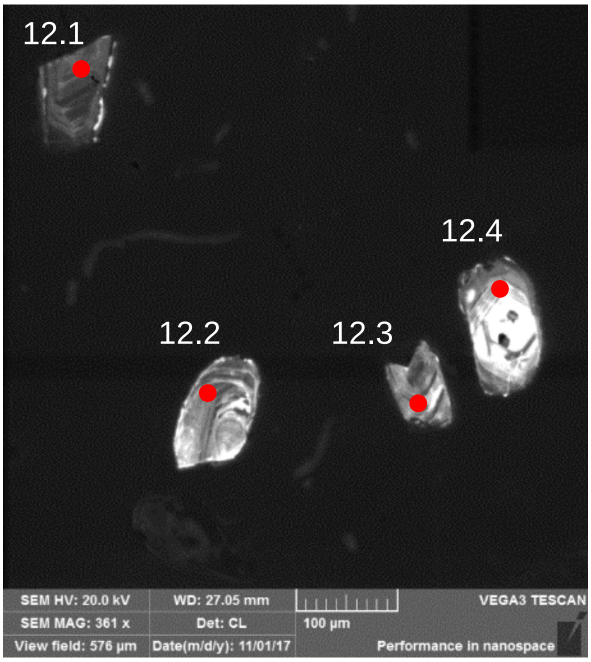
12.1
12.4
12.2
12.3
SEM HV: 20.0 kV
WD: 27.05 mm
VEGA3 TESCAN
SEM MAG: 361 x
Det: CL
100 µm
View field: 576 µm
Date(m/d/y): 11/01/17
Performance in nanospace

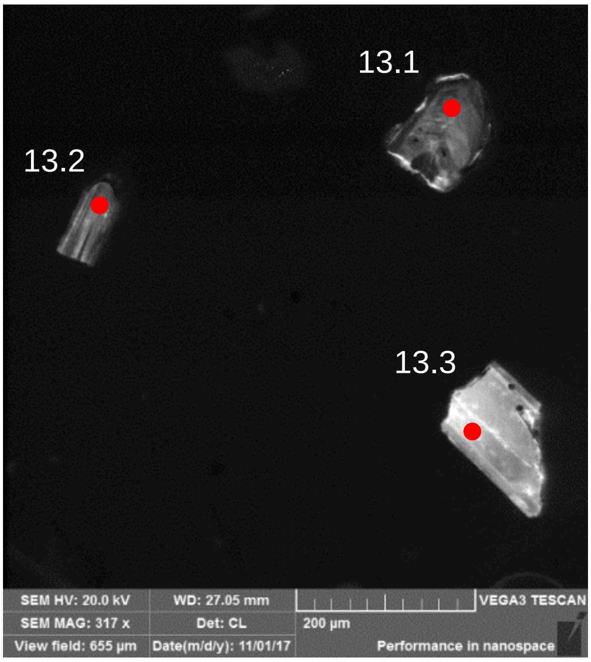
13.1
13.2
13.3
SEM HV: 20.0 kV
WD: 27.05 mm
VEGA3 TESCAN
SEM MAG: 317 x
Det: CL
200 µm
View field: 655 µm
Date(m/d/y): 11/01/17
Performance in nanospace

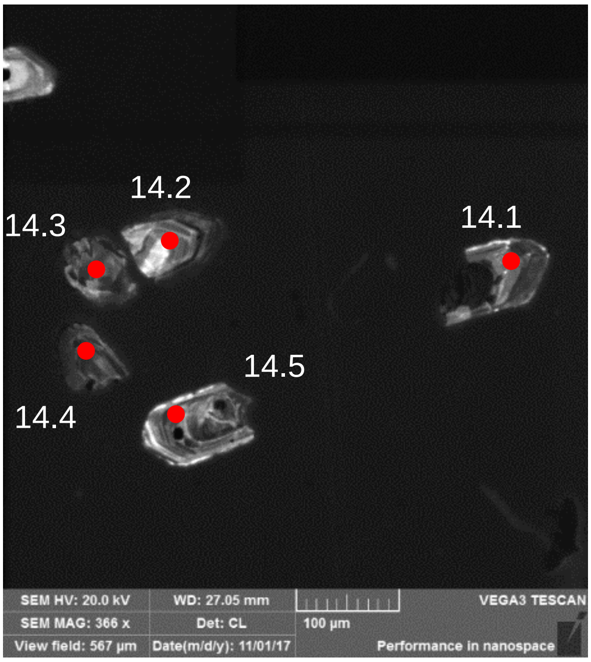
14.2
14.3
14.1
14.5
14.4
SEM HV: 20.0 kV
WD: 27.05 mm
VEGA3 TESCAN
SEM MAG: 366 x
Det: CL
100 µm
View field: 567 µm
Date(m/d/y): 11/01/17
Performance in nanospace

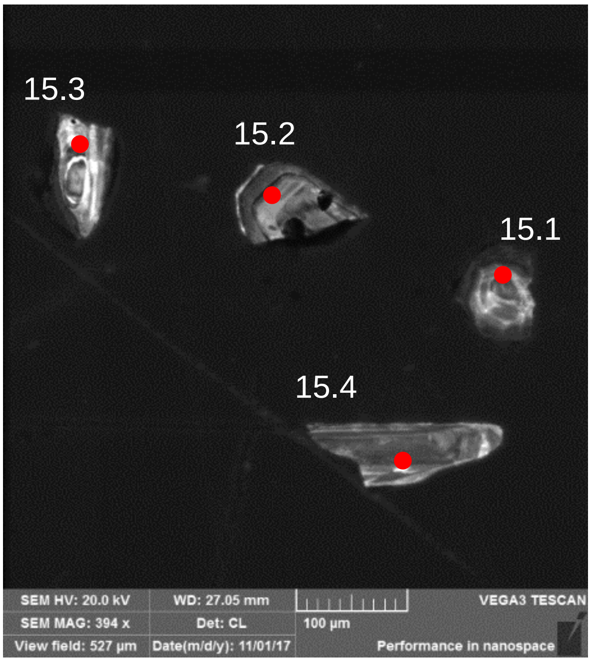
15.3
15.2
15.1
15.4
SEM HV: 20.0 kV
WD: 27.05 mm
VEGA3 TESCAN
SEM MAG: 394 x
Det: CL
100 µm
View field: 527 µm
Date(m/d/y): 11/01/17
Performance in nanospace

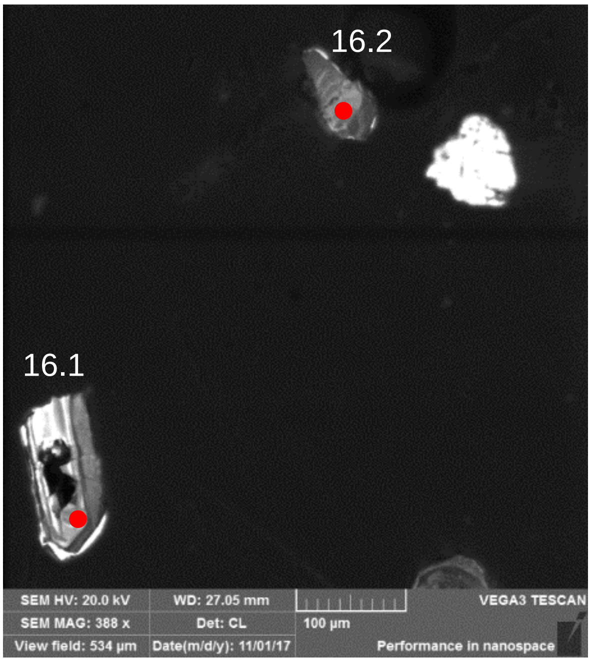
16.2
16.1
SEM HV: 20.0 kV
WD: 27.05 mm
VEGA3 TESCAN
SEM MAG: 388 x
Det: CL
100 µm
View field: 534 µm
Date(m/d/y): 11/01/17
Performance in nanospace

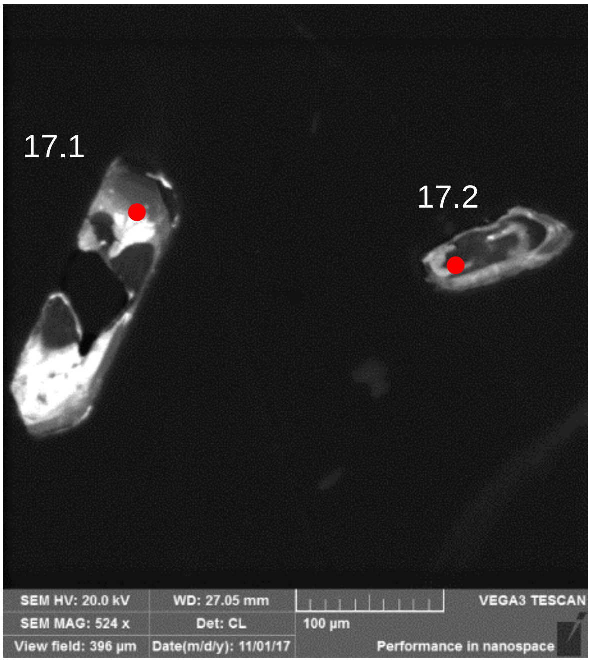
17.1
17.2
SEM HV: 20.0 kV
WD: 27.05 mm
VEGA3 TESCAN
SEM MAG: 524 x
Det: CL
100 µm
View field: 396 µm
Date(m/d/y): 11/01/17
Performance in nanospace

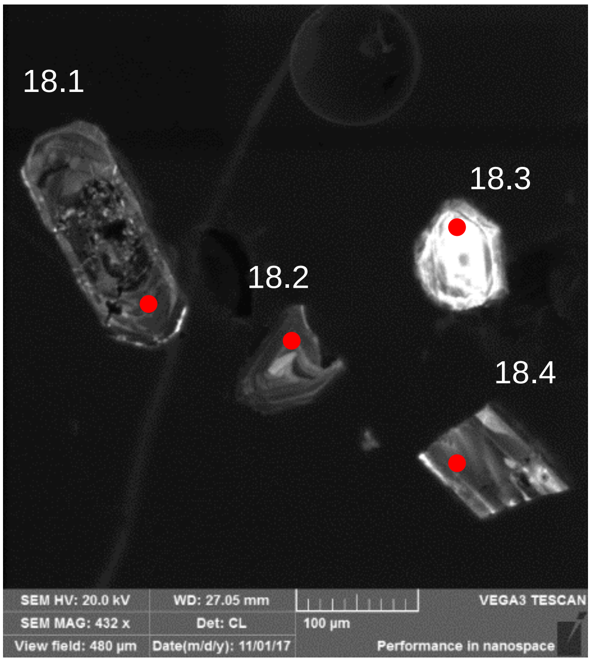
18.1
18.2
18.3
18.4
SEM HV: 20.0 kV
WD: 27.05 mm
VEGA3 TESCAN
SEM MAG: 432 x
Det: CL
100 µm
View field: 480 µm
Date(m/d/y): 11/01/17
Performance in nanospace

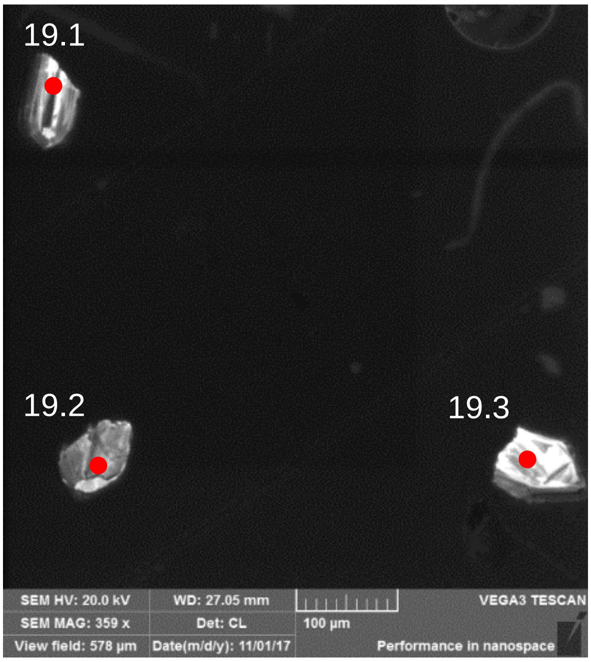
19.1
19.2
19.3
SEM HV: 20.0 kV
WD: 27.05 mm
VEGA3 TESCAN
SEM MAG: 359 x
Det: CL
100 µm
View field: 578 µm
Date(m/d/y): 11/01/17
Performance in nanospace

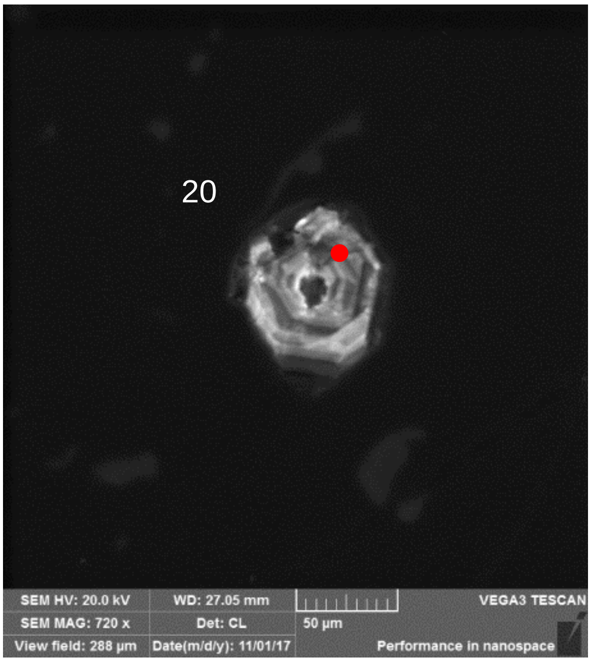
20
SEM HV: 20.0 kV
WD: 27.05 mm
VEGA3 TESCAN
SEM MAG: 720 x
Det: CL
50 µm
View field: 288 µm
Date(m/d/y): 11/01/17
Performance in nanospace

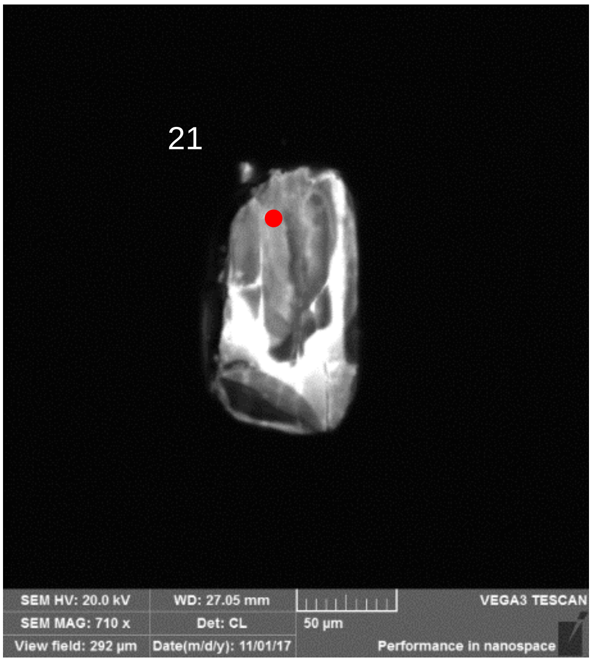
21
SEM HV: 20.0 kV
WD: 27.05 mm
VEGA3 TESCAN
SEM MAG: 710 x
Det: CL
50 µm
View field: 292 µm
Date(m/d/y): 11/01/17
Performance in nanospace

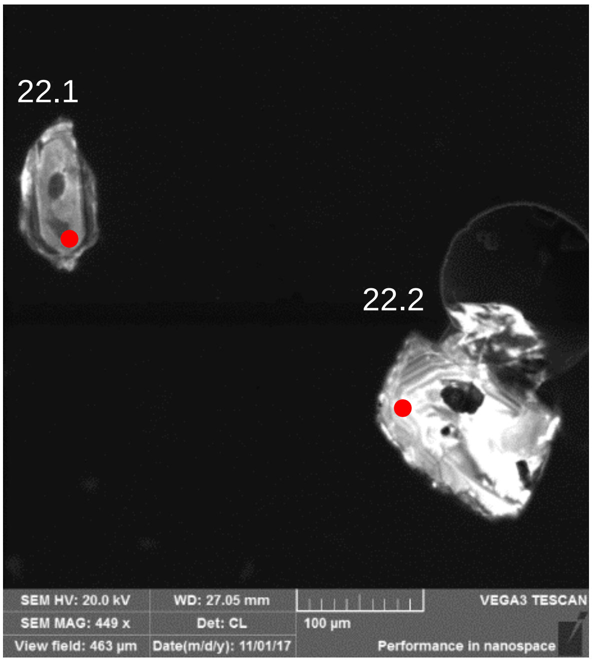
22.1
22.2
SEM HV: 20.0 kV
WD: 27.05 mm
VEGA3 TESCAN
SEM MAG: 449 x
Det: CL
100 µm
View field: 463 µm
Date(m/d/y): 11/01/17
Performance in nanospace

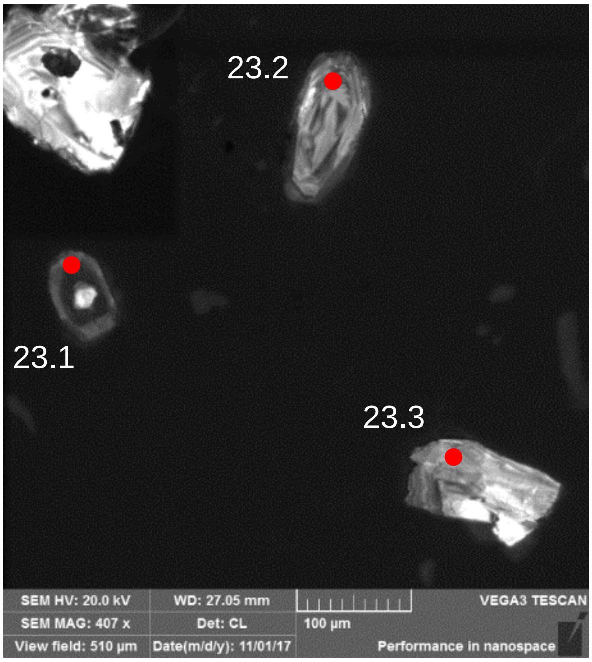
23.2
23.1
23.3
SEM HV: 20.0 kV
WD: 27.05 mm
VEGA3 TESCAN
SEM MAG: 407 x
Det: CL
100 µm
View field: 510 µm
Date(m/d/y): 11/01/17
Performance in nanospace

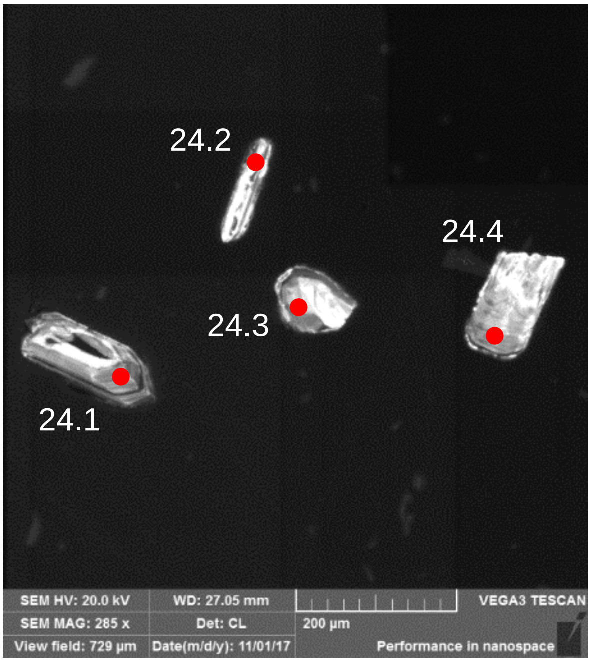
24.2
24.4
24.3
24.1
SEM HV: 20.0 kV
WD: 27.05 mm
VEGA3 TESCAN
SEM MAG: 285 x
Det: CL
200 µm
View field: 729 µm
Date(m/d/y): 11/01/17
Performance in nanospace

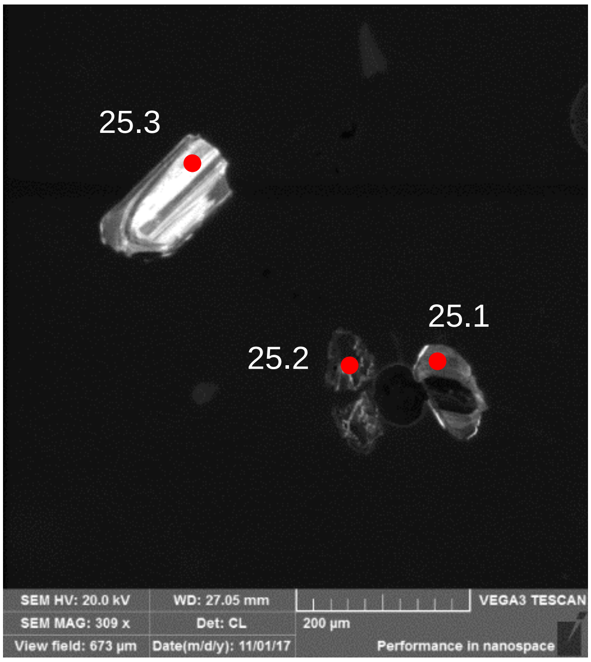
25.3
25.2
25.1
SEM HV: 20.0 kV
WD: 27.05 mm
VEGA3 TESCAN
SEM MAG: 309 x
Det: CL
200 µm
View field: 673 µm
Date(m/d/y): 11/01/17
Performance in nanospace

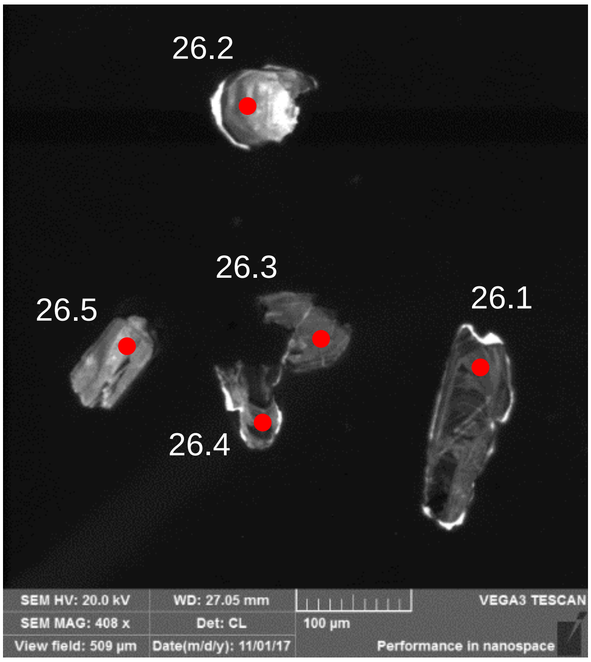
26.2
26.3
26.5
26.1
26.4
SEM HV: 20.0 kV
WD: 27.05 mm
VEGA3 TESCAN
SEM MAG: 408 x
Det: CL
100 µm
View field: 509 µm
Date(m/d/y): 11/01/17
Performance in nanospace

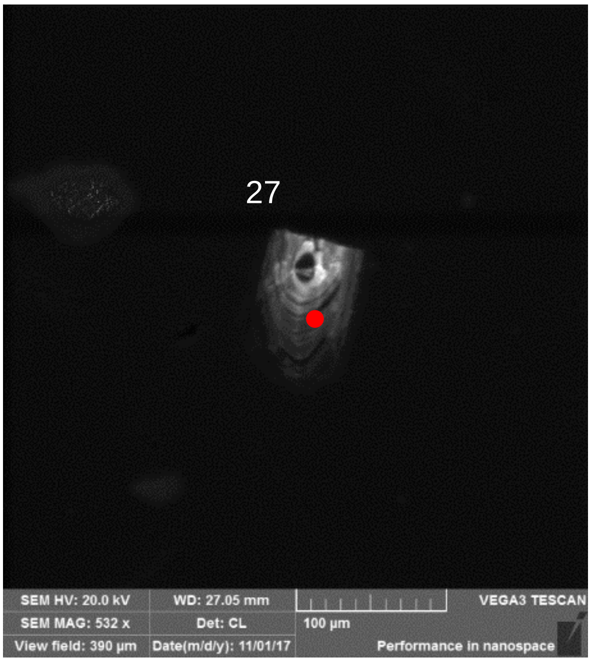
27
SEM HV: 20.0 kV
WD: 27.05 mm
VEGA3 TESCAN
SEM MAG: 532 x
Det: CL
100 µm
View field: 390 µm
Date(m/d/y): 11/01/17
Performance in nanospace

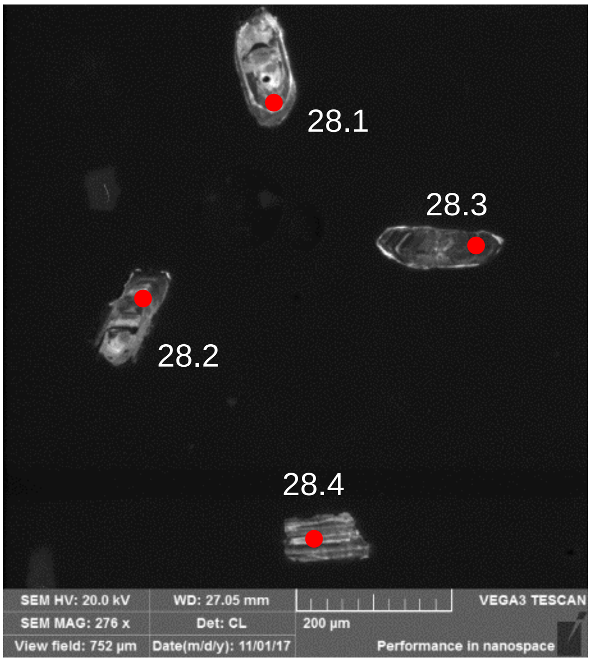
28.1
28.3
28.2
28.4
SEM HV: 20.0 kV
WD: 27.05 mm
VEGA3 TESCAN
SEM MAG: 276 x
Det: CL
200 µm
View field: 752 µm
Date(m/d/y): 11/01/17
Performance in nanospace

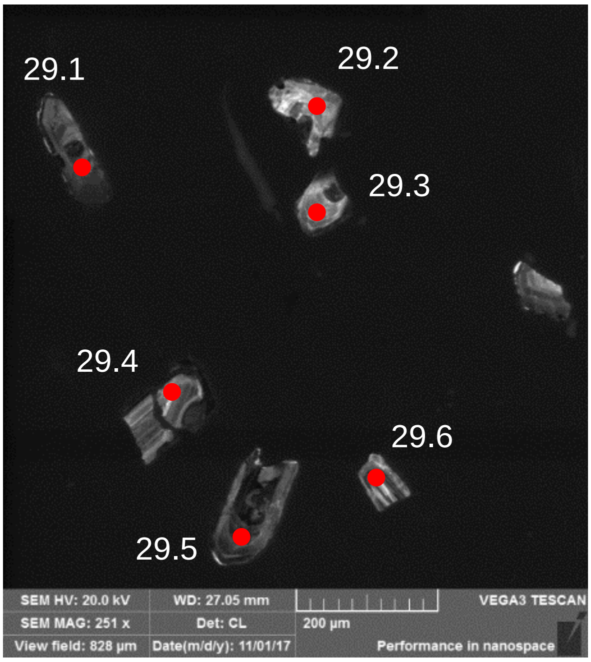
29.1
29.2
29.3
29.4
29.5
29.6
SEM HV: 20.0 kV
WD: 27.05 mm
VEGA3 TESCAN
SEM MAG: 251 x
Det: CL
200 µm
View field: 828 µm
Date(m/d/y): 11/01/17
Performance in nanospace

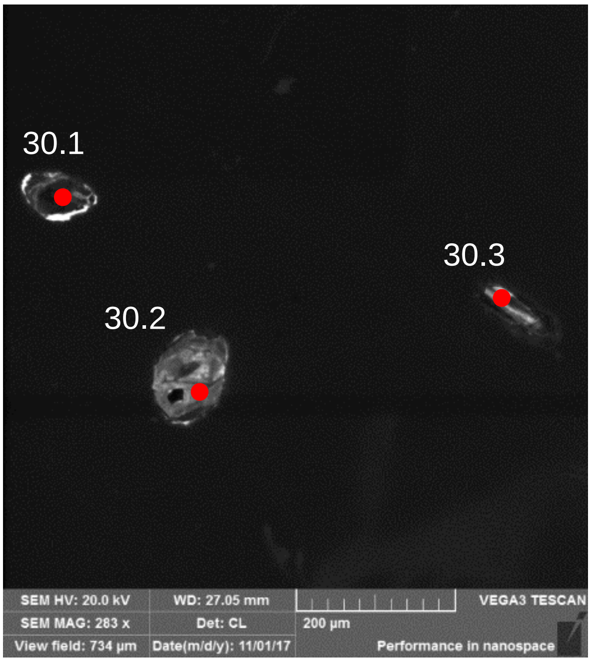
30.1
30.2
30.3
SEM HV: 20.0 kV
WD: 27.05 mm
VEGA3 TESCAN
SEM MAG: 283 x
Det: CL
200 µm
View field: 734 µm
Date(m/d/y): 11/01/17
Performance in nanospace

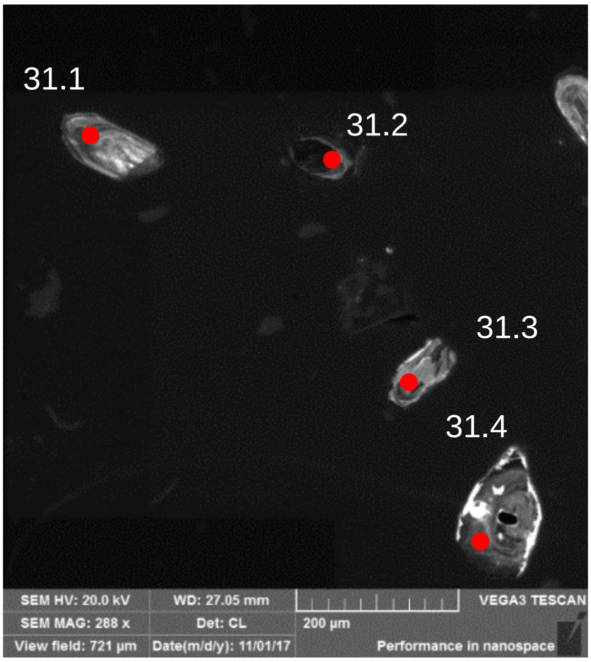
31.1
31.2
31.3
31.4
SEM HV: 20.0 kV
WD: 27.05 mm
VEGA3 TESCAN
SEM MAG: 288 x
Det: CL
200 µm
View field: 721 µm
Date(m/d/y): 11/01/17
Performance in nanospace

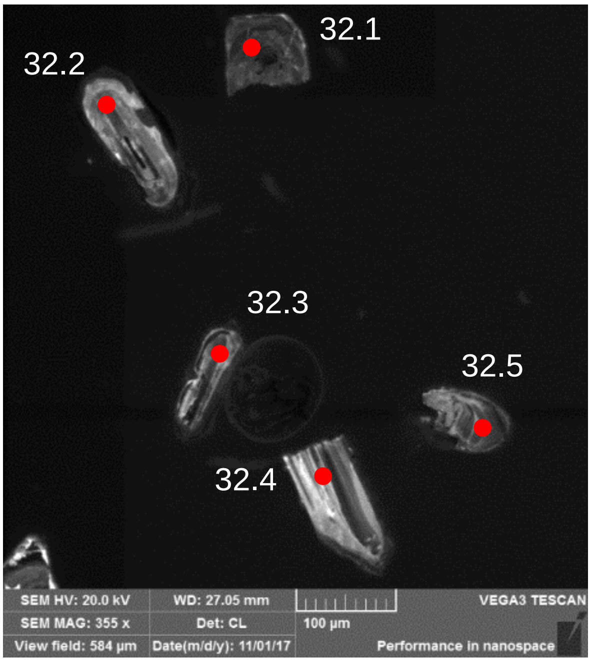
32.1
32.2
32.3
32.4
32.5
SEM HV: 20.0 kV
WD: 27.05 mm
VEGA3 TESCAN
SEM MAG: 355 x
Det: CL
100 µm
View field: 584 µm
Date(m/d/y): 11/01/17
Performance in nanospace

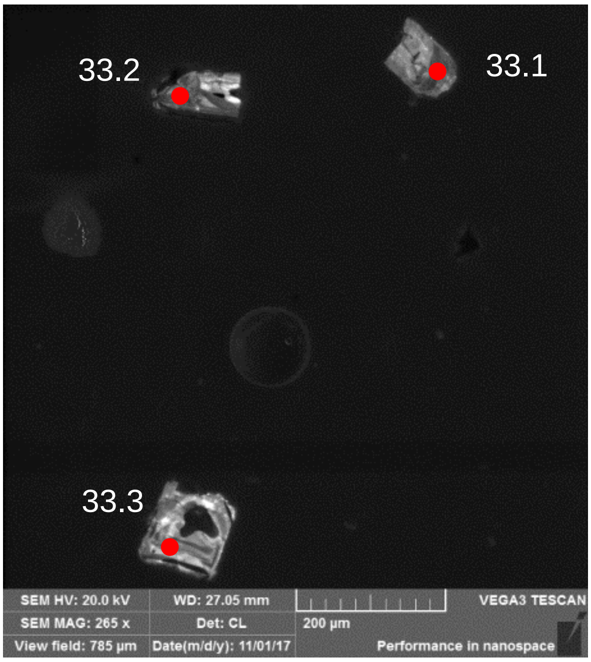
33.2
33.1
33.3
SEM HV: 20.0 kV
WD: 27.05 mm
VEGA3 TESCAN
SEM MAG: 265 x
Det: CL
200 µm
View field: 785 µm
Date(m/d/y): 11/01/17
Performance in nanospace

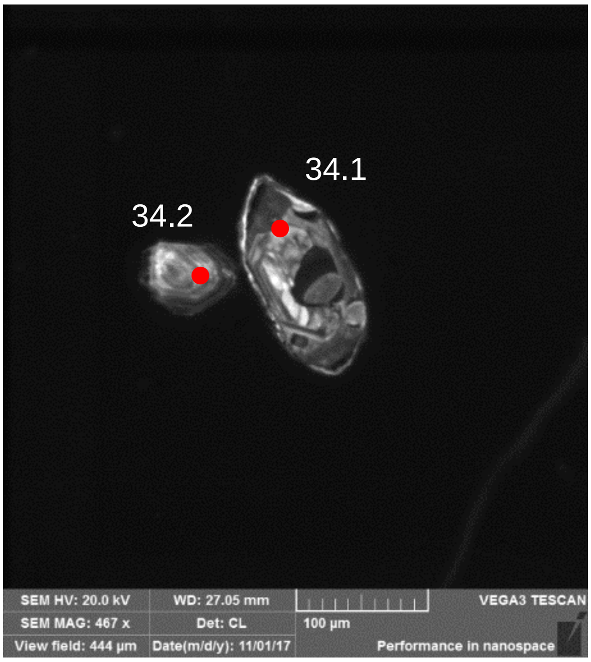
34.1
34.2
SEM HV: 20.0 kV
WD: 27.05 mm
VEGA3 TESCAN
SEM MAG: 467 x
Det: CL
100 µm
View field: 444 µm
Date(m/d/y): 11/01/17
Performance in nanospace

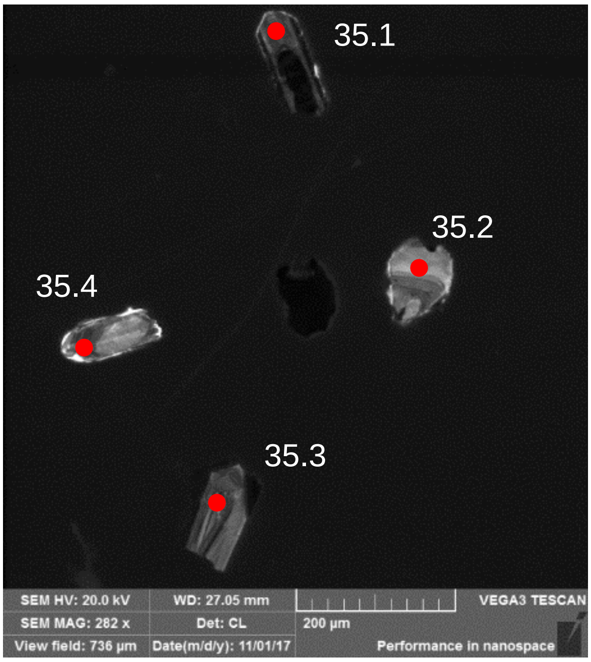
35.1
35.2
35.4
35.3
SEM HV: 20.0 kV
WD: 27.05 mm
VEGA3 TESCAN
SEM MAG: 282 x
Det: CL
200 µm
View field: 736 µm
Date(m/d/y): 11/01/17
Performance in nanospace

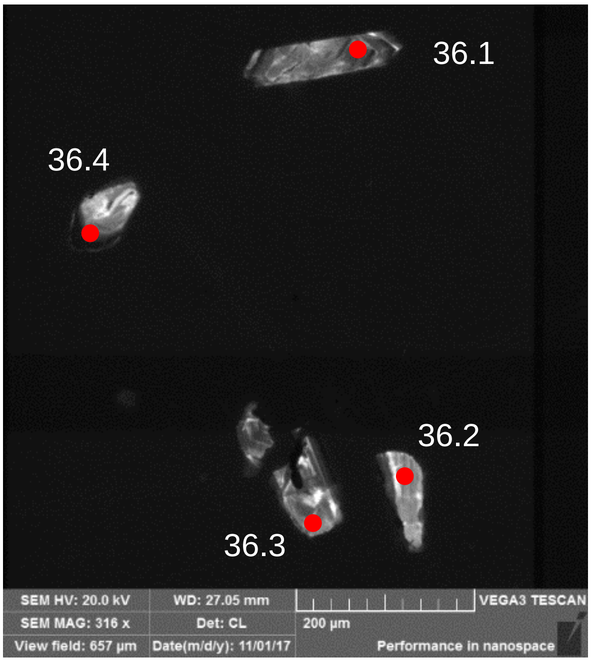
36.1
36.4
36.2
36.3
SEM HV: 20.0 kV
WD: 27.05 mm
VEGA3 TESCAN
SEM MAG: 316 x
Det: CL
200 µm
View field: 657 µm
Date(m/d/y): 11/01/17
Performance in nanospace

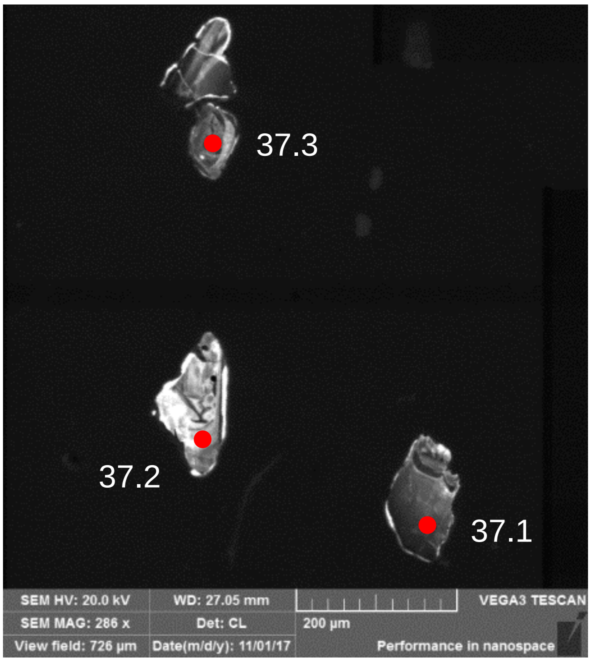
37.3
37.2
37.1
SEM HV: 20.0 kV
WD: 27.05 mm
VEGA3 TESCAN
SEM MAG: 286 x
Det: CL
200 µm
View field: 726 µm
Date(m/d/y): 11/01/17
Performance in nanospace

B1778: Cathode luminescence SEM images, red dot indicates ablation position.

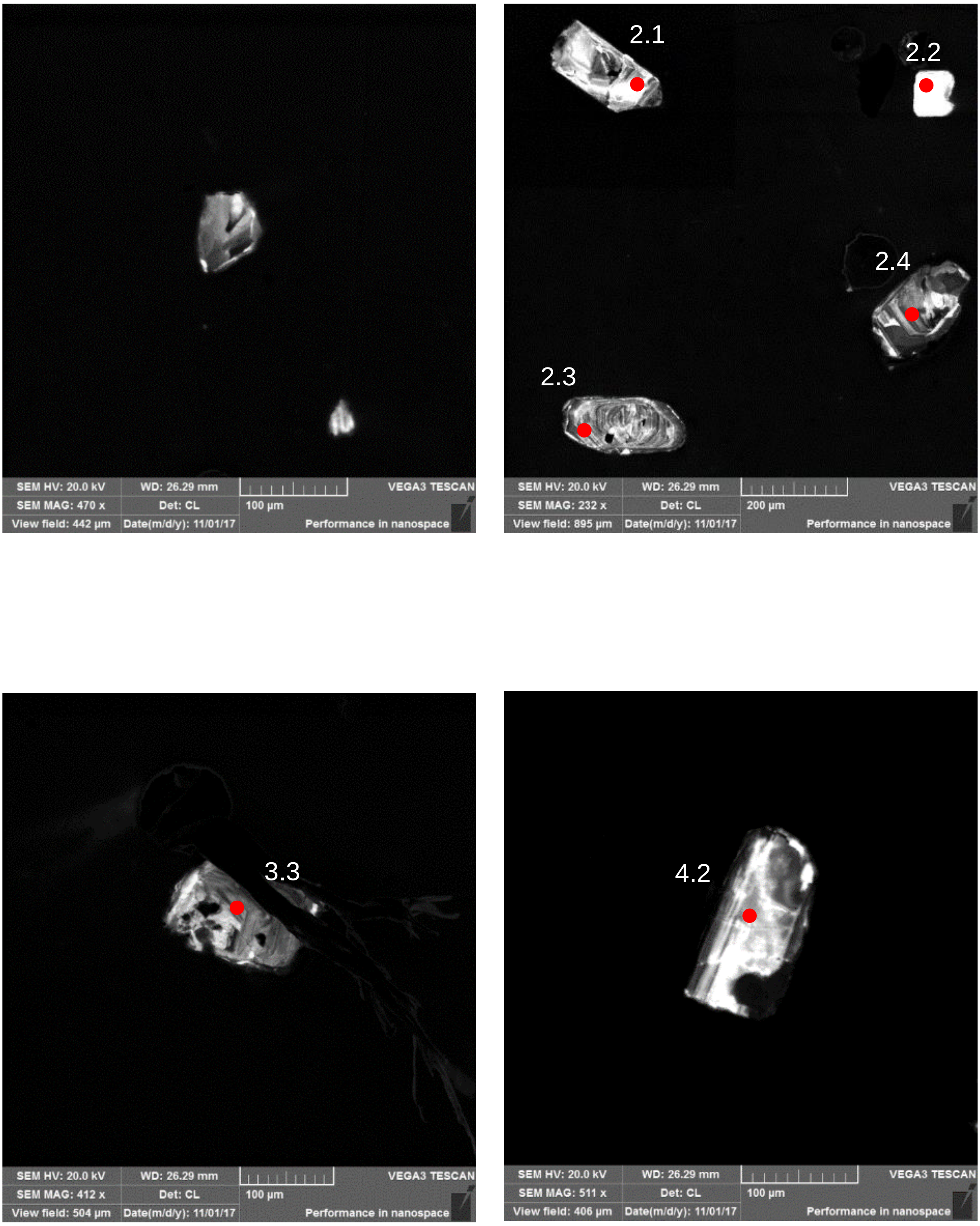

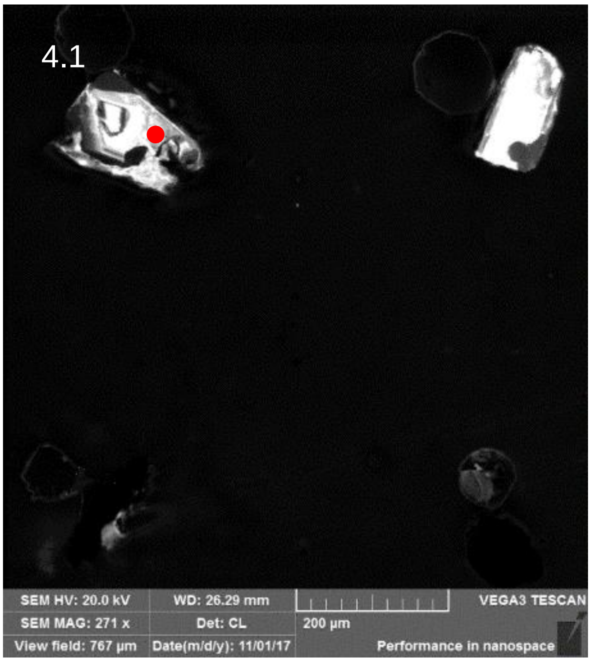
4.1
SEM HV: 20.0 kV
WD: 26.29 mm
VEGA3 TESCAN
SEM MAG: 271 x
Det: CL
200 µm
View field: 767 µm
Date(m/d/y): 11/01/17
Performance in nanospace

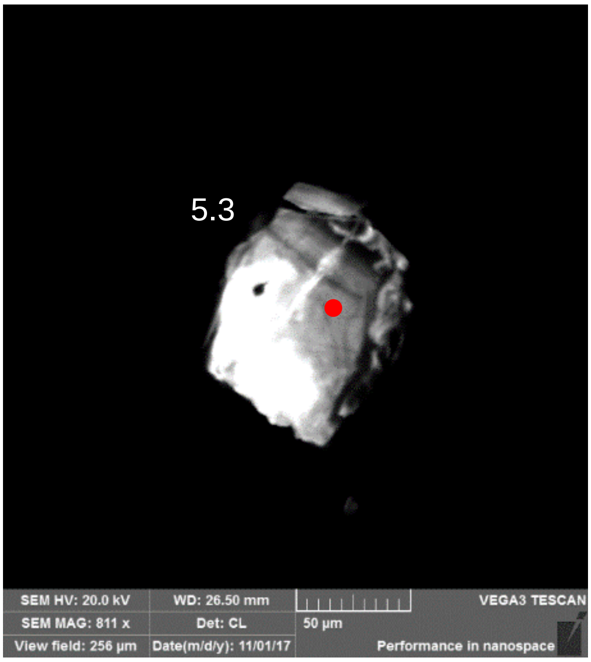
5.3
SEM HV: 20.0 kV
WD: 26.50 mm
VEGA3 TESCAN
SEM MAG: 811 x
Det: CL
50 µm
View field: 256 µm
Date(m/d/y): 11/01/17
Performance in nanospace

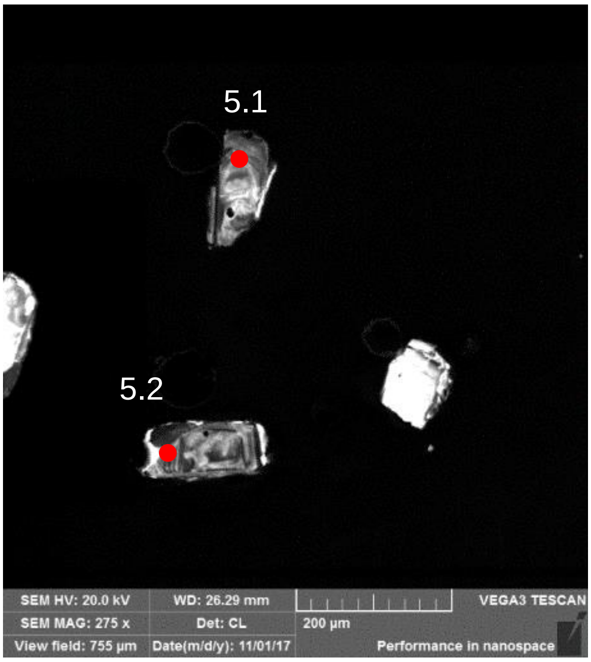
5.1
5.2
SEM HV: 20.0 kV
WD: 26.29 mm
VEGA3 TESCAN
SEM MAG: 275 x
Det: CL
200 µm
View field: 755 µm
Date(m/d/y): 11/01/17
Performance in nanospace

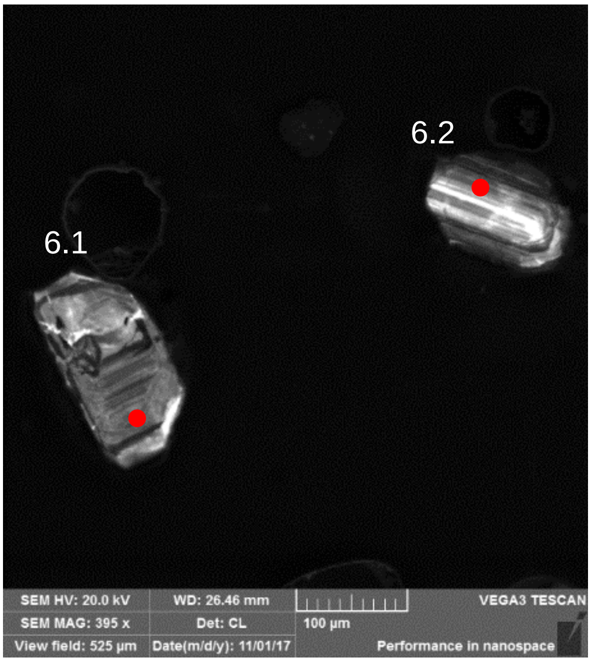
6.2
6.1
SEM HV: 20.0 kV
WD: 26.46 mm
VEGA3 TESCAN
SEM MAG: 395 x
Det: CL
100 µm
View field: 525 µm
Date(m/d/y): 11/01/17
Performance in nanospace

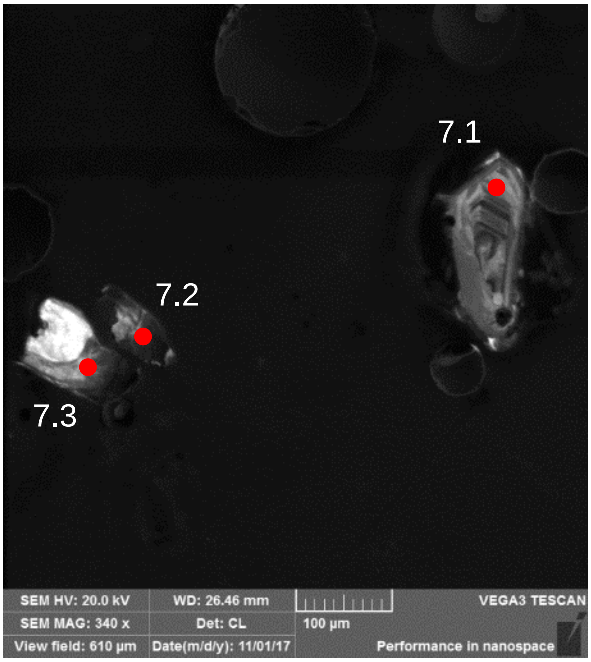
7.1
7.2
7.3
SEM HV: 20.0 kV
WD: 26.46 mm
VEGA3 TESCAN
SEM MAG: 340 x
Det: CL
100 µm
View field: 610 µm
Date(m/d/y): 11/01/17
Performance in nanospace

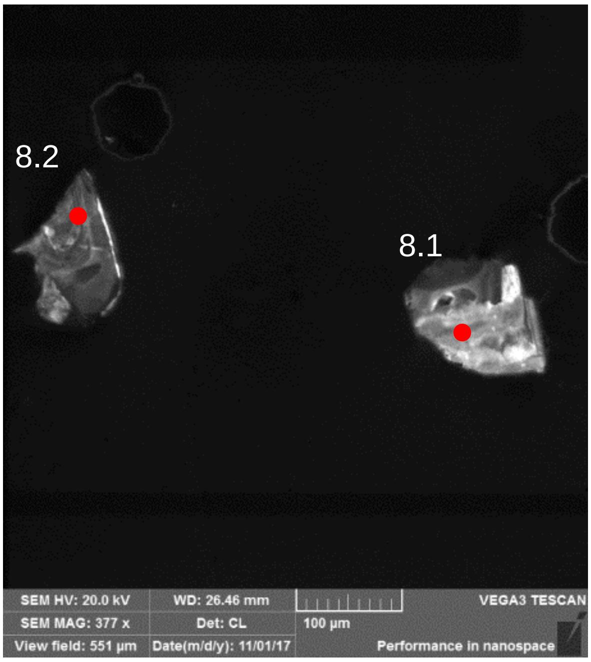
8.2
8.1
SEM HV: 20.0 kV
WD: 26.46 mm
VEGA3 TESCAN
SEM MAG: 377 x
Det: CL
100 µm
View field: 551 µm
Date(m/d/y): 11/01/17
Performance in nanospace

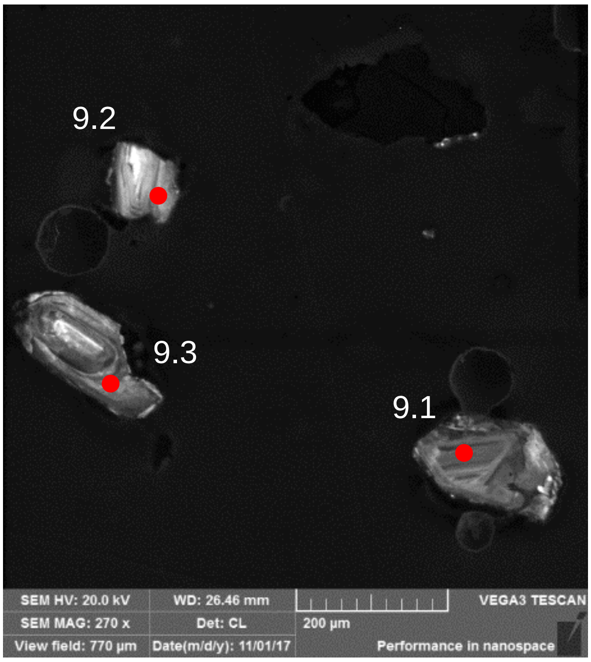
9.2
9.3
9.1
SEM HV: 20.0 kV
WD: 26.46 mm
VEGA3 TESCAN
SEM MAG: 270 x
Det: CL
200 µm
View field: 770 µm
Date(m/d/y): 11/01/17
Performance in nanospace

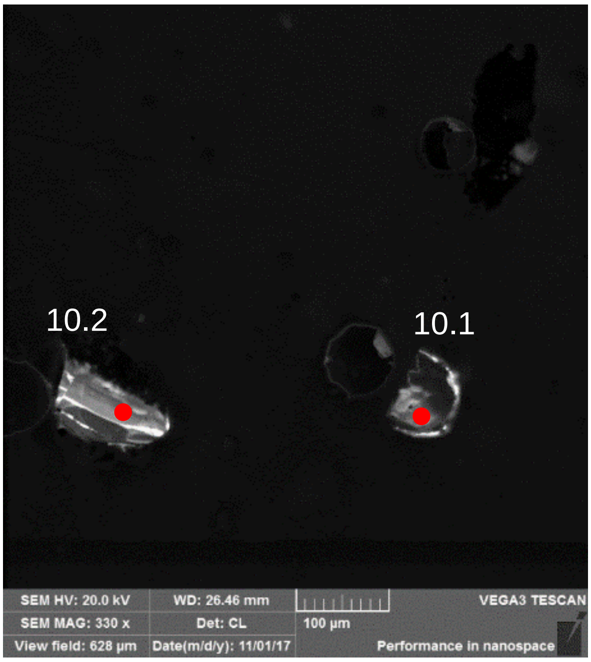
10.2
10.1
SEM HV: 20.0 kV
WD: 26.46 mm
VEGA3 TESCAN
SEM MAG: 330 x
Det: CL
100 µm
View field: 628 µm
Date(m/d/y): 11/01/17
Performance in nanospace

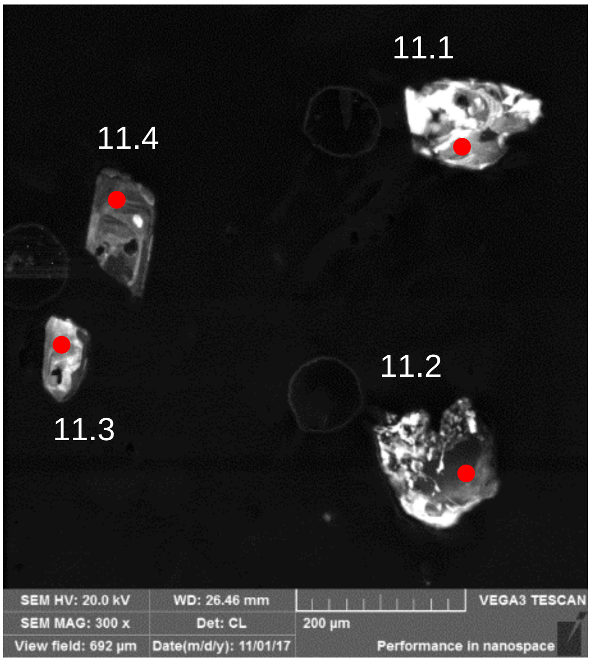
11.1
11.4
11.2
11.3
SEM HV: 20.0 kV
WD: 26.46 mm
VEGA3 TESCAN
SEM MAG: 300 x
Det: CL
200 µm
View field: 692 µm
Date(m/d/y): 11/01/17
Performance in nanospace

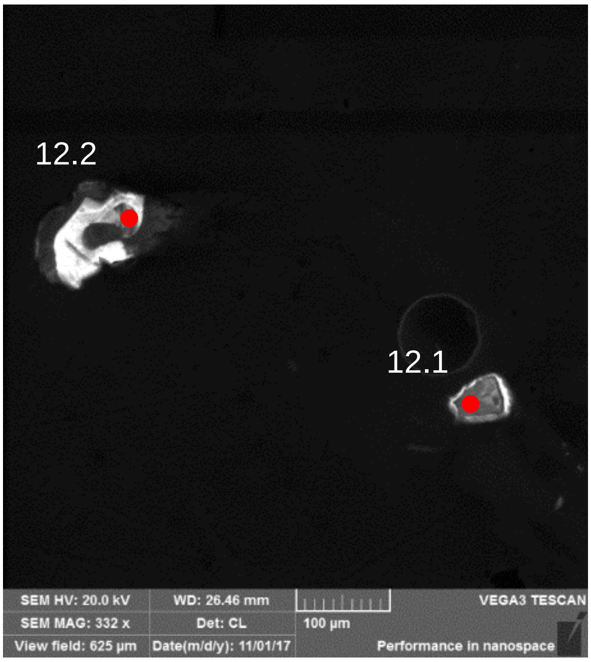
12.2
12.1
SEM HV: 20.0 kV
WD: 26.46 mm
VEGA3 TESCAN
SEM MAG: 332 x
Det: CL
100 µm
View field: 625 µm
Date(m/d/y): 11/01/17
Performance in nanospace

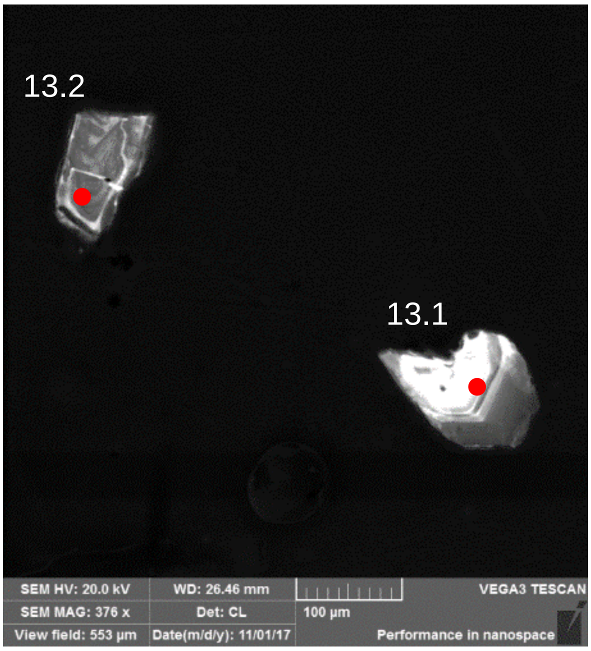
13.2
13.1
SEM HV: 20.0 kV
WD: 26.46 mm
VEGA3 TESCAN
SEM MAG: 376 x
Det: CL
100 µm
View field: 553 µm
Date(m/d/y): 11/01/17
Performance in nanospace

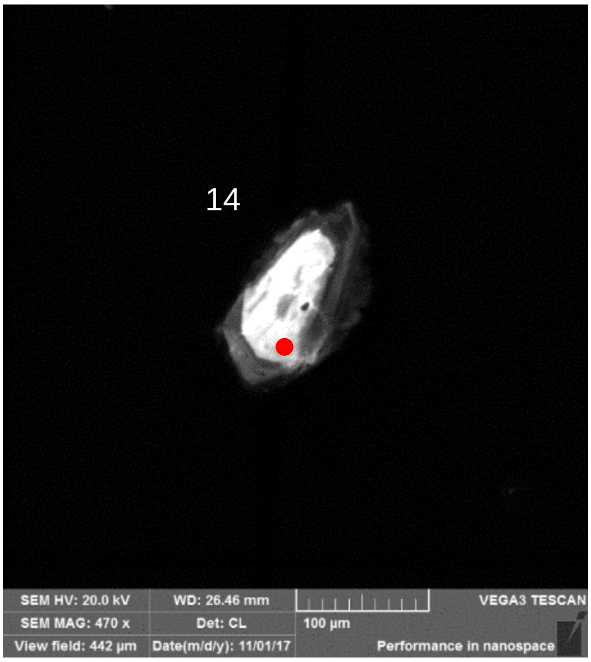
14
SEM HV: 20.0 kV
WD: 26.46 mm
VEGA3 TESCAN
SEM MAG: 470 x
Det: CL
100 µm
View field: 442 µm
Date(m/d/y): 11/01/17
Performance in nanospace

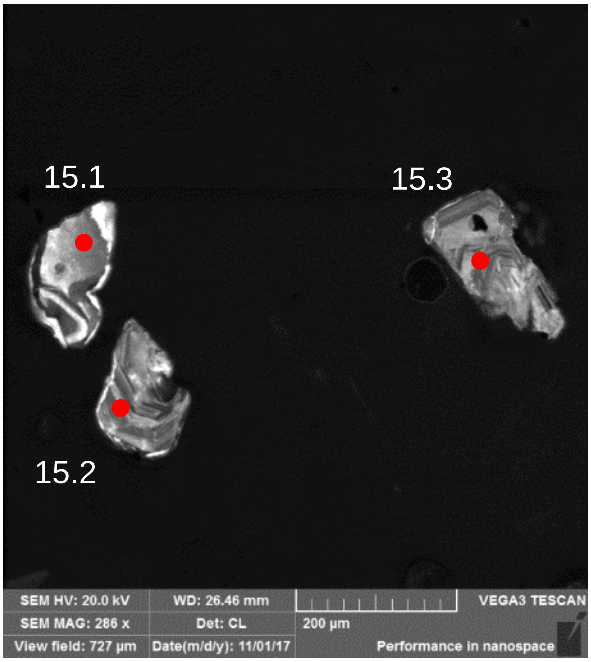
15.1
15.3
15.2
SEM HV: 20.0 kV
WD: 26.46 mm
VEGA3 TESCAN
SEM MAG: 286 x
Det: CL
200 μm
View field: 727 μm
Date(m/d/y): 11/01/17
Performance in nanospace

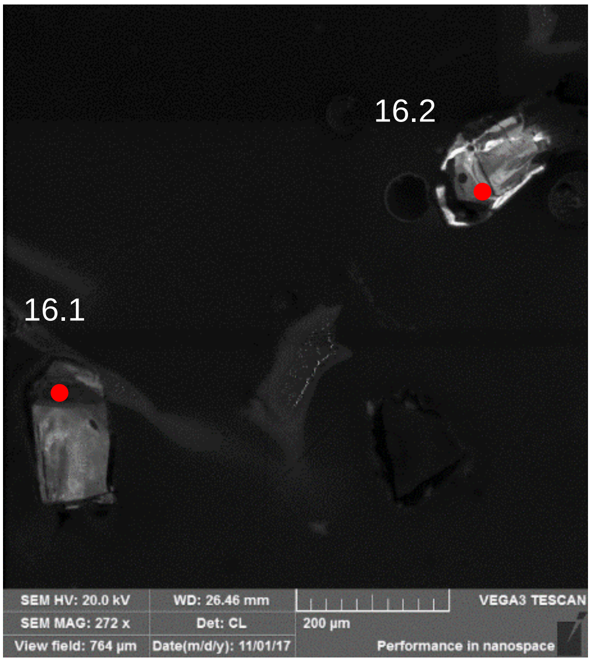
16.2
16.1
SEM HV: 20.0 kV
WD: 26.46 mm
VEGA3 TESCAN
SEM MAG: 272 x
Det: CL
200 μm
View field: 764 μm
Date(m/d/y): 11/01/17
Performance in nanospace

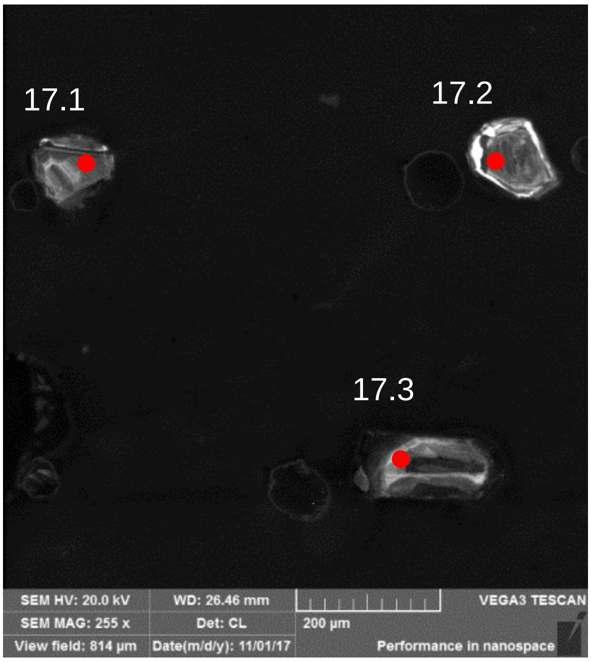
17.1
17.2
17.3
SEM HV: 20.0 kV
WD: 26.46 mm
VEGA3 TESCAN
SEM MAG: 255 x
Det: CL
200 μm
View field: 814 μm
Date(m/d/y): 11/01/17
Performance in nanospace

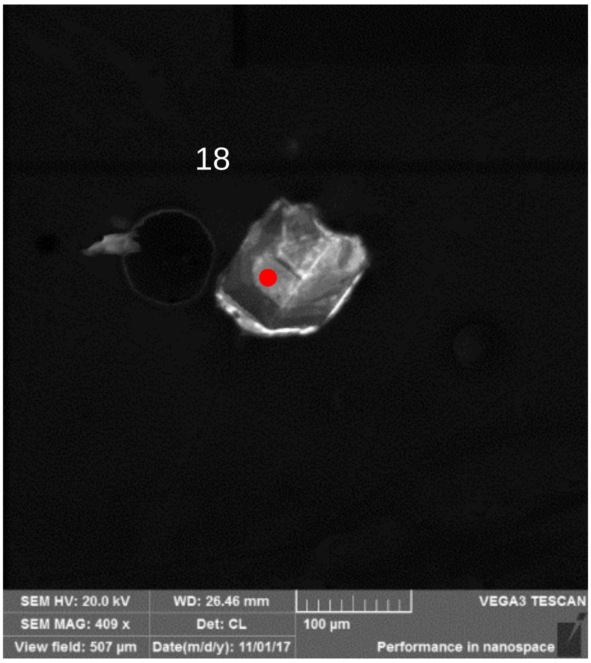
18
SEM HV: 20.0 kV
WD: 26.46 mm
VEGA3 TESCAN
SEM MAG: 409 x
Det: CL
100 μm
View field: 507 μm
Date(m/d/y): 11/01/17
Performance in nanospace

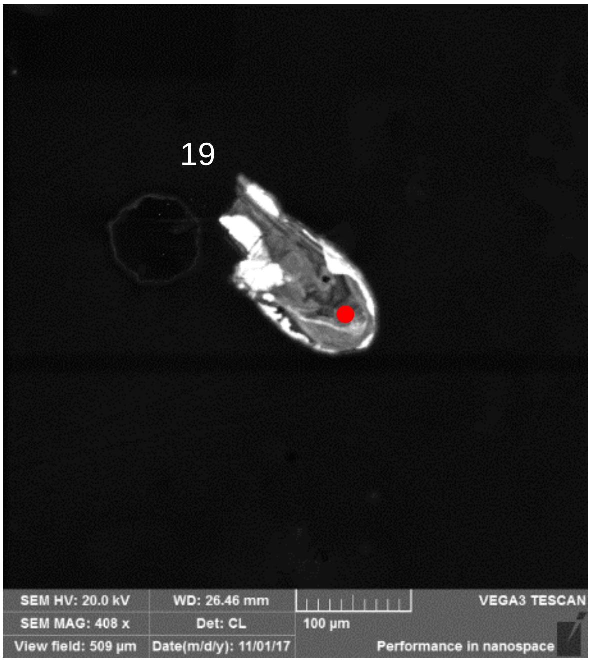
19
SEM HV: 20.0 kV
WD: 26.46 mm
VEGA3 TESCAN
SEM MAG: 408 x
Det: CL
100 µm
View field: 509 µm
Date(m/d/y): 11/01/17
Performance in nanospace

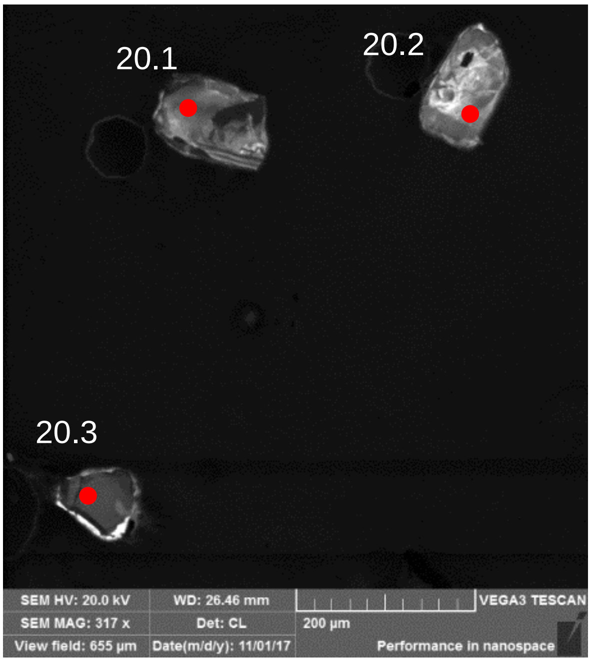
20.1
20.2
20.3
SEM HV: 20.0 kV
WD: 26.46 mm
VEGA3 TESCAN
SEM MAG: 317 x
Det: CL
200 µm
View field: 655 µm
Date(m/d/y): 11/01/17
Performance in nanospace

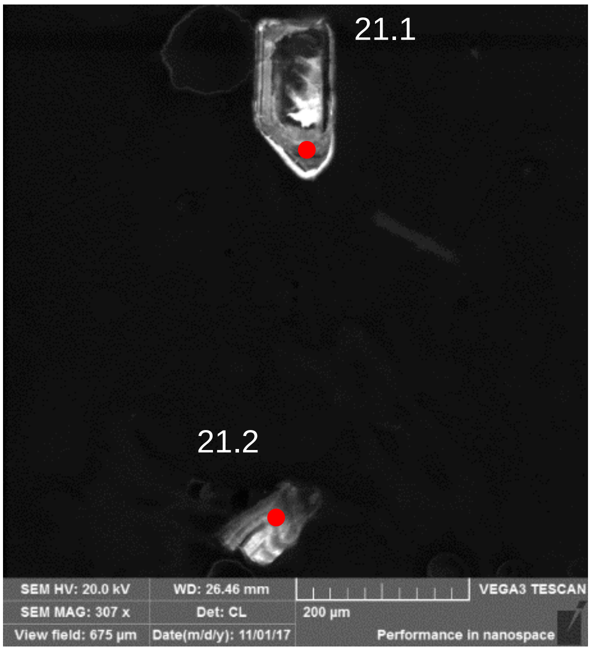
21.1
21.2
SEM HV: 20.0 kV
WD: 26.46 mm
VEGA3 TESCAN
SEM MAG: 307 x
Det: CL
200 µm
View field: 675 µm
Date(m/d/y): 11/01/17
Performance in nanospace

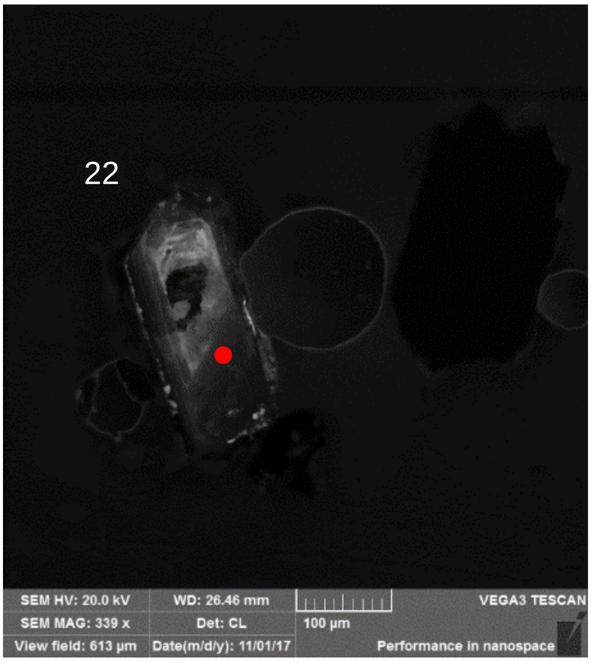
22
SEM HV: 20.0 kV
WD: 26.46 mm
VEGA3 TESCAN
SEM MAG: 339 x
Det: CL
100 µm
View field: 613 µm
Date(m/d/y): 11/01/17
Performance in nanospace

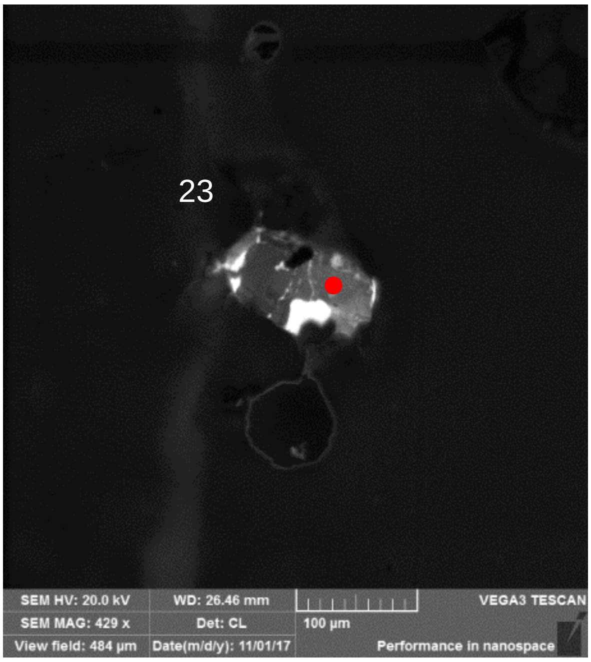
23
SEM HV: 20.0 kV
WD: 26.46 mm
VEGA3 TESCAN
SEM MAG: 429 x
Det: CL
100 μm
View field: 484 μm
Date(m/d/y): 11/01/17
Performance in nanospace

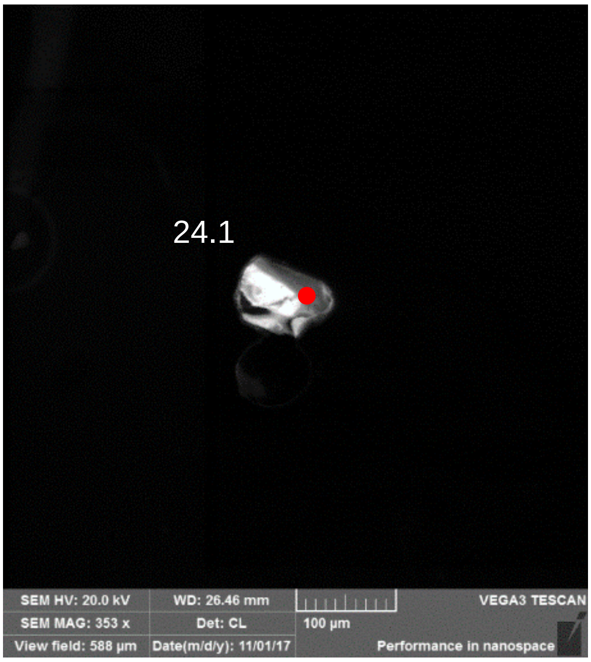
24.1
SEM HV: 20.0 kV
WD: 26.46 mm
VEGA3 TESCAN
SEM MAG: 353 x
Det: CL
100 μm
View field: 588 μm
Date(m/d/y): 11/01/17
Performance in nanospace

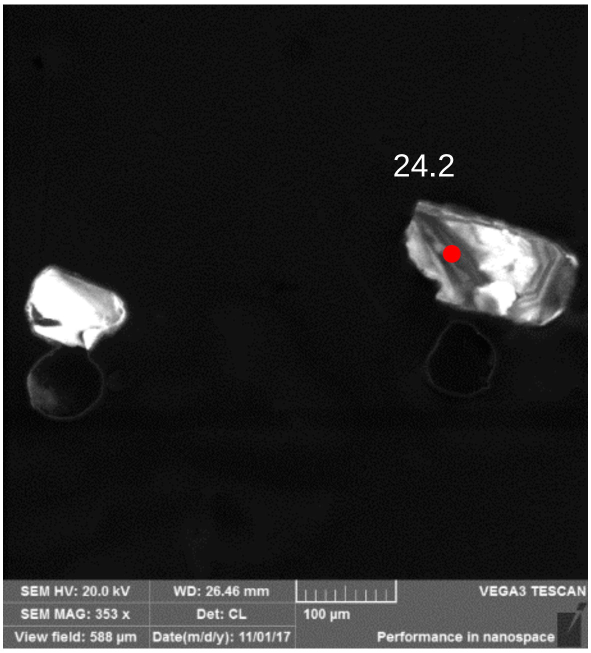
24.2
SEM HV: 20.0 kV
WD: 26.46 mm
VEGA3 TESCAN
SEM MAG: 353 x
Det: CL
100 μm
View field: 588 μm
Date(m/d/y): 11/01/17
Performance in nanospace

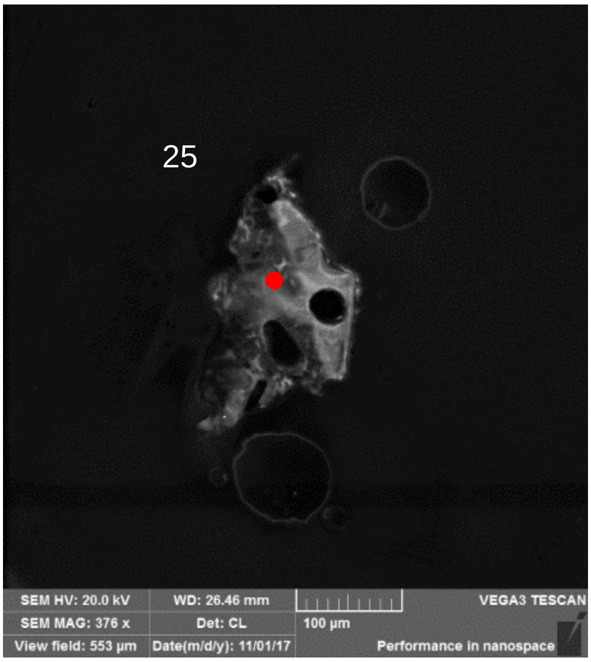
25
SEM HV: 20.0 kV
WD: 26.46 mm
VEGA3 TESCAN
SEM MAG: 376 x
Det: CL
100 μm
View field: 553 μm
Date(m/d/y): 11/01/17
Performance in nanospace

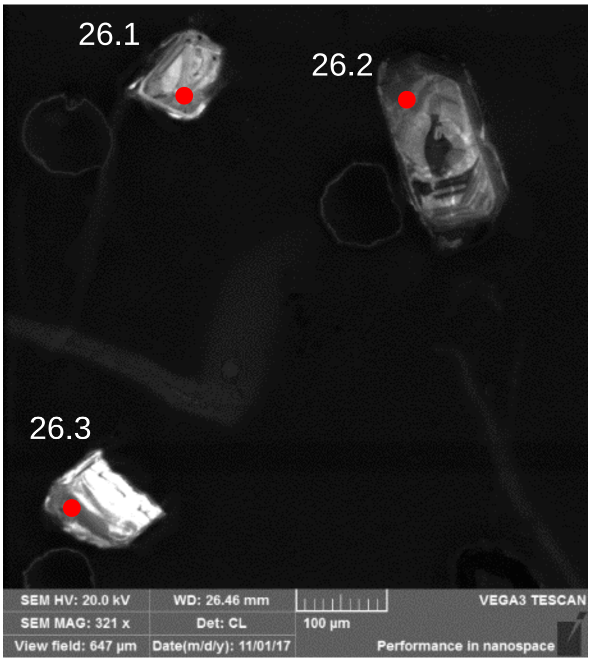
26.1
26.2
26.3
SEM HV: 20.0 kV
WD: 26.46 mm
VEGA3 TESCAN
SEM MAG: 321 x
Det: CL
100 µm
View field: 647 µm
Date(m/d/y): 11/01/17
Performance in nanospace

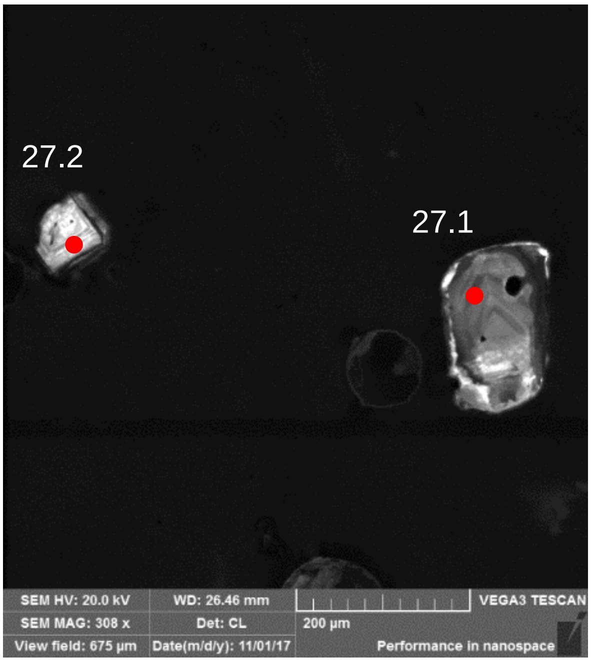
27.2
27.1
SEM HV: 20.0 kV
WD: 26.46 mm
VEGA3 TESCAN
SEM MAG: 308 x
Det: CL
200 µm
View field: 675 µm
Date(m/d/y): 11/01/17
Performance in nanospace

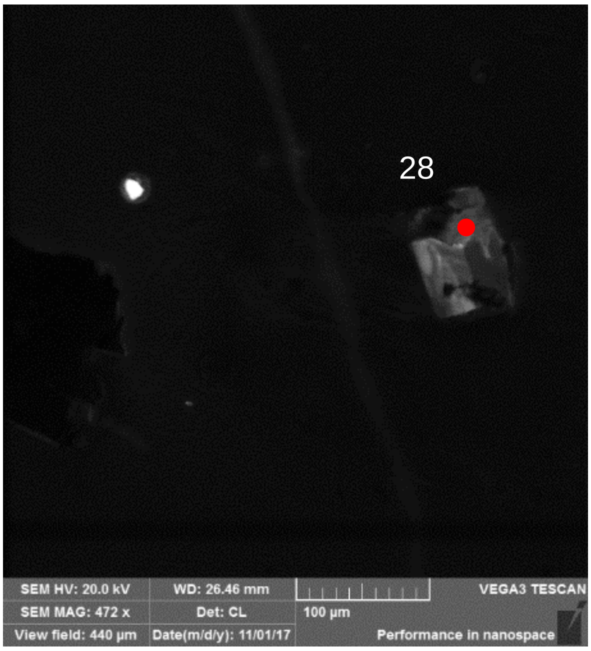
28
SEM HV: 20.0 kV
WD: 26.46 mm
VEGA3 TESCAN
SEM MAG: 472 x
Det: CL
100 µm
View field: 440 µm
Date(m/d/y): 11/01/17
Performance in nanospace

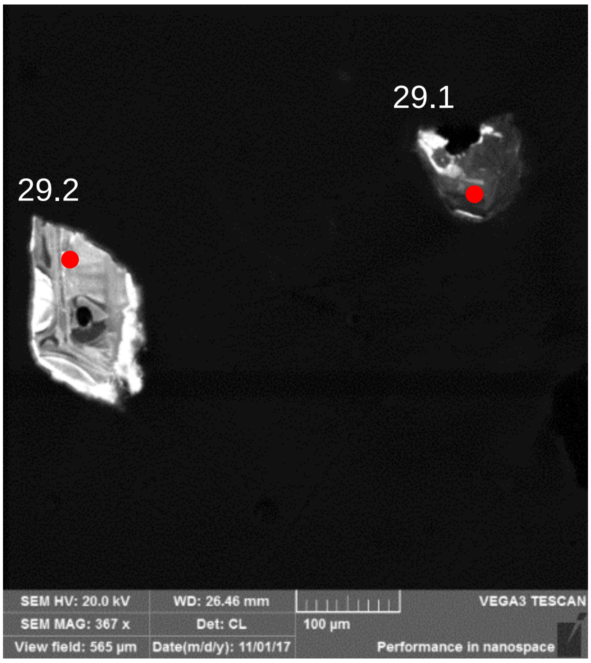
29.1
29.2
SEM HV: 20.0 kV
WD: 26.46 mm
VEGA3 TESCAN
SEM MAG: 367 x
Det: CL
100 µm
View field: 565 µm
Date(m/d/y): 11/01/17
Performance in nanospace

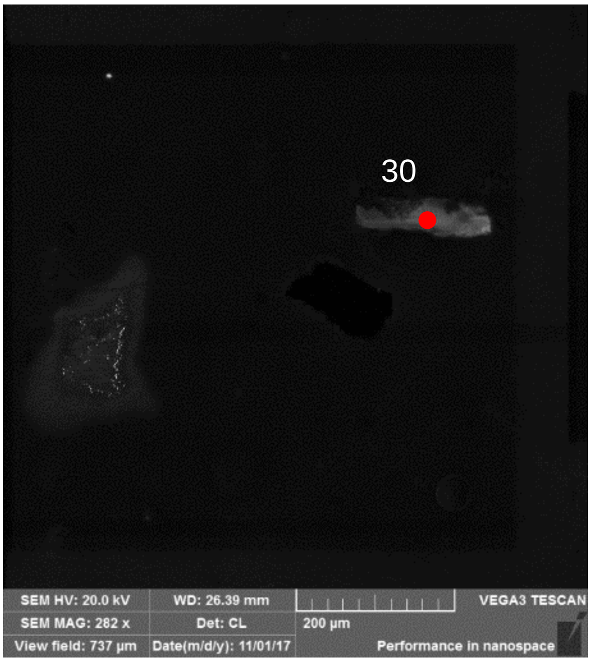
30
SEM HV: 20.0 kV
WD: 26.39 mm
VEGA3 TESCAN
SEM MAG: 282 x
Det: CL
200 µm
View field: 737 µm
Date(m/d/y): 11/01/17
Performance in nanospace

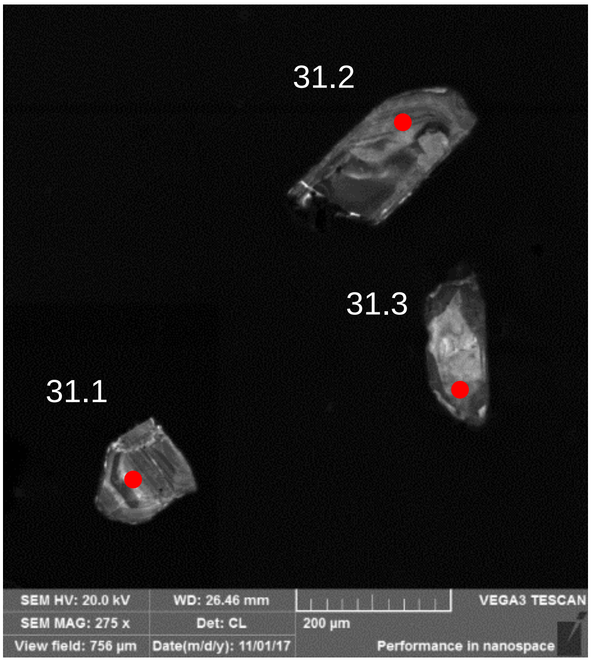
31.2
31.3
31.1
SEM HV: 20.0 kV
WD: 26.46 mm
VEGA3 TESCAN
SEM MAG: 275 x
Det: CL
200 µm
View field: 756 µm
Date(m/d/y): 11/01/17
Performance in nanospace

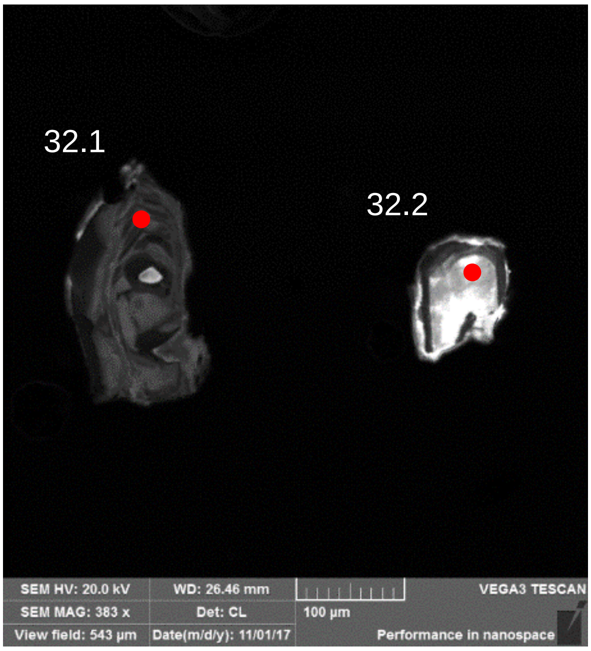
32.1
32.2
SEM HV: 20.0 kV
WD: 26.46 mm
VEGA3 TESCAN
SEM MAG: 383 x
Det: CL
100 µm
View field: 543 µm
Date(m/d/y): 11/01/17
Performance in nanospace

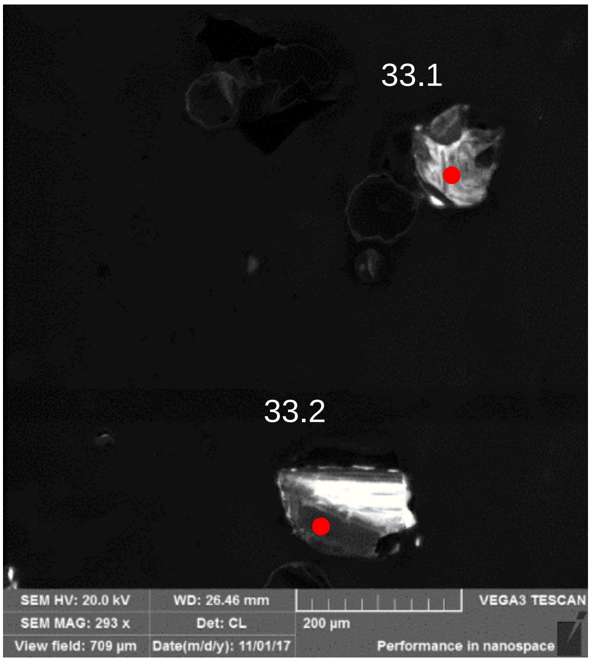
33.1
33.2
SEM HV: 20.0 kV
WD: 26.46 mm
VEGA3 TESCAN
SEM MAG: 293 x
Det: CL
200 µm
View field: 709 µm
Date(m/d/y): 11/01/17
Performance in nanospace

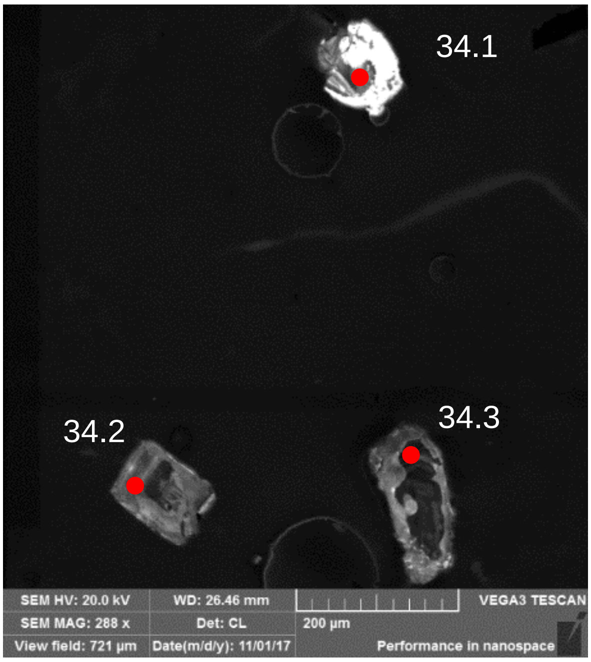
34.1
34.2
34.3
SEM HV: 20.0 kV
WD: 26.46 mm
VEGA3 TESCAN
SEM MAG: 288 x
Det: CL
200 µm
View field: 721 µm
Date(m/d/y): 11/01/17
Performance in nanospace

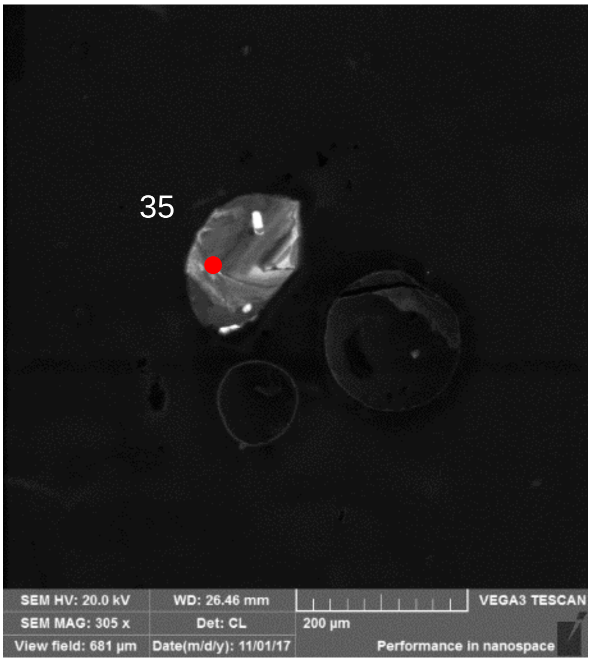
35
SEM HV: 20.0 kV
WD: 26.46 mm
VEGA3 TESCAN
SEM MAG: 305 x
Det: CL
200 µm
View field: 681 µm
Date(m/d/y): 11/01/17
Performance in nanospace

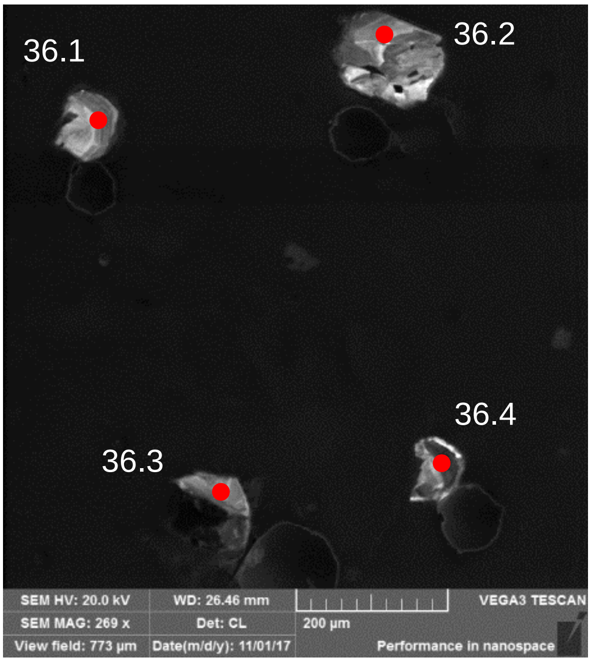
36.1
36.2
36.3
36.4
SEM HV: 20.0 kV
WD: 26.46 mm
VEGA3 TESCAN
SEM MAG: 269 x
Det: CL
200 µm
View field: 773 µm
Date(m/d/y): 11/01/17
Performance in nanospace

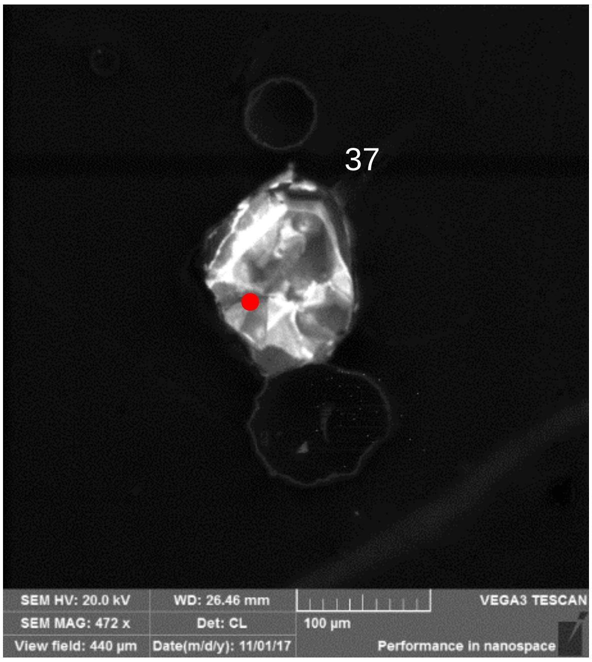
37
SEM HV: 20.0 kV
WD: 26.46 mm
VEGA3 TESCAN
SEM MAG: 472 x
Det: CL
100 µm
View field: 440 µm
Date(m/d/y): 11/01/17
Performance in nanospace

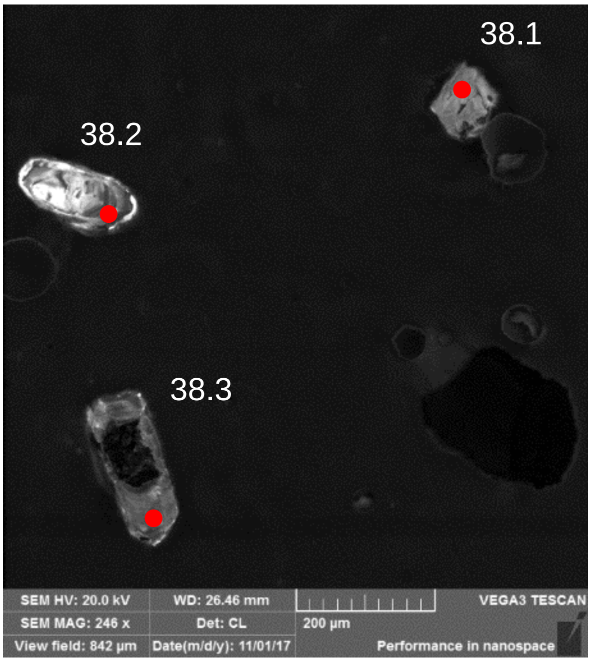
38.1
38.2
38.3
SEM HV: 20.0 kV
WD: 26.46 mm
VEGA3 TESCAN
SEM MAG: 246 x
Det: CL
200 µm
View field: 842 µm
Date(m/d/y): 11/01/17
Performance in nanospace

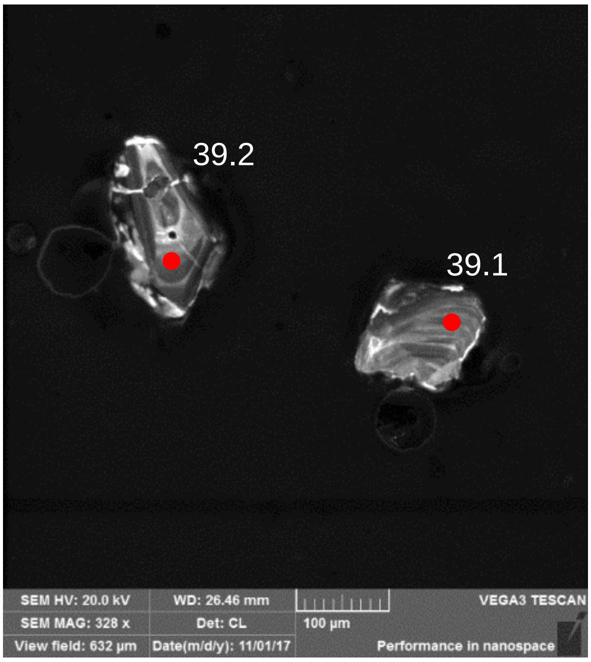
39.2
39.1
SEM HV: 20.0 kV
WD: 26.46 mm
VEGA3 TESCAN
SEM MAG: 328 x
Det: CL
100 µm
View field: 632 µm
Date(m/d/y): 11/01/17
Performance in nanospace

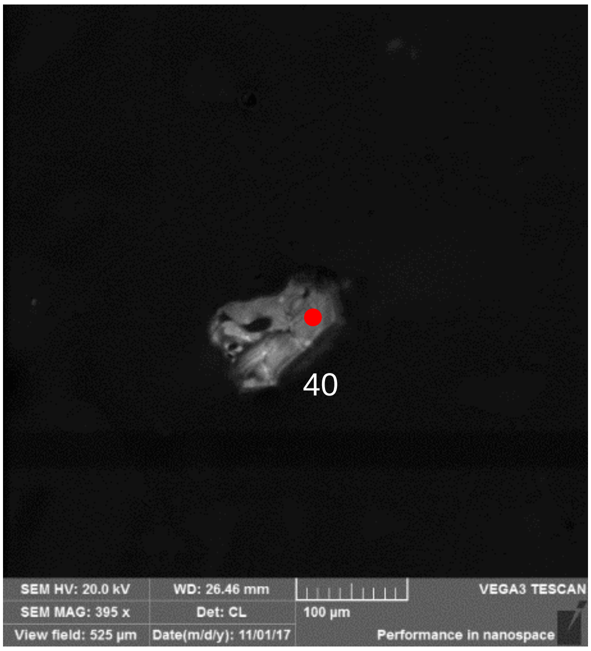
40
SEM HV: 20.0 kV
WD: 26.46 mm
VEGA3 TESCAN
SEM MAG: 395 x
Det: CL
100 µm
View field: 525 µm
Date(m/d/y): 11/01/17
Performance in nanospace

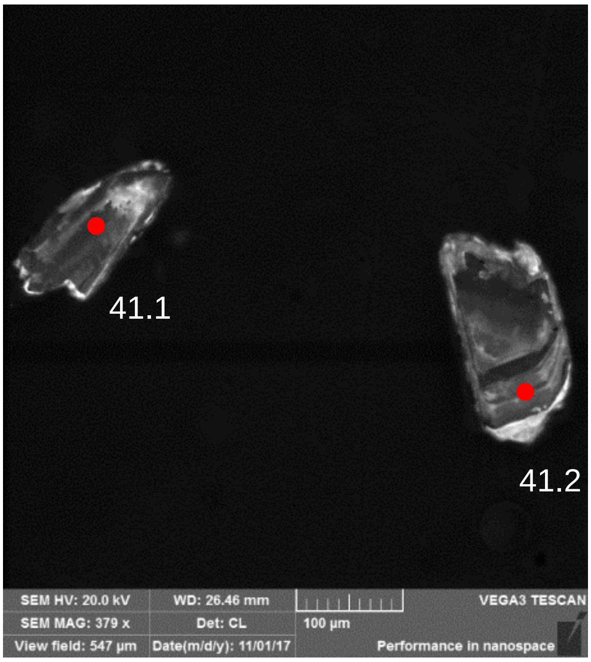
41.1
41.2
SEM HV: 20.0 kV
WD: 26.46 mm
VEGA3 TESCAN
SEM MAG: 379 x
Det: CL
100 µm
View field: 547 µm
Date(m/d/y): 11/01/17
Performance in nanospace

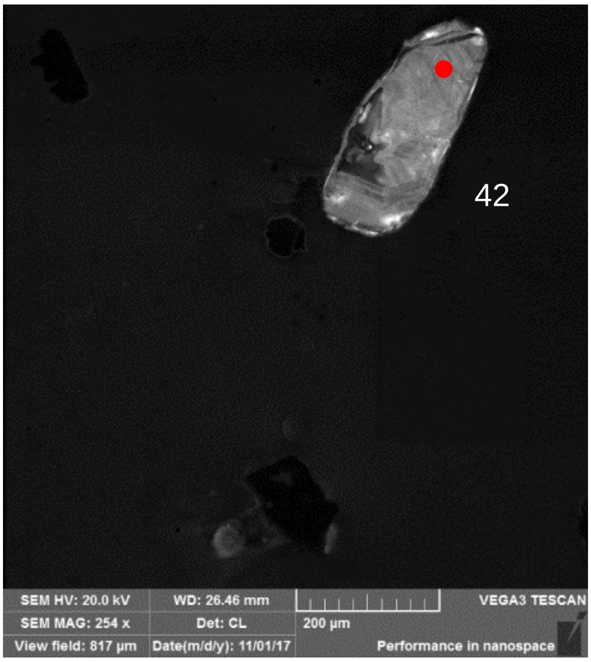
42
SEM HV: 20.0 kV
WD: 26.46 mm
VEGA3 TESCAN
SEM MAG: 254 x
Det: CL
200 µm
View field: 817 µm
Date(m/d/y): 11/01/17
Performance in nanospace

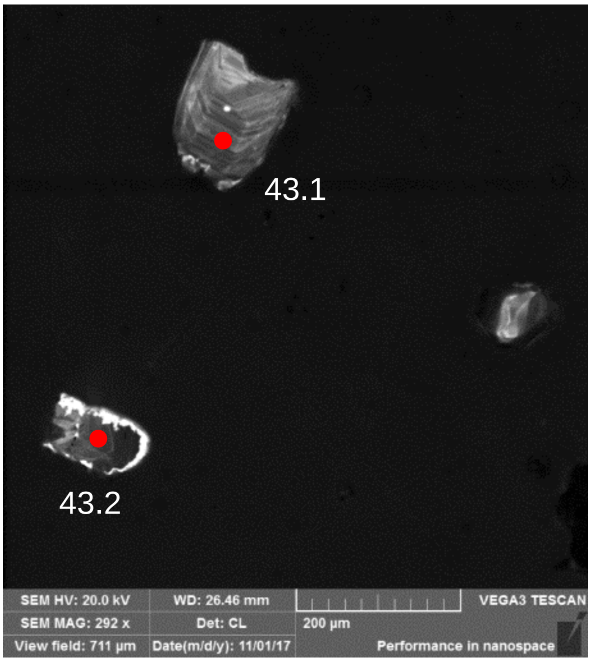
43.1
43.2
SEM HV: 20.0 kV
WD: 26.46 mm
VEGA3 TESCAN
SEM MAG: 292 x
Det: CL
200 µm
View field: 711 µm
Date(m/d/y): 11/01/17
Performance in nanospace

Tete 1: Cathode luminescence SEM images, red dot indicates ablation position.

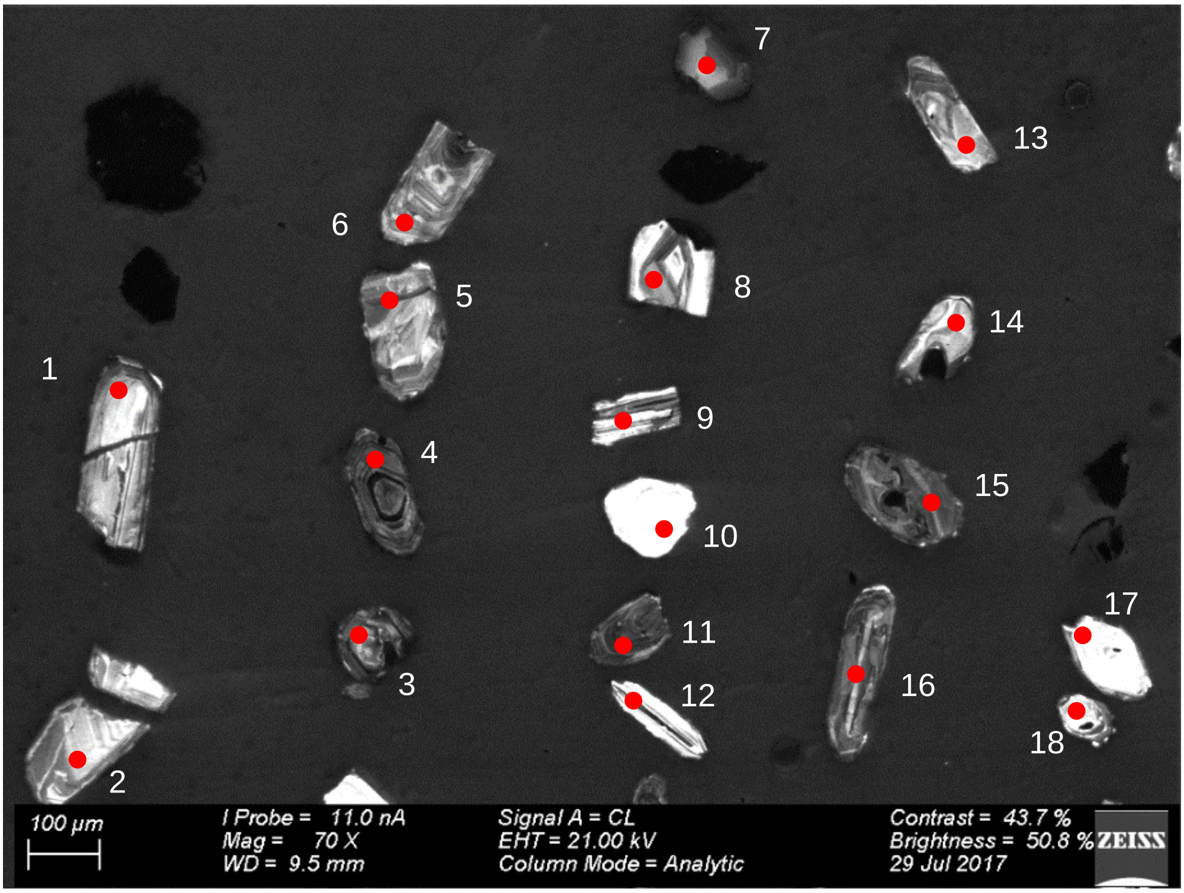

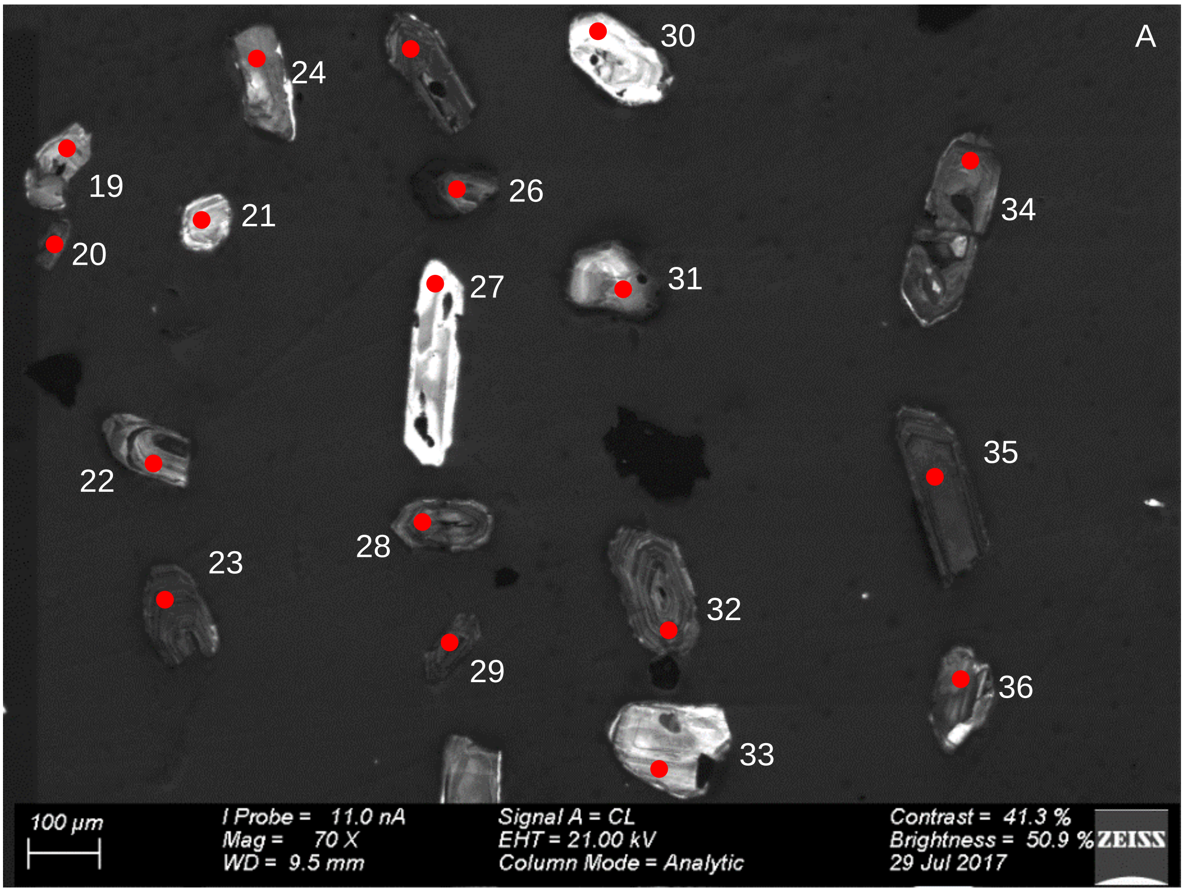
A
30
24
19
21
20
26
27
31
34
22
35
23
28
32
29
36
33
100 µm
I Probe = 11.0 nA
Mag = 70 X
WD = 9.5 mm
Signal A = CL
EHT = 21.00 kV
Column Mode = Analytic
Contrast = 41.3 %
Brightness = 50.9 %
29 Jul 2017
ZEISS

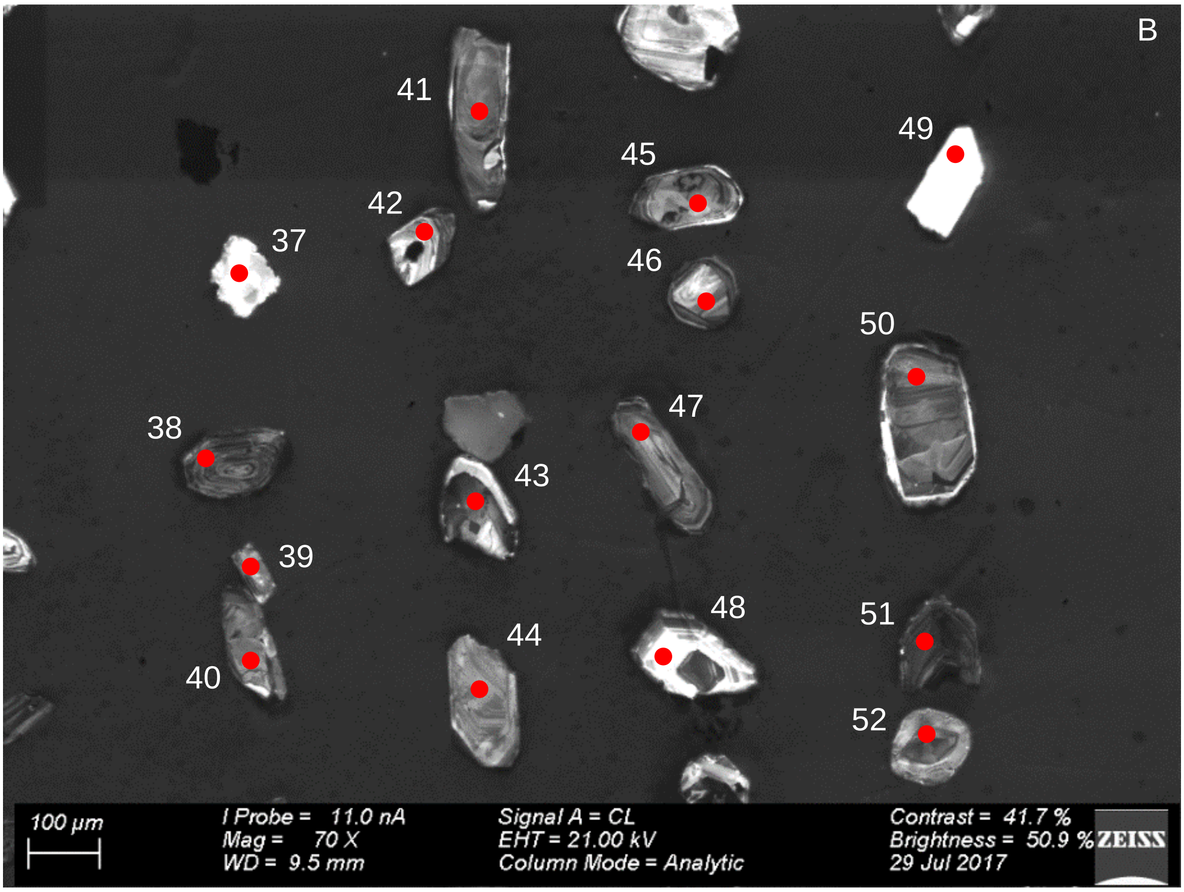
B
41
49
45
42
37
46
50
38
47
43
39
48
44
51
40
52
100 µm
I Probe = 11.0 nA
Mag = 70 X
WD = 9.5 mm
Signal A = CL
EHT = 21.00 kV
Column Mode = Analytic
Contrast = 41.7 %
Brightness = 50.9 %
29 Jul 2017
ZEISS

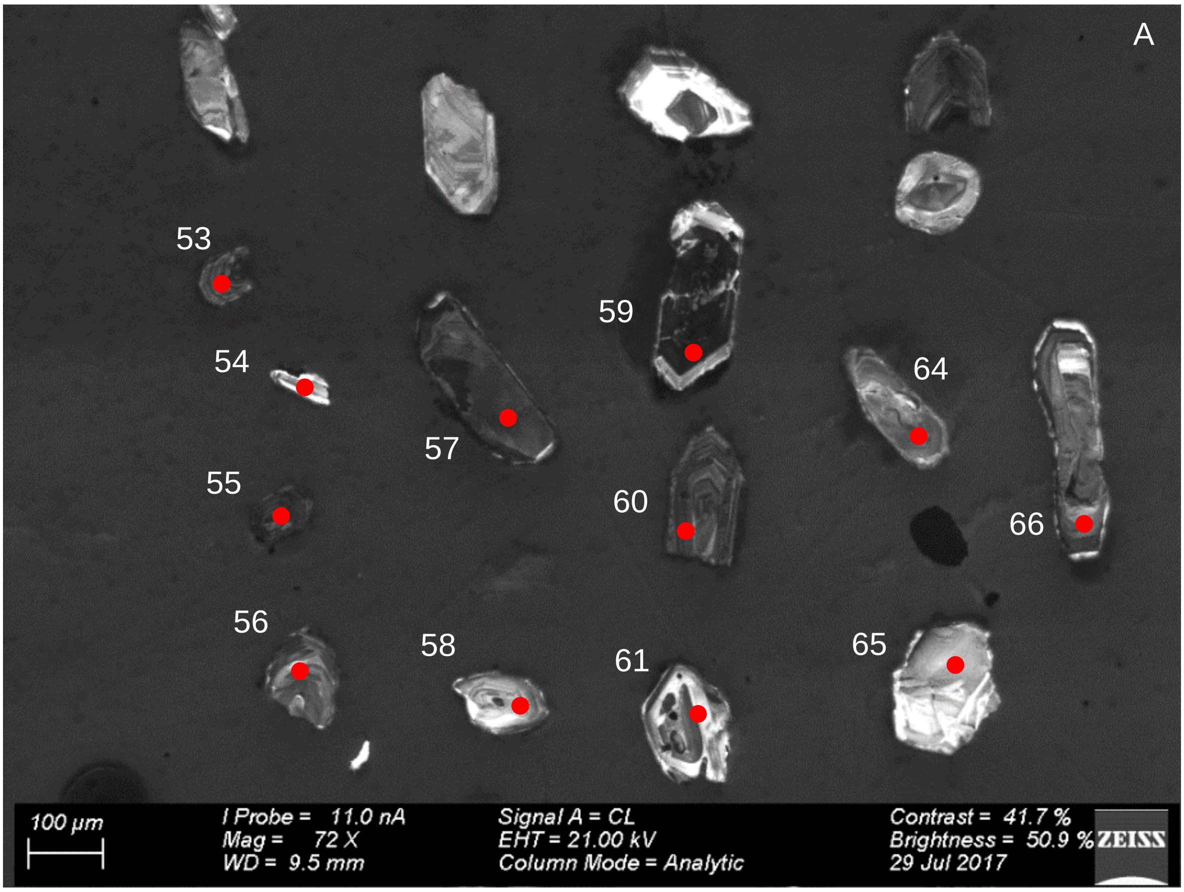
A
53
54
55
56
57
58
59
60
61
64
65
66
100 µm
I Probe = 11.0 nA
Mag = 72 X
WD = 9.5 mm
Signal A = CL
EHT = 21.00 kV
Column Mode = Analytic
Contrast = 41.7 %
Brightness = 50.9 %
29 Jul 2017
ZEISS

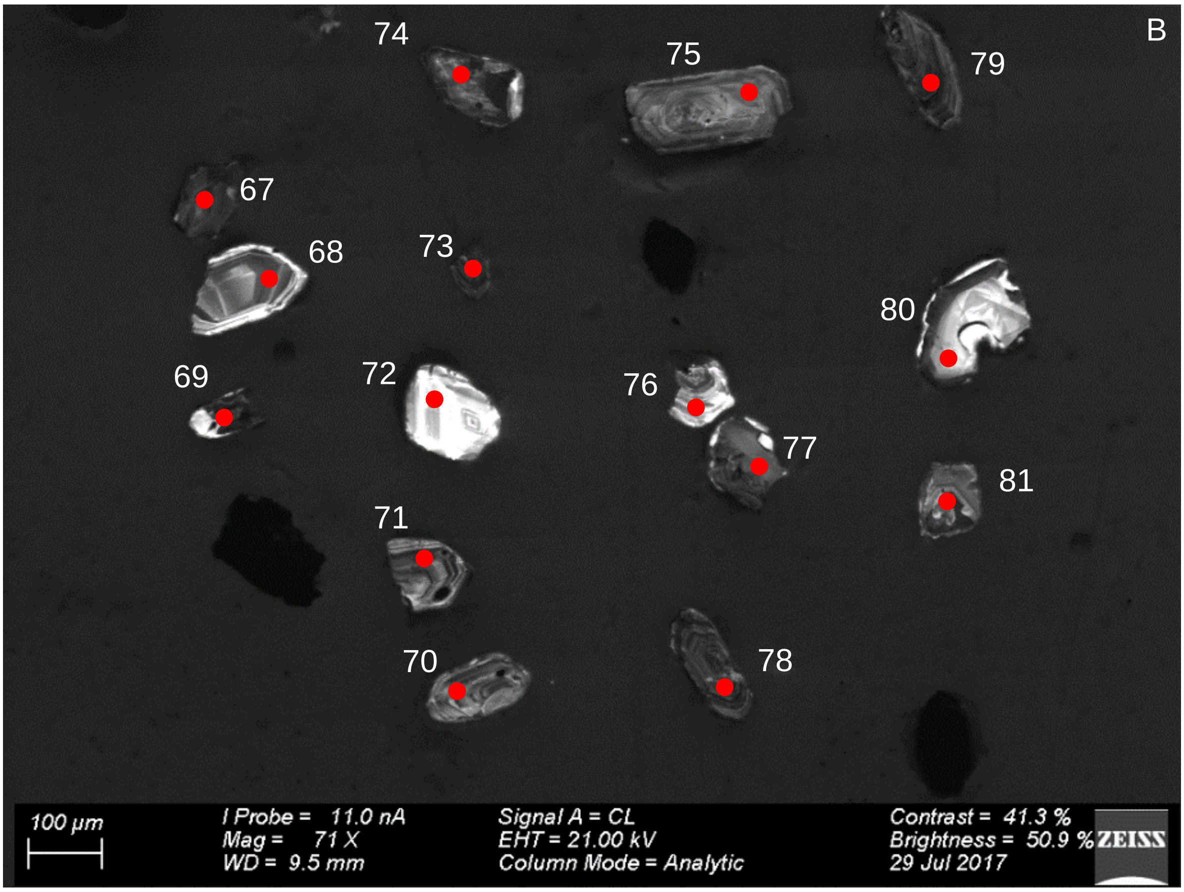
B
67
68
69
70
71
72
73
74
75
76
77
78
79
80
81
100 µm
I Probe = 11.0 nA
Mag = 71 X
WD = 9.5 mm
Signal A = CL
EHT = 21.00 kV
Column Mode = Analytic
Contrast = 41.3 %
Brightness = 50.9 %
29 Jul 2017
ZEISS

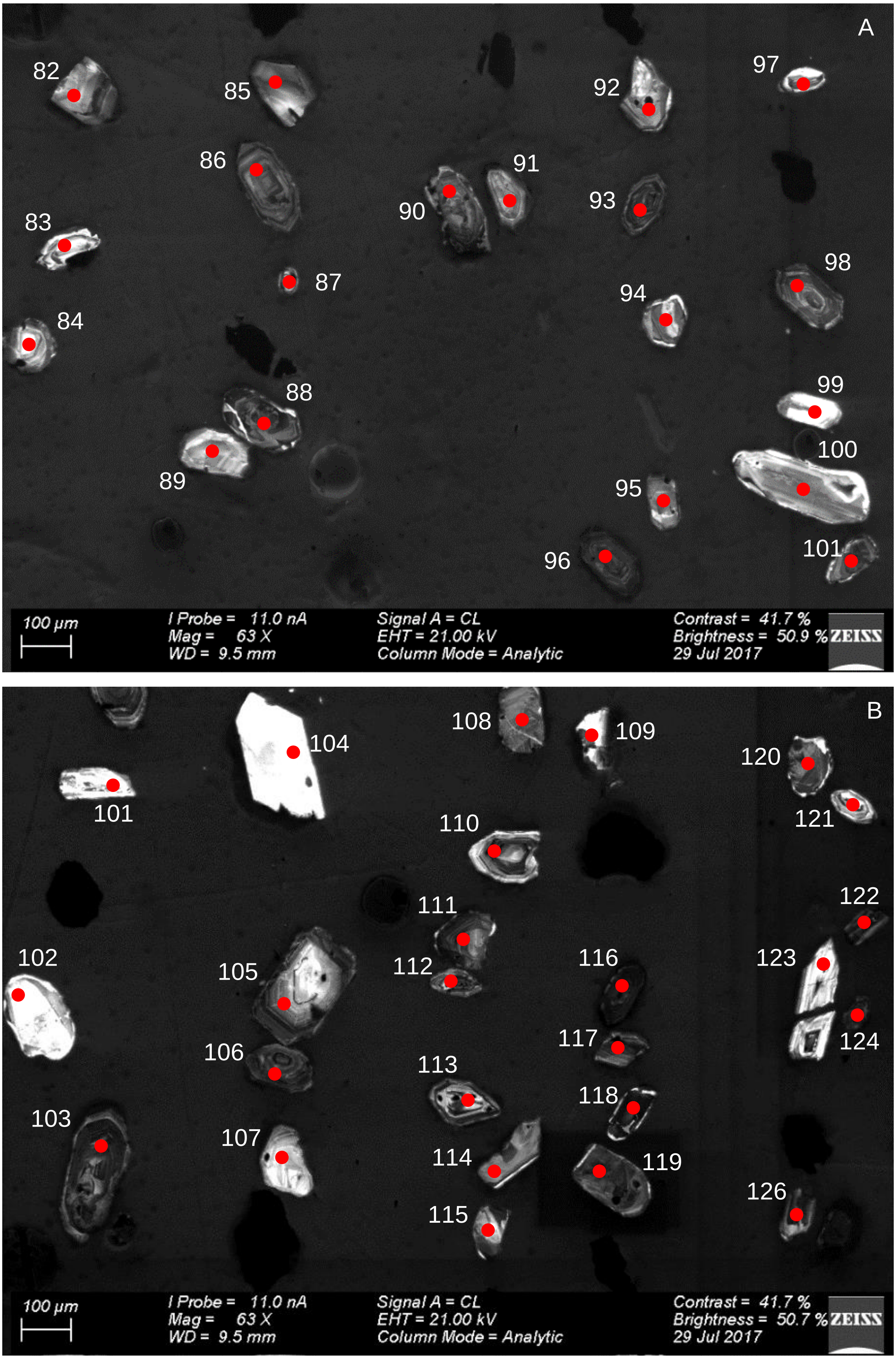
A
82
85
92
97
86
91
90
93
83
87
98
94
84
88
99
100
89
95
96
101
100 µm
I Probe = 11.0 nA
Mag = 63 X
WD = 9.5 mm
Signal A = CL
EHT = 21.00 kV
Column Mode = Analytic
Contrast = 41.7 %
Brightness = 50.9 %
29 Jul 2017
B
108
109
104
120
101
121
110
122
111
102
105
112
116
123
117
124
106
113
118
103
107
114
119
126
115
100 µm
I Probe = 11.0 nA
Mag = 63 X
WD = 9.5 mm
Signal A = CL
EHT = 21.00 kV
Column Mode = Analytic
Contrast = 41.7 %
Brightness = 50.7 %
29 Jul 2017

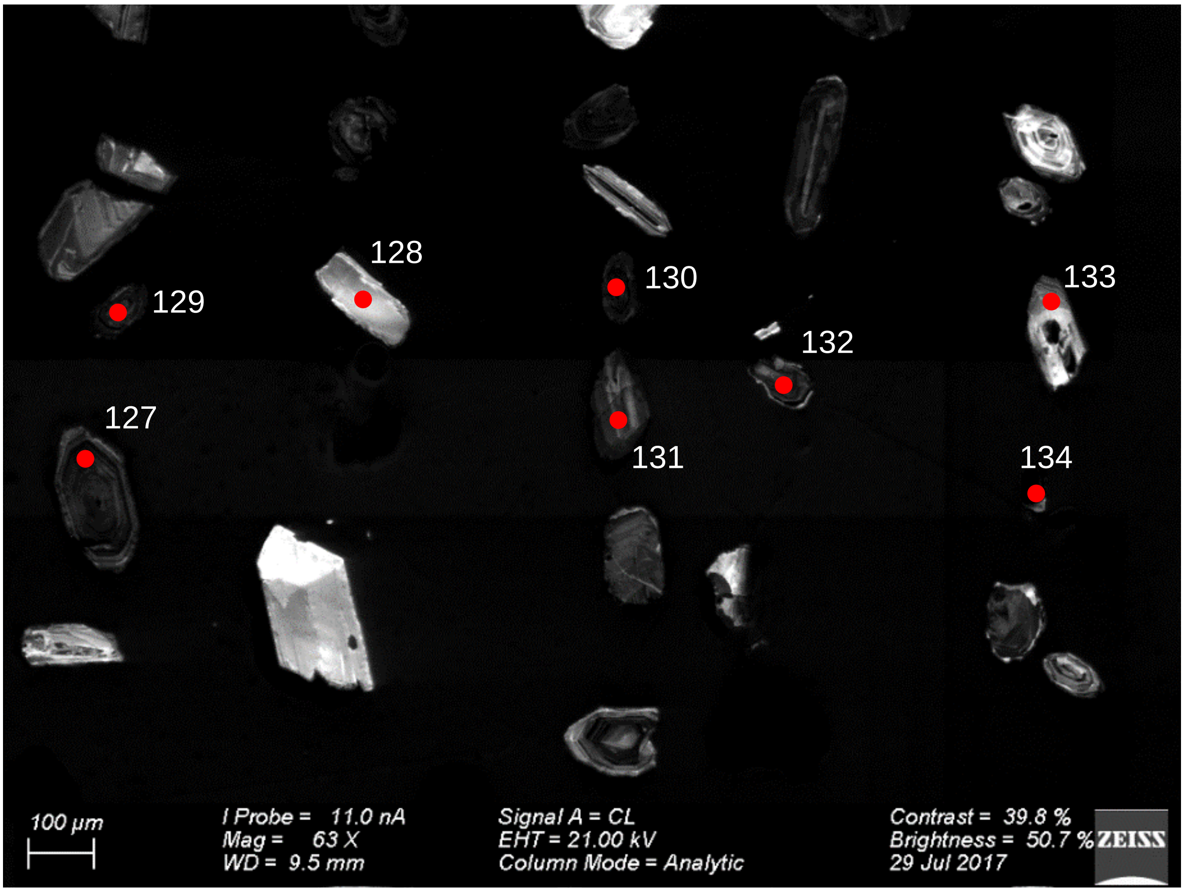
128
129
130
133
132
127
131
134
100 µm
I Probe = 11.0 nA
Mag = 63 X
WD = 9.5 mm
Signal A = CL
EHT = 21.00 kV
Column Mode = Analytic
Contrast = 39.8 %
Brightness = 50.7 %
29 Jul 2017
ZEISS

Tete 3: Cathode luminescence SEM images, red dot indicates ablation position.

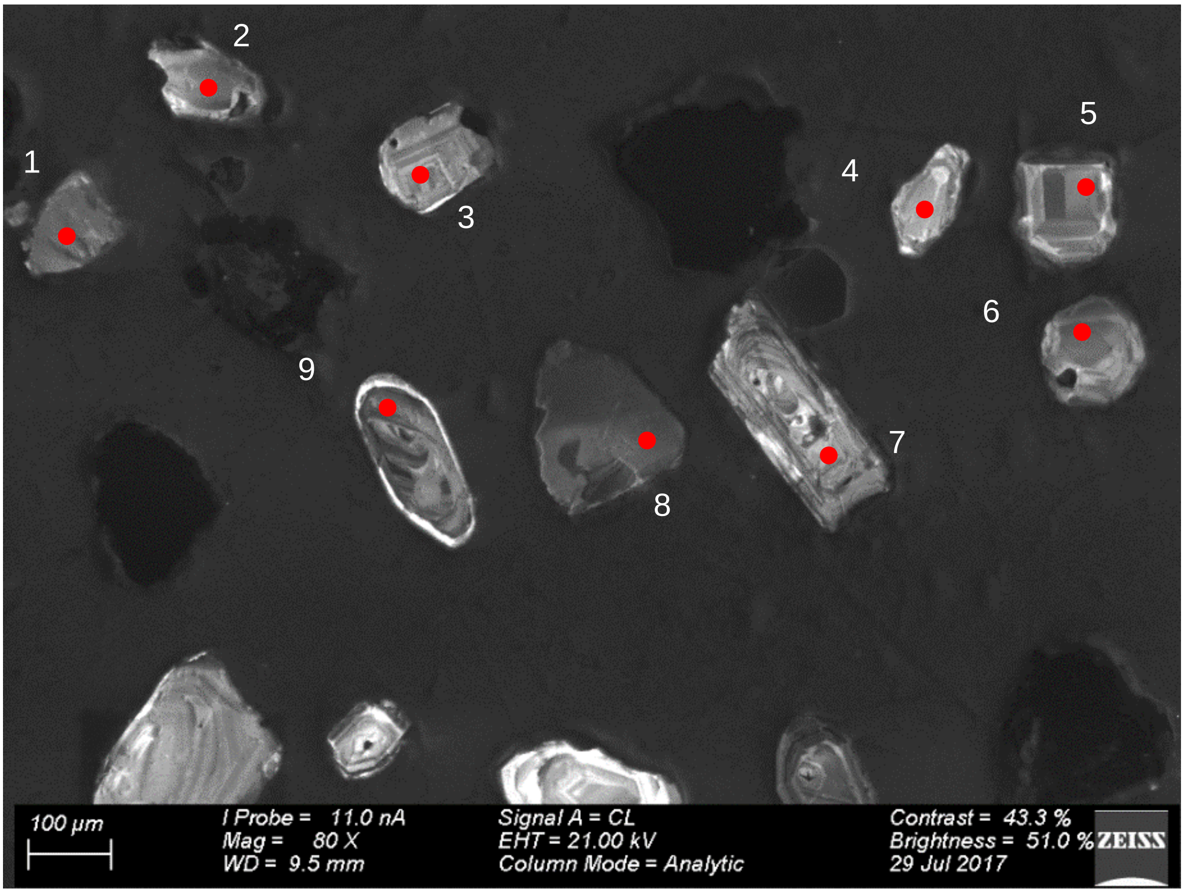

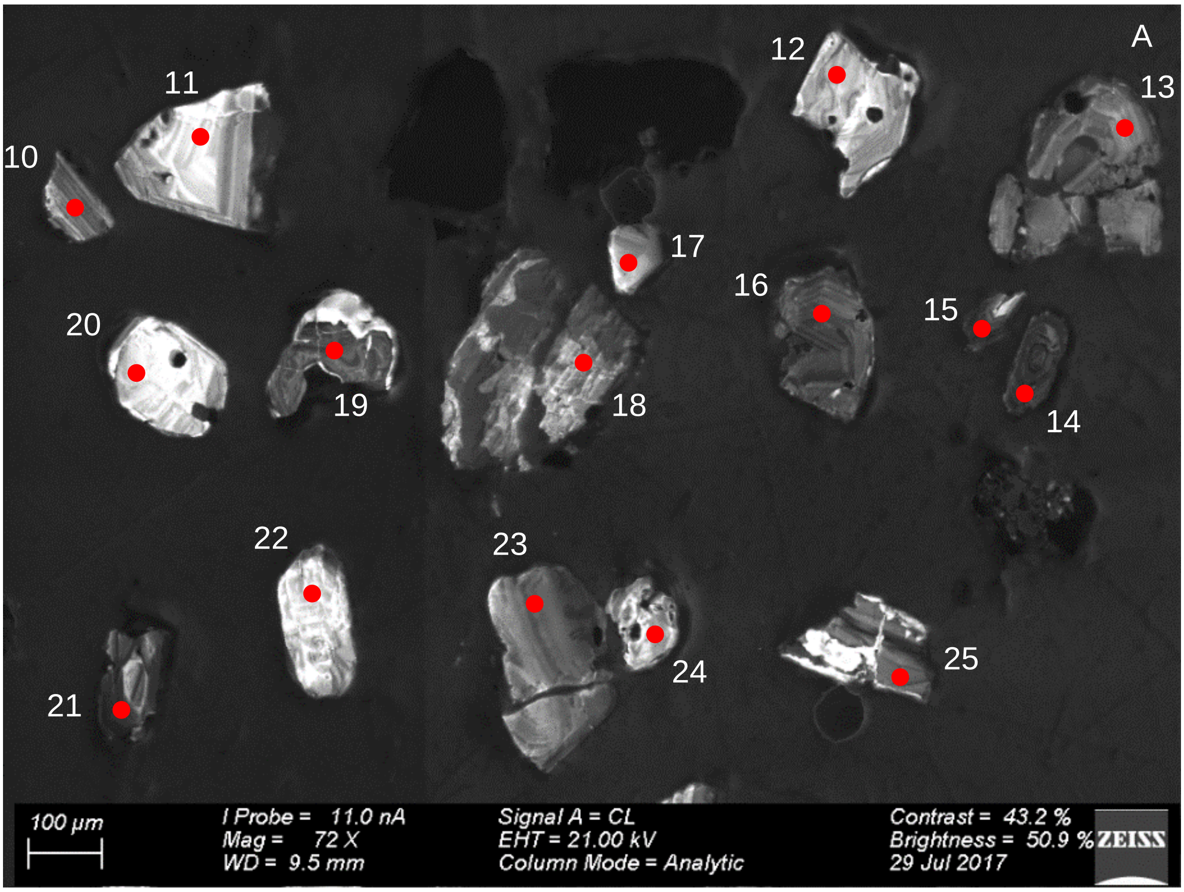
A
10
11
12
13
14
15
16
17
18
19
20
21
22
23
24
25
100 µm
I Probe = 11.0 nA
Mag = 72 X
WD = 9.5 mm
Signal A = CL
EHT = 21.00 kV
Column Mode = Analytic
Contrast = 43.2 %
Brightness = 50.9 %
29 Jul 2017

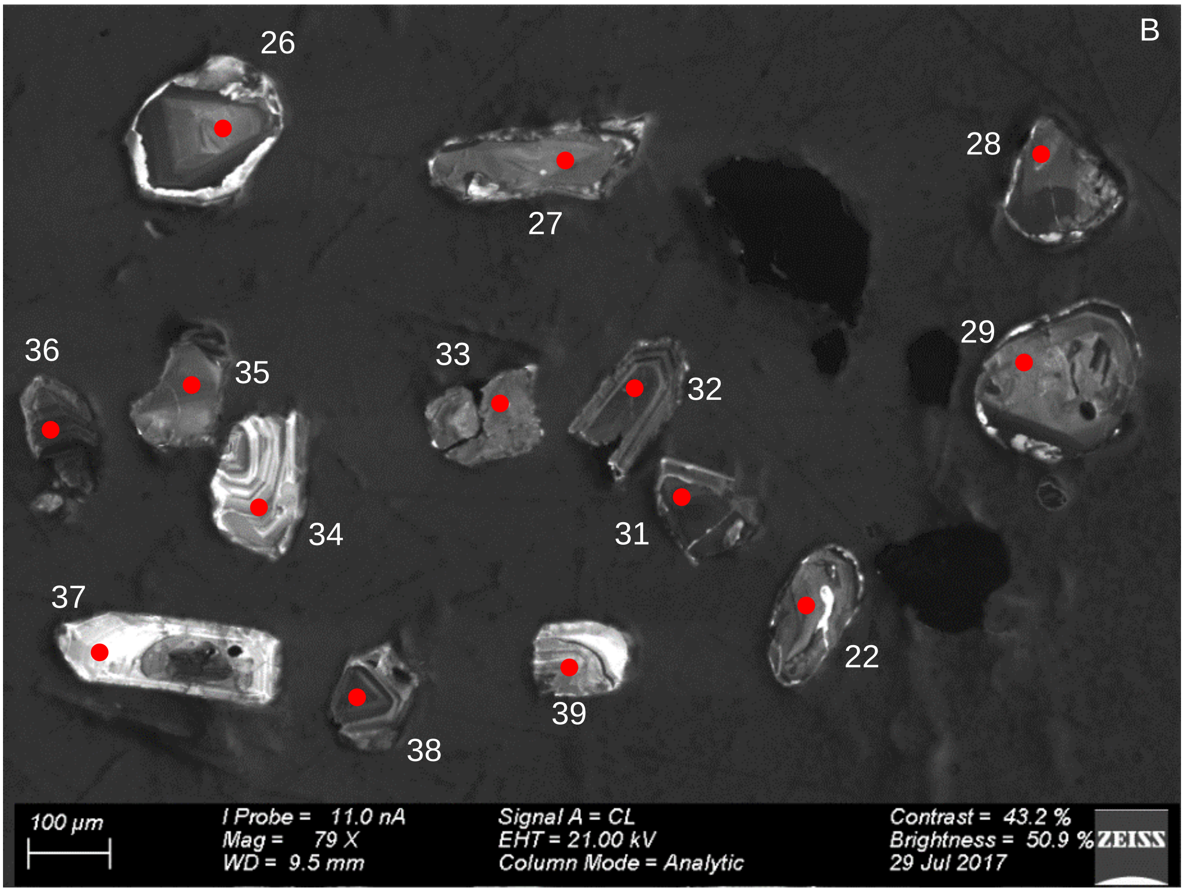
B
26
27
28
29
22
31
32
33
34
35
36
37
38
39
100 µm
I Probe = 11.0 nA
Mag = 79 X
WD = 9.5 mm
Signal A = CL
EHT = 21.00 kV
Column Mode = Analytic
Contrast = 43.2 %
Brightness = 50.9 %
29 Jul 2017

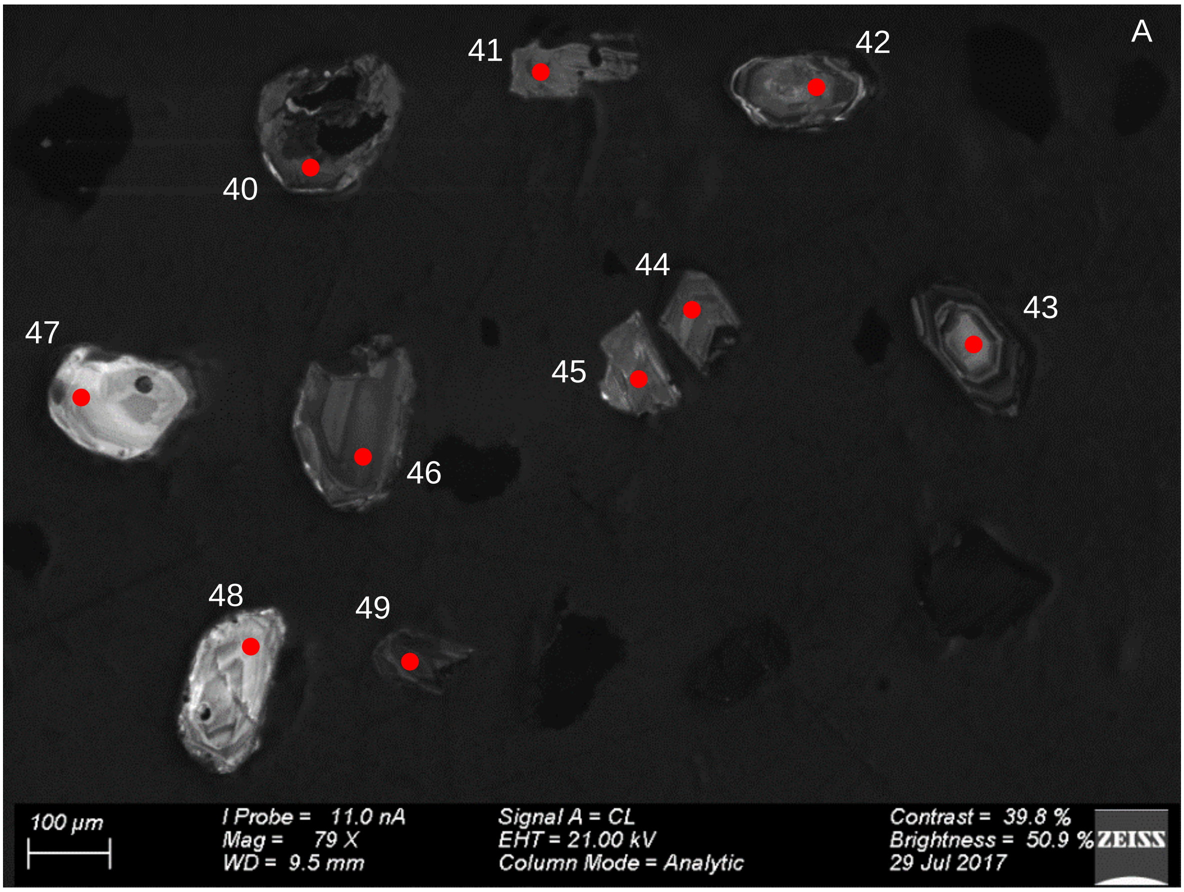
A
40
41
42
43
44
45
46
47
48
49
100 µm
I Probe = 11.0 nA
Mag = 79 X
WD = 9.5 mm
Signal A = CL
EHT = 21.00 kV
Column Mode = Analytic
Contrast = 39.8 %
Brightness = 50.9 %
29 Jul 2017
ZEISS

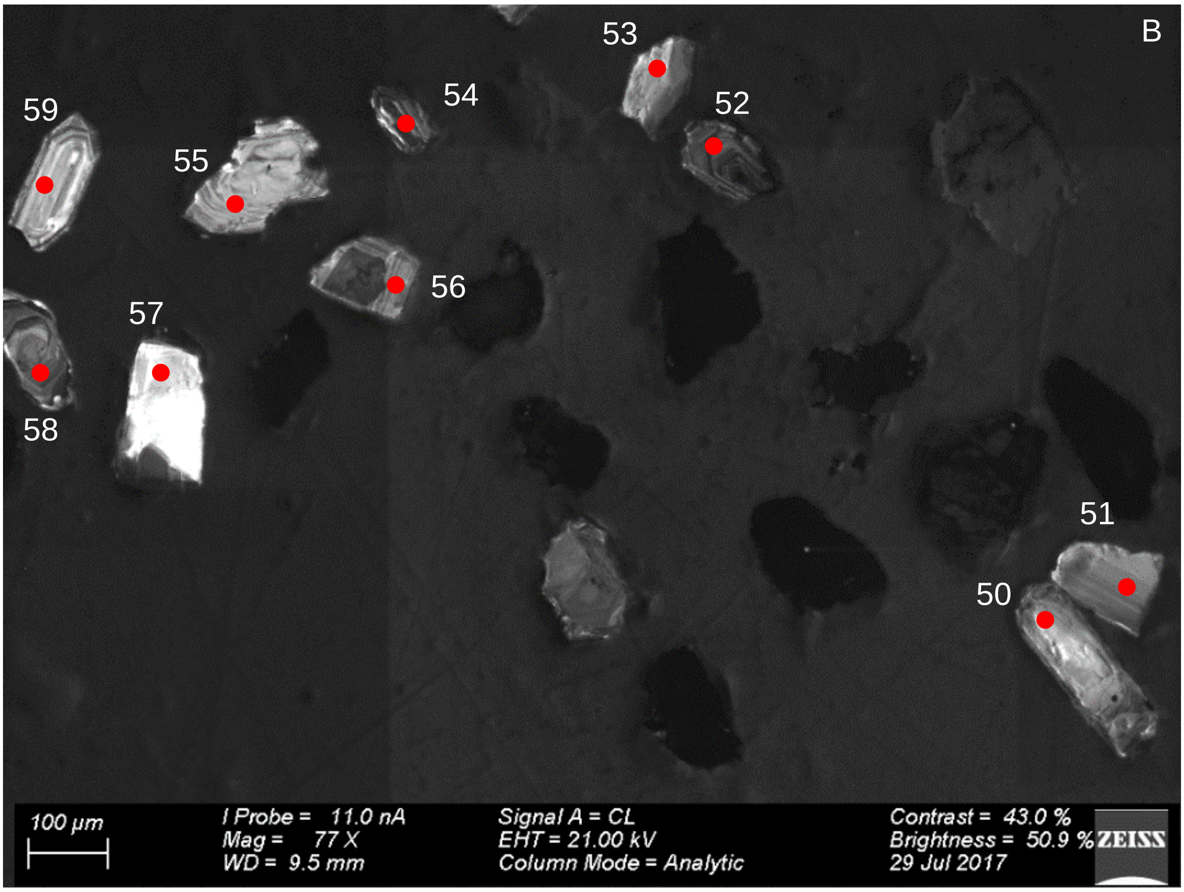
B
50
51
52
53
54
55
56
57
58
59
100 µm
I Probe = 11.0 nA
Mag = 77 X
WD = 9.5 mm
Signal A = CL
EHT = 21.00 kV
Column Mode = Analytic
Contrast = 43.0 %
Brightness = 50.9 %
29 Jul 2017
ZEISS

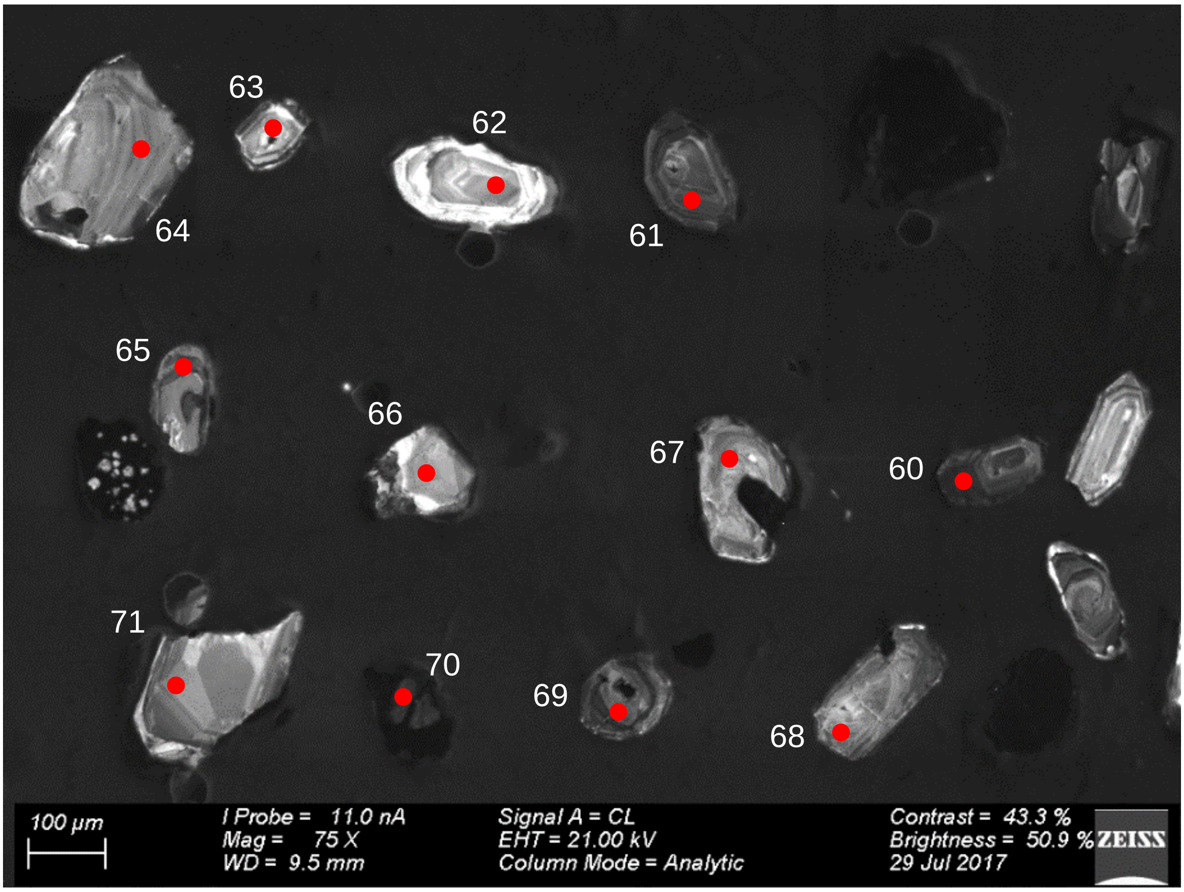

63
62
64
61
65
66
67
60
71
70
69
68
100 µm
I Probe = 11.0 nA
Mag = 75 X
WD = 9.5 mm
Signal A = CL
EHT = 21.00 kV
Column Mode = Analytic
Contrast = 43.3 %
Brightness = 50.9 %
29 Jul 2017

Appendix B: Detrital zircon age data

Table 17: Detrital zircon data for sample B1766.

Sample	U ppm	Th/U	206Pb/ 238U	+/-	207Pb/ 235U	+/-	208Pb/ 232Th	+/-	207Pb/ 206Pb	+/-	208Pb/ 206Pb	+/-	206Pb/238U age (Ga)	+/-	207Pb/235 U age (Ga)	+/-	207Pb/206Pb age (Ga)	+/-	208Pb/232Th age (Ga)	+/-	% Discordance	Concordia age (Ma)	+/-
1.6	42.9964	0.6642	0.1987	0.0143	2.2152	0.4006	0.0643	0.0106	0.0808	0.0134	0.2162	0.0418	1.1685	0.0763	1.1858	0.1192	1.2158	0.2979	1.2589	0.2002	4	1173	67
2.1	58.9859	0.3814	0.1739	0.0121	1.8571	0.3212	0.0538	0.0095	0.0774	0.0123	0.1188	0.0240	1.0337	0.0662	1.0660	0.1082	1.1328	0.2881	1.0592	0.1807	9	1041	59
4.1	104.8907	0.6887	0.1156	0.0078	1.0062	0.1745	0.0408	0.0063	0.0631	0.0101	0.2449	0.0451	0.7051	0.0451	0.7069	0.0847	0.7129	0.3076	0.8091	0.1227	1	705	41
7.1	57.3171	0.5039	0.1327	0.0096	1.2262	0.2434	0.0436	0.0076	0.0670	0.0124	0.1668	0.0335	0.8030	0.0546	0.8126	0.1053	0.8398	0.3418	0.8630	0.1463	4	805	50
7.3	505.6506	0.4381	0.1718	0.0104	1.7495	0.2099	0.0570	0.0081	0.0738	0.0077	0.1461	0.0250	1.0221	0.0569	1.0270	0.0747	1.0352	0.2002	1.1199	0.1548	1	1024	47
8.3	88.4901	1.1946	0.1860	0.0123	2.0245	0.3084	0.0547	0.0080	0.0789	0.0108	0.3535	0.0621	1.0996	0.0664	1.1238	0.0986	1.1719	0.2490	1.0768	0.1534	6	1106	57
9.1	114.0257	0.3316	0.0940	0.0065	0.7648	0.1409	0.0319	0.0055	0.0590	0.0101	0.1130	0.0225	0.5794	0.0380	0.5768	0.0780	0.5664	0.3320	0.6339	0.1084	2	579	35
10.1	46.3240	0.4130	0.1560	0.0115	1.4494	0.2937	0.0476	0.0088	0.0674	0.0127	0.1269	0.0265	0.9344	0.0638	0.9096	0.1150	0.8496	0.3516	0.9407	0.1690	10	929	57
10.2	300.9485	0.1416	0.1494	0.0092	1.4459	0.1866	0.0504	0.0080	0.0702	0.0080	0.0480	0.0088	0.8976	0.0514	0.9082	0.0747	0.9326	0.2197	0.9933	0.1540	4	901	44
10.3	168.2180	0.5417	0.1520	0.0097	1.4939	0.2111	0.0514	0.0076	0.0713	0.0090	0.1840	0.0322	0.9124	0.0538	0.9279	0.0825	0.9668	0.2344	1.0125	0.1458	6	917	47
12	137.3633	0.6837	0.1875	0.0119	1.9493	0.2727	0.0589	0.0086	0.0754	0.0094	0.2161	0.0375	1.1076	0.0644	1.0982	0.0898	1.0791	0.2344	1.1572	0.1640	3	1105	54
15.2	67.2146	0.6114	0.1944	0.0132	2.1090	0.3423	0.0541	0.0085	0.0787	0.0116	0.1709	0.0314	1.1451	0.0707	1.1517	0.1061	1.1621	0.2686	1.0642	0.1632	1	1147	61
16.1	138.1040	0.3123	0.1331	0.0087	1.2102	0.1870	0.0477	0.0076	0.0659	0.0092	0.1124	0.0207	0.8056	0.0491	0.8053	0.0825	0.8057	0.2686	0.9413	0.1460	0	806	44
16.3	26.9029	0.7150	0.1997	0.0157	2.1325	0.4637	0.0604	0.0106	0.0775	0.0157	0.2175	0.0436	1.1735	0.0841	1.1594	0.1402	1.1328	0.3564	1.1862	0.2006	4	1170	75
18.2	99.7091	0.7043	0.1846	0.0121	2.0189	0.3010	0.0560	0.0083	0.0793	0.0106	0.2146	0.0374	1.0923	0.0653	1.1219	0.0965	1.1816	0.2441	1.1014	0.1586	8	1101	56
19.2	91.4549	0.6360	0.1878	0.0124	2.0394	0.3096	0.0561	0.0085	0.0787	0.0108	0.1908	0.0336	1.1096	0.0667	1.1288	0.0985	1.1670	0.2490	1.1033	0.1613	5	1115	57
20.2	10.7552	0.3628	0.1612	0.0176	1.5670	0.5684	0.0508	0.0151	0.0705	0.0244	0.1148	0.0362	0.9632	0.0967	0.9572	0.2031	0.9424	0.5859	1.0013	0.2878	2	962	90
21.3	109.4499	0.7112	0.0967	0.0067	0.7961	0.1484	0.0273	0.0043	0.0597	0.0103	0.2012	0.0366	0.5953	0.0392	0.5946	0.0806	0.5908	0.3369	0.5434	0.0840	1	595	36
22.1	105.4938	1.1952	0.1990	0.0129	2.2456	0.3243	0.0515	0.0074	0.0818	0.0106	0.3106	0.0523	1.1700	0.0688	1.1954	0.0967	1.2402	0.2344	1.0149	0.1409	6	1178	58
25.1	31.6720	0.5914	0.1768	0.0138	1.8862	0.4070	0.0584	0.0103	0.0774	0.0156	0.1960	0.0391	1.0495	0.0753	1.0762	0.1340	1.1328	0.3540	1.1464	0.1950	7	1055	68
25.2	255.6333	1.2299	0.0862	0.0055	0.6888	0.1052	0.0233	0.0033	0.0579	0.0080	0.3331	0.0556	0.5331	0.0326	0.5321	0.0614	0.5273	0.2783	0.4647	0.0648	1	533	30
27.1	56.2822	0.6163	0.0991	0.0077	0.8014	0.1899	0.0294	0.0052	0.0587	0.0131	0.1833	0.0369	0.6091	0.0448	0.5976	0.1018	0.5566	0.4248	0.5849	0.1019	9	607	42
27.2	190.7397	0.6563	0.1938	0.0120	2.0921	0.2752	0.0535	0.0076	0.0783	0.0091	0.1818	0.0302	1.1420	0.0647	1.1462	0.0866	1.1523	0.2148	1.0526	0.1451	1	1143	54
28.1	71.2666	0.3097	0.1967	0.0132	2.0285	0.3295	0.0550	0.0094	0.0748	0.0111	0.0869	0.0167	1.1577	0.0710	1.1251	0.1049	1.0645	0.2686	1.0814	0.1800	9	1148	61
28.2	80.4888	0.5093	0.1425	0.0098	1.2872	0.2292	0.0430	0.0069	0.0655	0.0108	0.1543	0.0283	0.8588	0.0550	0.8401	0.0970	0.7910	0.3125	0.8512	0.1333	9	855	49
29.2	143.2154	0.4846	0.1719	0.0109	1.7334	0.2477	0.0572	0.0084	0.0731	0.0094	0.1620	0.0274	1.0224	0.0599	1.0210	0.0881	1.0156	0.2441	1.1248	0.1594	1	1022	51
29.3	170.9722	0.4085	0.1512	0.0096	1.5124	0.2143	0.0508	0.0075	0.0726	0.0092	0.1377	0.0235	0.9075	0.0534	0.9354	0.0831	1.0010	0.2393	1.0011	0.1436	9	915	47
29.4	240.0517	0.2502	0.1666	0.0103	1.6850	0.2211	0.0524	0.0078	0.0733	0.0085	0.0790	0.0135	0.9934	0.0566	1.0029	0.0803	1.0254	0.2148	1.0331	0.1497	3	996	48
30.4	100.9841	0.4502	0.1857	0.0121	1.9612	0.2953	0.0681	0.0102	0.0766	0.0104	0.1658	0.0285	1.0978	0.0655	1.1023	0.0965	1.1133	0.2490	1.3319	0.1917	1	1099	56
33.1	181.0790	0.4829	0.1605	0.0101	1.5571	0.2172	0.0480	0.0070	0.0704	0.0088	0.1451	0.0242	0.9594	0.0558	0.9533	0.0828	0.9375	0.2393	0.9485	0.1337	2	958	48
34.1	221.8468	0.5657	0.1872	0.0115	2.0640	0.2670	0.0567	0.0079	0.0800	0.0091	0.1718	0.0278	1.1060	0.0624	1.1370	0.0848	1.1963	0.2100	1.1140	0.1507	8	1116	52
38.2	260.5341	2.9342	0.0947	0.0060	0.7879	0.1172	0.0281	0.0038	0.0604	0.0081	0.8743	0.1379	0.5831	0.0352	0.5900	0.0645	0.6152	0.2686	0.5605	0.0740	5	585	32
39.1	53.5065	0.5198	0.2139	0.0148	2.5462	0.4269	0.0671	0.0106	0.0864	0.0132	0.1637	0.0293	1.2493	0.0784	1.2854	0.1154	1.3477	0.2686	1.3135	0.1998	7	1259	68
41.3	284.0352	0.4532	0.1713	0.0105	1.8115	0.2307	0.0557	0.0077	0.0767	0.0086	0.1478	0.0237	1.0195	0.0574	1.0496	0.0801	1.1133	0.2100	1.0955	0.1475	8	1029	49
42.1	221.5917	0.0918	0.0846	0.0055	0.6823	0.1094	0.0285	0.0058	0.0585	0.0086	0.0311	0.0067	0.5235	0.0325	0.5282	0.0640	0.5469	0.2930	0.5684	0.1129	4	524	30
42.2	139.7196	0.7800	0.1754	0.0112	1.8201	0.2605	0.0555	0.0078	0.0753	0.0096	0.2476	0.0401	1.0417	0.0610	1.0527	0.0897	1.0742	0.2393	1.0918	0.1482	3	1045	52

Table 18: Detrital zircon data for B1775.

Sample	U ppm	Th/U	206Pb /238U	+/-	207Pb /235U	+/-	208Pb/ 232Th	+/-	207Pb/ 206Pb	+/-	208Pb/ 206Pb	+/-	206Pb/238U age (Ga)	+/-	207Pb/235U age (Ga)	+/-	207Pb/206Pb age (Ga)	+/-	208Pb/232Th age	+/-	% Discordance	Concordia age	+/-
1.2	212.9836	0.7666	0.1819	0.0062	1.9721	0.2374	0.0594	0.0112	0.0786	0.0091	0.2525	0.0528	1.0776	0.0335	1.1060	0.0780	1.1621	0.2148	1.1654	0.2125	7	1081	31
1.3	401.0054	0.6998	0.1989	0.0062	2.1795	0.2405	0.0599	0.0112	0.0795	0.0084	0.2129	0.0441	1.1695	0.0331	1.1745	0.0740	1.1816	0.2002	1.1762	0.2123	1	1170	31
2.2	193.0010	0.3880	0.1517	0.0054	1.5172	0.1942	0.0510	0.0099	0.0725	0.0089	0.1317	0.0282	0.9105	0.0299	0.9374	0.0755	1.0010	0.2295	1.0052	0.1891	9	914	28
3.1	79.3059	0.6987	0.1447	0.0064	1.4038	0.2296	0.0483	0.0095	0.0704	0.0111	0.2355	0.0515	0.8710	0.0360	0.8905	0.0926	0.9375	0.2930	0.9530	0.1826	7	873	34
3.2	282.3192	0.5919	0.1801	0.0059	1.9577	0.2271	0.0561	0.0105	0.0788	0.0088	0.1863	0.0388	1.0676	0.0319	1.1011	0.0751	1.1670	0.2051	1.1040	0.2002	9	1072	30
3.3	450.8271	0.6340	0.1870	0.0058	1.9198	0.2121	0.0541	0.0100	0.0745	0.0079	0.1853	0.0383	1.1050	0.0312	1.0880	0.0712	1.0547	0.2002	1.0652	0.1916	5	1102	29
3.5	259.7143	0.5080	0.1828	0.0060	1.8897	0.2227	0.0558	0.0105	0.0750	0.0085	0.1566	0.0327	1.0820	0.0326	1.0775	0.0754	1.0693	0.2100	1.0974	0.1995	1	1081	30
4.2	119.0749	0.5270	0.1754	0.0067	1.8541	0.2531	0.0581	0.0112	0.0767	0.0101	0.1765	0.0377	1.0416	0.0364	1.0649	0.0863	1.1133	0.2393	1.1423	0.2126	6	1045	34
4.3	441.6667	0.5632	0.1937	0.0059	2.0010	0.2211	0.0589	0.0108	0.0749	0.0080	0.1730	0.0356	1.1413	0.0320	1.1159	0.0722	1.0645	0.2002	1.1571	0.2059	7	1137	30
5.1	309.5763	0.5908	0.1665	0.0054	1.7356	0.2024	0.0552	0.0102	0.0756	0.0085	0.1980	0.0409	0.9926	0.0297	1.0218	0.0725	1.0840	0.2100	1.0869	0.1947	8	993	28
5.4	94.5194	0.5222	0.2697	0.0099	3.6572	0.4605	0.0831	0.0158	0.0983	0.0118	0.1624	0.0344	1.5395	0.0503	1.5621	0.0957	1.5918	0.2100	1.6131	0.2923	3	1544	46
5.5	75.4713	0.8518	0.1792	0.0076	1.8714	0.2872	0.0586	0.0112	0.0757	0.0112	0.2812	0.0599	1.0628	0.0415	1.0710	0.0968	1.0889	0.2686	1.1508	0.2118	2	1064	39
6.3	101.3057	0.6574	0.1729	0.0068	1.8359	0.2620	0.0572	0.0108	0.0770	0.0106	0.2196	0.0466	1.0279	0.0375	1.0584	0.0897	1.1230	0.2490	1.1240	0.2063	8	1032	35
6.4	159.2670	0.4861	0.1977	0.0069	2.0420	0.2580	0.0567	0.0107	0.0749	0.0091	0.1409	0.0296	1.1628	0.0371	1.1296	0.0827	1.0645	0.2295	1.1153	0.2031	9	1158	34
7.1	322.2778	0.6012	0.1828	0.0058	1.8306	0.2113	0.0551	0.0101	0.0726	0.0081	0.1831	0.0376	1.0823	0.0316	1.0565	0.0731	1.0059	0.2100	1.0848	0.1923	8	1079	29
7.3	134.5869	0.4838	0.1997	0.0072	2.1355	0.2768	0.0600	0.0113	0.0776	0.0097	0.1467	0.0309	1.1738	0.0386	1.1604	0.0859	1.1377	0.2295	1.1768	0.2145	3	1172	36
7.4	75.8587	0.6269	0.1614	0.0070	1.6637	0.2642	0.0532	0.0103	0.0747	0.0114	0.2085	0.0451	0.9648	0.0389	0.9948	0.0960	1.0596	0.2832	1.0467	0.1963	9	968	37
8	239.5566	0.0950	0.1887	0.0062	2.0708	0.2454	0.0596	0.0122	0.0796	0.0091	0.0303	0.0068	1.1144	0.0336	1.1392	0.0781	1.1865	0.2100	1.1695	0.2311	6	1118	31
9.2	59.9224	0.3657	0.1733	0.0080	1.7504	0.2948	0.0551	0.0114	0.0733	0.0119	0.1175	0.0269	1.0302	0.0436	1.0273	0.1034	1.0205	0.2979	1.0849	0.2176	1	1030	41
10.1	39.1993	0.5626	0.2153	0.0102	2.3403	0.4012	0.0594	0.0096	0.0788	0.0130	0.1570	0.0292	1.2572	0.0538	1.2246	0.1152	1.1670	0.2979	1.1661	0.1827	8	1252	50
10.2	529.1617	0.6951	0.1826	0.0052	1.8877	0.2054	0.0546	0.0072	0.0750	0.0079	0.2102	0.0334	1.0810	0.0282	1.0768	0.0698	1.0693	0.1953	1.0739	0.1379	1	1080	27
10.3	201.0594	0.7685	0.1918	0.0061	2.1405	0.2553	0.0581	0.0078	0.0809	0.0093	0.2354	0.0380	1.1312	0.0329	1.1620	0.0794	1.2207	0.2100	1.1411	0.1493	7	1135	31
10.4	41.4548	0.7399	0.2558	0.0113	3.4135	0.5190	0.0800	0.0118	0.0968	0.0141	0.2340	0.0407	1.4684	0.0578	1.5075	0.1129	1.5625	0.2515	1.5549	0.2205	6	1475	53
11.1	451.6301	0.3951	0.1675	0.0049	1.6503	0.1841	0.0474	0.0064	0.0715	0.0077	0.1132	0.0182	0.9981	0.0268	0.9897	0.0682	0.9717	0.2051	0.9363	0.1233	3	997	25
11.2	141.1505	0.9358	0.1717	0.0060	1.7244	0.2269	0.0533	0.0073	0.0728	0.0092	0.2940	0.0479	1.0216	0.0327	1.0177	0.0812	1.0107	0.2344	1.0502	0.1389	1	1021	31
11.3	320.7963	0.6237	0.1927	0.0057	1.9909	0.2259	0.0546	0.0073	0.0749	0.0082	0.1786	0.0286	1.1362	0.0309	1.1124	0.0739	1.0645	0.2075	1.0738	0.1395	7	1133	29
12.1	183.8470	0.6482	0.1795	0.0058	1.9472	0.2392	0.0589	0.0080	0.0787	0.0093	0.2150	0.0350	1.0642	0.0319	1.0975	0.0792	1.1621	0.2197	1.1559	0.1524	8	1068	30
12.4	81.2245	0.7405	0.1956	0.0076	2.1187	0.3034	0.0637	0.0090	0.0786	0.0108	0.2440	0.0410	1.1516	0.0406	1.1549	0.0943	1.1621	0.2490	1.2487	0.1704	1	1152	38
13.1	86.6069	0.5738	0.1733	0.0068	1.8424	0.2689	0.0566	0.0082	0.0771	0.0108	0.1894	0.0325	1.0303	0.0371	1.0607	0.0918	1.1230	0.2588	1.1125	0.1566	8	1034	35
14.2	226.6910	0.4680	0.1879	0.0062	2.0820	0.2499	0.0563	0.0101	0.0804	0.0093	0.1416	0.0289	1.1100	0.0336	1.1429	0.0792	1.2061	0.2100	1.1077	0.1929	8	1114	32
14.5	453.6503	0.7030	0.1951	0.0059	2.1608	0.2394	0.0591	0.0103	0.0803	0.0086	0.2149	0.0429	1.1488	0.0318	1.1685	0.0741	1.2061	0.1953	1.1602	0.1962	5	1152	30
15.4	441.8997	0.5672	0.1853	0.0056	2.0450	0.2283	0.0595	0.0104	0.0800	0.0086	0.1837	0.0367	1.0961	0.0306	1.1306	0.0734	1.1963	0.2002	1.1679	0.1972	8	1101	29
16.1	32.4244	0.6401	0.1754	0.0100	1.7211	0.3652	0.0523	0.0107	0.0712	0.0145	0.1925	0.0444	1.0417	0.0546	1.0165	0.1279	0.9619	0.3711	1.0300	0.2052	8	1038	51
16.2	199.5627	0.6635	0.1822	0.0062	1.9150	0.2378	0.0583	0.0103	0.0762	0.0091	0.2143	0.0433	1.0790	0.0335	1.0863	0.0796	1.1035	0.2197	1.1455	0.1959	2	1080	31
18.2	402.9044	0.3157	0.1850	0.0057	1.8798	0.2136	0.0520	0.0092	0.0737	0.0081	0.0894	0.0180	1.0942	0.0308	1.0740	0.0727	1.0352	0.2051	1.0238	0.1752	6	1091	29
18.4	362.9535	0.9255	0.1844	0.0057	1.9584	0.2242	0.0567	0.0098	0.0770	0.0085	0.2872	0.0569	1.0911	0.0311	1.1013	0.0742	1.1230	0.2051	1.1155	0.1859	3	1092	29
19.1	234.9981	0.6025	0.1657	0.0055	1.7013	0.2101	0.0515	0.0090	0.0745	0.0089	0.1890	0.0380	0.9882	0.0305	1.0090	0.0761	1.0547	0.2246	1.0155	0.1728	6	991	29
19.2	196.1813	0.8495	0.1816	0.0062	1.9038	0.2380	0.0585	0.0102	0.0760	0.0091	0.2761	0.0552	1.0758	0.0335	1.0824	0.0800	1.0938	0.2246	1.1494	0.1932	2	1077	31
19.3	59.5189	0.8565	0.1589	0.0075	1.5787	0.2787	0.0499	0.0092	0.0720	0.0123	0.2714	0.0574	0.9509	0.0417	0.9618	0.1042	0.9863	0.3125	0.9848	0.1767	4	952	39
22.1	224.8683	0.3407	0.1924	0.0063	2.0321	0.2464	0.0610	0.0108	0.0766	0.0089	0.1089	0.0221	1.1345	0.0341	1.1263	0.0793	1.1084	0.2197	1.1967	0.2051	2	1133	32
22.2	154.2127	0.6717	0.1859	0.0066	1.9388	0.2526	0.0541	0.0095	0.0756	0.0095	0.1970	0.0398	1.0990	0.0356	1.0946	0.0837	1.0840	0.2344	1.0641	0.1814	1	1098	33
23.2	235.2537	0.5027	0.1857	0.0061	1.9890	0.2405	0.0569	0.0099	0.0777	0.0090	0.1552	0.0311	1.0981	0.0330	1.1118	0.0786	1.1377	0.2148	1.1181	0.1887	3	1100	31
23.3	149.1911	0.6706	0.1929	0.0068	2.1440	0.2765	0.0589	0.0103	0.0806	0.0100	0.2065	0.0416	1.1369	0.0367	1.1631	0.0856	1.2109	0.2295	1.1568	0.1958	6	1140	34
24.1	192.5748	0.5765	0.1957	0.0066	2.0505	0.2546	0.0559	0.0098	0.0760	0.0091	0.1661	0.0333	1.1519	0.0353	1.1325	0.0814	1.0938	0.2246	1.0997	0.1858	5	1149	33
24.3	246.4884	0.6353	0.1870	0.0061	1.8744	0.2270	0.0522	0.0090	0.0727	0.0085	0.1786	0.0356	1.1052	0.0329	1.0721	0.0772	1.0059	0.2197	1.0278	0.1722	10	1100	31
24.4	200.2843	0.6323	0.1905	0.0064	1.9639	0.2443	0.0550	0.0095	0.0748	0.0090	0.1842	0.0367	1.1240	0.0344	1.1032	0.0804	1.0645	0.2197	1.0831	0.1813	6	1121	32
26.1	242.3685	0.6848	0.1865	0.0061	2.0275	0.2443	0.0544	0.0093	0.0788	0.0091	0.2013	0.0398	1.1025	0.0329	1.1248	0.0788	1.1670	0.2148	1.0708	0.1773	6	1105	31
26.3	83.8738	0.6113	0.1532	0.0066	1.5205	0.2452	0.0458	0.0084	0.0720	0.0112	0.1841	0.0385	0.9191	0.0366	0.9387	0.0942	0.9863	0.2881	0.9054	0.1608	7	921	35
27	370.9682	0.2699	0.1825	0.0056	1.9537	0.2248	0.0553	0.0095	0.0777	0.0086	0.0823	0.0164	1.0804	0.0306	1.0997	0.0745	1.1377	0.2051	1.0871	0.1818	5	1083	29

28.3	212.2544	0.6734	0.1731	0.0058	1.8448	0.2305	0.0567	0.0096	0.0773	0.0093	0.2223	0.0439	1.0292	0.0318	1.0616	0.0791	1.1279	0.2246	1.1156	0.1834	9	1097	39
29.1	117.9145	0.4734	0.1414	0.0056	1.2912	0.1977	0.0416	0.0075	0.0662	0.0098	0.1403	0.0292	0.8527	0.0317	0.8418	0.0840	0.8105	0.2832	0.8245	0.1459	5	851	30
29.3	122.5206	0.5407	0.1813	0.0067	1.8588	0.2586	0.0514	0.0090	0.0744	0.0100	0.1545	0.0313	1.0739	0.0367	1.0666	0.0879	1.0498	0.2490	1.0140	0.1727	2	1073	34
29.4	102.6347	0.4345	0.1881	0.0073	1.9806	0.2833	0.0518	0.0094	0.0764	0.0105	0.1204	0.0250	1.1108	0.0392	1.1089	0.0922	1.1035	0.2539	1.0206	0.1789	1	1111	37
30.2	277.9529	0.9358	0.1765	0.0056	1.8974	0.2276	0.0536	0.0089	0.0780	0.0090	0.2858	0.0555	1.0478	0.0309	1.0802	0.0768	1.1475	0.2148	1.0547	0.1695	9	1052	29
31.1	117.0193	0.4253	0.2120	0.0077	2.4969	0.3314	0.0654	0.0114	0.0854	0.0109	0.1319	0.0267	1.2397	0.0410	1.2711	0.0919	1.3232	0.2295	1.2799	0.2158	6	1244	38
32.4	250.2449	1.0543	0.1935	0.0062	2.0899	0.2518	0.0540	0.0088	0.0783	0.0091	0.2960	0.0571	1.1402	0.0334	1.1455	0.0795	1.1572	0.2148	1.0637	0.1688	1	1141	31
34.1	115.5579	0.5524	0.1955	0.0073	2.1200	0.2924	0.0579	0.0099	0.0787	0.0104	0.1644	0.0329	1.1510	0.0390	1.1554	0.0910	1.1621	0.2441	1.1376	0.1886	1	1152	37
34.2	46.4329	0.4812	0.2143	0.0101	2.5164	0.4248	0.0668	0.0125	0.0852	0.0138	0.1507	0.0322	1.2518	0.0536	1.2768	0.1158	1.3184	0.2856	1.3071	0.2350	5	1256	50
35.2	124.4944	0.5848	0.1851	0.0068	1.9588	0.2704	0.0534	0.0091	0.0767	0.0102	0.1695	0.0337	1.0950	0.0370	1.1015	0.0888	1.1133	0.2441	1.0515	0.1737	2	1096	35
36.2	76.5255	0.2760	0.1508	0.0067	1.4802	0.2505	0.0499	0.0098	0.0712	0.0116	0.0918	0.0203	0.9056	0.0374	0.9223	0.0977	0.9619	0.3027	0.9844	0.1870	6	907	36
37.1	248.8313	0.7181	0.1844	0.0059	1.8611	0.2286	0.0519	0.0085	0.0732	0.0087	0.2031	0.0391	1.0910	0.0323	1.0674	0.0781	1.0205	0.2197	1.0234	0.1620	7	1088	30
37.2	168.3033	1.0488	0.1771	0.0062	1.8247	0.2405	0.0489	0.0080	0.0747	0.0095	0.2905	0.0561	1.0513	0.0336	1.0544	0.0830	1.0596	0.2393	0.9641	0.1530	1	1052	32
37.3	118.9748	0.7549	0.1778	0.0067	1.8083	0.2572	0.0494	0.0083	0.0738	0.0101	0.2106	0.0415	1.0548	0.0365	1.0485	0.0890	1.0352	0.2539	0.9743	0.1588	2	1054	34

Table 19: Detrital zircon data for B1778

Sample	U ppm	Th/U	206Pb/ 238U	+/-	207Pb/ 235U	+/-	208Pb/ 232Th	+/-	207Pb/ 206Pb	+/-	208Pb/ 206Pb	206Pb/238U age (Ga)	+/-	207Pb/235U age (Ga)	+/-	207Pb/206Pb age (Ga)	+/-	208Pb*/232Th age (Ga)	+/-	% Discordance	Concordia age	+/-
1	206.4830	0.7570	0.1230	0.0053	1.1129	0.1497	0.0368	0.0053	0.0656	0.0084	0.2303	0.7476	0.0304	0.7596	0.0695	0.7959	0.2441	0.7301	0.1029	6	749	28
1	187.4606	0.5529	0.1696	0.0068	1.6836	0.1973	0.0491	0.0067	0.0720	0.0079	0.1619	1.0097	0.0375	1.0023	0.0720	0.9863	0.2100	0.9694	0.1296	2	1008	34
2.1	135.2269	0.4937	0.1770	0.0078	1.8941	0.2479	0.0585	0.0088	0.0776	0.0096	0.1661	1.0503	0.0425	1.0790	0.0835	1.1377	0.2271	1.1498	0.1666	8	1055	39
3	631.2157	0.6586	0.1839	0.0065	1.8965	0.1757	0.0554	0.0074	0.0748	0.0064	0.2018	1.0883	0.0354	1.0799	0.0598	1.0645	0.1611	1.0907	0.1417	2	1086	31
5.2	149.8066	0.6608	0.1754	0.0075	1.7706	0.2276	0.0581	0.0083	0.0732	0.0089	0.2227	1.0417	0.0412	1.0348	0.0802	1.0205	0.2295	1.1424	0.1583	2	1040	38
5.3	132.1560	0.6910	0.1915	0.0083	2.1234	0.2693	0.0584	0.0084	0.0804	0.0096	0.2142	1.1292	0.0448	1.1564	0.0840	1.2061	0.2197	1.1473	0.1600	6	1135	41
6.1	610.4418	0.6402	0.1897	0.0067	2.0035	0.1847	0.0608	0.0081	0.0766	0.0065	0.2085	1.1200	0.0363	1.1167	0.0606	1.1084	0.1611	1.1932	0.1538	1	1119	32
6.2	116.0621	0.8030	0.2078	0.0091	2.3991	0.3053	0.0609	0.0087	0.0837	0.0100	0.2392	1.2171	0.0486	1.2423	0.0873	1.2842	0.2197	1.1956	0.1653	5	1222	44
7.1	1137.3174	0.7715	0.1596	0.0055	1.6031	0.1411	0.0487	0.0064	0.0728	0.0059	0.2390	0.9546	0.0305	0.9714	0.0536	1.0107	0.1563	0.9604	0.1231	6	958	27
8.1	120.1705	0.6695	0.1837	0.0082	1.8913	0.2540	0.0590	0.0085	0.0747	0.0095	0.2184	1.0873	0.0444	1.0780	0.0855	1.0596	0.2344	1.1589	0.1622	3	1086	40
9.1	289.8113	0.7286	0.1881	0.0071	1.8993	0.1999	0.0552	0.0075	0.0732	0.0072	0.2169	1.1112	0.0386	1.0808	0.0677	1.0205	0.1855	1.0851	0.1426	9	1104	34
9.2	267.1105	0.6174	0.1830	0.0070	1.8258	0.1973	0.0549	0.0075	0.0724	0.0073	0.1882	1.0833	0.0383	1.0548	0.0685	0.9961	0.1904	1.0812	0.1439	9	1077	34
9.3	593.6106	0.7449	0.1895	0.0067	1.9895	0.1833	0.0587	0.0077	0.0762	0.0065	0.2343	1.1184	0.0362	1.1119	0.0604	1.0986	0.1611	1.1532	0.1472	2	1117	32
10.1	170.5427	0.3933	0.1543	0.0066	1.5188	0.1945	0.0455	0.0069	0.0714	0.0086	0.1176	0.9252	0.0366	0.9380	0.0755	0.9668	0.2295	0.8988	0.1328	4	927	34
10.2	152.7581	1.0524	0.1938	0.0081	2.0493	0.2487	0.0548	0.0075	0.0767	0.0087	0.3020	1.1419	0.0436	1.1321	0.0796	1.1133	0.2100	1.0781	0.1434	3	1140	39
11.1	238.5043	0.6620	0.1776	0.0070	1.9176	0.2105	0.0576	0.0079	0.0783	0.0080	0.2179	1.0540	0.0380	1.0872	0.0707	1.1523	0.1953	1.1319	0.1499	9	1061	34
11.2	86.9023	0.7072	0.1902	0.0091	2.0566	0.2988	0.0589	0.0087	0.0784	0.0108	0.2221	1.1224	0.0489	1.1345	0.0947	1.1572	0.2490	1.1561	0.1657	3	1125	45
11.4	311.5483	0.6247	0.1763	0.0067	1.8545	0.1926	0.0559	0.0075	0.0763	0.0074	0.2008	1.0466	0.0364	1.0650	0.0663	1.1035	0.1807	1.0985	0.1439	5	1050	33
12.1	222.3837	0.6546	0.1905	0.0075	1.9697	0.2177	0.0575	0.0079	0.0750	0.0077	0.2006	1.1240	0.0403	1.1052	0.0718	1.0693	0.1953	1.1308	0.1501	5	1120	36
12.2	304.0308	0.3271	0.1887	0.0071	1.9800	0.2036	0.0594	0.0083	0.0761	0.0073	0.1045	1.1144	0.0384	1.1087	0.0671	1.0986	0.1807	1.1663	0.1585	1	1113	34
13.1	405.4685	0.6831	0.1931	0.0070	2.0879	0.2016	0.0615	0.0081	0.0784	0.0070	0.2208	1.1379	0.0378	1.1448	0.0642	1.1572	0.1709	1.2065	0.1545	2	1140	33
13.2	439.9333	0.5920	0.1829	0.0066	1.8373	0.1781	0.0560	0.0074	0.0729	0.0066	0.1839	1.0825	0.0360	1.0589	0.0618	1.0107	0.1709	1.1016	0.1418	7	1077	32
14	16.5619	1.7887	0.2109	0.0173	2.2927	0.6288	0.0592	0.0098	0.0788	0.0206	0.5092	1.2336	0.0915	1.2100	0.1775	1.1670	0.4492	1.1628	0.1855	6	1229	84
15.1	149.2190	0.4915	0.1784	0.0076	1.8093	0.2271	0.0562	0.0081	0.0735	0.0087	0.1570	1.0585	0.0412	1.0488	0.0789	1.0303	0.2197	1.1058	0.1549	3	1057	37
15.2	549.7557	0.6484	0.1915	0.0068	2.0293	0.1872	0.0619	0.0081	0.0769	0.0066	0.2125	1.1292	0.0365	1.1254	0.0609	1.1182	0.1611	1.2141	0.1535	1	1128	32
15.3	348.2468	0.7402	0.1820	0.0067	1.9781	0.1974	0.0588	0.0078	0.0788	0.0073	0.2423	1.0781	0.0366	1.1081	0.0652	1.1670	0.1758	1.1546	0.1478	8	1085	33
16.1	370.0486	0.5880	0.1833	0.0067	1.8868	0.1874	0.0561	0.0075	0.0746	0.0069	0.1823	1.0852	0.0366	1.0764	0.0639	1.0596	0.1758	1.1026	0.1424	2	1083	32
16.2	356.7704	0.7144	0.1744	0.0065	1.7032	0.1735	0.0498	0.0066	0.0708	0.0067	0.2066	1.0365	0.0354	1.0097	0.0632	0.9521	0.1807	0.9817	0.1269	9	1030	32
17.1	447.1377	0.5626	0.1698	0.0062	1.6665	0.1632	0.0506	0.0067	0.0712	0.0065	0.1699	1.0112	0.0338	0.9958	0.0603	0.9619	0.1758	0.9981	0.1288	5	1008	30
17.2	592.3443	0.6772	0.1882	0.0066	1.9646	0.1798	0.0573	0.0075	0.0757	0.0064	0.2090	1.1114	0.0358	1.1035	0.0598	1.0889	0.1611	1.1264	0.1421	2	1109	31
17.3	353.2366	0.4745	0.0877	0.0036	0.7025	0.0892	0.0243	0.0035	0.0581	0.0070	0.1335	0.5419	0.0210	0.5403	0.0518	0.5371	0.2393	0.4861	0.0687	1	542	20
18	83.6856	0.6475	0.1983	0.0094	2.1963	0.3124	0.0646	0.0095	0.0803	0.0108	0.2137	1.1663	0.0502	1.1799	0.0947	1.2061	0.2441	1.2652	0.1789	3	1169	46
20.2	81.8347	0.8721	0.1426	0.0073	1.3859	0.2333	0.0444	0.0066	0.0705	0.0113	0.2751	0.8595	0.0413	0.8830	0.0947	0.9424	0.2979	0.8786	0.1265	9	863	39
23	154.2778	0.3041	0.1420	0.0062	1.3426	0.1805	0.0453	0.0071	0.0686	0.0087	0.0982	0.8558	0.0348	0.8644	0.0754	0.8887	0.2393	0.8956	0.1362	4	857	32
24.1	18.4353	0.8261	0.1792	0.0147	1.8398	0.5202	0.0489	0.0098	0.0745	0.0202	0.2280	1.0624	0.0799	1.0598	0.1708	1.0547	0.4663	0.9642	0.1878	1	1062	75
25	85.9270	0.6408	0.1649	0.0080	1.6556	0.2543	0.0540	0.0080	0.0728	0.0106	0.2123	0.9838	0.0442	0.9917	0.0928	1.0107	0.2686	1.0626	0.1524	3	985	41
26.1	125.6943	0.6247	0.1887	0.0081	1.9507	0.2489	0.0541	0.0077	0.0750	0.0090	0.1814	1.1144	0.0438	1.0987	0.0822	1.0693	0.2246	1.0657	0.1462	4	1111	40
26.2	70.0953	0.6294	0.1572	0.0082	1.5614	0.2645	0.0471	0.0073	0.0720	0.0116	0.1907	0.9411	0.0455	0.9550	0.0998	0.9863	0.2979	0.9298	0.1413	5	943	42
26.3	42.9396	0.8685	0.2092	0.0118	2.2925	0.4076	0.0656	0.0100	0.0795	0.0134	0.2756	1.2244	0.0625	1.2100	0.1185	1.1865	0.2979	1.2843	0.1884	3	1222	57
27.1	350.2674	0.5730	0.1898	0.0069	2.0188	0.1981	0.0556	0.0073	0.0772	0.0070	0.1700	1.1201	0.0374	1.1219	0.0645	1.1230	0.1758	1.0945	0.1395	0	1121	33
28.1	212.4588	0.5474	0.1691	0.0067	1.7310	0.1959	0.0551	0.0075	0.0742	0.0079	0.1805	1.0073	0.0368	1.0201	0.0703	1.0498	0.2002	1.0846	0.1428	4	1010	33
29.1	914.8731	0.2880	0.1521	0.0052	1.4287	0.1274	0.0487	0.0063	0.0681	0.0056	0.0932	0.9130	0.0292	0.9010	0.0519	0.8691	0.1660	0.9609	0.1219	5	910	26

33.1	327.9657	0.7302	0.1826	0.0067	1.9613	0.1947	0.0586	0.0076	0.0779	0.0072	0.2367	1.0811	0.0365	1.1023	0.0647	1.1426	0.1758	1.1503	0.1437	5	1086	33
33.2	386.8248	0.8409	0.1674	0.0061	1.6939	0.1672	0.0502	0.0064	0.0734	0.0067	0.2550	0.9980	0.0336	1.0062	0.0611	1.0254	0.1758	0.9908	0.1235	3	1000	30
34.1	248.7269	0.5828	0.1846	0.0070	1.9676	0.2066	0.0545	0.0072	0.0773	0.0076	0.1740	1.0919	0.0380	1.1045	0.0683	1.1279	0.1855	1.0732	0.1380	3	1095	34
35	253.5028	0.9013	0.1875	0.0071	1.9448	0.2034	0.0534	0.0069	0.0752	0.0073	0.2592	1.1076	0.0383	1.0967	0.0678	1.0742	0.1855	1.0509	0.1319	3	1105	34
36.1	288.9561	0.6428	0.1797	0.0067	1.8486	0.1895	0.0553	0.0072	0.0746	0.0071	0.1999	1.0651	0.0365	1.0629	0.0654	1.0596	0.1807	1.0885	0.1371	1	1065	33
36.3	341.8467	0.5994	0.1853	0.0067	1.9489	0.1911	0.0541	0.0070	0.0763	0.0069	0.1769	1.0957	0.0366	1.0981	0.0638	1.1035	0.1709	1.0659	0.1337	1	1097	39
36.4	88.0201	0.4714	0.1663	0.0079	1.6575	0.2472	0.0550	0.0083	0.0723	0.0102	0.1575	0.9916	0.0435	0.9924	0.0903	0.9961	0.2637	1.0824	0.1579	0	992	40
38.1	255.2537	0.5726	0.1786	0.0068	1.8577	0.1951	0.0538	0.0071	0.0754	0.0074	0.1741	1.0592	0.0368	1.0662	0.0670	1.0791	0.1855	1.0587	0.1350	2	1061	33
38.2	401.3551	0.7372	0.1904	0.0068	2.0073	0.1900	0.0594	0.0075	0.0765	0.0067	0.2319	1.1237	0.0367	1.1180	0.0622	1.1084	0.1660	1.1654	0.1429	1	1122	32
39.1	162.3520	0.6606	0.1928	0.0077	2.1620	0.2448	0.0589	0.0078	0.0813	0.0086	0.2036	1.1363	0.0417	1.1689	0.0757	1.2305	0.1953	1.1562	0.1490	8	1143	38
39.2	233.5281	0.7247	0.1455	0.0057	1.4164	0.1619	0.0461	0.0060	0.0706	0.0076	0.2317	0.8758	0.0321	0.8959	0.0658	0.9473	0.2051	0.9111	0.1163	8	879	30
41.1	434.1244	0.6598	0.1762	0.0063	1.8190	0.1723	0.0546	0.0069	0.0749	0.0066	0.2064	1.0461	0.0343	1.0523	0.0602	1.0645	0.1660	1.0750	0.1321	2	1047	31
41.2	187.2838	0.8012	0.1601	0.0064	1.5828	0.1863	0.0458	0.0060	0.0717	0.0079	0.2315	0.9573	0.0357	0.9635	0.0707	0.9766	0.2100	0.9059	0.1164	2	958	33
43.1	612.0169	0.6692	0.1708	0.0059	1.7604	0.1590	0.0525	0.0066	0.0747	0.0062	0.2077	1.0167	0.0325	1.0310	0.0569	1.0596	0.1611	1.0351	0.1259	4	1020	29
43.2	471.9739	0.5706	0.1661	0.0059	1.7101	0.1611	0.0549	0.0069	0.0747	0.0065	0.1903	0.9903	0.0324	1.0123	0.0586	1.0596	0.1660	1.0802	0.1326	7	995	29
43.3	149.6047	0.3900	0.1777	0.0073	1.8538	0.2224	0.0547	0.0077	0.0757	0.0085	0.1210	1.0544	0.0399	1.0648	0.0762	1.0840	0.2148	1.0758	0.1479	3	1056	36

Table 20: Detrital zircon data for Tete 1.

Sample	U ppm	Th/U	206Pb/ 238U	+/-	207Pb/ 235U	+/-	208Pb/ 232Th	+/-	207Pb/ 206Pb	+/-	208Pb/ 206Pb	+/-	206Pb/238U age (Ga)	+/-	207Pb/235U age (Ga)	+/-	207Pb/206Pb age (Ga)	+/-	208Pb/ 232Th age	+/-	% Discordance	Concordia age	+/-
1	204.4436	0.6934	0.1840	0.0065	1.8459	0.2530	0.0539	0.0071	0.0728	0.0096	0.2076	0.0379	1.0887	0.0353	1.0620	0.0865	1.0059	0.2490	1.0605	0.1349	8	1085	33
2	56.5662	0.8581	0.1482	0.0088	1.3976	0.3245	0.0401	0.0065	0.0684	0.0154	0.2375	0.0499	0.8908	0.0492	0.8879	0.1289	0.8789	0.4102	0.7950	0.1257	1	890	47
3	379.1954	0.8366	0.1608	0.0051	1.5538	0.1927	0.0436	0.0055	0.0701	0.0084	0.2319	0.0414	0.9611	0.0280	0.9520	0.0739	0.9326	0.2295	0.8625	0.1058	3	960	53
5	88.6298	1.6912	0.0865	0.0053	0.6863	0.1766	0.0244	0.0035	0.0575	0.0144	0.4877	0.0963	0.5348	0.0311	0.5306	0.1011	0.5127	0.4736	0.4875	0.0688	4	535	27
6	103.7752	0.9159	0.1750	0.0077	1.8289	0.3039	0.0572	0.0078	0.0758	0.0121	0.3058	0.0572	1.0398	0.0420	1.0559	0.1036	1.0889	0.2930	1.1244	0.1477	5	1020	37
7	382.7022	1.1865	0.1910	0.0058	2.0459	0.2419	0.0535	0.0066	0.0777	0.0089	0.3394	0.0597	1.1267	0.0315	1.1309	0.0776	1.1377	0.2148	1.0533	0.1257	1	1127	30
8	81.1246	0.6556	0.1986	0.0093	2.1383	0.3719	0.0573	0.0085	0.0781	0.0131	0.1932	0.0380	1.1675	0.0496	1.1613	0.1137	1.1475	0.3027	1.1262	0.1620	2	1167	46
9	78.0391	0.8303	0.1886	0.0091	1.9909	0.3597	0.0525	0.0076	0.0766	0.0133	0.2360	0.0460	1.1135	0.0491	1.1124	0.1153	1.1084	0.3174	1.0342	0.1463	0	1113	46
10	45.3347	0.5024	0.1866	0.0112	2.0055	0.4453	0.0570	0.0103	0.0780	0.0167	0.1567	0.0351	1.1029	0.0606	1.1174	0.1403	1.1475	0.3711	1.1209	0.1966	4	1105	57
13	117.5774	1.1068	0.0845	0.0046	0.6690	0.1526	0.0223	0.0033	0.0574	0.0127	0.2976	0.0592	0.5231	0.0271	0.5201	0.0889	0.5078	0.4248	0.4456	0.0653	3	523	26
14	157.2725	0.6212	0.1895	0.0072	1.9817	0.2875	0.0522	0.0072	0.0759	0.0106	0.1744	0.0326	1.1185	0.0390	1.1093	0.0935	1.0938	0.2539	1.0280	0.1376	2	1117	37
15	290.4921	0.6876	0.1799	0.0059	1.8768	0.2376	0.0509	0.0066	0.0757	0.0093	0.1982	0.0356	1.0662	0.0321	1.0729	0.0806	1.0840	0.2295	1.0030	0.1257	2	1067	30
16	251.7465	1.4141	0.1809	0.0061	1.8264	0.2398	0.0502	0.0063	0.0732	0.0093	0.3996	0.0708	1.0718	0.0334	1.0550	0.0827	1.0205	0.2393	0.9893	0.1202	5	1070	31
17	14.2218	0.6963	0.2496	0.0226	3.0587	0.9473	0.0696	0.0156	0.0889	0.0263	0.1977	0.0524	1.4363	0.1154	1.4224	0.2130	1.4014	0.4834	1.3595	0.2929	2	1434	110
18	35.0877	0.7782	0.3810	0.0200	7.0272	1.1336	0.1075	0.0163	0.1338	0.0204	0.2236	0.0443	2.0810	0.0926	2.1149	0.1341	2.1484	0.2441	2.0640	0.2954	3	2091	79
19	281.4834	0.7885	0.1807	0.0060	1.8686	0.2385	0.0495	0.0064	0.0750	0.0092	0.2198	0.0394	1.0710	0.0325	1.0700	0.0811	1.0693	0.2295	0.9761	0.1220	0	1071	31
20	43.9145	1.0614	0.1871	0.0115	1.9318	0.4432	0.0512	0.0080	0.0749	0.0166	0.2958	0.0608	1.1059	0.0620	1.0922	0.1430	1.0645	0.3906	1.0098	0.1538	4	1104	58
21	102.2900	0.8192	0.1921	0.0084	1.9704	0.3274	0.0526	0.0074	0.0744	0.0119	0.2284	0.0434	1.1325	0.0454	1.1054	0.1062	1.0547	0.2930	1.0368	0.1421	7	1129	42
23	140.8377	0.9771	0.1748	0.0071	1.7324	0.2705	0.0481	0.0065	0.0719	0.0108	0.2734	0.0504	1.0384	0.0388	1.0206	0.0959	0.9814	0.2832	0.9493	0.1242	6	1036	37
24	156.1036	0.4948	0.1888	0.0073	2.0594	0.2979	0.0550	0.0078	0.0791	0.0110	0.1466	0.0278	1.1147	0.0392	1.1354	0.0943	1.1768	0.2539	1.0825	0.1492	5	1117	37
25	208.6965	0.6563	0.1757	0.0063	1.8135	0.2506	0.0492	0.0066	0.0749	0.0100	0.1867	0.0342	1.0433	0.0346	1.0503	0.0866	1.0645	0.2490	0.9701	0.1268	2	1044	33
26	142.3049	0.7755	0.1868	0.0074	1.8731	0.2852	0.0539	0.0073	0.0727	0.0107	0.2274	0.0421	1.1040	0.0402	1.0716	0.0961	1.0059	0.2734	1.0612	0.1403	10	1100	38
30	79.9457	0.6225	0.1677	0.0083	1.6562	0.3134	0.0456	0.0072	0.0716	0.0131	0.1721	0.0349	0.9994	0.0456	0.9919	0.1133	0.9766	0.3320	0.9022	0.1385	2	999	43
31	112.6201	0.8419	0.1963	0.0082	2.0515	0.3221	0.0544	0.0075	0.0758	0.0115	0.2370	0.0442	1.1551	0.0438	1.1328	0.1019	1.0889	0.2783	1.0714	0.1435	6	1152	41
32	200.5818	1.0024	0.1775	0.0064	1.7521	0.2433	0.0483	0.0063	0.0716	0.0096	0.2764	0.0497	1.0534	0.0348	1.0279	0.0860	0.9766	0.2490	0.9526	0.1206	8	1050	33
34	292.9043	0.6305	0.1810	0.0059	1.7874	0.2260	0.0523	0.0068	0.0716	0.0088	0.1847	0.0331	1.0725	0.0320	1.0409	0.0792	0.9766	0.2295	1.0300	0.1303	10	1068	30
35	316.6424	0.7870	0.1840	0.0059	1.9216	0.2361	0.0509	0.0065	0.0757	0.0090	0.2207	0.0391	1.0889	0.0318	1.0886	0.0789	1.0889	0.2197	1.0033	0.1248	0	1089	30
37	160.5974	0.2164	0.1895	0.0071	2.0203	0.2877	0.0580	0.0094	0.0773	0.0106	0.0671	0.0136	1.1184	0.0385	1.1224	0.0924	1.1279	0.2539	1.1387	0.1793	1	1119	36
38	134.7300	0.9400	0.1571	0.0066	1.5151	0.2468	0.0427	0.0059	0.0700	0.0110	0.2588	0.0481	0.9406	0.0366	0.9365	0.0950	0.9277	0.2930	0.8449	0.1135	1	940	35
39	152.3449	1.0486	0.1142	0.0051	0.9697	0.1755	0.0367	0.0050	0.0616	0.0108	0.3414	0.0634	0.6973	0.0294	0.6883	0.0866	0.6592	0.3369	0.7289	0.0973	6	697	28
40	179.7229	1.0529	0.1866	0.0068	1.9768	0.2748	0.0518	0.0068	0.0768	0.0103	0.2960	0.0532	1.1031	0.0370	1.1076	0.0896	1.1182	0.2441	1.0211	0.1293	1	1012	32
41	170.9159	0.8208	0.1807	0.0068	1.9180	0.2725	0.0538	0.0072	0.0770	0.0106	0.2472	0.0449	1.0707	0.0369	1.0874	0.0906	1.1230	0.2490	1.0586	0.1370	5	1073	35
42	194.6929	0.7078	0.1700	0.0062	1.7085	0.2413	0.0481	0.0065	0.0729	0.0099	0.2027	0.0370	1.0122	0.0343	1.0117	0.0866	1.0107	0.2539	0.9500	0.1248	0	1012	32
43	416.6943	0.8544	0.1800	0.0055	1.7742	0.2101	0.0493	0.0062	0.0715	0.0082	0.2368	0.0415	1.0671	0.0298	1.0361	0.0741	0.9717	0.2148	0.9732	0.1197	10	1063	28
44	178.9567	0.4853	0.1731	0.0065	1.7215	0.2483	0.0545	0.0077	0.0721	0.0100	0.1545	0.0288	1.0294	0.0355	1.0166	0.0886	0.9863	0.2637	1.0727	0.1462	4	1028	34
46	188.7186	0.6574	0.2957	0.0097	4.2418	0.5012	0.0879	0.0114	0.1040	0.0118	0.1976	0.0352	1.6700	0.0479	1.6822	0.0927	1.6968	0.1978	1.7033	0.2113	2	1672	44
48	52.1251	0.7860	0.2001	0.0111	2.1739	0.4415	0.0628	0.0098	0.0788	0.0154	0.2492	0.0500	1.1760	0.0593	1.1727	0.1323	1.1670	0.3442	1.2311	0.1848	1	1176	55
52	169.8295	0.2681	0.0908	0.0042	0.7260	0.1407	0.0257	0.0048	0.0580	0.0109	0.0766	0.0172	0.5604	0.0249	0.5542	0.0795	0.5273	0.3662	0.5135	0.0948	6	560	24
53	300.9933	1.4124	0.1877	0.0061	1.9745	0.2441	0.0520	0.0065	0.0763	0.0091	0.3947	0.0689	1.1088	0.0328	1.1068	0.0801	1.1035	0.2197	1.0245	0.1253	0	1109	31
56	498.6356	0.7922	0.1843	0.0054	1.8679	0.2133	0.0517	0.0065	0.0735	0.0081	0.2240	0.0390	1.0906	0.0294	1.0698	0.0728	1.0254	0.2100	1.0189	0.1251	6	1088	28

57	546.1840	0.8059	0.1695	0.0050	1.7857	0.2027	0.0511	0.0064	0.0764	0.0084	0.2448	0.0426	1.0095	0.0273	1.0403	0.0713	1.1035	0.2051	1.0072	0.1233	9	1013	26
58	218.4608	0.5997	0.1818	0.0064	1.8452	0.2486	0.0497	0.0068	0.0736	0.0096	0.1653	0.0301	1.0769	0.0348	1.0617	0.0851	1.0303	0.2441	0.9810	0.1300	5	1075	33
60	186.8986	1.3303	0.2014	0.0072	2.1029	0.2855	0.0552	0.0071	0.0757	0.0099	0.3675	0.0650	1.1829	0.0385	1.1497	0.0894	1.0889	0.2393	1.0868	0.1358	9	1178	36
61	263.3314	0.9963	0.1275	0.0047	1.1387	0.1653	0.0349	0.0046	0.0648	0.0091	0.2743	0.0492	0.7734	0.0266	0.7719	0.0756	0.7666	0.2734	0.6927	0.0899	1	773	25
64	533.5044	0.6270	0.1865	0.0054	1.9101	0.2153	0.0541	0.0069	0.0743	0.0081	0.1831	0.0319	1.1026	0.0294	1.0846	0.0725	1.0498	0.2051	1.0656	0.1317	5	1100	28
66	566.7430	0.6184	0.1792	0.0052	1.8502	0.2078	0.0505	0.0064	0.0749	0.0081	0.1753	0.0306	1.0627	0.0283	1.0635	0.0714	1.0645	0.2051	0.9961	0.1236	0	1063	27
67	181.5122	0.7092	0.2017	0.0073	2.2878	0.3076	0.0590	0.0080	0.0823	0.0107	0.2088	0.0377	1.1844	0.0390	1.2085	0.0908	1.2500	0.2344	1.1595	0.1513	5	1188	37
68	92.3536	0.6521	0.1832	0.0085	1.8383	0.3219	0.0501	0.0076	0.0728	0.0123	0.1792	0.0350	1.0842	0.0459	1.0593	0.1091	1.0059	0.3125	0.9872	0.1460	8	1081	43
70	132.0795	0.4804	0.1853	0.0075	1.9676	0.3005	0.0538	0.0080	0.0770	0.0113	0.1400	0.0268	1.0958	0.0409	1.1045	0.0979	1.1230	0.2686	1.0582	0.1531	2	1097	38
71	275.5743	0.8713	0.1907	0.0063	1.9304	0.2442	0.0546	0.0071	0.0734	0.0090	0.2508	0.0442	1.1253	0.0339	1.0917	0.0813	1.0254	0.2295	1.0754	0.1354	10	1121	32
74	367.9391	0.4601	0.1803	0.0056	1.9085	0.2287	0.0525	0.0070	0.0768	0.0089	0.1345	0.0240	1.0687	0.0307	1.0841	0.0769	1.1133	0.2148	1.0349	0.1341	4	1071	29
75	133.9711	0.4371	0.1696	0.0071	1.6318	0.2623	0.0503	0.0077	0.0698	0.0108	0.1301	0.0253	1.0099	0.0389	0.9825	0.0965	0.9229	0.2881	0.9925	0.1479	10	1006	37
76	31.1354	1.1866	0.2003	0.0140	2.1279	0.5437	0.0614	0.0099	0.0771	0.0189	0.3650	0.0758	1.1768	0.0748	1.1579	0.1627	1.1230	0.4248	1.2049	0.1883	5	1174	70
78	218.7620	1.2311	0.1717	0.0062	1.7901	0.2438	0.0505	0.0066	0.0756	0.0099	0.3633	0.0640	1.0213	0.0338	1.0419	0.0851	1.0840	0.2441	0.9964	0.1259	6	1024	32
80	57.0659	0.5663	0.1592	0.0094	1.5784	0.3532	0.0455	0.0081	0.0719	0.0155	0.1620	0.0354	0.9525	0.0520	0.9618	0.1304	0.9814	0.3882	0.8986	0.1569	3	954	49
81	348.2935	0.5402	0.1565	0.0051	1.5328	0.1937	0.0453	0.0061	0.0710	0.0087	0.1565	0.0280	0.9373	0.0284	0.9436	0.0748	0.9570	0.2344	0.8948	0.1171	2	938	27
82	26.6809	0.5891	0.2057	0.0153	2.2445	0.6016	0.0634	0.0128	0.0792	0.0204	0.1820	0.0435	1.2056	0.0812	1.1951	0.1727	1.1768	0.4395	1.2428	0.2417	2	1204	76
83	73.5407	0.6530	0.2098	0.0102	2.3727	0.4162	0.0619	0.0095	0.0820	0.0138	0.1928	0.0377	1.2277	0.0539	1.2344	0.1181	1.2451	0.3003	1.2138	0.1806	1	1229	50
85	143.8862	2.0713	0.1745	0.0071	1.7506	0.2702	0.0509	0.0066	0.0728	0.0108	0.6048	0.1067	1.0367	0.0387	1.0274	0.0952	1.0059	0.2783	1.0039	0.1266	3	1036	36
86	185.7281	0.8208	0.1924	0.0070	2.0039	0.2770	0.0551	0.0074	0.0756	0.0101	0.2353	0.0422	1.1342	0.0379	1.1168	0.0896	1.0840	0.2441	1.0847	0.1419	5	1132	35
87	63.2356	1.1104	0.2025	0.0105	2.2800	0.4289	0.0601	0.0088	0.0817	0.0148	0.3296	0.0627	1.1888	0.0563	1.2061	0.1248	1.2354	0.3223	1.1798	0.1663	4	1191	53
88	583.2581	0.4523	0.1759	0.0051	1.8284	0.2048	0.0500	0.0065	0.0754	0.0082	0.1286	0.0225	1.0447	0.0279	1.0557	0.0710	1.0791	0.2026	0.9867	0.1255	3	1046	26
89	54.2946	1.2897	0.1868	0.0106	1.9954	0.4179	0.0536	0.0080	0.0775	0.0156	0.3701	0.0716	1.1039	0.0576	1.1140	0.1326	1.1328	0.3564	1.0560	0.1520	3	1105	54
90	139.8514	1.2028	0.1825	0.0074	1.8846	0.2876	0.0533	0.0072	0.0749	0.0110	0.3514	0.0630	1.0804	0.0401	1.0757	0.0965	1.0645	0.2734	1.0505	0.1370	2	1080	38
92	47.0823	0.6260	0.1727	0.0108	1.6941	0.4005	0.0475	0.0087	0.0711	0.0162	0.1721	0.0381	1.0269	0.0590	1.0063	0.1407	0.9619	0.4053	0.9388	0.1670	7	1024	56
93	233.0689	1.2987	0.1801	0.0063	1.7945	0.2406	0.0499	0.0065	0.0723	0.0094	0.3595	0.0629	1.0673	0.0343	1.0435	0.0839	0.9961	0.2393	0.9851	0.1248	7	1064	32
94	33.1233	0.7679	0.1758	0.0127	1.7766	0.4801	0.0528	0.0098	0.0733	0.0191	0.2301	0.0519	1.0440	0.0694	1.0369	0.1619	1.0205	0.4541	1.0399	0.1872	2	1043	65
95	223.3451	1.0986	0.1254	0.0049	1.1103	0.1717	0.0372	0.0050	0.0642	0.0096	0.3249	0.0581	0.7618	0.0279	0.7583	0.0794	0.7471	0.2881	0.7380	0.0971	2	761	27
96	188.1876	1.1166	0.1877	0.0069	1.8924	0.2649	0.0543	0.0072	0.0731	0.0099	0.3220	0.0569	1.1087	0.0374	1.0784	0.0890	1.0156	0.2539	1.0681	0.1374	9	1105	35
97	132.0098	0.6827	0.1920	0.0078	1.9767	0.3031	0.0586	0.0083	0.0747	0.0110	0.2078	0.0383	1.1322	0.0422	1.1076	0.0985	1.0596	0.2734	1.1512	0.1585	7	1129	39
98	470.4559	1.0956	0.1833	0.0055	1.9821	0.2267	0.0542	0.0069	0.0784	0.0087	0.3228	0.0555	1.0850	0.0298	1.1095	0.0744	1.1572	0.2051	1.0663	0.1319	6	1088	28
99	36.9805	0.5547	0.1664	0.0118	1.6295	0.4357	0.0530	0.0105	0.0710	0.0183	0.1760	0.0413	0.9925	0.0646	0.9816	0.1557	0.9570	0.4541	1.0441	0.2003	4	991	61
100	61.3914	1.4910	0.1777	0.0099	1.8090	0.3757	0.0564	0.0080	0.0738	0.0148	0.4711	0.0886	1.0546	0.0538	1.0487	0.1275	1.0352	0.3613	1.1083	0.1533	2	1054	51
101	217.7956	0.6744	0.1809	0.0065	1.9530	0.2618	0.0556	0.0076	0.0783	0.0101	0.2064	0.0369	1.0720	0.0352	1.0995	0.0863	1.1523	0.2393	1.0933	0.1443	7	2662	58
102	146.8950	1.0672	0.1520	0.0064	1.5204	0.2450	0.0466	0.0064	0.0726	0.0113	0.3257	0.0590	0.9120	0.0359	0.9387	0.0942	1.0010	0.2881	0.9209	0.1235	9	915	34
105	186.2838	0.6029	0.1810	0.0068	1.8871	0.2659	0.0509	0.0072	0.0756	0.0103	0.1687	0.0308	1.0723	0.0368	1.0766	0.0895	1.0840	0.2539	1.0042	0.1380	1	1073	35
106	306.3133	1.1679	0.1752	0.0058	1.7553	0.2223	0.0517	0.0067	0.0727	0.0089	0.3423	0.0593	1.0407	0.0317	1.0291	0.0788	1.0059	0.2295	1.0181	0.1285	3	1039	30
108	105.7955	0.7401	0.1712	0.0078	1.6838	0.2933	0.0474	0.0071	0.0713	0.0120	0.2034	0.0388	1.0187	0.0430	1.0024	0.1053	0.9668	0.3101	0.9353	0.1367	5	1017	41
109	121.3272	0.7888	0.2793	0.0106	3.6673	0.4913	0.0779	0.0108	0.0952	0.0122	0.2185	0.0393	1.5878	0.0533	1.5643	0.1016	1.5332	0.2246	1.5160	0.2007	4	1583	48
111	138.6083	0.7464	0.1865	0.0076	1.9671	0.2989	0.0523	0.0075	0.0765	0.0112	0.2080	0.0382	1.1022	0.0411	1.1043	0.0975	1.1084	0.2686	1.0311	0.1429	1	1102	39
113	292.9270	0.8314	0.2012	0.0065	2.1907	0.2682	0.0553	0.0073	0.0790	0.0093	0.2266	0.0395	1.1819	0.0350	1.1781	0.0819	1.1719	0.2148	1.0875	0.1396	1	1181	33
114	353.6012	0.4645	0.1739	0.0056	1.7113	0.2114	0.0524	0.0072	0.0714	0.0085	0.1388	0.0246	1.0338	0.0306	1.0128	0.0762	0.9668	0.2246	1.0325	0.1369	7	1031	29
115	85.3587	1.0092	0.1771	0.0087	1.8801	0.3422	0.0550	0.0080	0.0770	0.0135	0.3106	0.0582	1.0510	0.0476	1.0741	0.1140	1.1230	0.3125	1.0818	0.1527	6	1054	45
116	161.9382	1.0056	0.1899	0.0073	1.9531	0.2841	0.0537	0.0073	0.0746	0.0105	0.2819	0.0503	1.1210	0.0396	1.0995	0.0933	1.0547	0.2637	1.0574	0.1401	6	1118	37

117	211.3996	1.0231	0.1864	0.0067	1.9867	0.2679	0.0579	0.0077	0.0773	0.0100	0.3149	0.0552	1.1021	0.0363	1.1110	0.0872	1.1279	0.2393	1.1378	0.1468	2	1103	34
118	868.0308	1.0248	0.1262	0.0036	1.1412	0.1288	0.0349	0.0045	0.0656	0.0072	0.2807	0.0479	0.7660	0.0207	0.7731	0.0593	0.7910	0.2148	0.6932	0.0872	3	767	20
119	374.2086	0.6432	0.1774	0.0056	1.7882	0.2167	0.0522	0.0070	0.0731	0.0085	0.1876	0.0327	1.0530	0.0306	1.0412	0.0760	1.0156	0.2197	1.0293	0.1332	4	1051	29
120	518.5129	0.6634	0.1805	0.0053	1.7865	0.2042	0.0494	0.0065	0.0718	0.0079	0.1797	0.0310	1.0695	0.0291	1.0405	0.0718	0.9814	0.2100	0.9741	0.1243	9	1066	27
121	109.4237	0.7402	0.1834	0.0082	1.9546	0.3223	0.0600	0.0087	0.0773	0.0123	0.2396	0.0445	1.0854	0.0443	1.1000	0.1051	1.1279	0.2881	1.1771	0.1657	4	1087	42
122	236.7651	0.5936	0.1786	0.0063	1.9124	0.2533	0.0539	0.0075	0.0777	0.0099	0.1771	0.0317	1.0593	0.0344	1.0854	0.0847	1.1377	0.2344	1.0604	0.1427	7	1062	32
123	144.5086	0.9582	0.1940	0.0078	2.0754	0.3077	0.0594	0.0082	0.0776	0.0111	0.2899	0.0519	1.1433	0.0417	1.1407	0.0968	1.1377	0.2588	1.1658	0.1554	0	1143	39
124	148.3040	1.2229	0.1775	0.0072	1.7799	0.2736	0.0438	0.0060	0.0727	0.0108	0.2982	0.0535	1.0535	0.0394	1.0381	0.0953	1.0059	0.2734	0.8663	0.1168	5	1051	37
126	196.1523	0.7986	0.1855	0.0068	1.8908	0.2634	0.0509	0.0070	0.0739	0.0099	0.2168	0.0387	1.0971	0.0371	1.0779	0.0885	1.0400	0.2490	1.0044	0.1349	5	1095	35
127	483.0679	0.6808	0.1919	0.0057	1.9771	0.2251	0.0544	0.0071	0.0747	0.0082	0.1906	0.0328	1.1318	0.0308	1.1077	0.0740	1.0596	0.2100	1.0699	0.1364	7	1128	29
128	12.5465	0.5402	0.2103	0.0226	2.2405	0.8658	0.0572	0.0167	0.0773	0.0287	0.1451	0.0468	1.2303	0.1193	1.1938	0.2404	1.1279	0.6030	1.1238	0.3172	9	1224	110
129	183.0472	1.4743	0.1789	0.0068	1.8726	0.2670	0.0509	0.0068	0.0759	0.0104	0.4139	0.0724	1.0611	0.0371	1.0715	0.0903	1.0938	0.2539	1.0026	0.1298	3	1062	35
131	326.7089	0.1910	0.1543	0.0052	1.4364	0.1879	0.0418	0.0067	0.0675	0.0085	0.0510	0.0100	0.9249	0.0290	0.9042	0.0754	0.8545	0.2441	0.8271	0.1304	8	923	27
132	397.6109	0.7302	0.1849	0.0057	1.8612	0.2214	0.0512	0.0068	0.0730	0.0084	0.1995	0.0345	1.0938	0.0312	1.0674	0.0757	1.0156	0.2148	1.0092	0.1302	8	1090	29
133	27.5794	0.7705	0.1786	0.0143	1.7713	0.5288	0.0501	0.0102	0.0719	0.0207	0.2133	0.0511	1.0592	0.0775	1.0350	0.1773	0.9863	0.4932	0.9882	0.1948	7	1056	73

Table 21: Detrital zircon data for Tete 3.

Sample	U ppm	Th/U	206Pb/ 238U	+/-	207Pb/ 235U	+/-	208Pb/ 232Th	+/-	207Pb/ 206Pb	+/-	208Pb/ 206Pb	+/-	206Pb/238U age (Ga)	+/-	207Pb/235U age (Ga)	+/-	207Pb/206Pb age (Ga)	+/-	208Pb*/232Th age (Ga)	+/-	% Discordance	Concordia age (Ma)	+/-
2	120.7840	2.0395	0.2044	0.0080	2.1934	0.3488	0.0566	0.0075	0.0778	0.0120	0.5747	0.0851	1.1992	0.0429	1.1789	0.1053	1.1426	0.2783	1.1135	0.1421	5	1197	40
3	104.6330	0.5010	0.1779	0.0076	1.7997	0.3096	0.0529	0.0081	0.0734	0.0122	0.1513	0.0253	1.0556	0.0412	1.0453	0.1065	1.0254	0.3027	1.0413	0.1542	3	1054	39
4	76.2783	0.7256	0.1410	0.0071	1.3073	0.2702	0.0397	0.0063	0.0673	0.0135	0.2075	0.0362	0.8502	0.0403	0.8489	0.1124	0.8447	0.3711	0.7864	0.1218	1	850	39
5	188.6123	1.1977	0.1741	0.0063	1.7460	0.2654	0.0501	0.0067	0.0728	0.0107	0.3502	0.0520	1.0344	0.0346	1.0257	0.0937	1.0059	0.2734	0.9884	0.1276	3	1034	33
6	259.9551	0.7267	0.1770	0.0060	1.7831	0.2560	0.0490	0.0066	0.0730	0.0102	0.2043	0.0304	1.0508	0.0326	1.0393	0.0894	1.0156	0.2588	0.9676	0.1263	3	1050	31
9	212.3424	0.5758	0.1766	0.0062	1.8233	0.2699	0.0489	0.0068	0.0749	0.0108	0.1616	0.0247	1.0486	0.0339	1.0539	0.0927	1.0645	0.2637	0.9658	0.1300	1	1049	32
10	221.6803	0.8049	0.2038	0.0069	2.1897	0.3133	0.0571	0.0076	0.0779	0.0108	0.2282	0.0338	1.1959	0.0368	1.1778	0.0951	1.1426	0.2539	1.1218	0.1447	5	1194	35
11	42.7312	0.5764	0.1488	0.0092	1.4770	0.3601	0.0504	0.0090	0.0720	0.0170	0.1974	0.0385	0.8942	0.0515	0.9210	0.1378	0.9863	0.4150	0.9942	0.1728	9	897	49
12	28.0167	0.6594	0.1770	0.0123	1.8358	0.4857	0.0584	0.0109	0.0752	0.0192	0.2200	0.0447	1.0503	0.0668	1.0584	0.1605	1.0742	0.4443	1.1478	0.2064	2	1051	63
13	283.4067	0.7537	0.1794	0.0059	1.8993	0.2683	0.0572	0.0075	0.0768	0.0106	0.2425	0.0355	1.0636	0.0321	1.0809	0.0899	1.1133	0.2539	1.1235	0.1431	4	1065	31
14	544.9378	1.2003	0.1912	0.0057	2.0053	0.2636	0.0532	0.0068	0.0761	0.0097	0.3372	0.0480	1.1280	0.0305	1.1173	0.0854	1.0986	0.2344	1.0483	0.1295	3	1127	29
15	526.1293	0.6885	0.1940	0.0057	2.0589	0.2710	0.0545	0.0070	0.0770	0.0099	0.1950	0.0280	1.1431	0.0310	1.1352	0.0862	1.1182	0.2393	1.0723	0.1341	2	1142	30
16	643.3478	0.3802	0.1784	0.0052	1.7744	0.2327	0.0552	0.0072	0.0721	0.0092	0.1185	0.0172	1.0581	0.0284	1.0361	0.0818	0.9912	0.2393	1.0852	0.1375	7	1056	27
17	40.3388	1.4636	0.1920	0.0111	2.1458	0.4697	0.0577	0.0085	0.0810	0.0171	0.4434	0.0735	1.1324	0.0595	1.1637	0.1413	1.2207	0.3687	1.1347	0.1611	7	1136	56
19	253.8571	0.5344	0.1906	0.0063	2.0305	0.2893	0.0522	0.0071	0.0773	0.0107	0.1474	0.0221	1.1247	0.0340	1.1258	0.0926	1.1279	0.2539	1.0293	0.1354	0	1125	32
20	72.4375	0.4588	0.1743	0.0083	1.7685	0.3394	0.0575	0.0093	0.0736	0.0137	0.1521	0.0267	1.0357	0.0454	1.0340	0.1174	1.0303	0.3369	1.1292	0.1765	1	1035	43
21	476.8314	1.2413	0.2029	0.0060	2.1226	0.2821	0.0533	0.0068	0.0759	0.0098	0.3276	0.0465	1.1911	0.0322	1.1562	0.0878	1.0938	0.2393	1.0505	0.1293	9	1187	31
22	106.3850	0.9181	0.1940	0.0079	2.1310	0.3531	0.0633	0.0087	0.0797	0.0128	0.3007	0.0459	1.1428	0.0424	1.1589	0.1085	1.1914	0.2856	1.2407	0.1638	4	1145	40
23	110.8168	0.3235	0.1689	0.0070	1.7788	0.3042	0.0532	0.0086	0.0764	0.0127	0.1022	0.0178	1.0061	0.0386	1.0377	0.1055	1.1035	0.3027	1.0473	0.1635	9	1009	37
24	15.3071	1.4418	0.1891	0.0165	1.9805	0.6513	0.0534	0.0096	0.0759	0.0241	0.4082	0.0833	1.1167	0.0890	1.1089	0.2007	1.0938	0.5322	1.0517	0.1834	2	1116	84
25	270.2857	0.4887	0.1719	0.0057	1.7387	0.2516	0.0566	0.0076	0.0733	0.0103	0.1612	0.0240	1.0227	0.0312	1.0230	0.0892	1.0254	0.2588	1.1128	0.1448	0	1023	30
26	98.0251	0.5971	0.1794	0.0076	1.8110	0.3178	0.0511	0.0076	0.0732	0.0125	0.1702	0.0278	1.0635	0.0415	1.0494	0.1087	1.0205	0.3125	1.0064	0.1451	4	1062	39
27	185.4442	0.5422	0.1792	0.0064	1.8189	0.2778	0.0502	0.0070	0.0736	0.0109	0.1521	0.0233	1.0624	0.0347	1.0523	0.0954	1.0303	0.2734	0.9902	0.1336	3	1061	33
28	158.6855	0.5602	0.1873	0.0068	1.8816	0.2940	0.0515	0.0072	0.0729	0.0111	0.1540	0.0238	1.1068	0.0371	1.0746	0.0986	1.0107	0.2783	1.0143	0.1382	10	1103	35
29	185.4966	0.3839	0.1822	0.0064	1.8124	0.2770	0.0540	0.0077	0.0722	0.0107	0.1138	0.0179	1.0788	0.0350	1.0499	0.0954	0.9912	0.2734	1.0633	0.1476	9	1076	33
30	434.8734	0.4260	0.1938	0.0058	2.1209	0.2857	0.0566	0.0074	0.0794	0.0104	0.1243	0.0181	1.1420	0.0313	1.1556	0.0889	1.1816	0.2393	1.1128	0.1413	3	1143	30
31	332.2176	0.5360	0.1861	0.0058	1.9590	0.2732	0.0509	0.0067	0.0764	0.0104	0.1463	0.0215	1.1001	0.0315	1.1015	0.0897	1.1035	0.2490	1.0036	0.1287	0	1100	30
32	192.0124	1.1148	0.1904	0.0066	1.9261	0.2903	0.0548	0.0071	0.0734	0.0108	0.3201	0.0466	1.1236	0.0356	1.0902	0.0960	1.0254	0.2686	1.0790	0.1360	10	1120	34
35	102.5450	2.3736	0.1691	0.0071	1.7387	0.3055	0.0504	0.0065	0.0746	0.0127	0.7039	0.1035	1.0073	0.0392	1.0230	0.1074	1.0547	0.3125	0.9938	0.1251	4	1009	37
36	862.6798	0.5622	0.1895	0.0053	2.0757	0.2692	0.0550	0.0069	0.0794	0.0101	0.1624	0.0229	1.1187	0.0284	1.1408	0.0852	1.1816	0.2344	1.0827	0.1323	5	1121	27
37	56.0390	0.5721	0.1796	0.0092	1.9334	0.3923	0.0580	0.0093	0.0781	0.0153	0.1838	0.0323	1.0648	0.0499	1.0927	0.1275	1.1475	0.3467	1.1401	0.1769	7	1068	47
38	214.4589	1.6277	0.1794	0.0061	1.9124	0.2845	0.0553	0.0070	0.0773	0.0112	0.4983	0.0713	1.0639	0.0333	1.0854	0.0946	1.1279	0.2637	1.0876	0.1339	6	1066	32
42	50.3217	0.9392	0.3033	0.0136	4.5590	0.7683	0.0871	0.0123	0.1090	0.0177	0.2671	0.0419	1.7076	0.0671	1.7418	0.1314	1.7822	0.2710	1.6879	0.2268	4	1714	62
43	73.7784	0.5352	0.1891	0.0086	2.0325	0.3752	0.0559	0.0086	0.0779	0.0139	0.1565	0.0265	1.1166	0.0462	1.1265	0.1184	1.1475	0.3174	1.0988	0.1643	3	1118	44
44	84.0130	0.6164	0.1684	0.0075	1.7083	0.3184	0.0475	0.0072	0.0736	0.0133	0.1720	0.0286	1.0036	0.0415	1.0116	0.1129	1.0303	0.3271	0.9381	0.1379	3	1004	40
45	194.3299	1.0439	0.1818	0.0063	1.9705	0.2975	0.0542	0.0070	0.0786	0.0116	0.3079	0.0447	1.0770	0.0341	1.1055	0.0969	1.1621	0.2686	1.0676	0.1339	7	1080	33
46	213.9860	0.8011	0.1831	0.0062	1.9148	0.2859	0.0543	0.0071	0.0759	0.0110	0.2348	0.0343	1.0837	0.0335	1.0862	0.0950	1.0938	0.2637	1.0686	0.1352	1	1084	32
48	56.7455	1.0882	0.1776	0.0090	1.7555	0.3648	0.0491	0.0071	0.0717	0.0144	0.2967	0.0484	1.0541	0.0489	1.0292	0.1262	0.9766	0.3662	0.9680	0.1372	8	1051	46
49	405.1679	0.7670	0.1906	0.0057	2.0808	0.2861	0.0557	0.0070	0.0792	0.0106	0.2211	0.0314	1.1245	0.0306	1.1425	0.0902	1.1768	0.2441	1.0951	0.1343	4	1126	29
50	148.5091	0.7359	0.1927	0.0070	2.0846	0.3270	0.0566	0.0076	0.0785	0.0120	0.2132	0.0319	1.1361	0.0376	1.1437	0.1023	1.1572	0.2783	1.1134	0.1446	2	1137	36
51	192.2557	1.5340	0.1707	0.0059	1.7149	0.2658	0.0486	0.0062	0.0728	0.0110	0.4302	0.0617	1.0161	0.0326	1.0141	0.0948	1.0107	0.2783	0.9598	0.1187	1	1016	31
52	492.8349	0.6990	0.1788	0.0052	1.8436	0.2525	0.0492	0.0062	0.0748	0.0100	0.1893	0.0268	1.0605	0.0284	1.0612	0.0864	1.0645	0.2441	0.9712	0.1192	0	1061	27
54	288.1177	0.7624	0.5493	0.0153	14.8197	1.9085	0.1472	0.0183	0.1957	0.0246	0.2008	0.0280	2.8223	0.0634	2.8037	0.1157	2.7905	0.1917	2.7757	0.3190	1	2818	57
55	78.2698	0.5569	0.1759	0.0079	1.8429	0.3442	0.0554	0.0083	0.0760	0.0138	0.1723	0.0286	1.0445	0.0431	1.0609	0.1161	1.0938	0.3271	1.0898	0.1590	5	1046	41
57	48.9475	0.8942	0.1725	0.0092	1.7477	0.3823	0.0475	0.0073	0.0735	0.0156	0.2415	0.0414	1.0261	0.0507	1.0263	0.1323	1.0254	0.3809	0.9378	0.1409	0	1026	48
58	274.7365	0.4223	0.1816	0.0058	1.8583	0.2708	0.0507	0.0068	0.0742	0.0106	0.1156	0.0172	1.0755	0.0313	1.0664	0.0919	1.0498	0.2588	0.9990	0.1300	2	1075	30
59	46.7819	1.1038	0.1914	0.0101	2.0297	0.4301	0.0548	0.0080	0.0769	0.0158	0.3097	0.0508	1.1292	0.0542	1.1255	0.1348	1.1182	0.3613	1.0782	0.1529	1	1129	51
60	187.0177	0.5161	0.1687	0.0059	1.7507	0.2729	0.0512	0.0070	0.0753	0.0114	0.1536	0.0232	1.0050	0.0324	1.0274	0.0960	1.0742	0.2783	1.0099	0.1334	6	1007	31
61	464.5283	0.6671	0.1821	0.0053	1.9116	0.2641	0.0523	0.0066	0.0761	0.0103	0.1873	0.0264	1.0786	0.0288	1.0852	0.0881	1.0986	0.2490	1.0299	0.1256	2	1079	28
62	29.8071	0.7510	0.1909	0.0120	2.0413	0.5050	0.0611	0.0103	0.0775	0.0186	0.2349	0.0437	1.1263	0.0648	1.1294	0.1560	1.1328	0.4150	1.1984	0.1954	1	1127	61
63	61.1746	0.7270	0.1945	0.0092	2.0115	0.3935	0.0551	0.0082	0.0750	0.0142	0.2012	0.0332	1.1459	0.0493	1.1194	0.1247	1.0693	0.3418	1.0840	0.1568	7	1143	47

67	**112.2355**	**0.5707**	**0.1687**	**0.0067**	**1.7300**	**0.3005**	**0.0521**	**0.0074**	**0.0744**	**0.0126**	**0.1717**	**0.0270**	**1.0051**	**0.0371**	**1.0198**	**0.1060**	**1.0498**	**0.3076**	**1.0257**	**0.1413**	**4**	**1006**	**36**
68	**64.9022**	**0.7714**	**0.1697**	**0.0081**	**1.7448**	**0.3498**	**0.0503**	**0.0074**	**0.0746**	**0.0145**	**0.2231**	**0.0367**	**1.0102**	**0.0447**	**1.0252**	**0.1218**	**1.0547**	**0.3516**	**0.9927**	**0.1428**	**4**	**1012**	**43**
69	**402.8129**	**0.5968**	**0.1852**	**0.0054**	**1.9189**	**0.2694**	**0.0545**	**0.0069**	**0.0751**	**0.0103**	**0.1710**	**0.0242**	**1.0956**	**0.0295**	**1.0877**	**0.0897**	**1.0742**	**0.2515**	**1.0723**	**0.1312**	**2**	**1095**	**28**